Università degli Studi di Palermo

AREA RICERCA E TRASFERIMENTO TECNOLOGICO
SETTORE DOTTORATI E CONTRATTI PER LA RICERCA
U. O. DOTTORATI DI RICERCA

Dottorato di Ricerca in:
SISTEMI AGRO-ALIMENTARI E FORESTALI MEDITERRANEI
Dipartimento di Scienze Agrarie, Alimentari e Forestali
Settore Scientifico Disciplinare – AGR-04/A Idraulica agraria e sistemazioni idraulico-forestali

OPTIMISING DRIP IRRIGATION DESIGN AND MANAGEMENT TO ENHANCE WATER AND ENERGY EFFICIENCY

IL DOTTORE
GIROLAMO VACCARO

IL COORDINATORE
PROF. ING. MASSIMO IOVINO

IL TUTOR
PROF. ING. MASSIMO IOVINO

I CO TUTORS
PROF. ING. GIORGIO BAIAMONTE
PROF. ANTONIO MOTISI

CICLO XXXVIII
ANNO 2026

Table of contents

General Introduction

Efficient management of water and energy is crucial for irrigated agriculture, particularly under climate change and increasing water scarcity in arid and semi-arid areas (Galindo et al., 2018), amid a persistent rise in energy costs. Intensifying droughts are expected to increase crop stress and reduce water resources, leading to declines in agricultural productivity (Ciais et al., 2005). At the same time, rising energy prices have heightened attention to energy-use efficiency, as irrigation pumping alone accounts for 23−48% of total on-farm energy consumption worldwide (Singh et al., 2002). The energy required for pumping depends on crop water demand, total dynamic head, discharge rate, and overall system efficiency, directly influencing both water-use effectiveness and operational costs.

Among irrigation methods, drip irrigation (DI) is widely recognised as one of the most water-efficient and precise systems, as it significantly reduces losses from evaporation, surface runoff, and deep percolation (Ravikumar, 2023; Singh and Su, 2022). Subsurface drip irrigation (SDI) advances this technology by employing buried emitters to further effectively reduce water loss due to evaporation, deliver water and nutrients directly to the rhizosphere, and improve water use efficiency and energy saving (Cahn and Hutmacher, 2024; Camp, 1998; Provenzano, 2007).

Although DI irrigation systems are designed based on energy criteria by imposing head-loss limits (Baiamonte, 2016, 2018a, 2018b; Jiang and Kang, 2010; Ma et al., 2019), this design approach remains poorly developed and limited for SDI. Additionally, the adoption and potential benefits of looped configurations in surface DI systems, such as further improvements in pressure head and flow rate distribution or energy savings, are not typically considered. This limitation arises because the looped networks determine different flow directions within the pipes, which cannot be accurately represented using the conventional hydraulic design methodologies developed for surface DI systems. The analysis of such systems involves solving nonlinear network equations, which require iterative numerical methods.

In consideration of the above, SDI systems or closed circuits of traditionally surface DI systems can be analysed as looped networks, in which each emitter is considered as a node. Among the various numerical methods available, the Hardy Cross method (Cross, 1936), originally developed for manual calculations in civil engineering, remains a reliable and conceptually straightforward technique for verifying flow rate and pressure head distributions in looped hydraulic networks. This method determines the discharge and pressure head distribution across pipes and nodes based on the network's geometric characteristics and boundary conditions. The Hardy Cross procedure iteratively adjusts the flow in each pipe by introducing corrective discharges to satisfy energy balance within each loop. However, as network size and complexity increase, the number of required iterations can become excessive, potentially reducing computational efficiency. Nevertheless, this limitation is generally not critical for irrigation systems, which are typically characterised by a relatively small number of loops.

Although SDI systems offer numerous advantages, they also present a few notable drawbacks. The main limitations include (i) the emitter clogging caused by root intrusion and soil particle suction, which can substantially reduce irrigation uniformity (Lamm et al., 2021; Shi et al., 2022), and (ii) the occurrence of positive pressure around the emitter, also denoted as back pressure (Philip, 1992), which may limit the emitter flow rate. The potential development of back pressure can lead to the delivery of smaller water volumes than those originally specified in the system design.

Various strategies have been proposed to prevent root intrusion, typically involving the application of diluted acids or herbicides, or the use of root-guard emitters (Suarez-Rey et al., 2006). Root-growth inhibitors are often incorporated into emitter or pipe materials, using polymers infused with controlled-release agents or by embedding herbicides directly within the emitter structure. Some emitter designs are also equipped with anti-siphon mechanisms; however, such systems have proven more effective in preventing soil particle ingestion than root intrusion (Petroselli et al., 2022).

The development of positive pressure around the emitter can also significantly influence the hydraulic performance of buried emitters. Philip (1992) first investigated water movement from a buried point source and demonstrated that, in most soils, when the emitter discharge exceeds the soil infiltration capacity, a spherical saturated zone characterised by positive pressure forms around the source, thereby reducing the local pressure gradient near the emitter. Furthermore, Philip (1992) derived an analytical expression for estimating back pressure as a function of the soil's hydraulic properties, the emitter flow rate, and the so-called cavity radius, defined as the radius of the saturated spherical region that develops around the discharge point source.

To enhance water use efficiency (WUE) in DI and SDI systems, a comprehensive understanding of soil water dynamics, particularly through the soil's hydraulic characterisation, is essential. The wetted bulb determined by buried or surface emitters should be developed in the active root zone, thereby maximising root water uptake while minimising losses due to evaporation and percolation (Fernández-Gálvez and Simmonds, 2006; Kandelous and Šimůnek, 2010a, 2010b; Subbaiah, 2013).

Philip (1984) developed an analytical solution to estimate the positions of the wetting front from both surface and buried point sources. Specifically, Philip (1984) provided closed-form dimensionless solutions in spherical polar coordinates for the travel times of water particles, assuming homogeneous soil hydraulic properties. However, the accuracy of the model diminishes in cases involving heterogeneous soils, dynamic boundary conditions, or when gravitational effects become significant (Subbaiah, 2013). Furthermore, Philip's model introduces uncertainties regarding the selection of the average volumetric water content behind the wetting front (θ_{avg}), a parameter that is insufficiently defined in the original work and inconsistently treated in subsequent literature.

Cook et al. (2003) and Thorburn et al. (2003) addressed this issue assuming the water content at the wetting front as the θ_{avg} value when the soil hydraulic conductivity was equal to 1 mm d^{-1} and 1 mm h^{-1}, respectively. In addition, Cook et al. (2003) estimated θ_{avg} at the burial plane, using the steady-state solution proposed by Raats (1971), which incorporates an exponential dependence of diffusivity on water content across a wide range of soils. Specifically, a comparison with a constant value of θ_{avg} was performed, generally resulting in θ_{avg} underestimation at small radii of the wetted bulb and θ_{avg} overestimation at large radii.

Because soil properties exhibit significant spatial variability, using a single representative wetting pattern may be inadequate for the efficient design of drip irrigation systems. Consequently, localised irrigation design should account not only for the mean values of soil hydraulic properties but also for their spatial variability. Several studies have investigated the variability of saturated and unsaturated hydraulic conductivity in agricultural soils (e.g., Das Gupta et al., 2006); however, the influence of such variability on soil-water dynamics under drip irrigation remains relatively underexplored.

To determine soil hydraulic characteristic curves, numerous laboratory and field-based methods have been developed (Angulo-Jaramillo et al., 2000; Mallants et al., 1997; Šimůnek et al., 1998; Raimbault, 1986). Haverkamp et al. (1996) introduced a simplified field-based procedure known as the Beerkan method, which enables rapid characterisation of soil hydraulic properties. This approach employs analytical formulations of the hydraulic characteristic curves and estimates their shape parameters based on soil texture, derived from basic particle-size analysis. Scale parameters, which depend on soil structure, are determined from field infiltration experiments conducted at zero pressure head. Subsequently, Lassabatère et al. (2006) proposed an enhanced version, the Beerkan Estimation of Soil Transfer (BEST) parameters method, which has shown considerable promise for accurately describing the hydrodynamic behaviour of soils under drip irrigation (Mubarak et al., 2009).

DI or SDI systems can deliver water with a high degree of uniformity. However, uniformity alone does not ensure efficient irrigation performance. To further optimise WUE, effective irrigation scheduling is equally essential in micro-irrigation systems (Barragan et al., 2010). Therefore, achieving optimal irrigation requires both the appropriate design of irrigation systems and the implementation of management practices that supply water in volumes precisely aligned with crop water requirements. A key component of refining irrigation scheduling is the accurate assessment of plant water status. Numerous studies have emphasised the importance of stem water potential (Ψ_{stem}), which is widely recognised as a reliable indicator of plant water status and a valuable criterion for irrigation management (Choné, 2001; Jones, 2004; Ortuño et al., 2006).

Traditionally, Ψ_{stem} is measured with the Scholander pressure chamber (Scholander et al., 1965). Although this is a reliable measurement, it is destructive, time-consuming, and does not provide real-time continuous data on the plant water status. Moreover, Levin (2019) examined several factors influencing the accuracy of Ψ_{stem} estimation using the pressure chamber (Ψ_{pc}), finding that the operator effect consistently exerted the greatest influence on measurement precision.

Recognising the importance of Ψ_{stem} as a key indicator of crop water status, several probes have been developed to enable its continuous monitoring. Among these, Pagay et al. (2014) developed the microtensiometer (MT), a microelectromechanical pressure sensor capable of measuring water potentials of external matrices below −10 MPa. The MT is inserted directly into plant tissue, allowing for continuous, real-time measurements of Ψ_{stem} and representing a significant advancement in monitoring plant water status. Recent studies have evaluated the field performance of MTs across a range of crops, including kiwifruit (Di Biase et al., 2025), cotton (Christenson et al., 2024), pear (Blanco and Kalcsits, 2023), nectarine (Conesa et al., 2023), and grapevine (Pagay, 2022). Despite the implementation of MTs in these crops, their application in mandarin species has not yet been explored. Citrus orchards are among the most adaptable perennial fruit systems to Mediterranean climatic conditions. In Sicily, mandarin orchards have traditionally been irrigated using under-canopy micro-sprinkler systems operating at low irrigation frequencies. However, in response to the region's semi-arid climate and recurrent water scarcity, there is an increasing trend toward adopting more efficient irrigation technologies, such as DI or SDI systems, to enhance water use efficiency and sustain crop productivity.

Building upon the theoretical and practical framework outlined above, this PhD thesis aims to address the dual water-energy challenge by integrating design criteria, soil hydrological processes, and plant water status monitoring to improve the efficiency of localised irrigation systems. Most of these studies were carried out in a long-term experimental mandarin orchard in Sicily between 2018 and 2023, combining multi-year field observations with analytical and numerical modelling, alongside continuous monitoring of crop water status. In the next section, the structure and objectives of the PhD thesis are briefly summarised.

Structure and Objectives of the PhD Thesis

This thesis aims to consolidate the results of three years of doctoral research, during which various topics were explored, all sharing a common focus on improving localised irrigation efficiency. Indeed, the objective of this thesis has been to address the theme of localised irrigation efficiency from multiple perspectives: (i) assessing hydraulic performance and energy saving potential by using closed drip irrigation circuits in substitution of open drip irrigation circuits, (ii) testing different emitters and quantifying the α coefficient of local losses due to root intrusion in subsurface drip irrigation systems, (iii) evaluating the wetted bulb size sensitivity to soil hydraulic properties for both surface and subsurface emitters, (iv) exploring the impact of average water content on wetting bulb expansion by using Philip's analytical model (1984) from a buried point source, and (v) assessing the efficiency of microtensiometers for monitoring stem water potential in mandarin (*Citrus reticulata* Blanco) orchard under different irrigation regimes by using a subsurface drip irrigation system and a micro-sprinkler irrigation system.

Chapter 1 is based on the paper *"Closed circuits of drip laterals versus open circuits: hydraulic performance and energy-saving potential"* published in *Irrigation Science* (Baiamonte et al., 2024b), which investigates and compares, for rectangular irrigation units of fixed geometry, the hydraulic performance and energy-saving potential of open and closed circuits of drip laterals. Given that closed circuits typically contain a limited number of loops, the original formulation of the Hardy Cross numerical method (Cross, 1936) can be effectively applied to determine the distribution of pressure heads and flow rates with a relatively small number of iterations. In this study, the Hazen-Williams resistance equation was considered in the Hardy Cross method, as it provides a more suitable representation of friction losses in polyethylene pipes commonly used in drip systems. Open circuits were designed using the analytical **IrriLab** method (Baiamonte, 2018b), whereas the corresponding closed circuits were evaluated through the Hardy Cross iterative approach. Furthermore, a simplified predictive relationship was developed for rectangular irrigation units with varying geometries, pipe diameters, emitter spacing, and discharge rates, enabling estimation of the energy savings achievable by converting open circuits into closed configurations through the addition of a secondary manifold.

Chapter 2 is based on the paper *"Quantifying local losses due to root intrusion in subsurface drip irrigation systems by monitoring inlet discharge and pressure head"* published in *Irrigation Science* (Baiamonte et al., 2024c), which focuses on quantifying local losses caused by root intrusion in experimental buried emitters of a subsurface drip irrigation system. An extended version of the Hardy Cross method (Cross, 1936), which considers local losses, the Hazen-Williams resistance equation for friction losses and the back pressure phenomenon at the emitter outlet, was used to assess the hydraulic performance of different emitters over six years of field operation (2018−2023). The study was conducted for four subunits of a subsurface drip irrigation system installed in the experimental field of Villabate (Sicily, Italy). Subunits #1, #3 and #4 were equipped with emitters containing root-growth inhibitors: Copper, Herbicide 1, and Herbicide 2. Whereas subunit #2 served as the control, with no root guard treatment. The hydraulic characterisation of the soil, necessary to estimate the back pressure, was first carried out with the BEST procedure (Lassabatère et al., 2006). Subsequently, the application of the revised Hardy Cross Method made it possible to detect the increase in the fraction α of the kinetic head, which accounts for local losses, also due to root intrusion.

Chapter 3 is based on the paper *"Influence of soil hydraulic parameters on bulb size for surface and buried emitters"* published in *Agricultural Water Management* (Baiamonte et al., 2024a), which investigates soil-water dynamics beneath emitters in drip irrigation systems. Using an extensive dataset of soil hydraulic parameters measured in an untilled citrus orchard with predominantly sandy-loam and loam textures, the study examined how variability in soil hydraulic properties influences the development of the wet bulb for both buried and surface emitters. Philip's (1984) analytical model was applied to both buried and surface point sources to evaluate the resulting wetting patterns and assess their dependence on soil hydraulic variability.

To bridge the existing knowledge gap concerning the average volumetric soil water content behind the wetting front (Philip,1984), Chapter 4, based on the paper *"Exploring the impact of average water content on wetting bulb expansion from a buried point source"* published in *Agricultural Water Management* (Baiamonte et al., 2025), further explores the influence of the average volumetric soil water content on the expansion of the wetted bulb generated by a buried point source. Continuous monitoring of soil moisture and wetting front travel time was conducted using a soil moisture probe over six consecutive years (2018−2023) in the Villabate subsurface drip irrigation system. Following soil hydraulic characterisation, performed with the BEST procedure (Lassabatère et al., 2006), Philip's model was calibrated using 832 paired measurements of initial soil water content and travel time. The intraseasonal variability of the average volumetric water content was then analysed and interpreted to provide deeper insight into soil-water interactions under field conditions. Results substantially improved the accuracy of travel time estimation, reducing the standard error of the estimate from 4 h to 26 min, which was moderate considering the temporal resolution of data acquisition (20 min).

Finally, Chapter 5, based on the paper *"Assessing microtensiometers for monitoring stem water potential in mandarin (Citrus reticulata Blanco) orchard under different irrigation regimes"* published in *Agricultural Water Management* (Vaccaro et al., 2025), explores the plant-scale response to water availability through the continuous monitoring of stem water potential using microtensiometers. The study aimed to assess the suitability of this innovative technology for evaluating the water status of mandarin trees under Mediterranean climatic conditions within the framework of precision irrigation. To this end, the performance of microtensiometers was tested under two contrasting irrigation regimes: a high-frequency regime, designed to maintain well-watered soil conditions through the Villabate subsurface drip irrigation system, and a conventional low-frequency regime representative of typical local practices, implemented via a micro-sprinkler system. The research evaluated the accuracy of stem water potential measurements obtained with microtensiometers in comparison with the standard Scholander pressure chamber technique, examined their responsiveness to short-term perturbations such as shading trials, and analysed their sensitivity to variations in climatic conditions.

Overall, the research activity presented in this thesis contributes to optimising surface and subsurface drip irrigation system hydraulic performance, elucidating soil-water dynamics, and refining plant-based irrigation management. Collectively, these advances improve both water and energy use efficiency, promoting the implementation of precision irrigation strategies under Mediterranean conditions, particularly in Citrus orchards.

References

Angulo-Jaramillo, R., Vandervaere, J.P., Roulier, S., Thony, J.L., Gaudet, J.P., Vauclin, M., 2000. Field measurement of soil surface hydraulic properties by disc and ring infiltrometers: A review and recent developments. Soil Tillage Res. 55(1-2): 1-29. https://doi.org/10.1016/S0167-1987(00)00098-2

Baiamonte, G., 2016. Simple Relationships for the Optimal Design of Paired Drip Laterals on Uniform Slopes. J. Irrig. Drain. Eng. 142, 04015054. https://doi.org/10.1061/(ASCE)IR.1943-4774.0000971

Baiamonte, G., 2018a. Advances in designing drip irrigation laterals. Agric. Water Manag. 199, 157–174. https://doi.org/10.1016/j.agwat.2017.12.015

Baiamonte, G., 2018b. Explicit relationships for optimal designing rectangular microirrigation units on uniform slopes: The IrriLab software application. Comput. Electron. Agric. 153, 151–168. https://doi.org/10.1016/j.compag.2018.08.005

Baiamonte, G., Alagna, V., Autovino, D., Iovino, M., Palermo, S., Vaccaro, G., Bagarello, V., 2024a. Influence of soil hydraulic parameters on bulb size for surface and buried emitters. Agric. Water Manag. 295, 108756. https://doi.org/10.1016/j.agwat.2024.108756

Baiamonte, G., Vaccaro, G., Palermo, S., 2024b. Closed circuits of drip laterals versus open circuits: hydraulic performance and energy-saving potential. Irrig. Sci. https://doi.org/10.1007/s00271-024-00981-z

Baiamonte, G., Vaccaro, G., Palermo, S., 2024c. Quantifying local losses due to root intrusion in subsurface drip irrigation systems by monitoring inlet discharge and pressure head. Irrig. Sci. https://doi.org/10.1007/s00271-024-00990-y

Baiamonte, G., Franco, L., Vaccaro, G., 2025. Exploring the impact of average water content on wetting bulb expansion from a buried point source. Agric. Water Manag. 321, 109889. https://doi.org/10.1016/j.agwat.2025.109889

Barragan, J., Cots, L., Monserrat, J., Lopez, R., Wu, I.P., 2010. Water distribution uniformity and scheduling in micro-irrigation systems for water saving and environmental protection. Biosyst. Eng. 107, 202–211. https://doi.org/10.1016/j.biosystemseng.2010.07.009

Blanco, V., Kalcsits, L., 2023. Long-term validation of continuous measurements of trunk water potential and trunk diameter indicate different diurnal patterns for pear under water limitations. Agric. Water Manag. 281, 108257. https://doi.org/10.1016/j.agwat.2023.108257

Cahn, M., Hutmacher, R., 2024. Subsurface drip irrigation. Microirrigation for Crop Production. Elsevier Science, pp 257–301

Camp, C.R., 1998. SUBSURFACE DRIP IRRIGATION: A REVIEW. Trans. ASAE 41, 1353–1367. https://doi.org/10.13031/2013.17309

Choné, X., 2001. Stem Water Potential is a Sensitive Indicator of Grapevine Water Status. Ann. Bot. 87, 477–483. https://doi.org/10.1006/anbo.2000.1361

Christenson, C.G., Gohardoust, M.R., Calleja, S., Thorp, K.R., Tuller, M., Pauli, D., 2024. Monitoring cotton water status with microtensiometers. Irrig. Sci. 42, 995–1011. https://doi.org/10.1007/s00271-024-00930-w

Ciais, Ph., Reichstein, M., Viovy, N., Granier, A., Ogée, J., Allard, V., Aubinet, M., Buchmann, N., Bernhofer, Chr., Carrara, A., Chevallier, F., De Noblet, N., Friend, A.D., Friedlingstein, P., Grünwald, T., Heinesch, B., Keronen, P., Knohl, A., Krinner, G., Loustau, D., Manca, G., Matteucci, G., Miglietta, F., Ourcival, J.M., Papale, D., Pilegaard, K., Rambal, S., Seufert, G., Soussana, J.F., Sanz, M.J., Schulze, E.D., Vesala, T., Valentini, R., 2005. Europe-wide reduction in primary productivity caused by the heat and drought in 2003. Nature 437, 529–533. https://doi.org/10.1038/nature03972

Conesa, M.R., Conejero, W., Vera, J., Ruiz-Sánchez, M.C., 2023. Assessment of trunk microtensiometer as a novel biosensor to continuously monitor plant water status in nectarine trees. Front. Plant Sci. 14, 1123045. https://doi.org/10.3389/fpls.2023.1123045

Cook, F.J., Thorburn, P.J., Bristow, K.L., Cote, C.M., 2003. Infiltration from surface and buried point sources: The Average wetting water content. Water Resour. Res. 39, 2003WR002554. https://doi.org/10.1029/2003WR002554

Cross, H., 1936. Analysis of flow in networks of conduits or conductors. University of Illinois

Das Gupta, S., Mohanty, B.P., Köhne, J.M., 2006. Soil Hydraulic Conductivities and their Spatial and Temporal Variations in a Vertisol. Soil Science Society of America Journal 70. https://doi.org/10.2136/sssaj2006.0201Engineering Experiment Station. Bulletin; no. 286

Di Biase, R., Calabritto, M., Mininni, A.N., Montanaro, G., Dichio, B., 2025. Microtensiometer-based trunk water potential as a plant water status indicator in kiwifruit under different soil water availability. Irrig. Sci. https://doi.org/10.1007/s00271-025-01020-1

Fernández-Gálvez, J., Simmonds, L.P., 2006. Monitoring and modelling the three-dimensional flow of water under drip irrigation. Agric. Water Manag. 83, 197–208. https://doi.org/10.1016/j.agwat.2005.11.008

Galindo, A., Collado-González, J., Griñán, I., Corell, M., Centeno, A., Martín-Palomo, M.J., Girón, I.F., Rodríguez, P., Cruz, Z.N., Memmi, H., Carbonell-Barrachina, A.A., Hernández, F., Torrecillas, A., Moriana, A., Pérez-López, D., 2018. Deficit irrigation and emerging fruit crops as a strategy to save water in Mediterranean semiarid agrosystems. Agric. Water Manag. 202, 311–324. https://doi.org/10.1016/j.agwat.2017.08.015

Haverkamp, R., Arrúe, J.L., Vandervaere, J.P., Braud, I., Boulet, G., Laurent, J.P., Taha, A., Ross, P.J., Angulo-Jaramillo, R., 1996. Hydrological and thermal behaviour of the vadose zone in the area of Barrax and Tomelloso (Spain). Experimental study, analysis and modeling. Project UE n. EV5C-CT 92 00 90

Jiang, S., Kang, Y., 2010. Simple Method for the Design of Microirrigation Paired Laterals on Sloped Fields. J. Irrig. Drain. Eng. 136, 271–275. https://doi.org/10.1061/(ASCE)IR.1943-4774.0000178

Jones, H.G., 2004. Irrigation scheduling: advantages and pitfalls of plant-based methods. J. Exp. Bot. 55, 2427–2436. https://doi.org/10.1093/jxb/erh213

Kandelous, M.M., Šimůnek, J., 2010a. Comparison of numerical, analytical, and empirical models to estimate wetting patterns for surface and subsurface drip irrigation. Irrig. Sci. 28, 435–444. https://doi.org/10.1007/s00271-009-0205-9

Kandelous, M.M., Šimůnek, J., 2010b. Numerical simulations of water movement in a subsurface drip irrigation system under field and laboratory conditions using HYDRUS-2D. Agric. Water Manag. 97, 1070–1076. https://doi.org/10.1016/j.agwat.2010.02.012

Lamm, F.R., Colaizzi, P.D., Sorensen, R.B., Bordovsky, J.P., Dougherty, M., Balkcom, K., Zaccaria, D., Bali, K.M., Rudnick, D.R., Peters, R.T., 2021. A 2020 Vision of Subsurface Drip Irrigation in the U.S. Trans. ASABE 64, 1319–1343. https://doi.org/10.13031/trans.14555

Lassabatère, L., Angulo-Jaramillo, R., Soria Ugalde, J.M., Cuenca, R., Braud, I., Haverkamp, R., 2006. Beerkan Estimation of Soil Transfer Parameters through

Infiltration Experiments—BEST. Soil Sci. Soc. Am. J. 70, 521–532. https://doi.org/10.2136/sssaj2005.0026

Levin, A.D., 2019. Re-evaluating pressure chamber methods of water status determination in field-grown grapevine (Vitis spp.). Agric. Water Manag. 221, 422–429. https://doi.org/10.1016/j.agwat.2019.03.026

Ma, P., Hu, Y., Liu, H., 2019. Optimal Design for Pressurized Irrigation Subunits with a Minimum Cost and Maximum Area for Uniformly Sloping Fields. Water Resour. Manag. 33, 2711–2726. https://doi.org/10.1007/s11269-019-02243-6

Mallants, D., Jacques, D., Tseng, P.-H., Van Genuchten, M.Th., Feyen, J., 1997. Comparison of three hydraulic property measurement methods. J. Hydrol. 199, 295–318. https://doi.org/10.1016/S0022-1694(96)03331-8

Mubarak, I., Mailhol, J.C., Angulo-Jaramillo, R., Ruelle, P., Boivin, P., Khaledian, M., 2009. Temporal variability in soil hydraulic properties under drip irrigation. Geoderma 150, 158–165. https://doi.org/10.1016/j.geoderma.2009.01.022

Ortuño, M.F., García-Orellana, Y., Conejero, W., Ruiz-Sánchez, M.C., Alarcón, J.J., Torrecillas, A., 2006. Stem and leaf water potentials, gas exchange, sap flow, and trunk diameter fluctuations for detecting water stress in lemon trees. Trees 20, 1–8. https://doi.org/10.1007/s00468-005-0004-8

Pagay, V., 2022. Evaluating a novel microtensiometer for continuous trunk water potential measurements in field-grown irrigated grapevines. Irrig. Sci. 40, 45–54. https://doi.org/10.1007/s00271-021-00758-8

Pagay, V., Santiago, M., Sessoms, D.A., Huber, E.J., Vincent, O., Pharkya, A., Corso, T.N., Lakso, A.N., Stroock, A.D., 2014. A microtensiometer capable of measuring water potentials below −10 MPa. Lab Chip 14, 2806–2817. https://doi.org/10.1039/C4LC00342J

Petroselli, A., Romerio, D., Santelli, P., Mariotti, R., Di Giacinti, S., Ceccarelli, I., Apollonio, C., 2022. Performance assessment of the TORO Company Neptune PC AS dripline. J. Agric. Eng. 53. https://doi.org/10.4081/jae.2022.1463

Philip, J.R., 1992. What happens near a quasi-linear point source? Water Resour. Res. 28, 47–52. https://doi.org/10.1029/91WR02600

Philip, J.R., 1984. Travel Times From Buried and Surface Infiltration Point Sources. Water Resour. Res. 20, 990–994. https://doi.org/10.1029/WR020i007p00990

Provenzano, G., 2007. Using HYDRUS-2D Simulation Model to Evaluate Wetted Soil Volume in Subsurface Drip Irrigation Systems. J. Irrig. Drain. Eng. 133, 342–349. https://doi.org/10.1061/(ASCE)0733-9437(2007)133:4(342)

Raats, P.A.C., 1971. Steady Infiltration from Point Sources, Cavities, and Basins. Soil Sci. Soc. Am. J. 35, 689–694. https://doi.org/10.2136/sssaj1971.03615995003500050020x

Raimbault, G., 1986. Diffusivite et conductivite hydrauliques de materiaux ou sols non satures en eau-mesure en laboratoire. Bull Liaison Lab Ponts Chauss, (145)

Ravikumar, V., 2023. Sprinkler and Drip Irrigation: Theory and Practice. Springer Nature Singapore, Singapore. https://doi.org/10.1007/978-981-19-2775-1

Scholander, P.F., Bradstreet, E.D., Hemmingsen, E.A., Hammel, H.T., 1965. Sap Pressure in Vascular Plants: Negative hydrostatic pressure can be measured in plants. Science 148, 339–346. https://doi.org/10.1126/science.148.3668.339

Shi, K., Lu, T., Zheng, W., Zhang, X., Zhangzhong, L., 2022. A Review of the Category, Mechanism, and Controlling Methods of Chemical Clogging in Drip Irrigation System. Agriculture 12, 202. https://doi.org/10.3390/agriculture12020202

Šimůnek, J., Angulo-Jaramillo, R., Schaap, M.G., Vandervaere, J.P., van Genuchten, M.T., 1998. Using an inverse method to estimate the hydraulic properties of crusted soils from tension-disc infiltrometer data. Geoderma 86(1-2):61-81

Singh, V.P., Su, Q., 2022. Irrigation engineering. Principles, processes, procedures, design, and management. Cambridge University Press, Cambridge

Singh, H., Mishra, D., Nahar, N.M., 2002. Energy use pattern in production agriculture of a typical village in arid zone, India—part I. Energy Convers. Manag. 43, 2275–2286. https://doi.org/10.1016/S0196-8904(01)00161-3

Suarez-Rey, E.M., Choi, C.Y., McCloskey, W.B., Kopec, D.M., 2006. Effects of chemicals on root intrusion into subsurface drip emitters. Irrig. Drain. 55, 501–509. https://doi.org/10.1002/ird.275

Subbaiah, R., 2013. A review of models for predicting soil water dynamics during trickle irrigation. Irrig. Sci. 31, 225–258. https://doi.org/10.1007/s00271-011-0309-x

Thorburn, P.J., Cook, F.J., Bristow, K.L., 2003. Soil-dependent wetting from trickle emitters: implications for system design and management. Irrig. Sci. 22, 121–127. https://doi.org/10.1007/s00271-003-0077-3

Vaccaro, G., Fusco, M., Alagna, V., Franco, L., Motisi, A., Iovino, M., 2025. Assessing microtensiometers for monitoring stem water potential in mandarin (Citrus reticulata Blanco) orchard under different irrigation regimes. Agric. Water Manag. 320, 109873. https://doi.org/10.1016/j.agwat.2025.109873

CHAPTER 1

Closed circuits of drip laterals versus open circuits: hydraulic performance and energy-saving potential

Based on the **published** paper:

Baiamonte, G., Vaccaro, G., Palermo, S., **2024**. Closed circuits of drip laterals versus open circuits: hydraulic performance and energy-saving potential. *Irrig. Sci.*
https://doi.org/10.1007/s00271-024-00981-z

CHAPTER 1: Closed circuits of drip laterals versus open circuits: hydraulic performance and energy-saving potential

Giorgio Baiamonte[1*], Girolamo Vaccaro[1], Samuel Palermo[1]

[1]Dept. of Agricultural, Food and Forest Sciences (SAAF), Univ. of Palermo, viale delle Scienze, Bldg. 4, 90128 Palermo. *Corresponding Author, E-mail: giorgio.baiamonte@unipa.it

Abstract

Drip irrigation systems are usually designed according to open circuits, characterised by branching pipe networks with many drip laterals and one manifold. However, the closure of the circuits with a secondary manifold connecting lateral ends makes it possible to apply a lower inlet pressure head than open circuits, with important implications for energy-saving. In this paper, a comprehensive comparison between the hydraulic performance of open and closed circuits of drip laterals is carried out. The open circuits (*op*) were analysed by using IrriLab software, which requires two arbitrarily set pressure head tolerances, one for the laterals (δ_L) and one for the manifold (δ_M), determining the pressure tolerance of the unit (δ_{op}). Meanwhile, the closed circuits were analysed using the well-known Hardy Cross method (HCM). For #3,800 drip irrigation units characterised by different geometric and hydraulic parameters, an approximated relationship is derived to accurately predict the energy saving associated with the closure of the open circuits. Results showed that open circuits are recommended when designing for low δ_M (low-pressure head variability in the manifold), since energy can be saved, although higher inside manifold diameters are required in this case. Contrarily, for high δ_M, the closure of the circuit is more appropriate to save energy, since the inlet pressure head is much lower than that required by open circuits.

Keywords: Drip irrigation, IrriLab software, Analytical solutions, Hardy Cross method

List of symbols

a	Parameter of the predictive relationship	k	Flow resistance equation coefficient
b	Parameter of the predictive relationship	K_L	Energy gradient associated with the emitter flow rate
c	Parameter of the predictive relationship	L_L	Lateral length (m)
C	Pipe smoothness factor equal to 135 for polyethylene pipes	M_1	Main manifold for both open and closed circuits
d	Parameter of the predictive relationship	M_2	Secondary manifold for closed circuits
D_*	Inside diameter of the manifold by using dimensionless groups	n	Flow rate exponent of Darcy's resistance equation
D_L	Lateral inside pipe diameter (mm)	N	Number of emitters
D_M	Manifold inside pipe diameter (mm)	N_{rows}	Number of laterals
D_{M1}	Main manifold inside pipe diameter (mm)	p'_m	Corrective flow rate (m^3 h^{-1})
D_{M2}	Secondary manifold inside pipe diameter (mm)	q_i	Discharge in pipe "i" meeting at node "n" (m^3 h^{-1})
h	Head loss described in general terms by Hardy Cross (m)	q_{in}	Inlet flow rate of the unit (m^3 h^{-1})
H_*	Ratio between $H_N^{(-r)}$ and $H_{N_{rows}}^{(-r)}$	q_n	Emitters' flow rate (l h^{-1})
h_i	Total head loss in the generic pipe "i" (m)	r	Flow rate exponent of the flow resistance equation
h_{in}	Inlet pressure head of the unit (m)	r_i	Head loss for a given unit quantity of flow described by Hardy Cross
h_{in*}	Inlet pressure head by using dimensionless groups	S	Emitters' spacing (m)
$h_{in,cl}$	Inlet pressure head of the closed circuit (m)	s	Inside diameter exponent of the flow resistance equation
$h_{in,op}$	Inlet pressure head of the open circuit (m)	S_*	Ratio between emitters' spacing and drip laterals spacing
h_M	Average pressure head of the manifold (m)	$S_{0,L}$	Slope of the laterals (%)
$h_{M,min}$	Minimum pressure head in the manifold (m)	$S_{0,M}$	Slope of the manifold (%)
h_{max}	Maximum pressure head along the laterals (m)	S_{rows}	Drip laterals' spacing (m)
h_{min}	Minimum pressure head along the laterals (m)	Δ'_m	Imbalance head loss (m)
$h_{min,cl}$	Minimum pressure head of the closed circuit (m)	Δ	Pressure head amplification factor
$h_{min,op}$	Minimum pressure head of the open circuit (m)	Δh	Pressure head range (m)
h_n	Nominal or average emitter pressure head (m)	δ	Pressure head tolerance of the unit
$h_{n,cl}^{(\delta)}$	Average pressure head of the closed circuit by imposing the same pressure head tolerance in *op* and *cl* circuits (m)	δ_{cl}	Pressure head tolerance of the closed circuit

$h_{n,cl}^{(in)}$	Average pressure head of the closed circuit by imposing the same inlet pressure head in *op* and *cl* circuits (m)	δ_L	Pressure head tolerance of the laterals
$H_{N_{rows}}^{(-r)}$	Generalized harmonic number truncated at lateral N_{rows}	δ_M	Pressure head tolerance of the manifold
$H_N^{(-r)}$	Generalized harmonic number truncated at emitter N	δ_{op}	Pressure head tolerance of the open circuit
h_{ratio}	Ratio between the *cl* inlet pressure head and the *op* inlet pressure head	δ_{ratio}	Ratio between the *cl* pressure head tolerance and the *op* pressure head tolerance
$h_{ratio}^{(est)}$	Estimated h_{ratio} by the predictive relationship	$\delta_{ratio}^{(est)}$	Estimated δ_{ratio} by the predictive relationship

1. Introduction

Over the past decades, irrigation research has primarily focused on minimising crop water consumption. One of the most efficient irrigation techniques is the drip irrigation system, able to minimise water losses related to evaporation, surface runoff, and deep percolation (Singh and Su 2022; Ravikumar 2023). The optimisation of water use efficiency, by using pressurised systems, may lead to unintended resource and environmental consequences, such as an increase in energy consumption (Jackson et al. 2010). Moreover, due to energy prices steadily increasing, there is growing attention on reducing energy use. Indeed, according to statistics, 23% to 48% of the total agricultural energy consumed worldwide is directly attributed to water irrigation pumping (Singh et al. 2002). The energy required for pumping is essential to ensure an effective water application at the field level, and it depends on many factors, including crop water requirement, total dynamic head, flow rate, and system efficiency.

Collective systems that deliver pressurised water to the fields are particularly sensitive to energy costs and are often well-structured to identify energy-saving opportunities (Belaud et al. 2019). Although the design of modern pipe irrigation systems, whether collective networks or drip irrigation systems, is based on energy criteria by setting head loss limits, new methodologies for achieving further energy-saving are being sought.

Keller and Bliesner (1990) suggested both graphical and numerical solutions, defining the best position of the manifold (BMP) as the optimal location of the manifold. The BMP is determined as the position of the manifold that ensures minimum uphill and downhill pressure heads along a pair of average laterals. Wu et al. (2010) devised a straightforward gravity-fed drip irrigation system design methodology for low-cost, single-manifold subunits featuring multiple pressure sections. Their approach assumed that the laterals were laid along elevation contours so that the ground slope along the lateral was equal to zero. Additionally, an iterative calculation process is required to determine both the number of emitters and the lateral length. Wang and Chen (2020) developed an improved finite element-based formulation for the design of drip irrigation subunits regardless of laterals or manifolds. Baiamonte et al. (2024) presented a novel analytical solution to determine the hydraulic emission uniformity of horizontal tapered drip laterals, which is a relevant issue in drip irrigation system design, especially when non-pressure compensating (N-PCE) emitters are considered.

Many research efforts have focused on optimising energy consumption through the application of different methodologies at the scale of hydraulic piping networks (Masoumi et al. 2016; Wang et al. 2023), and by detecting the optimal design solution of the drip systems at the field level (Jiang and Kang 2010; Baiamonte 2016; 2018a; Ma et al. 2019; Ravikumar 2023).

Recently, Baiamonte (2018b) developed the IrriLab software for the optimal hydraulic design of rectangular microirrigation units, situated on sloped or flat terrain. This method allows, without calculation attempts or iterations, to find solutions that enable maximum energy savings and requires the assignment of two pressure head tolerances, one for the laterals, δ_L, and the other for the manifold, δ_M (Baiamonte 2018a; 2018b).

In drip irrigation systems, enhancing performance, reliability, and energy-saving can also be achieved by installing a secondary manifold to connect all lateral ends, such as in subsurface drip irrigation (SDI). The main difference between SDI systems and closed circuits of surface drip irrigation (DI) systems lies in the fact that fine-pore soils induce a reduction in emitter discharge due to overpressure, also denoted as back pressure, at the discharge point of buried emitters (Shani et al. 1996; Lazarovitch et al. 2005; Gil et al. 2008). However, the closure of DI systems determines a different flow direction within the pipes, which is difficult to predict with the hydraulic design used for surface DI. Consequently, complex network problems require an iterative approach, involving multiple iterations of the problem through numerical procedures. Therefore, closed circuits of surface DI systems can be analysed as looped networks, with each emitter considered as a node.

In analysing the hydraulic performance of a looped network, many research efforts have focused on considering the altered flow discharge in the pipe systems. Three methods for analysing a looped water distribution network (the loop method, the nodal method, and the pipe method) account for the chosen unknown hydraulic parameters. These methods belong to two types of network analysis problems with increasing capabilities, namely forward and inverse problems. In the forward problem, the hydraulic behaviour of the system (i.e., the flow in each pipe, the pressure at each node, and the operating heads for pumps) is determined for specified pipe network characteristics, water demand, and operating conditions. The nonlinear system of equations can be solved by iterative procedures, such as the Hardy Cross method (Cross 1936; Abramov 1972), the Newton-Raphson method (Chandrasekhar and Stewart 1975; Wood and Rayes 1981), and the linear theory method (Issacs and Mills 1980). Particularly, the Hardy Cross method (HCM), originally developed in 1936 for manual calculations in civil engineering, is a reliable method for solving verification problems in hydraulic looped networks. This approach allows for determining the distribution of flows and pressures, respectively, in the pipes and nodes of a hydraulic network, given its geometric characteristics and the inlet and outlet flows. Furthermore, to satisfy the energy balance in each pipe of the network, the HCM relies on the progressive addition of corrective flows into each pipe of the network. Depending on the size and complexity of the networks, this approach may require an excessive number of iterations to achieve the desired accuracy. Consequently, this limitation has led to further research.

Following the Hardy Cross method, Martin and Peters (1963) developed several global linearisation techniques, culminating in the work of Todini and Pilati (1987) and Todini (2006), which are distinguished by the simultaneous solution of all the network equations. The latter method is highly popular and was implemented in EPANET software (Rossman 2002; Todini and Rossman 2013).

Lopes (2004) devised user-friendly software using the iterative HCM to solve looped distribution systems characterised by any arrangement of the pipes. A novel model proposed by Sarbu (2014) directly minimises an objective multivariable function without constraints, and it has been implemented into a computer program. Moreover, this author compared the proposed model with the classic and still applied HCM (Dumka et al. 2023) and showed a reliable performance of the model.

Following the finite element method in DI subunits proposed by Bralts and Segerlind (1985), a methodology was developed by Wang et al. (2016), who numerically implemented it in the MATLAB program for the hydraulic analysis of SDI systems. In addition, Wang et al. (2021) improved the finite element-based model by also considering the effect of the soil hydraulic properties in the analysis of SDI subunits, and a comparison of the hydraulic performance between DI and SDI systems was performed. Although the looped pipe network of SDI provided a more uniform distribution of pressure heads, the emission uniformity was much lower than that of the DI subunit due to the variation in saturated hydraulic conductivity, especially with low permeability. Lamm (2002) provides a conceptual discussion on the advantages and disadvantages of SDI systems. Specifically, SDI systems allow more efficient water use, greater water application uniformity, and decreased energy costs. Meanwhile, it also provides high initial investment costs compared to DI systems, maintenance issues, and root intrusion.

In consideration of the above, closed and open drip irrigation systems have been deeply studied separately. However, the literature review revealed that a comprehensive comparison between the two systems, evaluating both hydraulic performance and energy-saving potential, has poorly or never been attempted before.

In this paper, we address the aforementioned gap by comparing the energy-saving provided by closed circuits (*cl*) to that of traditional open circuits (*op*). The comparisons were conducted for fixed rectangular unit geometries, with *op* circuits designed according to the IrriLab method, and *cl* circuits designed using the HCM. For *cl* circuits, the HCM was applied using the Hazen-Williams resistance equation, which is more appropriate for characterising friction losses in polyethylene pipes than the Darcy equation considered in the original formulation. Finally, a new simple relationship was developed for rectangular irrigation units, characterised by different geometry, pipe diameters, emitters' spacing, and flow rates, to predict the energy-saving resulting from the closure of the *op* circuits with a secondary manifold. Several applications showing the consistency of the suggested predictive relationships were performed.

2. Materials and Methods

The effect of the closure of drip irrigation systems, with a secondary manifold, M_2, was investigated by using **IrriLab** software for open irrigation systems (open circuits, *op*) and by the Hardy Cross Method (HCM), for looped drip irrigation systems (closed circuit, *cl*). Figure 1 illustrates a sketch of an open drip irrigation system (Fig. 1a) and a looped drip irrigation system (Fig. 1b).

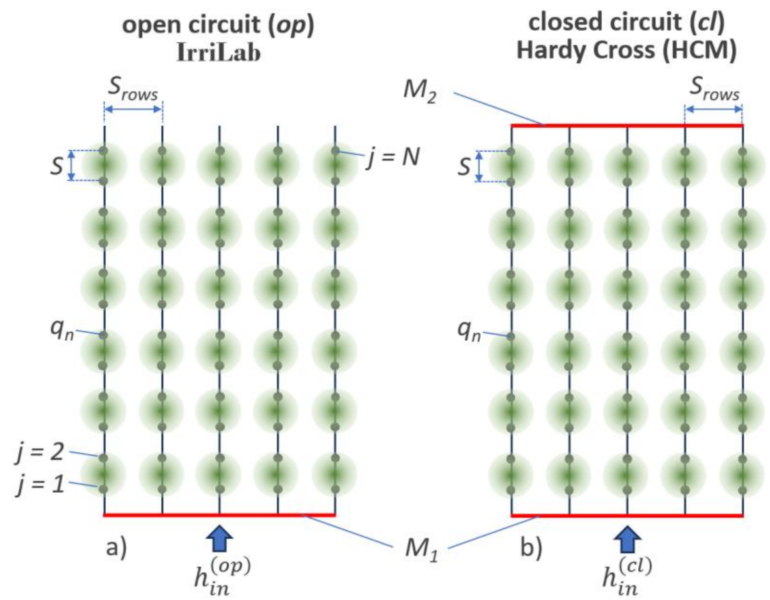

***Fig. 1** Sketch of **a)** an open drip irrigation system (open circuit, op), and **b)** a looped drip irrigation system (closed circuit, cl)*

In the next two sections, **IrriLab** software and HCM are shortly summarised. Of course, the same geometry and hydraulic parameters are attributed to both *op* and *cl* circuits. The only difference lies in the secondary manifold M_2 applied to *cl* circuits, having an internal diameter equal to that of the main manifold M_1, as illustrated in Fig. 1b.

2.1. Applying IrriLab software to open drip irrigation systems (open circuits)

The **IrriLab** software application (Baiamonte 2018b) is based on simple and explicit relationships that make it possible to design rectangular irrigation units on uniform sloping fields. Moreover, **IrriLab** provides a good approximation of the output parameters obtained by the commonly adopted, exact, and numerical step-by-step procedure (SBS); since **IrriLab** is based on analytical solutions, it neither requires trial-and-error attempts nor iterations.

Three hypotheses are considered in the design procedure. The pressure head range established by a fixed pressure head tolerance, δ, is entirely used by the emitters. The emitters' flow rate is uniform. However, under low values of the pressure head tolerances, as the commonly accepted δ = 10% (Baiamonte 2024), **IrriLab** can also be applied for non-pressure compensating emitters (N-PCE), not considered in this work. The last hypothesis is that minor losses are neglected. For this study, the latter hypothesis is not a big deal, because in both *op* and *cl* circuits, minor losses are neglected, giving more generality to the results that will be presented in comparative terms, as it will be discussed later.

In **IrriLab**, the rectangular irrigation unit, with N emitters per N_{rows} laterals, lays on uniform slopes and is characterised by two slope values, one for the laterals, $S_{0,L}$, and one for the manifold, $S_{0,M}$, and by two further parameters, the best manifold position (BMP) concerning the laterals, and the best inlet position (BIP) with respect to the manifold. By considering the possible combinations of i) horizontal, downward, or upward sloped laterals and manifold, ii) the manifold position (BMP) and iii) the inlet position (BIP) equal to 0%, 25% or 50% with respect to their lengths, **IrriLab** accounts for 5 × 5 irrigation unit layouts (Fig. 2). The layout considered in the present work, and illustrated in Fig. 1a, is Layout #18 ($S_{0,L} = S_{0,M} = 0$, BMP = 0, BIP = 0.5). However, because of the unit symmetry, design relationships for Layout #18 are derived starting from Layout #19 (BIP = 0). Indeed, the difference between the two layouts is in the number of laterals N_{rows}, and inlet discharge, q_{in}, which for Layout #18 needs to be doubled ($q_{in} = q_n \times N \times 2\, N_{rows}$), compared to that of Layout #19 ($q_{in} = q_n \times N \times N_{rows}$).

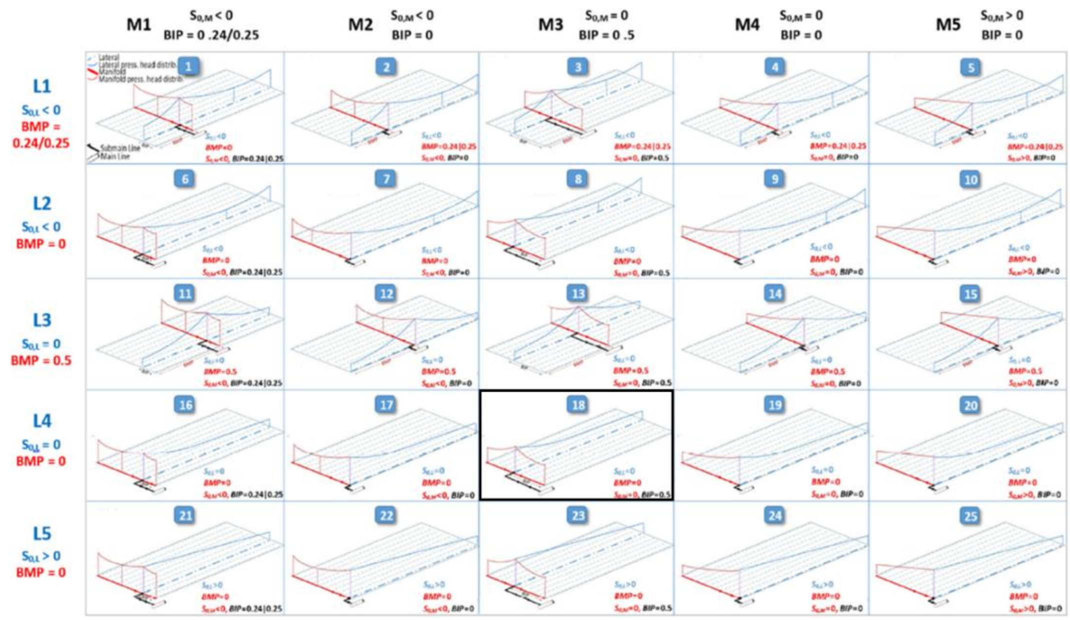

Fig. 2 *Irrigation Unit Layouts considered in IrriLab, by varying the lateral slope ($S_{0,L}$ < 0, $S_{0,L}$ > 0, $S_{0,L}$ = 0), the best manifold position (BMP = 0, 0.25, 0.5), the manifold slope ($S_{0,M}$ < 0, $S_{0,M}$ > 0, $S_{0,M}$ = 0), and the best inlet position (BIP = 0, 0.25, 0.5). Qualitative pressure head distribution lines for laterals and manifolds are represented. Layout #18 (black rectangle) refers to this study. Reprinted with permission from ref. Baiamonte, 2018b, Copyright 2018, Elsevier (Amsterdam, The Netherlands)*

According to Baiamonte (2018a, Eq. 23), for Layout #19, the nominal (average) emitter pressure head, h_n (L), can be expressed as (Fig. 3):

$$h_n = \frac{S\, K_L}{2\, \delta_L}\, H_N^{(-r)} \tag{1}$$

where S (L) is the emitters' spacing (Fig. 1a), δ_L is the pressure head tolerance associated with the lateral, $H_N^{(-r)}$ is the generalised harmonic number truncated at the emitter N, in power $-r$ (Abramowitz and Stegun 1972):

$$H_N^{(r)} = \sum_{k=1}^{N} \frac{1}{k^r}\ /; N \in \mathbb{N} \tag{2}$$

and K_L is the energy gradient associated with the emitter flow rate, q_n:

$$K_L = k\, \frac{q_n^r}{D_L^s} \tag{3}$$

According to Hazen-Williams resistance equation, r = 1.852 and s = 4.871, and k equals to:

$$k = \frac{10.675}{C^r} \tag{4}$$

where C is the pipe smoothness factor, which depends on the pipe material's characteristics and was assumed equal to 135, for polyethylene pipes usually adopted in drip irrigation systems (Moghazi 1998). Note that although the Hazen-Williams resistance equation is used here, the procedure can also be applied to any other resistance formula.

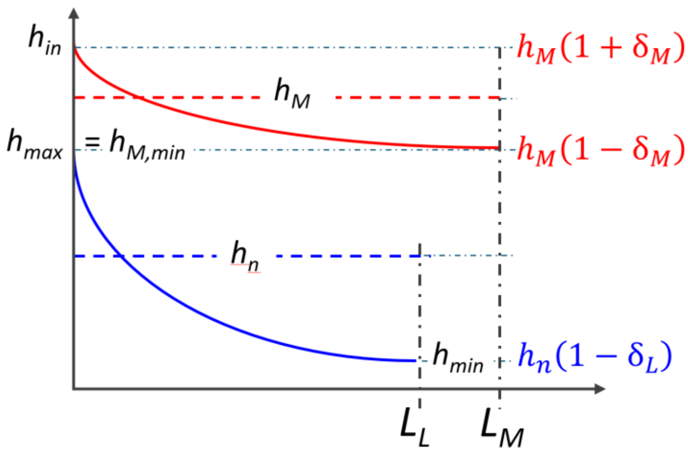

Fig. 3 *Sketch of Pressure Head Distribution (PHD) of the last lateral and of the manifold considered in IrriLab. The maximum pressure head is equal to the minimum of the manifold because of the connection*

According to Baiamonte (2018a; 2018b), the imposed pressure head tolerance, δ_L, the average emitter pressure head makes it possible to determine the minimum and the maximum emitter pressure head along the laterals, h_{min} and h_{max}, respectively (Fig. 3):

$$h_{min} = h_n(1 - \delta_L) \tag{5}$$

$$h_{max} = h_n(1 + \delta_L) \tag{6}$$

The inlet pressure head, h_{in}, was determined according to manifold pressure head tolerance, δ_M, which can be arbitrarily set:

$$h_{in} = \Delta\, h_n (1 + \delta_M) = h_M\, (1 + \delta_M) \tag{7}$$

where h_M (L) is the average pressure head of the manifold, and Δ is a pressure head amplification factor:

$$\Delta = 1 + \delta_L \tag{8}$$

that accounts for the fact that, while in the drip laterals, pressure heads vary around h_n, in the manifold, pressure heads vary around an amplified average pressure head of $h_M = \Delta h_n$.

To derive the inside diameter of the manifold, first Baiamonte (2018b) expressed the emitter flow rate by combining Eq. (1) and Eq. (3) and made explicit the emitter flow rate, q_n:

$$q_n = \left(\frac{2\, \delta_L h_n D_L^s}{k\;\, S\, H_N^{(-r)}}\right)^{1/r} \tag{9}$$

Moreover, considering that N_{rows} laterals, S_{rows} spaced (Fig. 1a), connected to the manifold, operate as N emitters, S spaced, installed in the laterals, by using Eq. (9), the lateral flow rate $q_{rows} = N\, q_n$, can be expressed as:

$$\left(\frac{2\, \delta_M h_M D_M^s}{k\;\, S_{rows} H_{N_{rows}}^{(-r)}}\right)^{1/r} = N\, \left(\frac{2\, \delta_L h_n D_L^s}{k\;\, S\, H_N^{(-r)}}\right)^{1/r} \tag{10}$$

Equation (10) makes it possible to derive the inside diameter of the manifold, D_M:

$$D_M = D_L\, N^{r/s} \left(\frac{S_{rows}}{S}\, \frac{\delta_L}{\Delta\, \delta_M}\, \frac{H_{N_{rows}}^{(-r)}}{H_N^{(-r)}}\right)^{1/s} \tag{11}$$

Finally, for the two arbitrarily set pressure head tolerances, δ_L and δ_M, the pressure head tolerance of the unit, δ, is equal to (Baiamonte 2018b):

$$\delta = (1 + \delta_L)(1 + \delta_M) - 1 \quad (12)$$

Vice versa, for arbitrarily set δ_L and δ, the manifold pressure head tolerance, δ_M, can be calculated:

$$\delta_M = \frac{1+\delta}{1+\delta_L} - 1 \quad (13)$$

An example application of IrriLab software is illustrated in Fig. 4, where it is possible to observe that, for a pressure head tolerance, δ = 10%, the pressure head distribution obtained by applying the numerical SBS procedure, with the IrriLab output parameters (h_n = 27.4 m, h_{in} = 30.2 m, Eq. 7 and D_M = 50.7 mm, Eq. 11), almost lay in between the minimum and the maximum pressure heads, h_{min} = 24.7 m (see the minimum h value in Fig. 4 that not exactly match 24.7 m) and h_{in} = 30.2 m, respectively. In Fig. 4, the inlet pressure head and flow rate, h_{in} (m) and q_{in} (L/s) = q_n N N_{rows}, the irrigation unit area, IUA (ha) = L_L L_M, and the water application rate, WAR (mm/h) = q_{in} /IUA = q_n /(S S_{rows}), are also reported.

Slight differences in the minimum h value between the analytical (IrriLab) and the numerical SBS procedure are due to the arbitrarily set pressure head amplification factor, Δ, and the related unit pressure head tolerance, δ, which were not theoretically based (Eq. 9). Towards the aim of an accurate comparison between the performance of open and closed circuits, these slight errors will be removed, by theoretically deriving both Δ and δ, the latter from now on denoted as δ_{op}.

Referring to Fig. 3, the amplification factor can be derived by $\Delta = h_M/h_n$ (see Eqs. 11−12), rather than imposing it as in Eq. (8). Additionally, the maximum pressure head in the last lateral must be equal to the minimum pressure head in the manifold, $h_{M,min}$, located at the distal end as shown in Fig. 3. Thus, h_M can be expressed as:

$$h_M = \frac{h_{M,min}}{(1-\delta_M)} = \frac{h_{max}}{(1-\delta_M)} \quad (14)$$

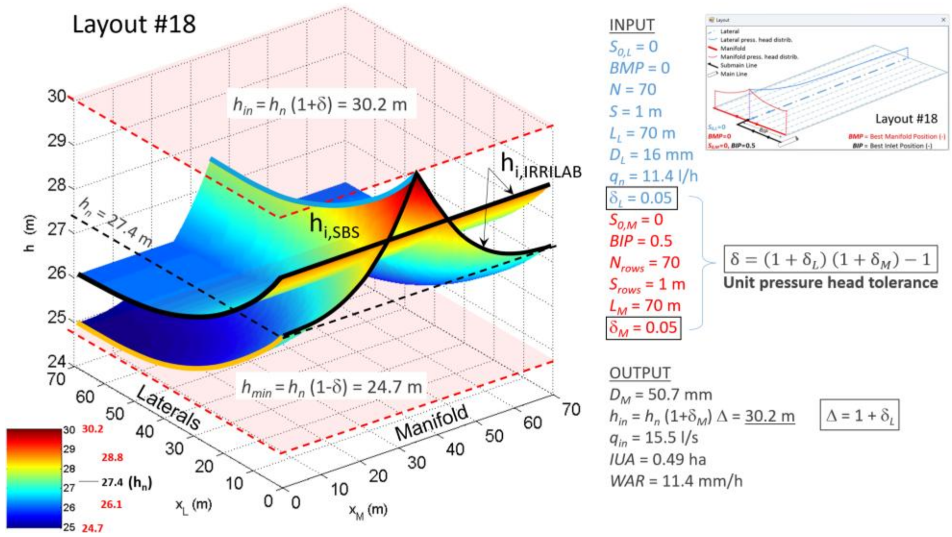

Fig. 4 *Application example of* $\boldsymbol{IrriLab}$ *software for Layout #18. The figure illustrates the pressure head distribution obtained by the numerical SBS, with the* $\boldsymbol{IrriLab}$ *output parameters, which are also indicated.* Δ *and* δ *parameters are expressed by Eq. (8 and 12), respectively. Reprinted with permission from ref. Baiamonte, 2018b, Copyright 2018, Elsevier (Amsterdam, The Netherlands)*

Accordingly, the corrected amplification factor results in:

$$\Delta = \frac{h_M}{h_n} = \frac{h_{max}}{h_n(1-\delta_M)} = \frac{1+\delta_L}{1-\delta_M} \tag{15}$$

that differs from Eq. (8). Also, the unit pressure head tolerance, δ_{op}, is defined as:

$$\delta_{op} = \frac{h_{in}-h_{min}}{h_{in}+h_{min}} \tag{16}$$

can be analytically derived, if expressing the numerator and the denominator according to Fig. 3:

$$h_{in} - h_{min} = h_M(1+\delta_M) - h_n(1-\delta_L) \tag{17}$$

$$h_{in} + h_{min} = 2\,h_{min} + h_M(1+\delta_M) - h_n(1 \pm \delta_L) \tag{18}$$

Substituting Eqs. (17 and 18) into Eq. (16), using Eqs. (5 and 14), and rearranging, provides a theoretically based δ_{op} or δ_M, respectively:

$$\delta_{op} = \frac{\delta_M + \delta_L}{1 + \delta_M \delta_L} \tag{19}$$

$$\delta_M = \frac{\delta_{op} - \delta_L}{1 - \delta_L \delta_{op}} \tag{20}$$

that differ from Eqs. (12 and 13), which were to be demonstrated. To express the design variables as a function of δ_M, as will be done for closed circuits, it is also useful to make explicit the lateral pressure head tolerance, δ_L:

$$\delta_L = \frac{\delta_M - \delta_{op}}{\delta_M \ \delta_{op} - 1} \tag{21}$$

According to the new δ and Δ relationships, the inlet pressure head (Eq. 7) and the manifold diameter (Eq. 11) can be rewritten:

$$h_{in} = \Delta\, h_n (1 + \delta_M) \ = h_n \frac{(1+\delta_{op})(1+\delta_M)}{1 - \delta_{op}\delta_M} \tag{22}$$

$$D_M = D_L\, N^{r/s} \left(\frac{S_{rows}}{S} \frac{\delta_{op} - \delta_M}{\delta_M + \delta_{op}\, \delta_M} \frac{H_{N_{rows}}^{(-r)}}{H_N^{(-r)}} \right)^{1/s} \tag{23}$$

where in Eq. (22), h_n is expressed by Eq. (1). Note that Eqs. (22 and 23), under uniform emitter flow rate, only slightly differ from the relationships considered in **IrriLab**, and can provide no errors in the drip irrigation unit design. The latter means that a 3D pressure head distribution, derived by the application of the exact SBS procedure, to an irrigation unit designed by using Eqs. (22 and 23), exactly lies between h_{min} and h_{in}. To show this, for a fixed δ_L = 0.05, the same application illustrated in Fig. 4 was replicated by using the newly derived relationships (Eqs. 22 and 23). Fig. 5 shows that the PHD distribution obtained by using the SBS procedure with the new output data reported in Fig. 5 legend (D_M, h_{in}, h_{min}, δ_M) provides a pressure head tolerance that exactly matches δ = 0.1 (Eq. 19), as imposed in the design.

In Fig. 6a and 6b, for δ_{op} = 0.1, Eq. (22) and Eq. (23) are plotted as a function of δ_M. The input parameters are those considered in the **IrriLab** application (Figs. 4 and 5), and for δ_M = 0.05, the same D_M and h_{in} values are illustrated (red dots). The red dots are very close to the new relationships provided here (Eq. 22 and Eq. 23), indicating the slight errors provided by **IrriLab**, which in this context were removed.

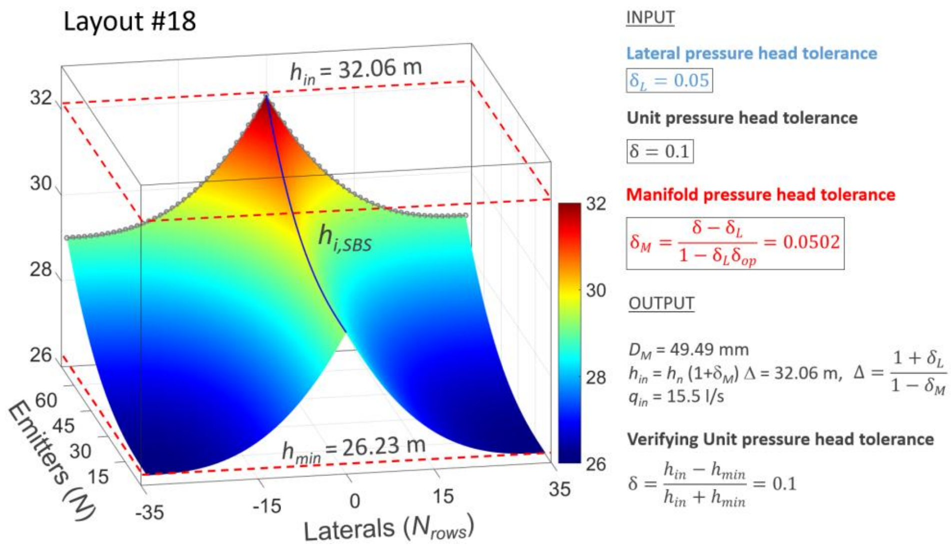

Fig. 5 *Application example of* **IrriLab** *software for Layout #18. The figure illustrates the pressure head distribution obtained by the numerical SBS, with the* **IrriLab** *output parameters, which are also indicated.* Δ *and* δ_{op} *parameters are expressed by Eqs. (16 and 19), respectively*

The same relationships (Eqs. 22 and 23) can be described by using dimensionless groups, making general the results of Figs. 6a and 6b, i.e. not dependent on the geometric and hydraulic parameters, but only on pressure head tolerances, respectively:

$$h_{*in} = \frac{h_{in}}{S\, K_L\, H_N^{(-r)}} = \frac{1+\delta_{op}+\delta_M+\delta_{op}\delta_M}{2\,(\delta_{op}-\delta_M)} \tag{24}$$

$$D_* = \frac{D_M\, S_*^{1/s} H_*^{1/s}}{D_L\, N^{r/s}} = \left(\frac{\delta_{op}-\delta_M}{\delta_M+\delta_{op}\,\delta_M}\right)^{1/s} \tag{25}$$

where Eq. (1) was substituted into Eq. (22), $S_* = S/S_{rows}$, and $H_* = H_N^{(-r)}/H_{N_{rows}}^{(-r)}$. Equation (24) and Eq. (25) are plotted in Figs. 6c and 6d, showing a similar but more general result than Figs. 6a,b.

The results obtained in Fig. 6 are compulsory for the objective of this work and, interestingly, show that when designing open circuits, for an assigned δ_{op}, the arbitrarily set δ_M needs to be accurately chosen, with pros and cons. Indeed, for low

δ_M, the drip irrigation units require low inlet pressure heads, and a lot of energy is saved, decreasing the operational costs (Fig. 6c).

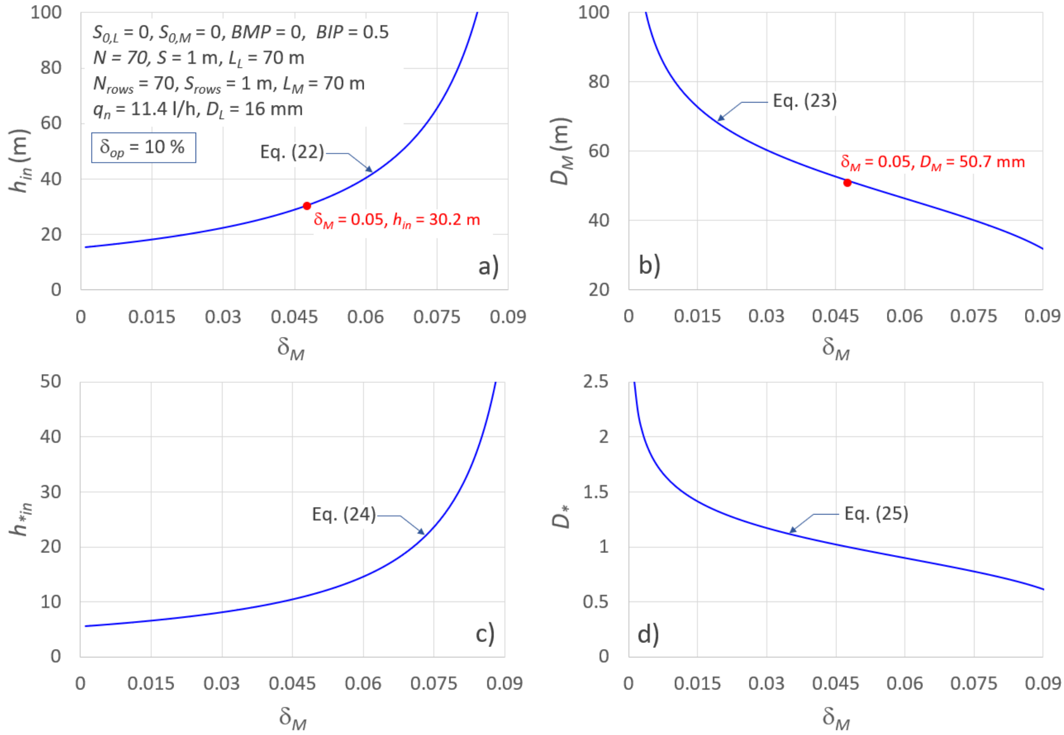

Fig. 6 *Relationship between **a)** inlet pressure head, h_{in}, **b)** manifold inside diameter, versus manifold pressure head tolerance, δ_M. The corresponding dimensionless relationships, **c)** Eq. (24) and **d)** Eq. (25), are also depicted*

But low δ_M values also increase the investment costs, because of the high values of the inside manifold diameters, as can be observed in Fig. 6d. The vice versa occurs for high δ_M. It will be interesting to compare the above-illustrated behaviour of open circuits with closed circuits, discussed in the next section.

2.2. Applying Hardy Cross method to looped drip irrigation systems (closed circuits)

Hardy Cross (1936) developed a mathematical approach for calculating the magnitude of moments of forces applied in indeterminate framed structures. Moreover, Cross discovered that this method can be applied to estimate the pressures and discharges in a water distribution network.

In a generic hydraulic network consisting of "*m*" loops, "*n*" nodes, and "*i*" pipes (Fig. 7), the system of equations governing the steady-state flow consists of "*i*" energy conservation equations (Eq. 26) and "*n*" mass conservation equations (Eq. 27):

$$\sum_m \pm h_i = 0 \tag{26}$$

$$\sum_n \pm q_i \pm q_n = 0 \tag{27}$$

where h_i is the total head loss in the generic pipe i, q_n is the nodal outflow, and q_i is the discharge in pipe "i" meeting at node "n".

In HCM, the head loss, h, is described in general terms using the following equation:

$$h = r_i q^n \tag{28}$$

where r_i is the head loss for a given unit quantity of flow, q (dependent on size and pipe roughness), and n is the flow rate exponent, which was assumed to be equal to 2 in Darcy's resistance equation.

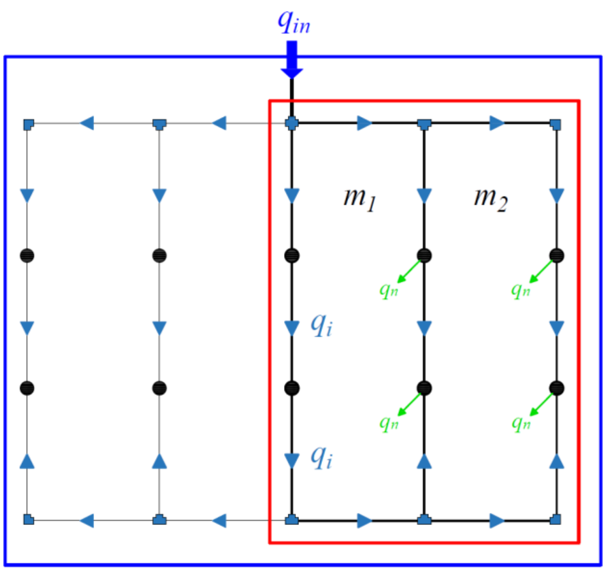

***Fig.** 7 Sketch of a looped irrigation network (closed circuit, cl), corresponding to Layout #18 and to Layout #19 considered in* **IrriLab**

According to HMC, if the inlet and outlet discharges are known, the "Method of Balancing Heads" can be employed, maintaining the continuity condition true all times and adjusting the flow in each pipe until the continuity is achieved. Given the geometric characteristics of the network and the inlet flow rate, q_{in}, the application of the HCM first assumes in the network, arbitrary flow rates, q_i, as long as the continuity condition (Eq. 27) at each node is satisfied (Fig. 7).

Subsequently, the total loss head along each loop (Eq. 26) should be calculated, considering the head loss sign, according to the arbitrarily set flow rates. This can be achieved by assuming that the flow rate in the clockwise direction yields a positive head loss and a negative sign in the counterclockwise direction. Of course, at the first iteration, the hydraulic network is usually unbalanced concerning the head loss by a certain amount, Δ'_m, different from zero:

$$\sum_m \pm h_i = \sum_m \pm r_i q_i^2 = \Delta'_m \neq 0 \tag{29}$$

To balance the hydraulic heads (Eq. 29), it is necessary to operate on each loop, considered isolated from the rest of the loops. The amount Δ'_m for the "m" loop can be closed to zero, if calculating the change in flow rate and introducing a corrective flow, p'_m:

$$\sum_m [\pm r_i (q_i \pm p'_m)^2] = 0 \tag{30}$$

Neglecting terms of degree higher than the first, Eq. (30), yields:

$$p'_m = -\frac{\sum_m(\pm r_i q_i^2)}{2\sum_m |r_i q_i|} = -\frac{\Delta'_m}{2\sum_m |r_i q_i|} \tag{31}$$

For each loop, the flow rate correction p'_m is added to the circulating flow rates, q_i, in the "i" pipes. Thus, by correcting the flow rates of the pipe common to multiple loops, a new imbalance of hydraulic heads is introduced in the loops that were already balanced. Therefore, it is necessary to proceed iteratively until the value of Δ'_m is less than a certain threshold, thus achieving head loss balancing in the network.

In the case of looped irrigation systems, the nodal outflow corresponds to the emitter flow rate, q_n, which is assumed uniform along the laterals. Since the HCM is an iterative method, it cannot be applied easily under the assumption of a non-uniform emitter flow rate. This is because the outflow from non-pressure-compensating emitters depends on the pressure head, in line with the emitter flow rate-pressure head relationship. Moreover, because polyethylene pipelines are commonly adopted in drip irrigation, Darcy's equation as envisaged in the original method cannot be employed

(Eq. 28 with $n = 2$). Consequently, other more appropriate resistance equations need to be considered, such as the Hazen-Williams resistance equation (Rossman 2002; Rai and Sanap 2017), already considered in **IrriLab**. Therefore, the calculation of the corrective flow to be introduced in the iterative method needs to be reformulated.

Reviewing the steps described earlier (Eqs. 29−31), and using the Hazen-Williams resistance equation, the pressure head imbalance, Δ'_m (Eq. 29), becomes:

$$\sum_m \pm k \, \frac{q_i^r}{D^s} L_i = \Delta'_m \tag{32}$$

where k is expressed by Eq. (4), and L_i is the length of the pipe. Following the Hazen-Williams resistance equation, the corrective flow, p'_m, can be expressed with the following relationship:

$$p'_m = \frac{\sum_m \pm k \, \frac{q_i^r}{D^s} L_i}{\sum_m \pm k \, r \, \frac{q_i^{r-1}}{D^s} L_i} \tag{33}$$

As for **IrriLab**, note that although the Hazen-Williams resistance equation is used (Eqs. 3, 4, 32, 33), the procedure can also be applied to any other resistance formula.

The described methodology will be applied to the looped network sketched in Fig. 7, where the corresponding Layout #18 and Layout #19 considered in **IrriLab** (*op*), are illustrated. As for open circuits, because of the unit symmetry, the results can be extended to irrigation units fed in the mid-manifold (Layout #18), by doubling q_{in}.

3. Results

3.1. Predicting pressure head tolerances ratio for fixed inlet pressure head

For fixed geometric and hydraulic characteristics of the irrigation unit, the comparison between open and closed circuits was first performed for a fixed inlet pressure head, $h_{in,cl} = h_{in,op}$, evaluating the less pressure head tolerance, δ_{cl}, that the close circuit determines compared to open circuit, δ_{op}. Indeed, for closed circuits, it is expected that a minimum pressure head $h_{min,cl}$ less than that of the open circuit, $h_{min,op}$, occurs.

First, for arbitrarily set pressure head tolerances, δ_{op}, **IrriLab** was applied to determine the inlet pressure head of the open circuit, $h_{in,op}$ (Eq. 22), and the inside diameter of the manifold M_1, D_M (Eq. 23). Then, the same D_M was imposed for both M_1 and M_2 of the closed circuit (Fig. 1b). For $h_{in,cl} = h_{in,op}$, by applying HCM, the minimum pressure head of the closed circuit, $h_{min,cl}$, was calculated to determine the pressure head tolerance of the *cl* circuit, δ_{cl}.

Applying Eq. (16) to *cl*, we can write:

$$\delta_{cl} = \frac{\Delta h}{h_{in,cl} + h_{min,cl}} = \frac{\Delta h}{2\, h_{n,cl}^{(in)}} \tag{34}$$

where Δh is the pressure head range, i.e. the difference between the inlet pressure head, $h_{in,cl}$, and the minimum pressure head, $h_{min,cl}$, of the *cl* circuit ($\Delta h = h_{in,cl} - h_{min,cl}$) and, $h_{n,cl}^{(in)}$, is the average pressure head of the closed circuit, obtained by imposing the same inlet pressure head in *op* and *cl* ($h_{in,cl} = h_{in,op}$).

For fixed inlet pressure head, the lower pressure head tolerance associated with *cl* than *op*, can be expressed as the ratio, δ_{ratio} (< 1), between the *cl* pressure head tolerance, δ_{cl}, with respect to that of *op*, δ_{op}. By using Eq. (34), δ_{ratio} reads:

$$\delta_{ratio} = \frac{\delta_{cl}}{\delta_{op}} = \frac{\Delta h}{2\, \delta_{op}\, h_{n,cl}^{(in)}} \tag{35}$$

A first application of Eq. (35) was performed here. By fixing in **IrriLab**, N_{rows} = 20 and δ_{op} = 10%, and for different design input parameters (q_n, D_L, S, S_{rows}), #20 irrigation units were designed, by varying δ_M (and the corresponding δ_L, Eq. 21). It was found that for fixed N_{rows}, δ_{ratio} calculated by Eq. (35) only depends on the manifold pressure head tolerance, δ_M, as shown in Fig. 8a (red dots).

Differently from **IrriLab** software, which is based on analytical solutions, for the numerical HCM, a closed-form solution of the design parameters is unavailable.

Thus, predicting δ_{ratio} required detecting an approximated solution. At this aim, it is useful to consider the following 4-parameter relationship:

$$\delta_L = a + \frac{b}{1+(c\,\delta_{ratio})^d} \tag{36}$$

The parameters *a* and *b* can be determined by imposing the boundary conditions, which can be also checked by extrapolating the results obtained by Eq. (35) in Fig. 8a (red dots).

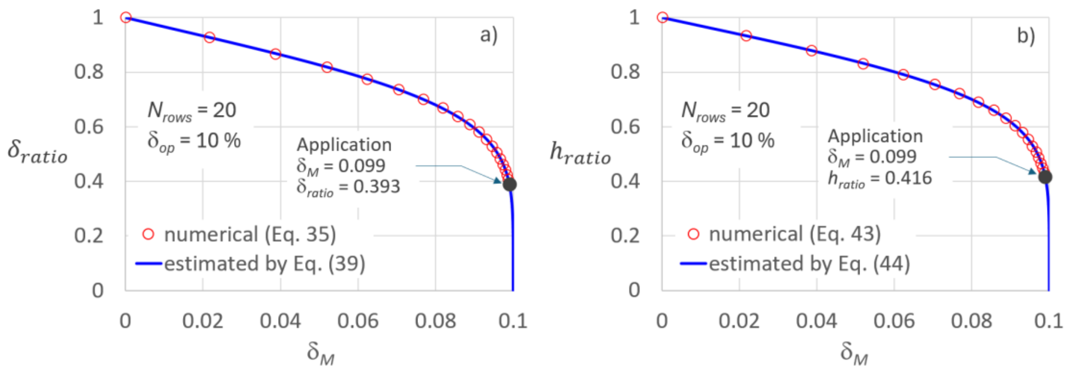

Fig. 8 *Relationship between* ***a)*** *the numerical pressure head tolerance ratio, δ_{ratio}, and the estimated one by Eq. (39), and* ***b)*** *the numerical pressure head ratio, h_{ratio}, and the estimated one by Eq. (44), versus the pressure head tolerance of the manifold, δ_M*

Indeed, when $\delta_L = 0$, $\delta_M = \delta_{op}$ (Eq. 20), meaning that all the pressure head variability is attributed to the manifold, and the closure of the circuit provides the highest benefit in making uniform the pressure heads, thus $\delta_{ratio} \sim 0$. According to Eq. (36), the latter provides:

$$\begin{matrix} \delta_L \to 0 \\ \delta_{ratio} \to 0 \end{matrix} \quad \to \quad b = -a \tag{37}$$

Contrarily, when $\delta_L = \delta_{op}$, $\delta_M = 0$ (Eq. 20), meaning that there is no pressure head variability in the manifold. Closed and open circuits behave in the same way, thus $\delta_{cl} = \delta_{op}$, and $\delta_{ratio} = 1$. According to Eq. (36), the latter provides:

$$\begin{matrix} \delta_L \to \delta_{op} \\ \delta_{ratio} \to 1 \end{matrix} \quad \to \quad a = \delta_{op}(1 + c^{-d}) \tag{38}$$

Substituting Eqs. (37 and 38), and δ_L relationship (Eq. 21) into Eq. (36), provides an explicit relationship of δ_{ratio} as a function δ_M, which only depends on the two parameters, *c* and *d*, and of course on δ_{op}:

$$\delta_{ratio}^{(est)} = \left(\frac{\delta_{op}-\delta_M}{\delta_{op}(1-\delta_M\delta_{op})+c^d\delta_M(1-\delta_{op}^2)}\right)^{1/d} \tag{39}$$

The ordinary least squares (OLS) method was applied to estimate the parameters *c* and *d*, thus minimising the standard error of the estimate, SEE, between the numerical δ_{ratio} and that estimated by using Eq. (39), providing $c = 0.981$ and $d = 5.550$. The SEE resulted in 0.0015, indicating that Eq. (39) is an excellent approximation of the exact but more numerical demanding Eq. (35), as can also be observed in Fig. 8a where Eq. (39) is also plotted. Of course, Fig. 8a shows that the imposed boundary conditions (Eqs. 37 and 38) are satisfied.

3.2. Predicting inlet pressure heads ratio for fixed pressure head tolerance

In this section, it is shown that δ_{ratio} relationship can also be used to derive, for fixed pressure head tolerance ($\delta_{cl} = \delta_{op}$), the ratio between the inlet pressure head associated with *cl* and *op* circuit, h_{ratio}. The latter is an important parameter to quantify the energy saving associated with *cl* circuits compared to *op* circuits.

Towards this aim, the required inlet pressure head of the *cl* circuit, $h_{in,cl}$, can be expressed with the following relationship:

$$h_{in,cl} = h_{n,cl}^{(in)}\left(1+\delta_{op}\right) = \frac{\Delta h}{2\,\delta_{op}\,\delta_{ratio}}\left(1+\delta_{op}\right) \tag{40}$$

where $h_{n,cl}^{(in)}$ is the average pressure head, obtained by imposing the same inlet pressure (*in*) in *op* and *cl*, which was also expressed by using Eq. (35).

Analogously to δ_{ratio}, for fixed pressure head tolerance ($\delta_{cl} = \delta_{op}$), by using Eq. (40), the ratio between the required inlet pressure head for closed circuit, $h_{in,cl}$, and that of the open circuit, $h_{in,op}$, can be written:

$$h_{ratio} = \frac{h_{in,cl}}{h_{in,op}} = \frac{\Delta h}{2\ \delta_{op}\ \delta_{ratio}\ h_{in,op}}\left(1+\delta_{op}\right) \tag{41}$$

Equation (41) can also be expressed as a function of δ_{ratio}, if considering that for fixed pressure head tolerance ($\delta_{cl} = \delta_{op}$), Δh does not depend on $h_{in,cl}$. Indeed, by varying $h_{in,cl}$, the circulating flow rates do not change, and the pressure head distribution shifts vertically by the same pressure head range:

$$\Delta h = 2\ \delta_{op} h_{n,cl}^{(\delta)} = 2\ \delta_{cl} h_{n,cl}^{(in)} \tag{42}$$

where, analogously to $h_{n,cl}^{(in)}$, $h_{n,cl}^{(\delta)}$ indicates the average pressure head of the closed circuits, obtained by imposing the same pressure head tolerance (δ) of the open circuit ($\delta_{cl} = \delta_{op}$).

Finally, by using Eq. (41) and Eq. (42), and rearranging, h_{ratio} can be interestingly expressed as a function of δ_{ratio}, for any $\delta_{op} = \delta_{cl}$:

$$h_{ratio} = \frac{h_{in,cl}}{h_{in,op}} = \frac{\left(1+\delta_{op}\right)\delta_{ratio}}{1+\delta_{op}\ \delta_{ratio}} \tag{43}$$

Of course, h_{ratio} can be written as a function of the estimated δ_{ratio} (Eq. 39):

$$h_{ratio}^{(est)} = \frac{1+\delta_{op}}{\delta_{op}+\left(\frac{\delta_{op}\left(1-\delta_M\delta_{op}\right)+c^d\delta_M\left(1-\delta_{op}^2\right)}{\delta_{op}-\delta_M}\right)^{1/d}} \tag{44}$$

By using the numerical δ_{ratio} values (Fig. 8a, red dots), the corresponding numerical h_{ratio} values obtained by Eq. (43) are plotted in Fig. 8b (red dots), which shows a similar (not equal) decreasing behaviour versus δ_M. Of course, the predictive $h_{ratio}^{(est)}$ relationship (Eq. 44), with the previously determined parameters c = 0.981 and d = 5.550, shows an excellent fitting, as for $\delta_{ratio}^{(est)}$.

It is important to note that the comparison results expressed in terms of δ_{ratio} and h_{ratio}, both numerical (Eqs. 35 and 43) and analytical (Eqs. 39 and 44), are independent on the adopted resistance equation. This implies that these results are of general validity.

In Fig. 8b, it is interesting to observe that unlike open circuits, where the inlet pressure head increases with increasing δ_M (Figs. 6a,c), for closed circuits h_{ratio} decreases as δ_M increases. This indicates that $h_{in,op}$ is more sensitive to δ_M, than $h_{in,cl}$. Consequently, when open circuits are designed for low δ_M, energy can be saved, albeit with higher investment costs due to the larger inside manifold diameters (see Figs. 6b,d). Contrarily, when open circuits are designed for high δ_M, closing the circuit is recommended as substantial energy can be saved compared to open circuits. Furthermore, thanks to higher δ_M, investment costs also decrease.

Equation (44) holds relevant implications in practice since it helps assess the potential energy-saving benefits related to the closure of microirrigation open circuits. However, at this stage, the application of Eq. (44) is limited to the specific values of $N_{rows} = 20$ and $\delta_{op} = 0.1$.

In the next section, to explore the influence of δ_{op} and N_{rows} on c and d parameters, thus generalising the applicability of both Eqs. (39 and 44), a high number of simulations were performed to address this issue.

3.3. *Estimating c and d parameters for different δ_{op} and N_{rows}*

To investigate the influence of N_{rows} and δ_{op} on c and d parameters, #3,800 simulations were performed by randomly varying the design variables, D_L, N, S, N_{rows}, S_{rows}, q_n, δ_{op}, and calculating the design variables of open circuits, h_{in} (Eq. 22) and D_M (Eq. 23). In particular, N_{rows} was selected in the range [3−40], thus covering a wide range of practical cases, while 5 values of δ_{op} were selected around the commonly accepted 10%, $\delta_{op} = \{0.04, 0.07, 0.1, 0.13, 0.16\}$. Therefore, the considered #3,800 irrigation units derived from 20 times δ_M × 38 times N_{rows} × 5 times δ_{op}.

For each δ_{op}, the corresponding 20 values of δ_M (and δ_L Eq. 21) were log-scaled as in Figs. 8a,b, to obtain a higher number of simulations for high δ_M than for low δ_M, where the δ_{ratio} relationship is almost linear (Fig. 8b).

For each geometry and hydraulic characteristic of the irrigation unit, HCM was applied, thus determining for the same *op* inlet pressure head, $h_{in,op}$, and emitter flow rate, q_n, the *cl* minimum pressure head, $h_{in,cl}$ ($< h_{in,op}$), the pressure head range, Δh, the average pressure head, $h_{n,cl}^{(in)}$, the pressure head tolerance, δ_{cl} (Eq. 34), and the corresponding δ_{ratio} (Eq. 35).

For each N_{rows}, c and d parameters were calculated by applying the OLS method, as discussed in Fig. 8a, for N_{rows} = 20 and δ_{op} = 10%. Figure 9a and 9b graph the c and d parameters, respectively, as a function of N_{rows}, for different δ_{op}. While c shows a minimum for low N_{rows} and then approaches a constant c value as N_{rows} increases, the d parameter increases versus N_{rows}.

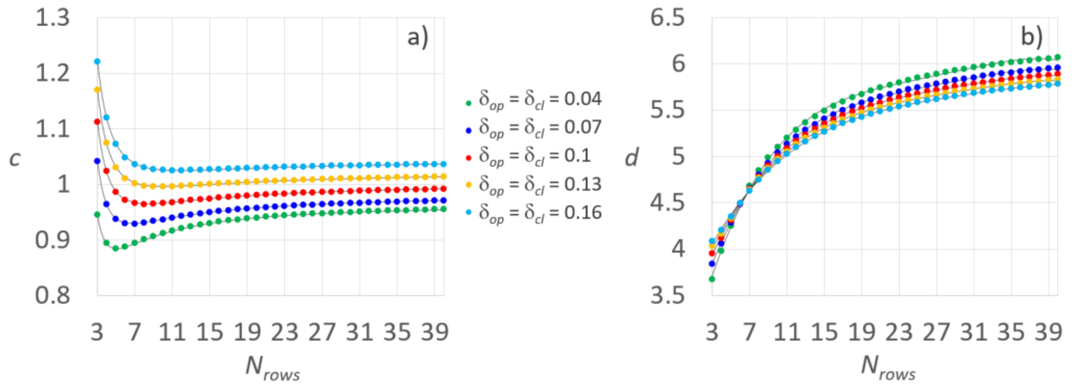

Fig. 9 *Relationship between **a)** c parameter and **b)** d parameter of predictive relationships (Eqs. 39 and 44), versus the number of the lateral N_{rows}, for different pressure head tolerances, δ_{op} = 0.04, 0.07, 0.1, 0.13, 0.16. Black lines in **a)** and **b)** refer to Eqs. (45 and 46), respectively*

To predict c and d parameters, and thus h_{ratio}, for any geometric and hydraulic characteristics of open and closed circuits, two different functions were fitted to c and d parameters:

$$c = a_0 - \left(\frac{a_1 N_{rows}^{a_2} + a_3}{e^{\left(a_1 N_{rows}^{a_2} + a_4\right)}}\right) \tag{45}$$

$$d = b_0 + b_1 N_{rows} + b_2 N_{rows}^2 + b_3 N_{rows}^3 + b_4 N_{rows}^4 \tag{46}$$

where, a_0, a_1, a_2, a_3, a_4, and b_0, b_1, b_2, b_3, b_4, are numerical coefficients to be obtained by applying OLS method (Table 1 and Table 2, respectively).

OLS method provided good results, as can be observed by the index statistics, reported in Table 3 for parameter c and in Table 4 for parameter d. In particular, a very low standard error in the estimate, SEE, has been found for both parameters.

Figure 9a and 9b also plot Eq. (45) and Eq. (46), respectively, versus N_{rows}, with the numerical coefficients reported in Table 1 and Table 2, evidencing that these equations are suitable to estimate both parameters and thus predict h_{ratio}. To further verify the latter, for the considered #3,800 irrigation units, in Fig. 10, a comparison between the numerical h_{ratio} values with those calculated by Eq. (44), is illustrated.

Table 1 *Numerical coefficients a_0, a_1, a_2, a_3, and a_4, to estimate c parameter by Eq. (45)*

parameter	δ_{op}	a_0	a_1	a_2	a_3	a_4
	0.04	0.963	36.147	0.0452	−37.896	−36.344
	0.07	0.981	73.903	0.0215	−75.987	−74.021
c	0.1	1.003	62.981	0.0237	−65.237	−62.956
	0.13	1.023	22.574	0.0611	−25.002	−22.376
	0.16	1.042	8.007	0.1512	−10.640	−7.564

Table 2 *Numerical coefficients b_0, b_1, b_2, b_3, and b_4, to estimate d parameter by Eq. (46)*

parameter	δ_{op}	b_0	b_1	b_2	b_3	b_4
	0.04	2.663	0.410	−2.15E-02	5.26E-04	−4.82E-06
	0.07	2.977	0.336	−1.67E-02	3.93E-04	−3.51E-06
d	0.1	3.186	0.289	−1.36E-02	3.10E-04	−2.69E-06
	0.13	3.340	0.254	−1.14E-02	2.51E-04	−2.11E-06
	0.16	3.460	0.226	−9.74E-03	2.05E-04	−1.66E-06

Figure 10 shows that the dots are very close to the line of the perfect agreement also reported, indicating that Eq. (44) is an excellent approximation of the exact numerical h_{ratio} values, thus it can be applied to explain the less energy that closed circuits require compared to open circuits. Dots that slightly deviate from the 1:1 line, refer to units characterised by low N_{rows} values (3 and 4), for which Eq. (44) fits a bit worse than for higher N_{rows}. The standard error in the h_{ratio} estimate, SEE, calculated for the 3,800 irrigation units, i.e. including the five considered δ_{op} values, was satisfying and equal to 0.0038.

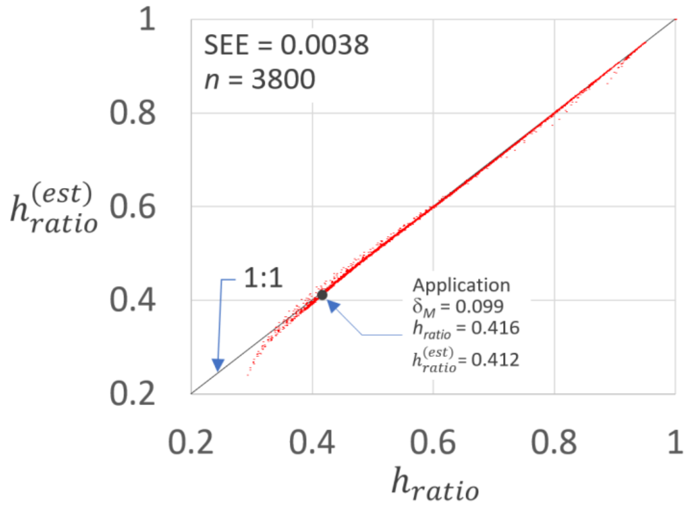

Fig. 10 *Comparison between the pressure head ratio, hratio, obtained by the numerical procedure with those calculated by Eq. (44), for # 3800 irrigation subunits characterised by different geometric and hydraulic parameters*

Table 3 *Sum squares error, SSE and standard error, SEE, in the estimate of c parameter, for different* δ_{op}

parameter	δ_{op}	SSE	SEE
	0.04	2.65E-06	0.00027
	0.07	5.54E-06	0.00039
c	0.1	1.36E-05	0.00061
	0.13	1.59E-05	0.00066
	0.16	1.12E-05	0.00055

Table 4 *Determination and correlation coefficients,* R^2 *and R, sum squares error, SSE, and standard error, SEE, in the estimate of d parameter, for different* δ_{op}

parameter	δ_{op}	R^2	R	SSE	SEE
	0.04	0.999	1.000	0.01174	0.01886
	0.07	1.000	1.000	0.00404	0.01107
d	0.1	1.000	1.000	0.00232	0.00838
	0.13	1.000	1.000	0.00220	0.00816
	0.16	1.000	1.000	0.00256	0.00881

The effects of the variables (N_{rows}, δ_{op}, δ_M) on $h_{ratio}^{(est)}$ was investigated. In Fig. 11, Eq. (44) is plotted versus the manifold pressure head tolerance, δ_M, with $N_{rows} = 3$, 4, 6, 10, 20, 40 as a parameter and for a fixed $\delta_{op} = 0.10$.

Particularly, Fig. 11a shows that $h_{ratio}^{(est)}$ is much more sensitive to δ_M than N_{rows}, especially for high N_{rows} values. Indeed, for a fixed δ_M and $N_{rows} > 10$, the influence of

N_{rows} on $h_{ratio}^{(est)}$ seems to vanish, as it would be expected. Of course, for very low δ_M, $h_{ratio}^{(est)}$ approaches to the unity.

Figure 11b shows the pressure head ratio, $h_{ratio}^{(est)}$, versus δ_M, for a fixed N_{rows} = 20 and different $\delta_{op} = \delta_{cl}$ = 0.04, 0.07, 0.10, 0.13, 0.16. Figure 11b shows that any $h_{ratio}^{(est)}$ can be obtained by varying both δ_M and δ_{op}. In both Fig. 11a and 11b, the black dot refers to the application that will be performed later.

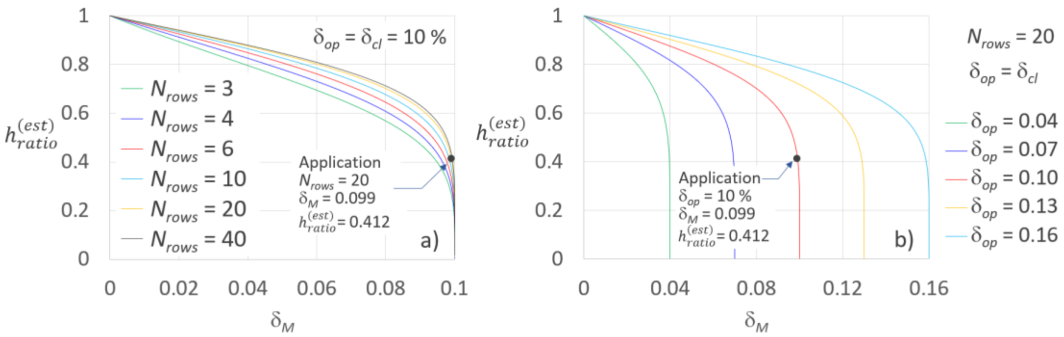

***Fig. 11** Relationship between the estimated pressure head ratio, $h_{ratio}^{(est)}$, versus manifold pressure head tolerance, δ_M, **a)** for fixed δ_{op} = 0.10 and different N_{rows} = 3, 4, 6, 10, 20, 40, and **b)** for fixed N_{rows} = 20 and different $\delta_{op} = \delta_{cl}$ = 0.04, 0.07, 0.10, 0.13, 0.16. Black dots refer to the application performed in Fig. 13*

In the next section, an application of the easy to apply predictive relationships of $\delta_{ratio}^{(est)}$ and $h_{ratio}^{(est)}$ with the *c* and *d* parameters estimated by Eqs. (45 and 46) is performed. The results will be verified by applying the more time-consuming SBS procedure and HCM.

4. Application and discussion

Consider a rectangular microirrigation unit, corresponding to layout #18 (Fig. 1 and Fig. 3), fed in the mid-manifold, laid on a flat field, with drip laterals length, L_L = 20 m, and N = 100 emitters, spaced S = 0.2 m, installed along the laterals. The inside lateral diameter is D_L = 17.7 mm, and the emitter flow rate q_n = 2 L/h (Table 5) was adopted for both methods under the assumption of uniform emitter flow rates. Also, the microirrigation unit is characterised by 40 drip laterals, spaced S_{rows} = 1 m. Because of unit symmetry, applications need to be performed for N_{rows} = 20 (manifold length, L_M = 20 m).

To expect a high energy-saving benefit induced by the closure of the open circuit, a high value of δ_M = 0.099 was chosen, as can be observed in Fig. 8b, where the black dot corresponds to the application performed here. For the commonly accepted δ_{op} = 0.10, the application of Eq. (23) provided D_M = 20.69 mm, and h_{in} = 23.66 m (Eq. 22). Since Layout #18 (BIP = 0.5) was considered, the inlet discharge is obtained by doubling $q_{in} = 2\ (q_n \times N \times N_{rows})$ = 8 m^3 h^{-1}, as reported in Table 5.

First, for fixed inlet pressure head ($h_{in,op} = h_{in,cl}$), to evaluate the less pressure head variability in the *cl* circuit compared to *op*, Eq. (39) was applied to estimate $\delta_{ratio}^{(est)}$, with *c* and *d* parameters provided by Eq. (45) and Eq. (46), giving c = 0.980 and d = 5.554, and thus $\delta_{ratio}^{(est)}$ = 0.389 (Table 5). In particular, the closure of the circuit determines a pressure head tolerance 61.1% less than that of the open circuit, providing δ_{cl} = 0.0389.

To verify the result obtained by Eq. (39), the SBS procedure and the HCM were applied to achieve the pressure head distribution of both *op* and *cl* circuits, which are illustrated in Fig. 12.

Specifically, for the open circuit, by imposing $h_{min,op}$ = 19.36 m, the SBS procedure provides $h_{in,op}$ = 23.66 m, which exactly matches the analytical value. Indeed, it can be easily checked that the pressure head tolerance δ_{op} calculated by Eq. (16) with these pressure head values, is exactly equal to the imposed 10% value.

For the closed circuit, by imposing the same inlet pressure head ($h_{in,op} = h_{in,cl}$ = 23.66 m), HCM provided $h_{min,cl}$ = 21.87 m, and thus a pressure head range Δh = 1.79 m, lower than open circuit Δh = 4.30 m (Table 5). Finally, the numerical δ_{ratio} was obtained by Eq. (35), giving δ_{ratio} = 0.393 m, which is very similar to the estimated value (0.389), which was to be demonstrated.

Second, for fixed pressure head tolerance ($\delta_{op} = \delta_{cl}$), Eq. (44) was applied to assess the energy saving ($h_{ratio}^{(est)}$) provided by the *cl* circuit compared to *op* circuit. Using *c* and *d* parameters previously determined (Table 5), Eq. (44) made it possible to estimate $h_{ratio}^{(est)}$, giving 0.412. The latter means that the closure of the circuit determines an energy consumption of 58.4% less than the open circuit.

Table 5 *Design variables of the open (op) and closed (cl) circuits, and corresponding numerical and estimated δ_{ratio} and h_{ratio} values, for the applications illustrated in Fig. 11 (for fixed $h_{in,op}$ = $h_{in,cl}$ = 23.66 m) and in Fig. 12 (for fixed δ_{op} = δ_{cl} = 0.1)*

Parameter	Symbol	Open Circuit (*op*)	Closed Circuit (*cl*)
Number of emitters	N	100	
Emitters' spacing	S (m)	0.2	
Lateral length	L_L (m)	20	
Number of rows	N_{rows}	20	
Interspace drip laterals	S_{rows} (m)	1	
Lateral length	L_M (m)	20	
Inside diameter of drip laterals	D_L (mm)	17.7	
Emitter flow rate	q_n (l/h)	2	
Inside diameter of the manifold M_1 (Eq. 23)	D_{M1} (mm)	20.69	
Inside diameter of the manifold M_2	D_{M2} (mm)	–	20.69
Inlet flow rate	q_{in} (m^3/h)	8	
Fixed inlet pressure head (Eq. 22) $\delta_{op} \neq \delta_{cl}$	h_{in} (m)	23.66	
Pressure head tolerance (fixed h_{in})	δ	0.1	0.039
Lateral pressure head tolerance	δ_L	0.001	–
Manifold pressure head tolerance (Eq. 20)	δ_M	0.099	–
c parameter (estimated, Eq. 45)	c	0.980	
d parameter (estimated, Eq. 46)	d	5.554	
$\delta_{ratio}^{(est)}$ (estimated, Eq. 39)		0.389	
Minimum pressure head	h_{min} (m)	19.36	21.87
Pressure head range	Δh (m)	4.30	1.79
Average pressure head	h_n (m)	21.53	22.8
δ_{ratio} (numerical, Eq. 35)		0.393	
Fixed pressure head tolerance $\delta_{op} = \delta_{cl}$	δ	0.1	
Inlet pressure Inlet (fixed h_{in})	h_{in} (m)	23.66	9.85
$h_{ratio}^{(est)}$ (estimated, Eq. 44)		0.412	
Minimum pressure head	h_{min} (m)	19.36	8.06
Pressure head range	Δh (m)	4.30	1.79
Average pressure head	h_n (m)	21.53	8.95
h_{ratio} (numerical, Eq. 43)		0.416	

Again, the result was verified by comparing the pressure head distribution of the *op* circuit already considered in Fig. 12, with that of the *cl* circuit obtained by HCM, which is illustrated in Fig. 13.

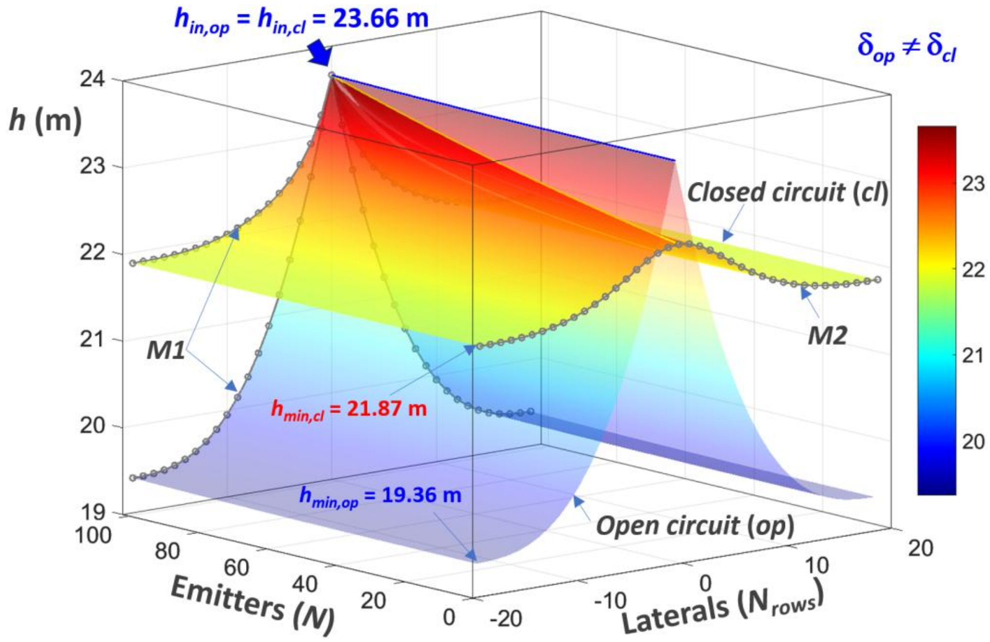

Fig. 12 *Comparison between the pressure head distributions for open circuit obtained by **IrriLab**, and for closed circuit obtained by Hardy Cross Method (HCM), for fixed inlet pressure head,* h_{in} *= 23.66 m*

HCM provided $h_{min,cl}$ = 8.06 m and $h_{in,cl}$ = 9.85 m, thus the resulting numerical h_{ratio} can be calculated by Eq. (43), providing h_{ratio} = 0.416. The result shows that the exact numerical h_{ratio} value is close to the estimated one (0.412), demonstrating also for the predictive $h_{ratio}^{(est)}$ the suitability of the practical relationship.

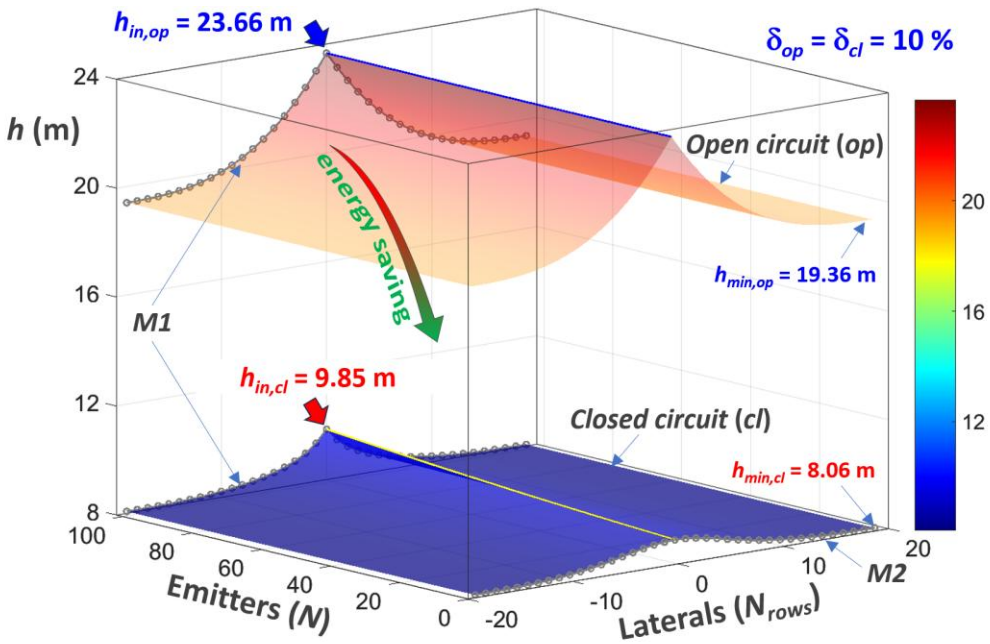

Fig. 13 *Comparison between the pressure head distributions for open circuit obtained by **IrriLab**, and for closed circuit obtained by Hardy Cross Method (HCM), for fixed pressure head tolerance,* $\delta_{op} = \delta_{cl}$ *= 10%*

5. Conclusions

In this paper, the closure of open drip irrigation systems with a secondary manifold connecting laterals ends was deeply analysed. A comprehensive comparison between open and closed circuits was carried out to assess the hydraulic performances and energy-saving implications in drip irrigation design. The open circuits were analysed by using IrriLab software, which is based on the concept of pressure head tolerances. The closed circuits were analysed by applying the Hardy Cross Method (HCM), by using the design parameters calculated by IrriLab.

The most important points covered in this work can be summarised as follows:

- In IrriLab software, a revised relationship of the unit pressure head tolerance (δ_{op}) and of the pressure head amplification factor (Δ) was applied to provide no errors in the drip irrigation system design;
- The comparison between open and closed circuits was performed i) for a fixed inlet pressure head ($h_{in,op} = h_{in,cl}$), evaluating the less pressure head tolerance (expressed as pressure head tolerance ratio, δ_{ratio}, and ii) for a fixed pressure head tolerance ($\delta_{op} = \delta_{cl}$), evaluating the inlet pressure head ratio, h_{ratio}, thereby the less inlet pressure head which the close circuit requires;
- Results showed that for open circuits, the inlet pressure head, $h_{in,op}$, increases as δ_M also increases, while for closed circuits, the inlet pressure head ratio, h_{ratio}, decreases versus δ_M. This would suggest that for low δ_M, open circuits are recommended since energy can be saved, although the higher inside manifold diameters. Contrarily, for high δ_M, the closure of the circuit is more appropriate to choose, since a lot of energy can be saved compared to open circuits;
- For #3,800 drip irrigation units characterised by different geometric and hydraulic parameters, approximated relationships were derived to predict both i) the pressure head tolerance ratio, δ_{ratio}, and ii) the pressure head tolerance ratio, h_{ratio}, which can be useful for the design of drip irrigation systems.

6. References

Abramov NN (1972) Theory and calculation technique for water supply systems. Stroizdat, Moscow

Abramowitz M, Stegun IA (1972) Handbook of mathematical functions. Dover, New York

Baiamonte G (2016) Simple Relationships for the Optimal Design of Paired Drip Laterals on Uniform Slopes. J Irrig Drain Eng-ASCE 142: 04015054. https://doi.org/10.1061/(ASCE)IR.1943-4774.0000971

Baiamonte G (2018a) Advances in designing drip irrigation laterals. Agric Water Manage 199:157-174. https://doi.org/10.1016/j.agwat.2017.12.015

Baiamonte G (2018b) Explicit relationships for optimal designing rectangular microirrigation units on uniform slopes: The IrriLab software application. Comput Electron Agric 153:151-168. https://doi.org/10.1016/j.compag.2018.08.00

Baiamonte G (2024) Closed-Form solution of the length of drip laterals and easy selection of commercial emitters for low-slope field under Hazen-Williams and Blasius resistance equations. Irrig Drain Journal 1–13. https://doi.org/10.1002/ird.2969

Baiamonte G, Palermo S, Sadeghi H, Peters RT (2024) Design Emission Uniformity of Horizontal Tapered Drip Laterals from the Normalized Pressure Head Distribution Approach. J Irrig Drain Eng-ASCE. Doi: 10.1061/JIDEDH/IRENG-10300

Belaud G, Mateos L, Aliod R, et al. (2020) Irrigation and energy: issues and challenges. Irrig Drain 69:177-185. https://doi.org/10.1002/ird.2343

Bralts VF, Segerlind LJ (1985) Finite element analysis of drip irrigation submain units. Trans ASAE 28: 809-814

Chandrasekhar M, Stewart K (1975) Sparsity oriented analysis of large pipe networks. J Hydraul Div 101:341-355

Cross H (1936) Analysis of flow in networks of conduits or conductors. University of Illinois. Engineering Experiment Station. Bulletin; no. 286

Dumka P, Samaiya N, Gandhi S, Mishra DR (2023) Modelling of Hardy Cross Method for Pipe Networks. SSRG Int J Mech Eng 10(2):1-8

Gil M, Rodríguez-Sinobas L, Juana L, Sánchez R, Losada A (2008) Emitter discharge variability of subsurface drip irrigation in uniform soils. Effect on water application uniformity. Irrig Sci 26:451-458. https://doi.org/10.1007/s00271-008-0116-1

Issacs LT, Mills KG (1980) Linear theory methods for pipe network analysis. J Hydraul Div 106:1191-1201

Jackson TM, Khan S, Hafeez M (2010) A comparative analysis of water application and energy consumption at the irrigated field level. Agric Water Manage 97:1477-1485. https://doi.org/10.1016/j.agwat.2010.04.013

Jiang S, Kang Y (2010) Simple method for the design of microirrigation paired laterals. J Irrig Drain Eng 136: 271-275. https://doi.org/10.1061/(ASCE)IR.1943-4774.0000178

Lamm FR (2002) Advantages and disadvantages of subsurface drip irrigation. In: International meeting on advances in drip/micro irrigation, Puerto de La Cruz, Tenerife, Canary Islands, pp 1–13

Keller J, Bliesner RD (1990) Sprinkle and Trickle Irrigation. The Blackburn Press, New York

Lazarovitch N, Simunek J, Shani U (2005). System dependent boundary conditions for water flow from a subsurface source. Soil Sci Soc Am J 69:46-50. https://doi.org/10.2136/sssaj2005.0046

Lopes AMG (2004) Implementation of the Hardy-Cross method for the solution of piping networks. Comput Appl Eng Educ 12:117-125. https://doi.org/10.1002/cae.20006

Ma P, Hu Y, Liu H (2019) Optimal Design for Pressurized Irrigation Subunits with a Minimum Cost and Maximum Area for Uniformly Sloping Fields. Water Resour Manage 33:2711-2726. https://doi.org/10.1007/s11269-019-02243-6

Martin D, Peters G (1963) The application of Newton's method to network analysis by digital computer, J Inst Water Eng 17:115-129

Masoumi M, Kashkooli BS, Monem MJ et al. (2016) Multi- Objective Optimal Design of on- Demand Pressurized Irrigation Networks. Water Resour Manage 30:5051-5063. https://doi.org/10.1007/s11269-016-1468-6

Moghazi HE-DM (1998) Estimating Hazen-Williams coefficient for polyethylene pipes. J Transp Eng 124:197–199. https://doi.org/ 10.1061/(ASCE)0733-947X(1998)124:2(197)

Rai, RK, Sanap NG (2017) Analysis of hydraulic network using hardy-cross method and EPANET. Int J Innov Res Sci Eng 3 (03)Ravikumar V (2023) Sprinkler and Drip Irrigation: Theory and Practice. Springer Nature

Ravikumar V (2023) Sprinkler and drip irrigation: theory and practice. Springer Nature, Cham

Rossman LA (2002) EPANET 2 Users Manual. Water Supply and Water Resources Division, National Risk Management Research Laboratory, Cincinnati, OH45268

Sarbu I (2014) Nodal Analysis of Urban Water Distribution Networks. Water Resour Manage 28:3143 -3159. https://doi.org/10.1007/s11269-014-0660-9

Shani U, Xue S, Gordin-Katz R, Warrick AW (1996) Soil-limiting from subsurface emitters. I: Pressure measurements. J Irrig Drain Eng-ASCE 122:291-295

Singh VP, Su Q (2022) Irrigation engineering. Principles, processes, procedures, design, and management. Cambridge University Press, UK

Singh H, Mishra D, Nahar NM (2002) Energy use pattern in production agriculture of a typical village in arid zone, India—part I. Energy Convers Manag 43:2275-2286. https://doi.org/10.1016/S0196-8904(01)00161-3

Todini E, Pilati S (1987) A gradient method for the analysis of pipe networks, in: Proceedings of the International Conference on Computer Applications for Water Supply and Distribution, Leicester Polytechnic, UK, 1987

Todini E and Rossman (2013) Unified Framework for Deriving Simultaneous Equation Algorithms for Water Distribution Networks. J Hydraul Eng 139(5): 511-526

Todini E (2006) On the convergence properties of the different pipe network algorithms. 8th Annual Water Distribution Systems Analysis Symposium, Cincinnati, Ohio, USA, August 27-30

Wang J, Zhu D, Bralts VF, Zhang L (2016) Hydraulic Analysis of Looped Microirrigation Submain Units Using the Finite Element Method. Trans ASABE 59:909-923

Wang J, Chen R, Yang T, Wei T, Wang X (2021) A computationally-efficient finite element method for the hydraulic analysis and design of subsurface drip irrigation subunits. J. Hydrol 595:125990. https://doi.org/10.1016/j.jhydrol.2021.125990

Wang Y, Zhang Y, Wang W, Liu Z, Yu X, Li H, Wang W, Hu X. (2023) A Review of Optimal Design for Large-Scale Micro-Irrigation Pipe Network Systems. Agronomy 13:2966. https://doi.org/10.3390/agronomy13122966

Wood D, Rayes A (1981) Reliability of algorithms for pipe network analyses. J Hydraul Div 107: 982-991

Wu PT, Zhu DL, Wang J (2010) Gravity-fed drip irrigation design procedure for a single-manifold subunit. Irrig Sci 28 (4): 359–369

CHAPTER 2

Quantifying local losses due to root intrusion in subsurface drip irrigation systems by monitoring inlet discharge and pressure head

Based on the **published** paper:

Baiamonte, G., Vaccaro, G., Palermo, S., **2024b**. Quantifying local losses due to root intrusion in subsurface drip irrigation systems by monitoring inlet discharge and pressure head. *Irrig. Sci.*
https://doi.org/10.1007/s00271-024-00990-y

CHAPTER 2: Quantifying local losses due to root intrusion in subsurface drip irrigation systems by monitoring inlet discharge and pressure head

Giorgio Baiamonte[1], GirolamoVaccaro[1], Samuel Palermo[1]

[1]Dept. of Agricultural, Food and Forest Sciences (SAAF), Univ. of Palermo, viale delle Scienze, Bldg. 4, 90128 Palermo. *Corresponding Author, E-mail: giorgio.baiamonte@unipa.it

Abstract

In subsurface drip irrigation systems (SDI), the emitter flow rate is affected by the root intrusion phenomena and by the so-called back pressure that limits the buried emitters' outflow. This paper suggests a methodology to investigate the effect of root intrusion and back pressure on SDI performance, for different root guard emitter treatments in a 6-year experimental campaign (2018−2023), carried out in Sicily (Italy). Inlet discharges and pressure heads were collected over time, and their variations were used to quantify the effect of root intrusion in terms of local losses. The change in the SDI hydraulic performance was studied using a modified Hardy Cross method (HCM), which is suitable for lopped drip irrigation networks. The HCM applications also considered local losses and back pressure, requiring a comprehensive hydraulic characterisation of the soil to accurately estimate the factors influencing back pressure. Specifically, the influence of root intrusion in different emitters was analysed by considering the time variation of the fraction α of the kinetic head. The results showed diverse behaviours among the root guard emitter treatments. Emitters treated with different herbicides (He 1 and He 2) revealed no significant α-fraction variation over time, denoting the effectiveness of He 1 and He 2 treatments in root intrusion protection. Whilst for Copper (Cu) and control (Ctrl) treatments, a severe decrease in emitter flow rate was observed, confirmed by high α-fraction variations over the investigated period.

Keywords: Cavity radius estimation, Experimental measurements, Soil hydraulic properties, Hardy Cross method, Looped drip irrigation system

List of symbols

A	Constant of Haverkamp's model (mm^{-1})	q_n	Average emitter flow rate ($L\ h^{-1}$)
b	Capillary scale parameter	Q_n	Average inlet flow rate ($m^3\ h^{-1}$)
b_s	Intercept of the straight line fitted to the data describing steady-state conditions on the I vs. t plot (mm)	q_N	Nominal emitter flow rate or nodal outflow ($L\ h^{-1}$)
c	Constant of Haverkamp's model	r	Flow rate exponent of the flow resistance equation
C	Pipe smoothness factor	r_i	Radius of the infiltration surface (mm)
D	Inside pipe diameter (mm)	r_0	Cavity radius (mm)
D_N	Nominal pipe diameter (mm)	S	Emitter spacing (m)
h	Pressure head (mm)	s	Inside diameter exponent of the flow resistance equation
h_{*s}	Normalised back pressure	S_{rows}	Laterals spacing (m)
H_{dn}	Downstream observed pressure head (m)	S_S	Soil sorptivity ($mm\ h^{-0.5}$)
$H_{dn,2018}$	Downstream pressure head for the reference year 2018 (m)	t	Time (h)
h_i	Total head loss in the generic pipe "*i*" (m)	w_0	Antecedent gravimetric soil water content ($g\ g^{-1}$)
h_N	Nominal emitter's pressure head (m)	x	Exponent of the emitter flow relation
h_s	Back pressure (m)	α	Coefficient of local losses expressed as α-fraction of the kinetic head
H_{up}	Observed inlet pressure head (m)	α_{GR}	Shape parameter of the Gardner hydraulic conductivity function (m^{-1})
$H_{up,2018}$	Upstream pressure head for the reference year 2018 (m)	β	Shape constant of Haverkamp's mode
I	Cumulative infiltration of the water in the soil (mm)	γ	Correction constant of Haverkamp's model
i_s	Slope of the straight line fitted to the data describing steady-state conditions on the *I* vs. *t* plot ($mm\ h^{-1}$)	ΔH_{obs}	Difference between the observed upstream and downstream pressure heads (m)
k	Flow resistance equation coefficient	ΔH_s	Increase in pump pressure head for each subunit (m)
K	Soil hydraulic conductivity ($mm\ h^{-1}$)	$\Delta H_{s,1}$	Increase in pump pressure head for subunit #1 (m)
K_0	Initial soil hydraulic conductivity ($mm\ h^{-1}$)	$\Delta H_{s,2}$	Increase in pump pressure head for subunit #2 (m)
k_e	Coefficient of the emitter flow relation ($l\ h^{-1}\ m^{-x}$)	ΔK	Difference between K_s and K_0 ($mm\ h^{-1}$)
k_L	Flow resistance equation coefficient for the laterals	Δ'_m	Imbalance head loss (m)

K_s	Soil hydraulic conductivity (mm h^{-1})	$\Delta Q_{s,1}$	Average inlet flow rate for subunit #1 (m^3 h^{-1})
L_i	Lateral or pipe length (m)	$\Delta Q_{s,2}$	Average inlet flow rate for subunit #2 (m^3 h^{-1})
N	Number of emitters	$\Delta\theta$	Difference between θ_s and θ_0 (cm^3 cm^{-3})
N_{rows}	Number of laterals	θ_0	Antecedent volumetric soil water content (cm^3 cm^{-3})
p'_m	Corrective flow rate (m^3 h^{-1})	θ_s	Volumetric water content of the saturated soil (cm^3 cm^{-3})
q_{*n}	Normalised emitter flow rate	λ_c	Macroscopic capillary length (mm)
$q_{*n,min}$	Threshold of q_{*n} below which no back pressure head exists	ρ_b	Dry soil bulk density (g cm^{-3})
q_i	Discharge in pipe "i" meeting at node "n" (L h^{-1})	ϕ	Soil porosity (cm^3 cm^{-3})
Q_{in}	Inlet flow rate (m^3 h^{-1})	Φ_m	Matric flux potential (mm^2 h^{-1})

1. Introduction

In subsurface drip irrigation (SDI) systems, the drip laterals are installed below the ground level, and unlike surface drip irrigation, the water loss due to evaporation is reduced (Camp 1998; Cahn and Hutmacher 2024). A comprehensive discussion on the advantages of SDI systems was performed by Lamm (2002), who evidenced that SDI systems provide high water use efficiency, high water application uniformity, energy saving and improved cultural practices. In addition, if the SDI is managed correctly, deep percolation losses due to irrigation can be highly limited.

The main drawbacks of these systems are (i) the emitters' clogging caused by root intrusion and soil particle suction, which can significantly impact irrigation uniformity (Lamm et al. 2021; Shi et al. 2022), and (ii) the positive pressure occurring around the source, also denoted as back pressure (Philip 1992), which may limit the emitter flow rate. The back pressure may result in the delivery of less water than originally established in the SDI system.

Concerning emitters' clogging, Muhammad et al. (2022) evaluated the effect of root intrusion on SDI system performance, in 5-year sugarcane growth, demonstrating that the system's overall performance, namely emitter relative discharge and Christiansen's uniformity coefficient, can decrease by 25%.

Different methods to prevent root intrusion typically involve the application of diluted acids, herbicides or root guard emitters (Suarez-Rey et al. 2006). Root-growth inhibitors are embedded within the emitter or pipe materials, using polymers infused with controlled-release agents or integrating herbicides directly into the emitters, thereby providing long-term protection against root intrusion and enhancing system longevity.

To avoid the use of chemical products, Souza et al. (2014) developed a prototype emitter to be used in SDI systems, which is composed of three concentric cylindrical elements, an elastic silicone membrane, a polyethylene tube with two holes drilled into its wall for water discharge, and a vinyl polychloride protector system to wrap the other elements. Some kinds of emitters are also equipped with an anti-siphon system. However, this mechanism appeared more suitable to prevent soil particle ingestion, rather than root intrusion (Petroselli et al. 2022).

The positive pressure around the source can also highly affect the performance of buried emitters. First, Philip (1992) investigated the water movement from a buried point source, concluding that in most soils, when the emitter flux is higher than the soil infiltration capacity, a spherical saturated region characterised by positive pressure is formed around the source, decreasing the pressure gradient near the emitters. Moreover, Philip (1992) developed an analytical solution to estimate the back pressure, which depends on soil hydraulic properties, the emitter flow rate and the so-called cavity radius, namely the radius of a saturated spherical region that forms around the discharge point source with soil water.

Many researchers have evaluated the suitability of Philip's solution in SDI systems. Shani et al. (1996) investigated the effect of back pressure on the emitter's flow rate for both pressure-compensating (PC) and non-compensating emitters (N-PC) of three representative soil types. Back pressure was measured when the emitter's discharges were higher than the soil infiltration capacity; thus, the soil-saturated hydraulic conductivity is crucial to choosing the emitter type carefully. Other studies evaluated the flow rate for both PC and N-PC emitters, concluding that soil hydraulic characterisation is compulsory to properly account for back pressure, which affects the actual performance of the emitters (Gil et al. 2008; Nogueira et al. 2021; Wang et al. 2024).

Several methods have been developed to determine the hydraulic characteristic curves of the soil, both in the laboratory and field (Raimbault 1986; Mallants et al. 1997; Simunek et al. 1998; Angulo-Jaramillo et al. 2000). Determining these properties using traditional methods is both expensive and time-consuming; thus, new simplified techniques have been developed.

Haverkamp et al. (1996) introduced a simplified procedure known as the "Beerkan Method" that makes it possible to characterise easily the soil's hydraulic properties. This approach involves employing certain analytical formulas for the hydraulic characteristic curves and estimating their shape parameters, which are dependent on soil texture, based on basic particle-size analysis. Additionally, the method enables the determination of scale parameters, which are also influenced by soil structure, through field infiltration experiments conducted at zero-pressure heads. Later, an improved version of the Beerkan method, denoted Beerkan Estimation of Soil Transfer parameters (BEST), was developed by Lassabatère et al. (2006). This procedure seems to be a promising method for effectively describing the soil hydrodynamic properties in drip-irrigated soils (Mubarak et al. 2009; Baiamonte et al. 2024).

The estimated hydraulic properties must be considered in the hydraulic analysis of SDI systems, as well as local losses, to perform a rigorous evaluation of irrigation uniformity. Towards this aim, Wang et al. (2021) developed an improved finite element model by incorporating the effect of back pressure, which requires the knowledge of soil hydraulic properties and local losses to analyse the performance of SDI systems. Indeed, compared to surface drip irrigation systems, for which hydraulic performance is well known (Baiamonte 2018a; 2018b), in addition to the above-mentioned back pressure, the looped configuration of SDI systems needs a different analysis due to the unpredictable direction of circulating discharges (Wang et al. 2016, 2021).

In general, to design looped hydraulic networks, a nonlinear system of motion and continuity equations must be solved. Depending on the complexity of the network, iterative or approximated procedures have been applied, such as the Hardy Cross method (Cross 1936; Abramov 1972), the Newton-Raphson method (Chandrasekhar and Stewart 1975; Wood and Rayes 1981), and the linear theory method (Issacs and Mills 1980). Following the Hardy Cross method (HCM), Martin and Peters (1963) developed several global linearization techniques, culminating in the work of Todini and Pilati (1987) and Todini (2006), which are distinguished by the simultaneous solution of all the network equations. The latter method is highly popular and was implemented in EPANET software (Rossman 2002; Todini and Rossman 2013).

HCM was developed in 1936 for manual calculations in civil engineering, for not-too-complex looped networks, it remains a dependable approach for solving verification problems and, in this work, is applied to SDI systems. This method enables the determination of flow and pressure head distributions within the pipes and nodes of the hydraulic network, given its geometric characteristics and the inlet and outlet flows. Therefore, it is possible to analyse the hydraulic performance of SDI systems, and subsequently evaluate the emitters' performance by monitoring the inlet flow rate over time. To satisfy the energy balance in each pipe of SDI systems, friction and local losses must be considered. In this paper, the Hazen-Williams resistance equation, which is commonly used for polyethylene pipes, was applied to estimate friction losses. Instead, local losses due to the emitters' insertions were considered as a fraction α of the kinetic head (Provenzano and Pumo 2004; Baiamonte 2020).

This work aims to quantify local losses due to root intrusion in SDI systems using a new methodology that integrates a modified Hardy Cross method with the average inlet discharges and pressures monitored during a six-year experimental campaign. The paper is organised as follows. Following this introduction, the methodology to assess the soil hydraulic properties, which are essential for estimating the back pressure head and the modified HCM, is discussed. The experimental field setup and the method used to determine the cavity radius are then described. Finally, the results of the soil hydraulic characterisation are reported, followed by the cavity radius estimation and the effect of root intrusion expressed in terms of local losses.

2. Theoretical background

2.1. Soil hydraulic characterisation

Soil hydraulic properties can be determined by using the Beerkan method, consisting of a single infiltration experiment performed at a null pressure head. This method, involving the repetitive application of a fixed and small volume of water on the soil surface and recording the infiltration time for each volume, provides the cumulative infiltration curve that can be used in the BEST procedure for soil hydraulic characterisation (Lassabatère et al. 2006). Specifically, the BEST-steady algorithm is applied for the estimation of soil sorptivity, S_S (mm h$^{-0.5}$), and saturated soil hydraulic conductivity, K_s (mm h^{-1}), by utilising two parameters, the intercept, b_s (mm), and slope, i_s (mm h^{-1}), of the straight line fitted to the experimental data that describe the steady-state condition on the cumulative infiltration, I (mm), versus the time, t (h), respectively (Bagarello et al. 2014):

$$S_S = \sqrt{\frac{i_S}{A+\frac{c}{b_S}}} \quad (1)$$

$$K_s = \frac{C\, i_S}{A\, b_S + c} \quad (2)$$

where A (mm^{-1}) and c are numerical constants, which according to Haverkamp et al. (1994) and Lassabatère et al. (2006), for antecedent volumetric soil water content, θ_0, below 0.25 times the volumetric water content of the saturated soil, θ_s, can be expressed as:

$$A = \frac{\gamma}{r_i\, \Delta\theta} \quad (3)$$

$$c \approx \frac{1}{2(1-\beta)} \ln\left(\frac{1}{\beta}\right) \quad (4)$$

where $\Delta\theta$ (cm^3 cm^{-3}) is the difference between θ_s (cm^3 cm^{-3}) and θ_0 (cm^3 cm^{-3}), r_i (mm) is the radius of the infiltration surface, while γ and β are coefficients typically assumed equal to 0.75 and 0.6, respectively (Haverkamp et al. 1994; Smettem et al. 1994).

The macroscopic capillary length, λ_c (mm), which indicates the relative weight of capillarity compared to gravity forces in the movement of water through unsaturated soil, is defined by the following equation introduced by White and Sully (1987):

$$\lambda_c = \frac{b\, {S_S}^2}{\Delta\theta\, \Delta K} \quad (5)$$

where b is a dimensionless capillary scale parameter usually set equal to 0.55 (White and Sully 1987) and ΔK is the difference between K_s and the initial soil hydraulic conductivity, K_0 (mm h^{-1}). Low λ_c values (e.g., $0 < \lambda_c \leq 10$ mm) signify a prevalence of gravity over capillarity and are commonly observed in coarse-textured or highly structured porous media. Vice versa, high λ_c values (i.e., > 1000 mm) indicate capillarity's dominance over gravity, a common occurrence in many fine-textured or poorly structured porous media. According to Di Prima et al. (2020), λ_c can be derived from a steady-state beerkan infiltration run using the following relationship:

$$\lambda_c = 0.861 \frac{b_s}{\Delta\theta} \tag{6}$$

The inverse of the capillarity length can be expressed as (Gardner 1958; White and Sully 1987):

$$\lambda_c^{-1} = \frac{K_s - K_0}{\Phi_m} = \alpha_{GR} \tag{7}$$

where Φ_m is the matric flux potential ($mm^2\ h^{-1}$) and α_{GR} (mm^{-1}) is the so-called sorptive number, i.e., the shape parameter of the Gardner hydraulic conductivity function:

$$K(h) = K_s\, exp(\alpha_{GR} h) \tag{8}$$

where K ($mm\ h^{-1}$) is the soil hydraulic conductivity and h (mm) is the pressure head.

In the next section, the estimate of the back pressure head that may occur around the buried point source is briefly summarised and an analysis of the same back pressure expressed in dimensionless terms is also provided.

2.2. Back pressure head

In SDI systems, the soil hydraulic properties affect the emitter flow rate. A saturated spherical region with a radius r_0 (mm) is formed around the discharge point source with soil water under a positive pressure head (Philip 1992), i.e., the back pressure head (Shani et al. 1996).

It was proved that the back pressure increases as K_s decreases (Shani et al. 1996; Lazarovitch et al. 2005) and determines a decrease in the hydraulic gradient across the emitter orifice. The well-known nominal emitter flow rate - pressure head relation needs to be modified to account for the back pressure head, h_s, (Warrick and Shani 1996; Gil et al. 2008):

$$q_N = k_e(h_N - h_s)^x \tag{9}$$

where q_N (L h^{-1}) is the nominal emitter flow rate, k_e (L h^{-1} m^{-x}) is the coefficient of the emitter flow relation, h_N (m) is the nominal emitter's pressure head and x is the exponent of the emitter flow relation.

The back pressure, h_s, (m) can be expressed according to Shani et al. (1996):

$$h_s = \frac{\alpha_{GR}\, q_N(2-\alpha_{GR}\, r_0)-8\, K_s\, \pi\, r_0}{8\, \alpha_{GR}\, K_s\, \pi\, r_0} = \frac{2-\alpha_{GR}\, r_0}{8\, \pi\, K_s\, r_0} q_N - \frac{1}{\alpha_{GR}} \tag{10}$$

The same relationship can be described by using dimensionless groups, thus offering a key advantage to reduce the number of parameters it encompasses (Ram and Singh 1985):

$$h_{*s} = \frac{2-\alpha_{GR}\, r_0}{8} q_{*n} - \frac{1}{\alpha_{GR}\, r_0} \tag{11}$$

where h_{*s} is the back pressure normalised with respect to the cavity radius, r_0, and q_{*n} (dimensionless) is the emitter flow rate normalised with respect to the discharge flowing with velocity K_s across the sectional area of the spherical cavity with a radius r_0 (mm), $\pi\, r_0^2\, K_s$.

Equation (11) makes it possible to plot the normalised back pressure, h_{*s}, versus q_{*n}, with $\alpha_{GR}\, r_0$ as a dimensionless parameter, as shown in Fig. 1. The $\alpha_{GR}\, r_0$ values were chosen by considering their possible range of variability, r_0 = [0.001−0.014 m] (Shani et al. 1996; Wang et al. 2024) and α_{GR} = [0.3−30 m^{-1}] (Ghezzehei et al. 2007). In Fig. 1, the normalised back pressure heads corresponding to the application that will be performed later ($\alpha_{GR}\, r_0$ = 0.12305) are also plotted.

Equation (11) shows the occurrence of threshold q_{*n} values, $q_{*n,min}$, below which no back pressure head exists:

$$q_{*n,min} = \frac{8}{\alpha_{GR}\, r_0\, (2-\alpha_{GR}\, r_0)} \tag{12}$$

whereas for $\alpha_{GR}\, r_0 = 2$, $q_{*n,min}$ diverges to infinity. The latter means that for a fixed r_0, when $\alpha_{GR} > 2/r_0$, no back pressure head occurs for any normalised emitter flow rate. For the $\alpha\, r_0$ values considered in Fig. 1, the corresponding q_{*min} obtained by Eq. (12) are also plotted.

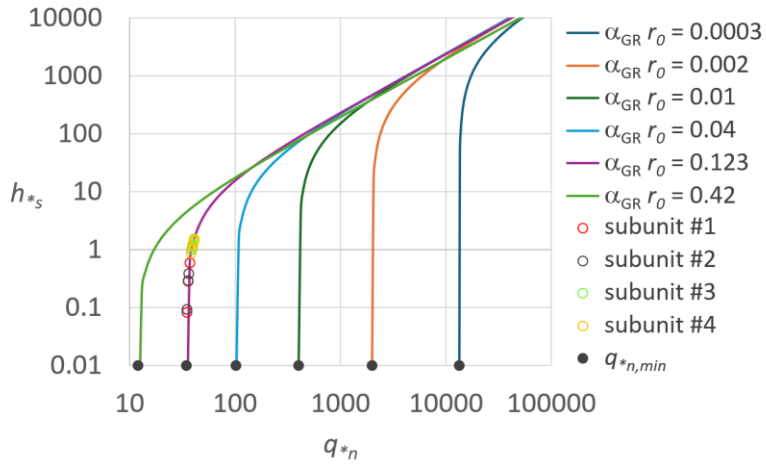

Fig. 1 *Normalised back pressure head, h_{*s}, versus normalised emitter flow rate, q_{*n}, with $\alpha_{GR}\, r_0$ as a parameter. The h_{*s} values corresponding to the four investigated subunits, and minimum normalised emitter flow rates, $q_{*n,min}$, below which $h_{*s} = 0$, are also indicated*

In the next section, HCM is briefly summarised, and back pressure and local losses are included into the method to analyse the flow rate within the network and pressure heads of the emitters.

2.3. Considering back pressure and local losses in the Hardy Cross Method

The Hardy Cross method (HCM) is a reliable method for solving looped pipe networks under hydraulic steady-state conditions (Cross 1936) and represents an early adaptation of the method of moment distribution from structural engineering. Since SDI systems are designed as looped networks, HCM can be applied for their hydraulic analysis. To satisfy energy conservation on every path within the network, HCM is based on the successive addition of flow-rate corrections in each branch. Mass conservation condition requires that the total flow rates entering a node should be equal to the total flow rates exiting the node:

$$\sum_n \pm q_i \pm q_n = 0 \tag{13}$$

where q_i (L h^{-1}) is the discharge in pipe "*i*" meeting at node "*n*", and q_N (L h^{-1}) is the nodal outflow.

Meanwhile, energy conservation equations imply that the sum of head losses along any closed path "*m*" must be equal to zero:

$$\sum_m \pm h_i = 0 \tag{14}$$

where h_i (m) is the total head loss in the generic pipe "*i*".

In a generic SDI system, consisting of "*m*" loops, "*n*" nodes, and "*i*" pipes (Fig. 2), and characterised by polyethylene pipes, it is appropriate to use the Hazen Williams resistance equation (discharge exponent, *r*, equal to 1.852, and inside diameter exponent, *s*, equal to 4.871) to describe friction losses.

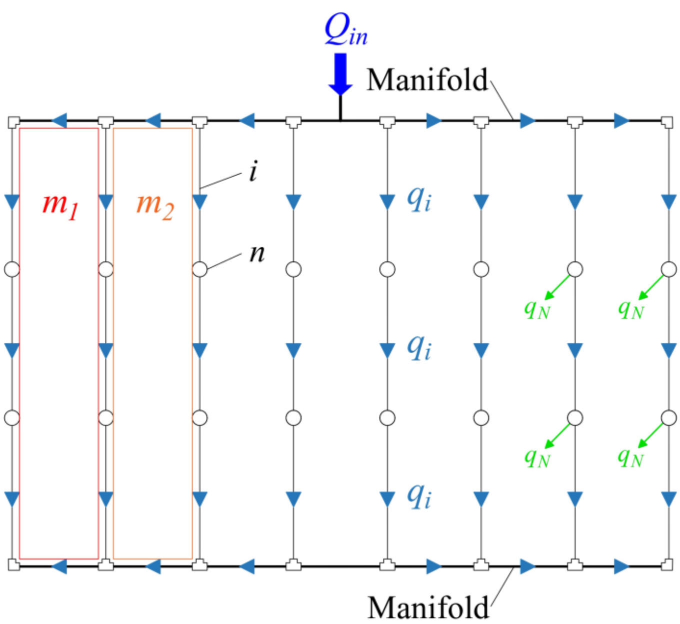

Fig. 2 *Sketch of the looped subsurface drip irrigation (SDI) network characterised by "m" loops, "n" nodes or emitters, and "i" pipes or laterals*

In consideration of the above, in applying HCM, the energy conservation equation must account for local losses and back pressure, h_s. Therefore, Eq. (14) can be rewritten:

$$\sum_m \pm h_i = \pm k \, \frac{q_i^r}{D^s} L_i \pm \alpha \, k_L \, \frac{q_i^2}{D^4} \pm h_s = 0 \tag{15}$$

where L_i (m) is the length of the pipe i, D (m) is the pipe inside diameter, α is the coefficient of local losses expressed as α-fraction of the kinetic head, k_L is equal to 8/g π^2 = 0.083, and k is equal to 10.675/C^r. The latter C is the pipe smoothness factor, which depends on the pipe material's characteristics. In this work, for polyethylene pipes, the C value was assumed 135, which is usually adopted in drip irrigation systems (Moghazi 1998).

Given the geometric characteristics of the SDI system and the inlet flow rate, Q_{in}, the initial step in the HCM application, requires assuming an arbitrary set of flow rates, q_i, within the network, provided that the continuity condition (Eq. 13) is met at each node. During the iterative process, the total loss along a closed path will be non-zero, resulting unbalanced by a certain amount, Δ'_m, until the final solution is reached:

$$\sum_m \pm h_i = \pm k \, \frac{q_i^r}{D^s} L_i \pm \alpha \, k_L \, \frac{q_i^2}{D^4} = \Delta'_m \neq 0 \tag{16}$$

To balance the hydraulic heads, following the Hazen-Williams resistance equation, it is necessary to introduce in each loop a corrective flow, p'_m, which considers local losses that also depend on the circulating discharge:

$$p'_m = \frac{\sum_m \pm k \frac{q_i^r}{D^s} L_i \pm \alpha \; k_L \frac{q_i^2}{D^4}}{\sum_m \pm k \, r \frac{q_i^{r-1}}{D^s} L_i \pm \alpha \, k_L 2 \frac{q_i}{D^4}} \tag{17}$$

For each loop, the flow rate correction, p'_m, must be added to the circulating flow rates, q_i, within the "i" pipes. Correcting pipe flow rates common to multiple loops determines a new hydraulic head imbalance into the previously balanced loops. Consequently, it is necessary to proceed iteratively until the value of Δ'_m falls below a specific threshold, ensuring the balancing of head losses across the entire network.

3. Material and methods

3.1. Experimental setup

The experiment was conducted over 6 years, from 2018 to 2023, in a 30-year-old citrus orchard (*Citrus reticulata* Blanco cv. Tardivo di Ciaculli), spaced 5 × 5 m, located near Palermo, Italy (38°4′53.4″ N, 13°25′8.2″ E). The soil remains untilled; only mechanical cutting of weeds was performed.

The field site, characterised by a flat surface and an altitude of 35 m a.s.l., was divided into four plots (Fig. 3), named Subunit #1, #2, #3 and #4, each approximately 1000 m^2, hosting 36−40 trees per subunit.

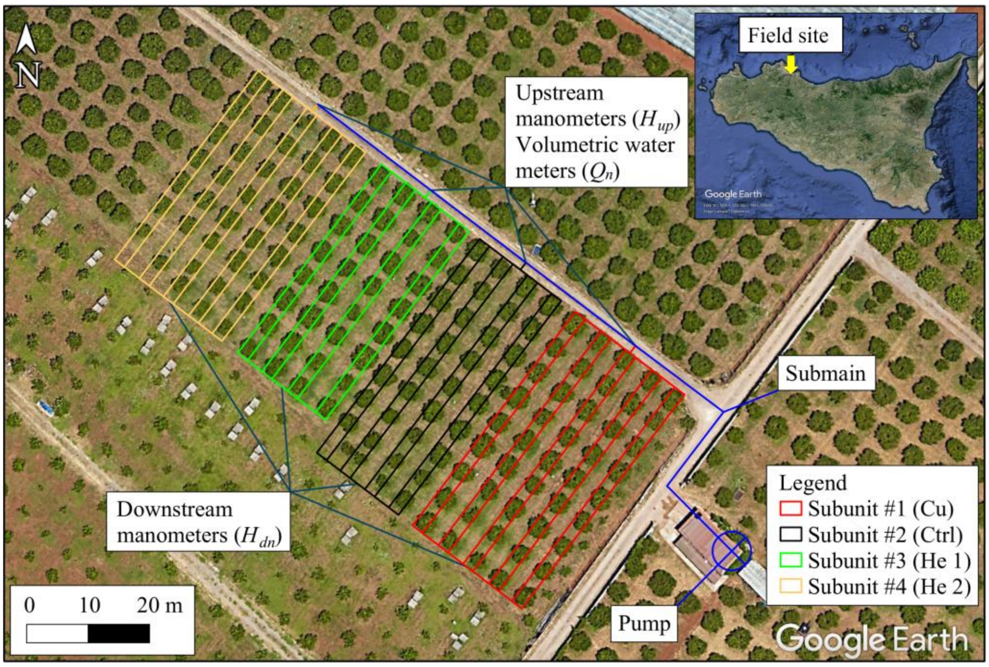

Fig. 3 *Experimental layout of the four investigated subunits differently treated (Cu, Ctrl, He 1, He 2)*

According to the United States Department of Agriculture (USDA) classification system, the soil can be classified as sandy-clay-loam or sandy loam to a depth of 0.4 m, with a moderate gravel content on the surface. The textural and structural properties of the soil exhibit an uncommonly low spatial variability. Soil texture was analysed at 21 randomly selected sampling points distributed across the experimental plot, as illustrated in Fig. 4. In particular, Fig. 4a and Fig. 4b show the spatial variability of content in clay and sand obtained by applying the weighted inverse distance interpolation to experimental data, corresponding to low values of the coefficients of variation, CV, which are also reported, together with the means.

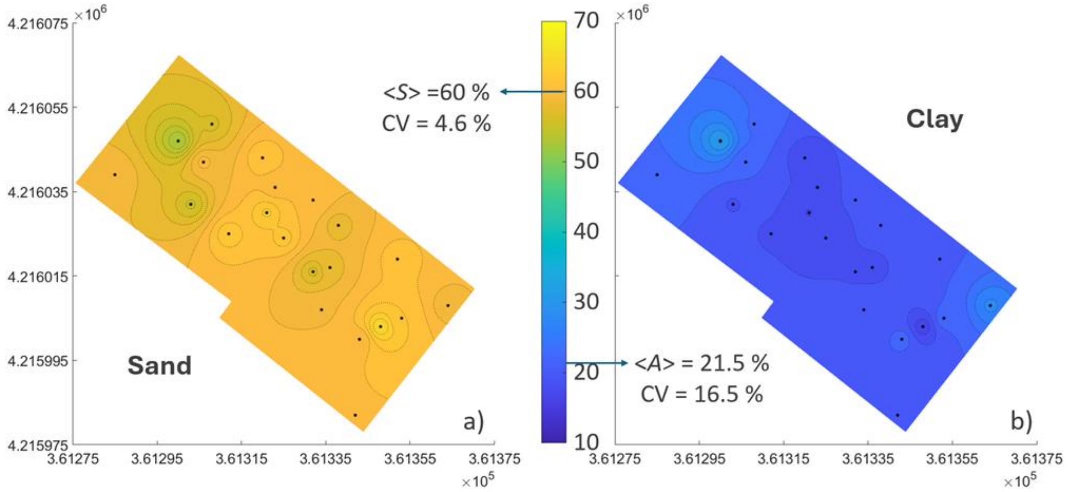

Fig. 4 *Spatial distribution of the content* ***a)*** *in sand and* ***b)*** *in clay, obtained by applying the weighted inverse distance interpolation to 24 randomly sampling points across the experimental field*

The high sand content (Fig. 4b) suggests that the soil homogeneity described for the texture could also be attributed to the soil structure, which is generally much less variable for sandy soils compared to loamy or clayey soils.

To study the influence of the root guard treatment, cylindrical integrated in-line labyrinth emitters with embedded root-growth inhibitors, namely Copper (Cu), Herbicide 1 (He 1), and Herbicide 2 (He 2), were installed in Subunits #1, #3 and #4 (Fig. 3, Table 1). In contrast, Subunit #2 was considered a reference (Ctrl) since no root growth inhibitor was embedded.

All four plots were irrigated utilising an SDI system installed in 2017 and operational in 2018. As shown in Fig. 3, in each plot, the SDI system is characterised by two drip laterals with nominal diameter D_N = 20 mm and inside diameter D = 17.5 mm per plant row, positioned at a depth of 0.3 m, and spaced 1 m from the tree trunk. Each lateral was equipped with self-compensating Multibar^{TM} C emitters spaced S = 0.5 m, with a nominal emitter flow rate q_N = 2.1 L h^{-1} and a pressure compensating range from 50 kPa to 300 kPa.

For each subunit, Table 1 reports the geometric and hydraulic characteristics of the SDI system, as well as the number of emitters, N. The laterals were connected to a manifold with a nominal diameter D_N = 32 mm and inside diameter D = 28.2 mm, whereas the nominal diameter of the submain was $D_N = 50$ mm and the inside diameter $D = 44$ mm.

In the upstream mid-manifold of each plot, an electric control valve, a 100 µm disc filter, a manometer (0-250 kPa scale, 10 kPa resolution) and a volumetric water meter (resolution 0.1 L) were installed to monitor upstream pressure heads and irrigation volumes, whereas in the downstream mid-manifold, only a manometer was installed.

***Table 1** Characteristics of experimental subunits*

Subunit	Treatment	Lateral length L_L (m)	S (m)	Manifold length L_M (m)	S_{rows} (m)	N	N_{rows}
#1	Cu	43.0	0.5	25	2 m and 3 m alternating (Fig. 2)	860	10
#2	Ctrl	42.5		20		680	8
#3	He 1	38.0		20		608	8
#4	He 2	37.0		25		740	10

The 10 kPa manometer's resolution was inadequate to directly evaluate the difference between the observed upstream and downstream pressure heads, ΔH_{obs}, due to root intrusion, except during the starting year (2018) when the SDI subunits were new. Therefore, from 2019 to 2023, the effect of root intrusion was evaluated by quantifying local losses as a consequence of the observed inlet flow rate variations in HCM. Contrary to ΔH_{obs}, the observed inlet pressure head, H_{up}, was deemed reliable throughout the measurement campaign. Indeed, as described later, the observed H_{up} variations made it possible to investigate the effect of each root guard treatment.

To assess the soil properties that need to estimate the back pressure, h_s, a total of 15 infiltration beerkan runs were conducted at locations randomly chosen in the field site. Small rings, with an inside diameter of 0.08 m, were inserted in the soil surface to a depth of 0.01 m for performing infiltration runs (Lassabatère et al. 2006).

The rings were inserted either manually or with the gentle use of a rubber hammer, ensuring the horizontal alignment of the upper rim during insertion. The choice of relatively small rings was influenced by the slightly stony soil surface layer, which simplified the finding of appropriate surfaces for soil sampling.

For each infiltration run, 20 water volumes, each consisting of 57 mL, were poured successively in nearly 3 seconds for each volume on the confined infiltration surface, thus the initial ponded depth of water was equal to 11.3 mm. The infiltration time for each water volume (1st, 2nd, ..., 20th) was measured from the start of water application until the disappearance of all water, immediately before the subsequent water volume was poured on the infiltration surface (Lassabatère et al. 2006). Moreover, to minimise soil disturbance due to water application, the energy from the applied water was dissipated on the fingers.

This process resulted in obtaining a cumulative infiltration, I (mm), vs. time, t (h), curve, comprising 20 data points at each sampling point. Additionally, two undisturbed soil cores (0.05 m in height and 0.05 m in diameter) were collected from three different points within the area at depths of 0−0.05 m and 0.05−0.10 m. Six cores ($N = 6$) were used to determine the dry soil bulk density, ρ_b (g cm^{-3}), and the antecedent gravimetric soil water content, w_0, hence the antecedent volumetric soil water content θ_0. The averages of ρ_b and θ_0 were then associated with beerkan runs and assumed to represent the field site condition.

The cavity radius estimation was performed by using the soil hydraulic characteristics obtained by the experimental runs, the average emitter flow rate, q_n (L h^{-1}), obtained by the inlet discharge (Q_{in} (m^3 h^{-1}), $q_n = Q_{in}/N$ emitters, see Table 1) and the pressure head measurements, H_{up} (m), collected in the reference year (2018). The latter was used to exclude the influence of root intrusion, which should have minimal effect on the emitters' behaviour in the first year.

In particular, the cavity radius, r_0, was estimated by imposing in HCM, (i) h_s by Eq. (10) with $K_s = 91.3$ mm h^{-1} and $\alpha_{GR} = 8.6$ m^{-1}, (ii) the average emitter flow rate, q_n, (iii) the difference between the observed upstream and downstream pressure heads in the starting year (2018), ΔH_{obs}, and (iv) the local losses coefficient α = 0.5, and checking iteratively at the downstream the achievement of the observed pressure head, H_{dn}. Therefore, r_0 was the only one unknown.

Under no effect of root intrusion, the α parameter only accounts for the variation of velocity due to emitter insertion and was set equal to 0.5, since this is a common value for cylindrical emitters (Provenzano and Pumo, 2004).

After estimating the r_0 values for each irrigation event, in the reference year (2018), the Lilliefors test was applied to assess whether the dataset followed a normal distribution. Specifically, the Lilliefors test is a modification of the Kolmogorov-

Smirnov test, which computes the maximum difference between the empirical cumulative distribution function and that of the normal distribution (kstat of the Kolmogorov-Smirnov test statistic), accounting for the sample's mean and variance (Lilliefors, 1967).

4. Results and discussion

4.1. Soil characteristics

The average dry soil bulk density, ρ_b, and the average antecedent gravimetric soil water content, w_0, of the six samples (N = 6) were equal to 1.269 g cm^{-3} (coefficient of variation, CV = 4.0%,) and 0.094 g g^{-1} (CV = 11%), respectively, hence the mean antecedent volumetric soil water content, $\theta_0 = \rho_b\, w_0$, was calculated 0.119 m^3 m^{-3}. The saturated volumetric soil water content, θ_s (m^3 m^{-3}), which is also required in the BEST-steady procedure, was set equal to the soil porosity, ϕ (cm^3 cm^{-3}), which was easily determined from the ρ_b measurements, assuming a soil particle density of 2.65 g cm^{-3}, resulting in 0.521 cm^3 cm^{-3} (Bagarello et al. 2011; Mubarak et al. 2010). The θ_0/θ_s ratio resulted in 0.228 cm^3 cm^{-3}, thus lower than the recommended threshold value to apply the BEST-steady procedure (0.25 cm^3 cm^{-3}, Lassabatère et al. 2006).

The soil sorptivity, S_S (mm h$^{-0.5}$), and the saturated soil hydraulic conductivity, K_s (mm h^{-1}), were estimated for the 15 sample points. By using Eq. (6) and Eq. (7), the capillarity length, λ_c, and the α_{GR} parameter were estimated.

Figure 5 shows the cumulative frequency empirical distribution of S_S (Fig. 5a), $ln\ K_s$ (Fig. 5b), and α_{GR} (Fig. 5c), respectively, together with the fitting of the normal distribution (N2).

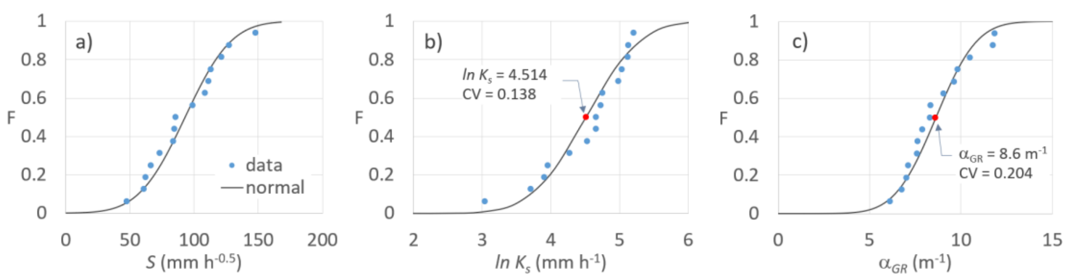

***Fig. 5** Cumulated frequency distribution of **a)** soil sorptivity, S_S, **b)** saturated hydraulic conductivity, log K_s, and **c)** Gardner shape parameter, α_{GR}. Solid lines refer to the fitted Normal Distribution (N2), and red dots indicate the mean value*

Although the soil texture was nearly uniform, as previously discussed, soil hydraulic parameters showed moderate variability, as can be observed by the CV values reported in Fig. 5, which should be considered (Baiamonte et al. 2024). However, for the purpose of this study, which only aimed to suggest a methodology to quantify local losses due to root intrusion in SDI systems, and also considering the N2 good fitting, to estimate the back pressure, h_s, the mean values, K_s = 91.3 mm h^{-1} and α_{GR} = 8.6 m^{-1}, were assumed to be as representative of the field site.

4.2. Cavity radius estimation

When applying Eq. (10) to estimate the back pressure, a major concern is that there is no rigorous methodology to determine the exact value of the cavity radius, r_0, and many researchers performed their analyses by fixing multiple r_0 (Shani et al. 1996; Gil et al. 2008). The cavity is usually considered a sphere with a constant radius, regardless of soil characteristics or source properties.

Although previous research highlighted the possible effect of infiltration cavity on soil pressure and emitter discharges (Gil et al. 2011; Lazarovitch et al. 2005), the evolution mechanism and characteristics of the cavity around a buried point source remain unclear (Wang et al. 2024).

For the reference year (2018), when the subunits and manometers were newly installed, ΔH_{obs} (N = 73) were used to estimate r_0, with the variability of ΔH_{obs} limited in the range [10, 30 kPa]. In the following years, from 2019 to 2023, the effect of root intrusion was investigated by analysing inlet discharge variations.

Figure 6 shows the estimated r_0 values for each water application performed in 2018 (N = 73) to the four subunits. Interestingly, in Fig. 6, it can be observed that the variability of cavity radius is minimal (CV = 0.055), resulting in the range [0.0125–0.0162 m]. The normal distribution (N2) was fitted to the experimental values, indicating that the mean value of cavity radius (r_0 = 0.0143 m) can be considered representative of the regarded soil and can be used to estimate the back pressure h_s.

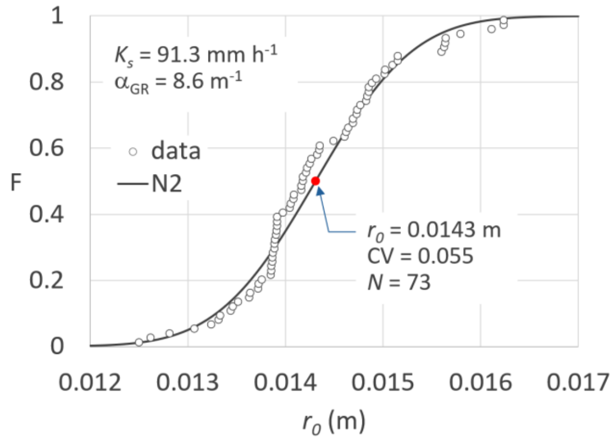

Fig. 6 *Cumulated frequency distribution of cavity radius, r_0, obtained by applying HCM for the # 73 water applications performed in the starting year (2018). The solid line refers to the fitted Normal Distribution (N2) and the red dot to the mean r_0 value*

The Lilliefors test statistic (kstat) was equal to 0.0978, lower than the critical value of 0.1037 at a significance level of 0.05. Consequently, there is enough evidence to accept the null hypothesis of normality (Lilliefors, 1967), thereby the representativeness of the mean. The *p*-value associated with the fitted normal distribution was equal to 0.0817.

4.3. Quantifying local losses due to root intrusion

In Fig. 7a and 7b, the average inlet discharge, Q_n, and pressure head, H_{up}, which were measured during the 6 years of SDI operating (2018−2023) are illustrated, respectively. The figures also depict the whiskers corresponding to the standard deviation observed for each experimental campaign.

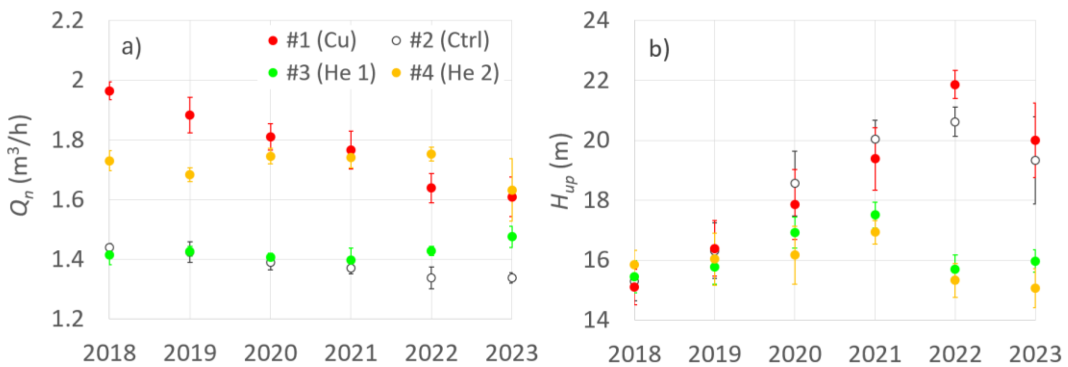

Fig. *7 Observed average **a)** inlet discharge, Q_n, and **b)** inlet pressure head, H_{up}, monitored in the 6-year experimental campaign (2018−2023), for the four investigated subunits differently treated (Cu, Ctrl, He 1, He 2). Whiskers refer to the standard deviation of the collected data*

The figure shows a clear Q_n decreasing and H_{up} increasing trend for subunits #1 and #2, meaning that Ctrl and Cu treatments were highly affected by root intrusion. Whereas for subunits #3 and #4, the He 1 and He 2 treatments were able to contrast the root intrusion phenomena, not altering the hydraulic performance of the SDI system, as can be observed for both inlet discharge (Fig. 7a) and inlet pressure head (Fig. 7b). Fig. 7b clearly shows that, contrarily to ΔH_{obs}, H_{up} was sensitive to pressure head variations during the years 2018−2023, as previously discussed.

The results displayed in Fig. 7 were used to quantify the effect of root intrusion in terms of local losses. Indeed, the very small roots if introduced into the emitters' labyrinth, alter their cross-sectional area, determining additional local losses that need to be considered in the energy balance equation (Eq. 15), as earlier discussed for the HCM.

Since in the SDI system self-compensating emitters have been considered, the average emitter flow rate, q_n, is also affected by the Q_n decrease illustrated in Fig. 7a. In conclusion, it is assumed that the reduction in emitter flow rate is a consequence of the root intrusion phenomenon.

To express the effect of root intrusion in terms of local losses, the increase in pump pressure head corresponding to the reduction in inlet discharge was obtained by the pump characteristic curve, which is displayed in Fig. 8a, for pump Speroni RSM 4 (Speroni SpA 2023) that was installed in the SDI system. Therefore, the increase in pump pressure head, for each subunit, ΔH_s, and operating year (2019−2023), was compared to that of the reference year (2018). Note that the pressure heads provided by the pump (Fig. 8a) are higher than those at the inlet of each subunit due to submain friction losses. Moreover, local loss caused by the disc filter (made by IRRITEC, type YDV, 1"), which was regularly cleaned, was calculated based on the inlet discharge.

Since the pump simultaneously feds two contiguous subunits connected in parallel (subunits #1 and #2, and subunits #3 and #4, see Fig. 3), the increase in pump pressure head for each subunit (e.g. $\Delta H_{s,1}$, $\Delta H_{s,2}$), was obtained by linearly weighting the pump pressure head with respect to the average inlet discharge in each subunit, ($Q_{n,1}$ and $Q_{n,2}$) as displayed in Fig. 8b, for the subunits #1 and #2. Fig. 8a also plots the increase in pump pressure head, for each subunit pair and each operating year.

Once the ΔH_s values were obtained by the characteristic curve of the pump (by accounting for the decrease in inlet discharge, Q_n, and the increase in pump pressure head, ΔH), the local losses coefficient, α, was estimated to evaluate the level of emitters' clogging with respect to the reference year 2018.

First, for the reference year 2018, the pressure head at the upstream, $H_{up,2018}$, and downstream, $H_{dn,2018}$, were determined, by imposing in HCM, i) h_s by Eq. (10) with K_s = 91.3 mm h^{-1}, α_{GR} = 8.6 m^{-1}, and r_0 = 0.0143 m, ii) the average emitter flow rate, q_n, iii) the difference between the observed upstream and downstream pressure heads, ΔH_{obs}, and iv) the local losses coefficient α = 0.5.

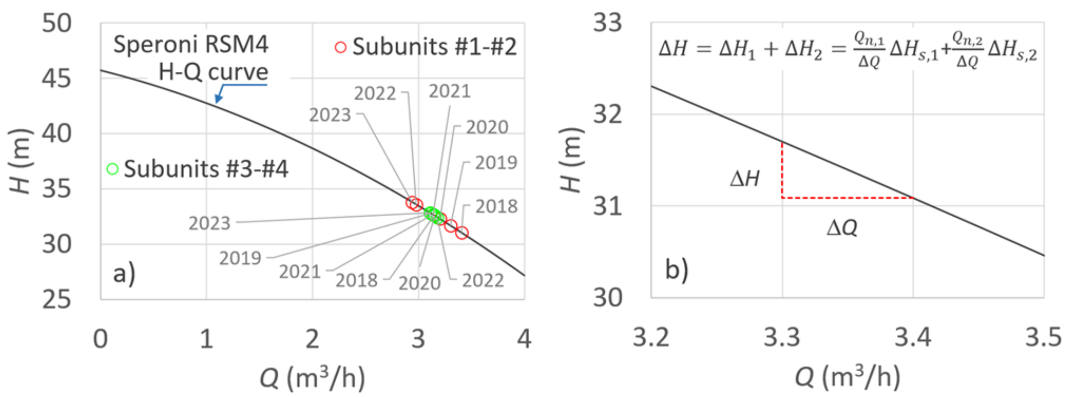

Fig. 8 *For Speroni pump RSM4,* ***a)*** *characteristic H-Q curve together with the H-Q experimental pairs obtained for each subunit and observation year, and* ***b)*** *same H-Q curve qualitatively showing the increase in pump pressure head corresponding to the inlet discharge decrease. For example, the difference in pump pressure head, ΔH, weighted with respect to the inlet discharge of subunit #1 ($Q_{n,1}$) and #2 (Q_{n2}) connected in parallel, is illustrated*

Since the ΔH_{obs} measurements were not accurate due to the manometer resolution (10 kPa), for the subsequent years 2019−2023, α values were estimated by HCM, imposing the average emitter flow rate, q_n, of the current year, and checking iteratively at the upstream, the achievement of the calculated pressure head, H_{up} = $H_{dn,2018}$ + ΔH_s, and maintaining the same measured pressure head at the downstream, $H_{dn,2018}$. This is because, for the subunits, where a decrease in emitter flow rate occurred, an increase in pump pressure head was measured, as can also be observed in Fig. 8a. Of course, it is expected that the α-parameter assumes high values for severe clogging levels and vice versa.

In Fig. 9a and 9b, the α values estimated by considering and neglecting the influence of the back pressure, h_s, for each subunit are plotted. It is interesting to observe that for subunits #3 and #4 treated with He 1 and He 2 treatments, respectively, low α values occurred, meaning that root intrusion provided a low level of emitter clogging.

Accordingly, time-invariant inlet discharges were observed during the 6-year period, 2018−2023 (Fig. 7a). For subunits #1 and #2 the α-parameter increased during the years, reaching values of 50 and 32, respectively, by 2023, thus indicating the ineffectiveness of treatments Cu and Ctrl in the root intrusion protection.

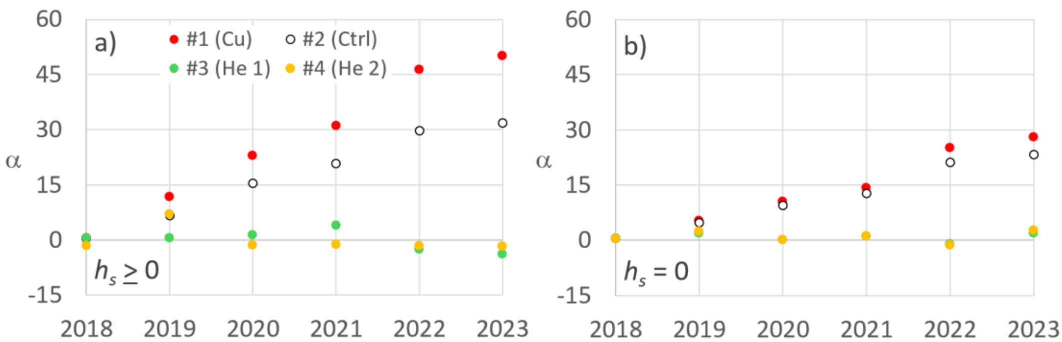

Fig. 9 *The α-fraction of the kinetic head obtained by applying the implemented HCM over time, for the four investigated subunits differently treated (Cu, Ctrl, He 1, He 2),* ***a)*** *considering the back pressure ($h_s \geq 0$), and* ***b)*** *neglecting the back pressure ($h_s = 0$)*

The α-parameter estimation performed by imposing $h_s = 0$ (Fig. 9b) makes evident that the effect of back pressure needs to be considered in SDI systems, especially for the purpose of this work, since neglecting h_s (Fig. 9b) would underestimate the effect of root intrusion, as displayed in Fig. 9a.

It is important to note that, although the indirect results (Fig. 9) lack experimental evidence of emitter root intrusion, they appear reasonable. This is because other occlusion effects, such as clogging due to water quality (physical, chemical and biological causes), should have similarly affected the emitters in the He 1 and He 2 treatments. However, these treatments did not exhibit such behaviour, allowing us to exclude other potential causes of emitter clogging and attribute the observed clogging in the Cu and Ctrl treatments solely to root intrusion. Additionally, the Multibar C emitters are equipped with an anti-siphon mechanism that prevents soil ingestion.

Table 2 reports the estimated values of the α parameter of each subunit depicted in Fig. 9a,b. The calculated difference in pressure heads between upstream and downstream subunit, ΔH_s, and the average discharge of emitters, q_n, calculated by dividing the average inlet discharge, Q_n, by the number of emitters N, are also reported. Interestingly, for subunits #1 and #2, the decrease in average emitter flow rates determined an increase in ΔH_s values, confirming the upward trend of α parameters due to root intrusion.

***Table 2** Input parameters (ΔH_s and q_n) and output parameters (α and h_s) of the HCM application, for the four investigated subunits in the period (2018−2023). The normalised h_s, h_{*s}, and the α parameter obtained by neglecting h_s, α (h_s = 0), are also reported*

Subunit	year	ΔH_s	q_n (l/h)	α	h_s (m)	h_{*s}	α (h_s = 0)
#1	**2018**	**1.396**	**2.28**	**0.5**	**0.0143**	**0.999**	**0.5**
	2019	1.757	2.18	11.83	0.0086	0.598	5.35
	2020	2.098	2.11	23.05	0.0041	0.285	10.62
	2021	2.310	2.05	31.07	0.0012	0.083	14.32
	2022	2.802	1.91	46.39	0	0	25.19
	2023	2.906	1.87	50.10	0	0	28.07
#2	**2018**	**0.585**	**2.13**	**0.5**	**0.0056**	**0.388**	**0.5**
	2019	0.858	2.11	6.75	0.0041	0.289	4.85
	2020	1.124	2.06	15.44	0.0013	0.094	9.52
	2021	1.294	2.03	20.77	0	0	12.73
	2022	1.731	1.98	29.66	0	0	21.23
	2023	1.835	1.97	31.77	0	0	23.28
#3	**2018**	**1.365**	**2.32**	**0.5**	**0.0164**	**1.148**	**0.5**
	2019	1.452	2.34	0.62	0.0175	1.220	1.96
	2020	1.349	2.31	1.45	0.0155	1.086	0.23
	2021	1.393	2.28	3.94	0.0143	1.002	1.05
	2022	1.281	2.34	−2.49	0.0176	1.229	−0.95
	2023	1.462	2.41	−3.86	0.0217	1.514	1.94
#4	**2018**	**1.554**	**2.38**	**0.5**	**0.0196**	**1.368**	**0.5**
	2019	1.657	2.32	7.12	0.0162	1.132	2.49
	2020	1.534	2.40	−1.37	0.0208	1.455	0.12
	2021	1.589	2.39	−1.23	0.0205	1.432	1.08
	2022	1.451	2.40	−1.61	0.0211	1.473	−1.33
	2023	1.662	2.25	−1.63	0.0125	0.871	2.81

Whilst for subunits #3 and #4, namely He 1 and He 2 treatments, no significant variations in average emitter flow rates occurred, with ΔH_s and α values fluctuating.

Finally, in Table 2, a decreasing trend of h_s values can be observed for subunits #1 and #2, whereas almost constant values can be observed for subunits #3 and #4. Of course, because K_s, α_{GR}, and r_0 were imposed, at decreasing q_n, h_s decreases during the years, until reaching zero in some cases (subunits #1, 2022−2023, and #2, 2021−2023). The latter indicates that emitter flow rates became so low ($q_{*n} < q_{*min}$, Eq. 12) that no back pressure head effect occurred. The negative α values, reported in Table 2 for h_s

> 0, have no meaning from a physical point of view, but explain the uncertainties in soil hydraulic characterisation, as well as in cavity radius, influencing h_s. Indeed, as previously mentioned, the evolution mechanism of cavity radius against time has not been explored yet (Wang et al. 2024), and its estimation by monitoring inlet discharge and pressure head seems to be an affordable and suitable method to investigate this important issue.

5. Conclusions

Based on the monitored average inlet discharge and pressure head in an SDI system, the yearly performance that spanned 6 years (2018−2023) was analysed using a modified Hardy Cross Method (HCM), which accounted for local losses and back pressure. The analysis was conducted for four subunits, each equipped with emitters of different characteristics. subunits #1, #3 and #4 were equipped with emitters containing root-growth inhibitors: Copper (Cu), Herbicide 1 (He 1), and Herbicide 2 (He 2). Whereas subunit #2 served as the control (Ctrl), with no root guard treatment. The monitored inlet discharges and pressure heads showed that treatments with He 1 and He 2 maintained consistent performance, with no emitter flow rate variation over time. In contrast, the Cu-treated and Ctrl subunits experienced a decline in inlet discharge, coupled with an increase in inlet pressure head. Application of the revised HCM made it possible to detect the increase in the fraction of the kinetic head, which accounts for local losses, also due to root intrusion. Results showed that the fraction of the kinetic head increased for Subunits #1 (Cu) and #2 (Ctrl), reaching 50 and 32, respectively, by 2023. This rise reflects the ineffectiveness of the Cu treatment and the control in preventing root intrusion. Conversely, Subunits treated with He 1 and He 2 showed no changes in the fraction of the kinetic head, aligning with the stable inlet discharge and pressure head values observed over the 2018−2023 period, thereby demonstrating the effectiveness of root-growth inhibitors.

6. References

Abramov NN (1972) Theory and calculation technique for water supply systems. Stroizdat, Moscow

Angulo-Jaramillo R, Vandervaere JP, Roulier S, Thony JL, Gaudet JP, Vauclin M (2000) Field measurement of soil surface hydraulic properties by disc and ring infiltrometers: A review and recent developments. Soil Tillage Res. 55(1-2): 1-29. https://doi.org/10.1016/S0167-1987(00)00098-2

Bagarello V, Castellin M, Di Prima S, Iovino M (2014) Soil hydraulic properties determined by infiltration experiments and different heights of water pouring. Geoderma 213:492–501. https://doi.org/10.1016/j.geoderma.2013.08.032

Bagarello V, Di Prima S, Iovino M, Provenzano G, Sgroi A (2011) Testing different approaches to characterize Burundian soils by the BEST procedure. Geoderma 162:141–150. https://doi.org/10.1016/j.geoderma.2011.01.014

Baiamonte G (2018a) Advances in the optimal design of irrigation laterals laid on uniform slopes. Agric Water Manage 199:157–174. https://doi.org/10.1016/j.agwat. 2017.12.015

Baiamonte G (2018b) Explicit relationships for optimal designing rectangular microirrigation units on uniform slopes: The IRRILAB software application. Comput Electron Agric 153:151-168. https://doi.org/10.1016/j.compag.2018.08.005

Baiamonte G (2020) Linking kinetic energy fraction and equivalent length method to determine local losses in trickle irrigation. J Irrig Drain Eng 146(8):04020024. https://doi.org/10.1061/(ASCE)IR.1943-4774.0001492

Baiamonte G, Alagna V, Autovino D, Iovino M, Palermo S, Vaccaro G, Bagarello V (2024) Influence of soil hydraulic parameters on bulb size for surface and buried emitters. Agric Water Manag 295:108756. https://doi.org/10.1016/j.agwat.2024.108756

Cahn M, Hutmacher R (2024) Subsurface drip irrigation. In: Microirrigation for Crop Production. Elsevier Science, pp 257-301

Camp CR (1998) Subsurface drip irrigation: a review. Trans. ASAE 41:1353–1367. https://doi.org/10.13031/2013.17309

Chandrasekhar M, Stewart K (1975) Sparsity oriented analysis of large pipe networks. J Hydraul Div 101:341-355

Cross H (1936) Analysis of flow in networks of conduits or conductors. University of Illinois. Engineering Experiment Station. Bulletin; no. 286

Di Prima S, Stewart RD, Castellini M, Bagarello V, Abou Najm MR, Pirastru M, Giadrossich F, Iovino M, Angulo-Jaramillo R, Lassabatère L (2020) Estimating the macroscopic capillary length from Beerkan infiltration experiments and its impact on saturated soil hydraulic conductivity predictions. J Hydrol 589:125159. https://doi.org/10.1016/j.jhydrol.2020.125159

Gardner WR (1958) Some steady state solutions of the unsaturated moisture flow equation with application to evaporation from a water table. Soil Sci 85:228–232

Ghezzehei TA, Kneafsey TJ, Su GW (2007) Correspondence of the Gardner and van Genuchten–Mualem relative permeability function parameters. Water Resour Res 43(10):W10417. https://doi.org/10.1029/2006WR005339

Gil M, Rodríguez-Sinobas L, Juana L, Sánchez R, Losada A (2008) Emitter discharge variability of subsurface drip irrigation in uniform soils: effect on water-application uniformity. Irrig Sci 26: 451–458. https://doi.org/10.1007/s00271-008-0116-1

Gil M, Rodríguez-Sinobas L, Sánchez R, Juana L (2011) Procedures for Determining Maximum Emitter Discharge in Subsurface Drip Irrigation. J Irrig Drain Eng 137:287–294. https://doi.org/10.1061/(ASCE)IR.1943-4774.0000299

Haverkamp R, Arrúe JL, Vandervaere JP, Braud I, Boulet G, Laurent JP, Taha A, Ross PJ, Angulo-Jaramillo R (1996) Hydrological and thermal behaviour of the vadose zone in the area of Barrax and Tomelloso (Spain). Experimental study, analysis and modeling. Project UE n. EV5C-CT 92 00 90

Haverkamp R, Ross PJ, Smettem KRJ, Parlange JY (1994) Three-dimensional analysis of infiltration from the disc infiltrometer: 2. Physically based infiltration equation. Water Resour Res 30:2931–2935. https://doi.org/10.1029/94WR01788

Issacs LT, Mills KG (1980) Linear theory methods for pipe network analysis. J Hydraul Div 106:1191-1201

Lamm FR (2002) Advantages and disadvantages of subsurface drip irrigation. In Proc. Intl. Meeting on Advances in Drip/Micro Irrigation. Tenerife, Canary Islands: Instituto Canario de Investigaciones Agrarias

Lamm FR, Colaizzi PD, Sorensen RB, Bordovsky JP, Dougherty M, Balkcom K, Zaccaria D, Bali KM, Rudnick DR, Peters RT (2021) A 2020 Vision of Subsurface Drip Irrigation in the U.S. Trans ASABE 64:1319–1343. https://doi.org/10.13031/trans.14555

Lassabatère L, Angulo-Jaramillo R, Soria Ugalde JM, Cuenca R, Braud I, Haverkamp R (2006) Beerkan Estimation of Soil Transfer Parameters through Infiltration Experiments—BEST. Soil Sci Soc Am J 70:521–532. https://doi.org/10.2136/sssaj2005.0026

Lazarovitch N, Šimůnek J, Shani U (2005) System-Dependent Boundary Condition for Water Flow from Subsurface Source. Soil Sci Soc Am J 69:46. https://doi.org/10.2136/sssaj2005.0046

Lilliefors HW (1967) On the Kolmogorov-Smirnov test for normality with mean and variance unknown. J Am Stat Assoc 62 (318):399–402. https://doi.org/10.1080/01621459.1967.10482916

Mallants D, Jacques D, Tseng PH, van Genuchten MT, Feyen J (1997) Comparison of three hydraulic property measurement methods. J Hydrol 199(3-4):295-318

Martin D, Peters G (1963) The application of Newton's method to network analysis by digital computer. J Inst Water Eng 17:115-129

Moghazi HE-DM (1998) Estimating Hazen-Williams Coefficient for Polyethylene Pipes. J Transp Eng 124:197–199. https://doi.org/10.1061/(ASCE)0733-947X(1998)124:2(197)

Mubarak I, Angulo-Jaramillo R, Mailhol JC, Ruelle P, Khaledian M, Vauclin M (2010) Spatial analysis of soil surface hydraulic properties: Is infiltration method dependent? Agric Water Manag 97:1517–1526. https://doi.org/10.1016/j.agwat.2010.05.005

Mubarak I, Mailhol JC, Angulo-Jaramillo R, Ruelle P, Boivin P, Khaledian M (2009) Temporal variability in soil hydraulic properties under drip irrigation. Geoderma 150:158–165. https://doi.org/10.1016/j.geoderma.2009.01.022

Muhammad T, Zhou B, Puig-Bargu´es J, Ding C, Li S, Manan I, Zhou Y, Liu Z, Li Y (2022) Assessment of emitter clogging with multiple fouling and root intrusion in sub-surface drip irrigation during 5-year sugarcane growth. Agric Water Manag 274:107981. https://doi.org/10.1016/j.agwat.2022.107981

Nogueira VHB, Diotto AV, Thebaldi MS, Colombo A, Silva YF, Lima EMDC, Resende GFL (2021) Variation in the flow rate of drip emitters in a subsurface irrigation system for different soil types. Agric Water Manag 243:106485. https://doi.org/10.1016/j.agwat.2020.106485

Petroselli A, Romerio D, Santelli P, Mariotti R, Di Giacinti S, Ceccarelli I, Apollonio C (2022) Performance assessment of the TORO Company Neptune PC AS dripline. J Agric Eng 53(4). https://doi.org/10.4081/jae.2022.1463

Philip JR (1992) What happens near a quasi-linear point source? Water Resour Res 28:47–52. https://doi.org/10.1029/91WR02600

Provenzano G, Pumo D (2004) Experimental analysis of local pressure losses for microirrigation laterals. J Irrig Drain Eng 130(4):318-324

Raimbault G (1986) Diffusivite et conductivite hydrauliques de materiaux ou sols non satures en eau-mesure en laboratoire. Bull Liaison Lab Ponts Chauss, (145)

Ram RS, Singh VP (1985) Application of Kinematic Wave Equations to Border Irrigation Design. J Agric Eng Res 32: 57-71

Rossman LA (2002) EPANET 2 Users Manual. Water Supply and Water Resources Division, National Risk Management Research Laboratory, Cincinnati, OH45268

Shani U, Xue S, Gordin-Katz R, Warrick AW (1996) Soil-Limiting Flow from Subsurface Emitters. I: Pressure Measurements. J Irrig Drain Eng 122:291–295. https://doi.org/10.1061/(ASCE)0733-9437(1996)122:5(291)

Shi K, Lu T, Zheng W, Zhang X, Zhangzhong LA (2022) Review of the Category, Mechanism, and Controlling Methods of Chemical Clogging in Drip Irrigation System. Agriculture 12(2): 202. https://doi.org/10.3390/agriculture12020202

Šimůnek J, Angulo-Jaramillo R, Schaap MG, Vandervaere JP, van Genuchten MT (1998) Using an inverse method to estimate the hydraulic properties of crusted soils from tension-disc infiltrometer data. Geoderma 86(1-2):61-81

Smettem KRJ, Parlange JY, Ross PJ, Haverkamp R (1994) Three-dimensional analysis of infiltration from the disc infiltrometer: 1. A capillary-based theory. Water Resour Res 30(11):2925-2929

Souza WDJ, Sinobas LR, Sánchez R, Botrel TA, Coelho RD (2014) Prototype emitter for use in subsurface drip irrigation: Manufacturing, hydraulic evaluation and experimental analyses. Biosyst Eng 128:41–51. https://doi.org/10.1016/j.biosystemseng.2014.09.011

Speroni water pumps (2023) Catalogo generale. https://www.speroni.it/index.php/cataloghi/

Suarez-Rey EM, Choi CY, McCloskey WB, Kopec DM (2006) Effects of chemicals on root intrusion into subsurface drip emitters. Irrig Drain 55(5):501-509. https://doi.org/10.1002/ird.275

Todini E (2006) On the convergence properties of the different pipe network algorithms. 8th Annual Water Distribution Systems Analysis Symposium, Cincinnati, Ohio, USA, August 27-30

Todini E, Pilati S (1987) A gradient method for the analysis of pipe networks, in: Proceedings of the International Conference on Computer Applications for Water Supply and Distribution, Leicester Polytechnic, UK, 1987

Todini E, Rossman (2013) Unified Framework for Deriving Simultaneous Equation Algorithms for Water Distribution Networks. J Hydraul Eng 139(5):511-526

Wang J, Zhu DL, Bralts VF, Zhang L (2016) Hydraulic analysis of looped microirrigation submain units using the finite element method. Trans ASABE 59(3):909–923

Wang J, Chen R, Yang T, Wei T, Wang X (2021) A computationally-efficient finite element method for the hydraulic analysis and design of subsurface drip irrigation subunits. J Hydrol 595: 125990. https://doi.org/10.1016/j.jhydrol.2021.125990

Wang J, Tian Z, Yang T, Li X, He Q, Wang D, Chen R (2024) Characteristics of limited flow and soil water infiltration boundary of a subsurface drip irrigation emitter in silty loam soil. Agric Water Manag 291:108636. https://doi.org/10.1016/j.agwat.2023.108636

Warrick AW, Shani U (1996) Soil-limiting flow from subsurface emitters. II: Effect on uniformity. J Irrig Drain Eng 122(5):296–300

White I, Sully MJ (1987) Macroscopic and microscopic capillary length and time scales from field infiltration. Water Resour Res 23:1514–1522. https://doi.org/10.1029/WR023i008p01514

Wood D, Rayes A (1981) Reliability of algorithms for pipe network analyses. J Hydraul Div 107: 982-991

CHAPTER 3

Influence of soil hydraulic parameters on bulb size for surface and buried emitters

Based on the **published** paper:

Baiamonte, G., Alagna, V., Autovino, D., Iovino, M., Palermo, S., Vaccaro, G., Bagarello, V., **2024c**. Influence of soil hydraulic parameters on bulb size for surface and buried emitters. *Agric. Water Manag.* 295, 108756.
https://doi.org/10.1016/j.agwat.2024.108756

CHAPTER 3: Influence of soil hydraulic parameters on bulb size for surface and buried emitters

Giorgio Baiamonte[1]*, Vincenzo Alagna[1], Dario Autovino[1], Massimo Iovino[1], Samuel Palermo[1], Girolamo Vaccaro[1], Vincenzo Bagarello[1]

[1]Dept. of Agricultural, Food and Forest Sciences (SAAF), Univ. of Palermo, viale delle Scienze, Bldg. 4, Palermo 90128. *Corresponding Author, E-mail: giorgio.baiamonte@unipa.it

Abstract

Predicting the size expansion of wetting bulbs during surface and subsurface drip irrigation is compulsory for water saving and helps drive irrigation design and scheduling. To solve these issues, various numerical and analytical models, which take into account the soil hydraulic parameters, have been suggested in the literature. The model introduced by Philip (1984) is based on closed-form dimensionless solutions to determine the vertical and horizontal dimensions of the bulb expansion for both buried and surface point sources, under the assumption of homogeneous soil hydraulic properties. In this paper, the solutions provided by Philip (1984) were reformulated in dimensional terms and applied to an already available large data set of soil hydraulic parameters measured in a citrus orchard to evaluate the impact of soil hydraulic properties variability on the development of the wetting front. The results showed that the range of variability of the bulb geometric variables is similar for both buried and surface sources, with a slightly smaller boundary width observed for surface versus buried emitters. More importantly, the geometric bulb variables corresponding to the soil dataset, which characterises the same soil, turned out to be very different, demonstrating that the soil hydraulic parameters have a strong control over the bulb size. In particular, the soil hydraulic properties have an important effect on the downward vertical expansion of the bulb for both surface (CV = 15.5%) and buried (CV = 18.5%) point sources. While the horizontal expansion of the bulb from the surface source (CV = 10.6%) and the upward vertical expansion from the buried source (CV = 12.7%) are a bit less affected. Therefore, the risk of an inadequate soil hydraulic characterisation could be an incorrect estimate of the irrigation volume to be imposed, thus underwatering or overwatering the root zone.

Keywords: Wetting bulb, Drip irrigation systems, Buried sources, Surface sources, Soil spatial variability, Philip's model

List of symbols

$(s_0)_{surface}$	Horizontal expansion of the bulb for surface point sources (cm)	R^2	Coefficient of determination (-)
$(z_{up} + z_{dn})_{buried}$	Total vertical bulb length for the buried source (cm)	S	Soil sorptivity (mm $h^{-0.5}$)
$(z_{dn})_{buried}$	Vertical downward bulb dimension for buried point sources (cm)	S_0	Dimensionless horizontal bulb expansion from surface sources (-)
$(z_{dn})_{surface}$	Vertical downward bulb dimension of the bulb for surface point sources (cm)	s_0	Bulb horizontal expansion from surface point sources (cm)
$(z_{dn})_{surface}/(s_0)_{surface}$	Bulb shape index for surface point sources (cm)	t	Time (h)
$(z_{up})_{buried}$	Vertical upward bulb dimension for buried point sources (cm)	T	Dimensionless travel time of marked particles (-)
$\overline{\theta}$	Difference between θ_{av} and θ_i (cm^3 cm^{-3})	V	Water volume applied by the emitter (L)
A	Constant of Haverkamp's model (mm^{-1})	w_i	Initial gravimetric soil water content (g g^{-1})
b	Capillary scale parameter (-)	z_{dn}	Dimensional downward bulb size for the buried and the surface sources (cm)
b_s	Intercept of the straight line fitted to the data describing steady-state conditions on the I vs. t plot (mm)	Z_{dn}	Dimensionless downward bulb size for the buried and the surface sources (-)
C	Constant of Haverkamp's model (-)	z_e	Burial depth of the emitter (cm)
CV	Coefficients of variation (%)	z_{up}	Dimensional vertical upward bulb size for buried point sources (cm)
D	Diameter of the ring used on beerkan runs (m)	Z_{up}	Dimensionless vertical upward bulb size for buried point sources (-)
h	Soil water pressure head (m)	ΔK	Difference between K_s and K_i (mm h^{-1})
I	Cumulative infiltration of the water in the soil (mm)	$\Delta\theta$	Difference between θ_s and θ_i (cm^3 cm^{-3})
i_s	Slope of the straight line fitted to the data describing steady-state conditions on the I vs. t plot (mm h^{-1})	α	Parameter of the Gardner's hydraulic conductivity function (m^{-1})
K	Soil hydraulic conductivity (mm h^{-1})	β	Shape constant of Haverkamp's model (-)

K_i	Initial soil hydraulic conductivity (mm h^{-1})	γ	Correction constant of Haverkamp's model (-)
K_s	Saturated soil hydraulic conductivity (mm h^{-1})	λ_c	Macroscopic capillary length (mm)
p	Probability value (-)	θ_{av}	Average volumetric soil water content behind the wetting front (cm^3 cm^{-3})
q	Source strength, i.e. emitter flow rate (L h^{-1})	θ_i	Initial volumetric water content before wetting (cm^3 cm^{-3})
r	Radius of the infiltration surface (mm)	θ_s	Saturated volumetric soil water content (cm^3 cm^{-3})
R	Polar distance from the point source (cm)	ρ_b	Dry soil bulk density (g cm^{-3})
ϕ	Angle from the polar direction (rad)		

1. Introduction

Among the different irrigation methods, drip irrigation represents the most efficient system to satisfy the crop water demand while maintaining high yield rates (Baiamonte, 2016; Provenzano et al., 2016). The high efficiency of drip irrigation systems is related to the small volume of the wetted soil compared to the entire volume of soil (Goyal, 2014). If well designed, the system can achieve values of water use efficiency well above 90% (Autovino et al., 2016).

Besides the correct design, the irrigation system must be correctly managed (Barragan et al., 2010). Autovino et al. (2016) proposed a methodology to evaluate the optimal irrigation volume of a crop based on the crop production function, field distribution uniformity and economic evaluations. This approach, however, does not consider the spatial variability of soil hydraulic properties.

Knowledge of water dynamics during drip irrigation is of crucial importance for the design of efficient systems. The wet bulb should develop just in the zone where the active roots are present, thus enhancing root water uptake and reducing water losses by evaporation or percolation (Fernández-Gálvez and Simmonds, 2006; Kandelous and Šimůnek, 2010a, 2010b; Subbaiah, 2013). Addressing this issue is necessary to maximise water use efficiency, thus saving water in agricultural management contexts. Moreover, predicting bulb size is expected to allow for appropriate choices concerning subsurface emitters' depth and emitters' spacing.

The lateral movement of water away from a dripper, compared to its depth of penetration, is determined by the relative importance of the soil hydraulic conductivity and sorptivity (Revol et al., 1997). It is widely recognised that the volume of the bulb, its shape, and the spatial distribution of soil moisture under micro-irrigation vary with irrigation volume and soil hydraulic properties (Lafolie et al., 1989; Lubana et al., 2004). Therefore, the ability to predict the size of the wetted bulb is important, both to ensure efficient irrigation and to avoid the environmentally deleterious drainage of irrigation water below the root zone (Nakayama and Bucks, 1986; Keller and Bliesner, 1990). Since the exact wetting pattern and moisture distribution depend on many factors, including initial soil conditions, emitter flow rate, irrigation volume, frequency and root distribution pattern, different methods to estimate the wetted bulb size were developed (Subbaiah, 2013).

The wetting pattern can be obtained through direct measurements or estimated by infiltration models. To estimate the wetting front distance from a surface or subsurface dripper, several approaches have been proposed that rely on empirical, analytical, or numerical models (Lubana and Narda, 2001).

The empirical models are developed from regression analysis, dimensional analysis an artificial neural network (Singh et al., 2006). These models are simple and do not need specific knowledge of the soil hydraulic properties. However, the reliability of the results is strongly affected by the dataset used for their calibration/validation process. As a consequence, their use for soils different from those for which the models have been developed should be conducted with caution.

The analytical models allow determining the horizontal and vertical dimensions of the wetting pattern through a solution of differential equations generally derived under simplified assumptions for the geometry and the initial and boundary flow conditions (Subbaiah, 2013). The strength of these models is represented by their relative simplicity of use, associated with accurate solutions. Subbaiah (2013) defined the analytical models as “irreplaceable” since they can provide a direct insight into the physics of unsaturated flow, especially when dealing with the effects of several parameters.

The numerical models are based on the solution of the Richards (1931) equation. Unlike empirical or analytical models (Broadbridge et al., 2017; Baiamonte et al., 2023), they offer greater flexibility, thus allowing a realistic simulation of natural flow systems under different initial conditions and imposed boundary constraints. However, numerical models require a detailed knowledge of the soil hydraulic properties of soils, expertise and experience in use and can be computationally intensive.

Philip (1984) provided a closed-form dimensionless solution in spherical polar coordinates for the travel time of a marked particle emitted from a buried infiltration point source and a surface point source. Several authors have applied different models to study the effect of emitter discharge rate, initial soil moisture and soil texture on the size of the wetting pattern (Ayers and Westcot, 1985; Thorburn et al., 2003; Al-Ogaidi et al., 2016). These studies are based on the assumption of homogeneous soil with uniform initial moisture content. However, due to structural heterogeneities (i.e., biological and structural macropores, cracks), the soil hydraulic properties exhibit both small- and large-scale spatial variability that may influence the wetted bulb size (Warrick, 1998). Regalado and Muñoz-Carpena (2004) investigated the spatial variability of the saturated hydraulic conductivity, K_s, of a drip-irrigated volcanic soil. Depending on the measurement method (laboratory, Guelph and Philip-Dunne permeameters) and the flow dimensionality, coefficients of variation (CV) from 5.7% to 72.4% for saturated hydraulic conductivity were detected. Due to the spatial variability within a field, simulation of a single mean wetting pattern for drip irrigation may not be sufficient to design an irrigation system efficiently. For this reason, when designing a localised irrigation system, it is important not only to know the average soil hydrodynamic properties but also their variability. Several spatial variability studies of saturated and unsaturated hydraulic conductivities of agricultural soils have been conducted by different researchers (e.g., Das Gupta et al., 2006), while the influence of the spatial variability of soil hydraulic properties on the water dynamics during drip irrigation has been poorly addressed. The BEST (Beerkan Estimation of Soil Transfer parameters) procedure of soil hydraulic characterisation (Lassabatere et al., 2006) appears to be a good candidate method to simply describe the variability of soil hydrodynamic properties in drip irrigated soils (Mubarak et al., 2009). This topic is of great relevance because neglecting or improperly considering the influence of the soil hydraulic characteristics in irrigation management can negatively affect water saving, which deserves more and more attention in the next few years.

This study aimed at assessing the impact of soil hydraulic properties on predicting infiltration and wetting front from point sources located both on the soil surface and buried in the soil. By using an already available large data set of soil hydraulic parameters measured in an untilled and no-trafficked citrus orchard (Typic Rhodoxeralf), where the soil was classified as mostly sandy-loam or loam, the impact of the range of variability of the soil hydraulic properties on the development of the wetting front was investigated. Soil variability effects on the bulb geometric variables, for both buried and surface point sources, were also analysed.

2. Theoretical background

2.1. Soil hydraulic characterisation

The cumulative infiltration curve obtained by a beerkan run, which consists in repeatedly applying a fixed and small water volume on the soil surface and recording the infiltration time of each water volume, can be used to determine the soil hydraulic properties by the so-called BEST procedure of soil hydraulic characterisation (Lassabatere et al., 2006). In particular, the BEST-steady algorithm yields and estimate of soil sorptivity, S (mm h$^{-0.5}$), and saturated soil hydraulic conductivity, K_s (mm h^{-1}), using the intercept, b_s (mm), and the slope, i_s (mm h^{-1}), of the straight line fitted to the data that describe steady-state conditions on the cumulative infiltration, I (mm), versus time, t (h), plot (Bagarello et al., 2014):

$$S = \sqrt{\frac{i_s}{A + \frac{C}{b_s}}} \tag{1}$$

$$K_s = \frac{C\, i_s}{A\, b_s + C} \tag{2}$$

in which A (mm^{-1}) and C are constants that, for an antecedent volumetric soil water content, θ_i, less than 0.25 times the volumetric water content of the saturated soil, θ_s, can be set at (Haverkamp et al., 1994; Lassabatère et al., 2006):

$$A = \frac{\gamma}{r\, \Delta\theta} \tag{3a}$$

$$C \approx \frac{1}{2(1-\beta)} \ln\left(\frac{1}{\beta}\right) \tag{3b}$$

where $\Delta\theta$ is the difference between θ_s and θ_i, r (mm) is the radius of the infiltration surface and γ and β are coefficients commonly assumed equal to 0.75 and 0.6, respectively.

The macroscopic capillary length, λ_c (mm), that expresses the relative importance of capillarity over gravity forces during water movement in unsaturated soil, is given by (White and Sully, 1987):

$$\lambda_c = \frac{b\, S^2}{\Delta\theta\, \Delta K} \tag{4}$$

where b is a dimensionless capillary scale parameter frequently set equal to 0.55 and ΔK is the difference between K_s and the initial soil hydraulic conductivity, K_i (mm h^{-1}). Low λ_c values (e.g., $0 < \lambda_c \leq 10$ mm) indicate a dominance of gravity over capillarity and are typically found in coarse-textured or highly structured porous media. Instead, high λ_c values (i.e., >1000 mm) indicate the dominance of capillarity over gravity, as found in many fine-textured or poorly structured porous media. According to Di Prima et al. (2020), λ_c can be obtained from a steady-state beerkan infiltration run as follows:

$$\lambda_c = 0.861\, \frac{b_s}{\Delta\theta} \tag{5}$$

2.2. Wetting patterns for surface and subsurface drip irrigation

Under the assumption of homogeneous soil hydraulic properties, for buried and surface infiltration point sources, Philip (1984) provided closed-form dimensionless solutions for the travel times of marked particles. For particular cases of the considered spherical polar coordinates (R, ϕ) (Fig. 1), $\phi = 0, \pi$ (vertical direction) and $\phi = \pi/2$ (horizontal direction), these solutions are very simple, and although implicit with respect to the geometric variables denoting the size of the expanding bulb, allow assessing the impact of soil hydraulic properties on the predicted infiltration and on the related wetting front advancement, which is compulsory for the appropriate design of drip irrigation systems.

For a buried (burial depth, $z_e > 0$) and a surface (burial depth, $z_e = 0$) point source, Figure 1 shows a schematic representation of the bulb, where the geometric variables investigated in this work, vertical upward and downward, z_{up} (cm) and z_{dn} (cm), for buried source (Fig. 1a) and horizontal and downward, s_0 (cm) and z_{dn} (cm), for surface source (Fig. 1b), are indicated. For both cases, these geometric variables do not explore the entire bulb size. However, it is expected that they provide an exhaustive analysis of the effect of the variability of soil hydraulic parameters on the bulb expansion, since it is possible to consider that all the other points belonging to the bulb have a similar behaviour.

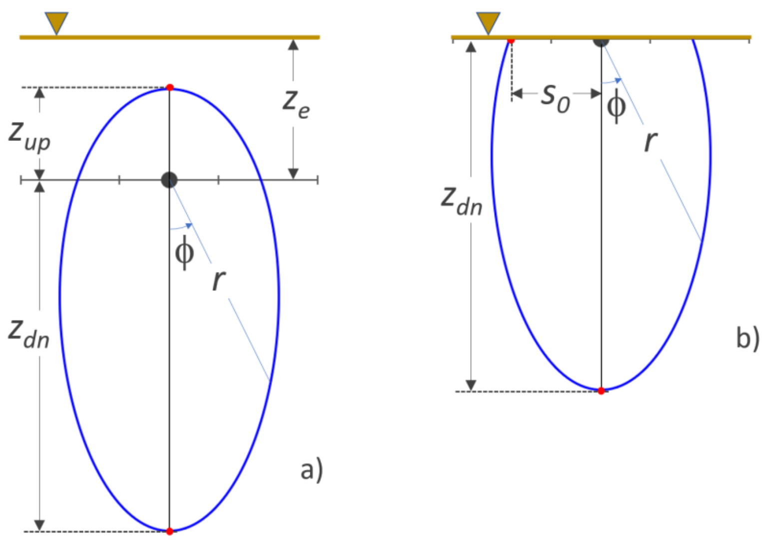

Fig. 1 *Schematic representation of the bulb size from* ***a)*** *a buried point source (burial depth, $z_e > 0$) and* ***b)*** *a surface point source (burial depth, $z_e = 0$). The investigated variables z_{up} and z_{dn}, for the buried emitter (black dot), and s_0 and z_{dn}, for the surface emitter, are indicated*

In order to limit water losses, the design and management of a buried irrigation system must ensure that the value of z_{up} will not exceed the water line installation depth, while the sum of z_{dn} and z_e should not exceed the rooting depth. In the case of surface irrigation, it is important that the value of s_0 is as limited as possible to reduce the evaporating soil surface and, also in this case, that the z_{dn} value should not exceed the rooting depth. On the other hand, low s_0 values could compromise the necessary overlap of the wetting bulb and the root zone. For this reason, the calculation of these four lengths will be treated in detail below.

2.2.1. Dimensionless parameters

According to Philip (1984), the dimensionless travel time T can be defined as:

$$T = \frac{\alpha^3 q\, t}{16\, \pi\, \bar{\theta}} \qquad (6)$$

where α (m^{-1}) is the parameter of the exponential hydraulic conductivity function by Gardner (1958), q ($mm^3\ h^{-1}$) is the source strength, i.e. the emitter flow rate, t (h) is the irrigation time, V (L) is the water volume applied by the emitter, and $\bar{\theta} = \theta_{av} - \theta_i$, where θ_{av} ($cm^3\ cm^{-3}$) is the average volumetric water content in the soil behind the wetting front and θ_i ($cm^3\ cm^{-3}$) is the initial volumetric water content before wetting. In this investigation, θ_{av} was approximated as $(\theta_s + \theta_i)/2$. A certain approximation in the choice of the water contents to be used for calculating $\bar{\theta}$ was unavoidable, also considering that definitions do not seem univocal. For example, the water content at the wetting front was assumed as the θ value when K was equal to 1 mm day^{-1} by Cook et al. (2003) and 1 mm h^{-1} by Thorburn et al. (2003).

The α parameter in Eq. (6) is the slope of the ln K vs. soil water pressure head, h, relationship by Gardner (1958). For a Gardner soil (Youngs et al., 1993), α could potentially be estimated from the K values corresponding to any two values of h. In general, estimating α requires fitting the hydraulic conductivity model to a set of $K(h)$ data. Taking into account that, with drip irrigation, an initially nearly dry soil is wetted up to near saturation, the range of interest of h is rather wide, varying from very negative (dry soil) to little negative or nearly null (wetted soil) values. This circumstance has to be taken into account if λ_c is used to determine α (e.g., Thorburn et al., 2003) since α describes the entire hydraulic conductivity function, but λ_c decreases as θ_i increases (White and Sully, 1987). Therefore, a determination of λ_c, and hence $\alpha = \lambda_c^{-1}$, performed in an initially wet soil can be expected to yield a different result than that of an experiment performed in an initially dry soil. In particular, a wet soil could yield a larger α value than a dry soil.

For both buried and surface sources, the dimensionless downward size, Z_{dn}, is denoted as (Fig. 1):

$$Z_{dn} = \frac{\alpha\, z_{dn}}{2} \tag{7}$$

whereas, for the buried and the surface sources, the dimensionless upward size and horizontal size are denoted, respectively:

$$Z_{up} = \frac{\alpha\, z_{up}}{2} \tag{8}$$

$$S_0 = \frac{\alpha\, s_0}{2} \tag{9}$$

where z_{up} (cm) and s_0 (cm) are the corresponding dimensional variables.

2.2.2. Dimensionless relationships

For a buried source, the dimensionless solutions of the wetting front travel-time provided by Philip (1984) are:

$$T = \frac{e^{2\, Z_{up}}\left(1 - 2\, Z_{up} + 2\, Z_{up}^2\right) - 1}{2} \tag{10}$$

$$T = \frac{\left(Z_{dn}^2 - Z_{dn}\right)}{2} + \frac{log\,(1 + 2\, Z_{dn})}{4} \tag{11}$$

whereas for a surface source, the following relationships were derived (Philip, 1984):

$$T = \frac{Z_{dn}^2}{2} - Z_{dn} + log\,(1 + Z_{dn}) \tag{12}$$

$$T = 2\, e^{S_0}\left(1 - S_0 + \frac{S_0^2}{2}\right) - 2 \tag{13}$$

2.2.3. Dimensional relationships

A great advantage of the above-mentioned dimensionless solutions derived by Philip (1984) lies in the reduced number of parameters contained in them. Therefore, it is easy to interpret the effect of proportional variations of one variable on the other.

For the purpose of this study, which aims at detecting the impact of the soil hydraulic parameters on bulb sizes, the same relationships reformulated in dimensional terms are necessary to investigate the impact of the soil hydraulic properties.

In particular, for the buried source, associated with Eq. (10) and Eq. (11), we obtain:

$$V = \frac{4\,\pi\,\bar{\theta}}{\alpha^3}\left[e^{\frac{\alpha\, z_{up}}{2}}\left(2 + \alpha\, z_{up}(\alpha\, z_{up} - 2)\right) - 2\right] \quad (14)$$

$$V = \frac{2\,\pi\,\bar{\theta}}{\alpha^3}\left[\alpha\, z_{dn}(\alpha\, z_{dn} - 2) + 2\, log\,(1 + \alpha\, z_{dn})\right] \quad (15)$$

whereas for the surface source, associated with Eq. (12) and Eq. (13), we derive:

$$V = \frac{2\,\pi\,\bar{\theta}}{\alpha^3}\left[\alpha\, z_{dn}(\alpha\, z_{dn} - 4) + 8\, log\left(1 + \frac{\alpha\, z_{dn}}{2}\right)\right] \quad (16)$$

$$V = \frac{4\,\pi\,\bar{\theta}}{\alpha^3}\left[e^{\frac{\alpha\, s_0}{2}}\left(8 + \alpha\, s_0(\alpha\, s_0 - 4)\right) - 8\right] \quad (17)$$

The water volume applied by the emitter, *V*, was considered as a dependent variable, so that any combination of the emitter flow rate, *q*, and the irrigation time, *t*, can be explained by *V*.

The above dimensional relationships also allow practical applications, as determining the water volumes required to achieve an assigned vertical bulb length. For surface sources, Eq. (16) solves this issue, whereas for buried sources, Eq. (14) and Eq. (15) need to be combined. Putting Eq. (14) and Eq. (15) as equal yields:

$$\frac{4\,\pi\,\bar{\theta}}{\alpha^3}\left[e^{\frac{\alpha\, z_{up}}{2}}\left(2 + \alpha\, z_{up}(\alpha\, z_{up} - 2)\right) - 2\right] = \frac{2\,\pi\,\bar{\theta}}{\alpha^3}\left[\alpha\, z_{dn}(\alpha\, z_{dn} - 2) + 2\, log\,(1 + \alpha\, z_{dn})\right] \quad (18)$$

From Eq. (18), an implicit equation linking z_{dn} and z_{up}, which does not depend on $\bar{\theta}$, can be derived:

$$z_{dn} = \frac{4-2e^{\alpha z_{up}\left(2-\alpha z_{up}\left(2-\alpha z_{up}\right)\right)+2\log\left(1+\alpha z_{dn}\right)}}{\alpha\left(2-\alpha z_{dn}\right)} \quad (19)$$

For a given water volume, V, Eq. (19) allows estimating the total vertical length for the buried source $(z_{up} + z_{dn})_{buried}$. Eq. (14) or Eq. (15) are used to determine z_{up} or z_{dn}. Then, Eq. (19) is solved for the other unknown variable (z_{dn} or z_{up}).

Applications of the above dimensional relationships take into account the influence of the soil hydraulic properties simply with the α parameter. Consequently, by applying the reformulated Philip's model, it is possible to estimate the variability of the bulb expansion by having a dataset relating to the spatial variability of the α parameter, which can be obtained with simplified approaches, e.g. BEST procedures.

3. Material and methods

The field experiment was performed at the Agricultural, Food and Forest Sciences Department of the University of Palermo (Italy), in a no-tilled and no-trafficked citrus orchard with trees spaced 4 m × 4 m apart (coordinates 33S 355511E 4218990N). The soil at the field site (Typic Rhodoxeralf) has a relatively high gravel content, and it is mostly sandy-loam or loam down to a depth of at least 0.30 m. This soil has been chosen since it is representative of the agricultural area around Palermo city (Sicily), where the prevailing crop is citrus orchard, mostly irrigated with surface and subsurface drip irrigation systems. Data for this investigation were collected in an area of approximately 200 m^2, in which the soil had mainly a loam texture, according to the USDA classification system (clay = 15.4%, silt = 36.2%, sand = 48.4%). The soil surface was gently levelled and smoothed by manual implements before sampling. To sample a bare area, the superficial herbaceous vegetation has been cut with a knife when it was present, while the roots remained in situ. Small diameter (D = 0.08 m) rings were inserted on the soil surface to a depth of 0.01 m for the beerkan infiltration runs. Ring insertion was conducted manually or by gently using a rubber hammer and ensuring that the upper rim of the ring remained horizontal during insertion.

A total of 56 beerkan runs were performed at randomly selected locations from May to July 2022. For each run, 20 water volumes, each of 57 mL, were successively poured, each in approximately 3 s, on the confined infiltration surface by applying water at a small distance from the infiltration surface, i.e. approximately at a height of

0.03 m. Therefore, a total of 227 mm of water was applied with a beerkan run. Water energy was dissipated on the fingers of the hand to minimise soil disturbance due to water application (Reynolds et al., 2002). For each water volume (1^{st}, 2^{nd}, …, 20^{th}), the infiltration time was measured from water application to the disappearance of all water, when the subsequent water volume was poured on the infiltration surface.

At the beginning of a working day, two undisturbed soil cores (0.05 m in height by 0.05 m in diameter) were collected in three different points of the area at the 0 to 0.05 m and 0.05 to 0.10 m depths. These cores were used to determine the dry soil bulk density, ρ_b, and the antecedent gravimetric soil water content, w_i, and hence θ_i. The means of the ρ_b and θ_i determinations were then associated with the beerkan runs performed on that day. Overall, 21 soil cores were collected for a given sampling depth. A two-tailed, paired t-test was applied to compare the ρ_b and the w_i values obtained at the two depths.

The dataset used in this investigation was developed by re-analysing some of the infiltration curves obtained by Agosta et al. (2023). In particular, these authors performed three subsequent infiltration runs at a given sampling point during a nearly two-week period, and they established comparisons between subsequent runs by considering the infiltration parameters of the Horton model (Horton, 1941). For each sampling point, only the first run was considered in this investigation since, in the other cases, the soil was initially too wet for applying BEST methods of data analysis (Lassabatere et al., 2006) or representative antecedent soil water content data were not collected, and hence soil hydrodynamic parameters could not be calculated.

For each run, S, K_s and λ_c were calculated by Eqs. (1), (2) and (5), respectively. The normal distribution hypothesis of these data was then checked with the Lilliefors (1967) test. A regression analysis between two datasets was performed by considering the exponential, linear, logarithmic and power relationships and retaining the relationship having the highest coefficient of determination, R^2, for further analysis. A two-tailed t-test was used to establish the statistical significance of a fitted regression line to the data (Glantz, 2012). All statistical tests were carried out at $P = 0.05$.

4. Results and discussion

4.1. Soil hydraulic characterisation

The subsoil (5−10 cm) was less compacted and wetter than the upper soil layer (0−5 cm) (Table 1). However, both the ρ_b and the w_i values differed by only a little between the two sampling depths, that is, by 0.07 g cm^{-3} and 0.03 g g^{-1}, respectively. Therefore, differences between the two soil layers were overall small.

The θ_i/θ_s ratio, with θ_s estimated from the dry soil bulk density, varied between 0.10 and 0.21. Therefore, BEST calculations were possible since θ_i/θ_s was steadily smaller than 0.25 (Lassabatere et al., 2006). In this perspective, performing beerkan infiltration runs and using BEST methods to analyse the data seems appropriate to obtain usable λ_c values for bulb size prediction according to Philip (1984). The reason is that the infiltration experiment has to be performed in an initially nearly dry soil ($\theta_i \leq 0.25\ \theta_s$; Lassabatere et al., 2006), and it establishes saturated soil conditions close to the infiltration surface. This situation is similar to that realised by point source irrigation. In other words, the infiltration experiment characterises a soil by considering a relevant range of θ values from the perspective of predicting the size of the wetted bulb.

Table 1 *Summary of the dry soil bulk density, ρ_b, and antecedent gravimetric soil water content, w_i, values for the 0−5, 5−10 and 0−10 cm sampling depths obtained before the beerkan runs (sample size, N = 21 for each dataset) (adapted from Agosta et al., 2023)*

Statistic	ρ_b (g cm^{-3})			w_i (g g^{-1})		
	0−5 cm	5−10 cm	0−10 cm	0−5 cm	5−10 cm	0−10 cm
Min	1.069	1.049	1.090	0.029	0.060	0.044
Max	1.303	1.185	1.222	0.117	0.122	0.120
Mean	1.175 a	1.107 b	1.141	0.053 a	0.086 b	0.070 a
CV (%)	5.0	3.2	3.3	44.2	23.4	30.3

The hypothesis that S, K_s and λ_c were normally distributed was not rejected by the Lilliefors (1967) test. Consequently, the data were summarised by the arithmetic mean and the associated coefficient of variation, *CV* (Table 2). The S and K_s values were rather close to those previously obtained at the same field site and in the same period of the year by Bagarello et al. (2023). In particular, these last authors obtained a mean sorptivity of 126 mm h$^{-0.5}$ in May and of 160 mm h$^{-0.5}$ in July. These mean values differed at most by 1.2 times from the mean *S* value obtained in this investigation. The corresponding means of K_s were equal to 194 and 158 mm h^{-1}, and they differed at most by 1.4 times from the results of this investigation. The similarity between the two investigations suggested that the developed dataset was representative enough of the field site for a nearly dry or rather dry soil. Moreover, the *CV* of K_s found in this investigation was very close to that (*CV* = 35.7%) obtained by another BEST algorithm at the same site by Bagarello et al. (2014). However, variability of the soil hydrodynamic parameters should be expected to vary with several factors, including the sampling period in the year. According to Warrick (1998), all soil hydrodynamic parameters obtained in this investigation exhibited a medium variation.

On average, capillarity was moderate since it was approximately equal to 90 mm (Table 2), and λ_c values of 42−125 mm are indicative of a moderate capillarity (Elrick and Reynolds, 1992; Di Prima et al., 2020). This capillarity category was detected at 89% of the 56 sampled points. In five cases, capillarity was strong but close to moderate since λ_c did not exceed 160 mm and strong conditions are expected for λ_c values ranging between 125 and 1000 mm. In a single case, capillarity was weak and close to negligible according to the ranges reported by Di Prima et al. (2020) since λ_c was equal to 12.4 mm, and $\lambda_c \leq 10$ mm denotes a negligible capillarity.

Soil sorptivity increased with saturated soil hydraulic conductivity according to a statistically significant relationship ($R^2 = 0.50$, $R > 0$) (Fig. 2).

***Table 2** Summary statistics of the soil hydrodynamic parameters (sample size, N = 56 for each parameter)*

Parameter	Min	Max	Mean	*CV* (%)
S (mm $h^{-0.5}$)	57.5	207.1	128.7	25.0
K_s (mm h^{-1})	35.9	410.5	227.2	37.6
λ_c (mm)	12.4	157.7	89.6	33.1

This result was physically plausible taking into account that, according to Stewart et al. (2013), sorptivity also depends, in addition to soil capillarity representing the driving force, on soil hydraulic conductivity that expresses the dissipation. The relationships between λ_c and both K_s and *S* were weak (R^2 = 0.13 and 0.19, respectively), albeit statistically significant. In particular, λ_c decreased as K_s increased, whereas an increase of *S* determined an increase of λ_c. Even these results were physically convincing since low λ_c values indicate a dominance of gravity over capillarity (e.g., Di Prima et al., 2020). This dominance is more and more expected as the soil becomes more conductive and less sorptive.

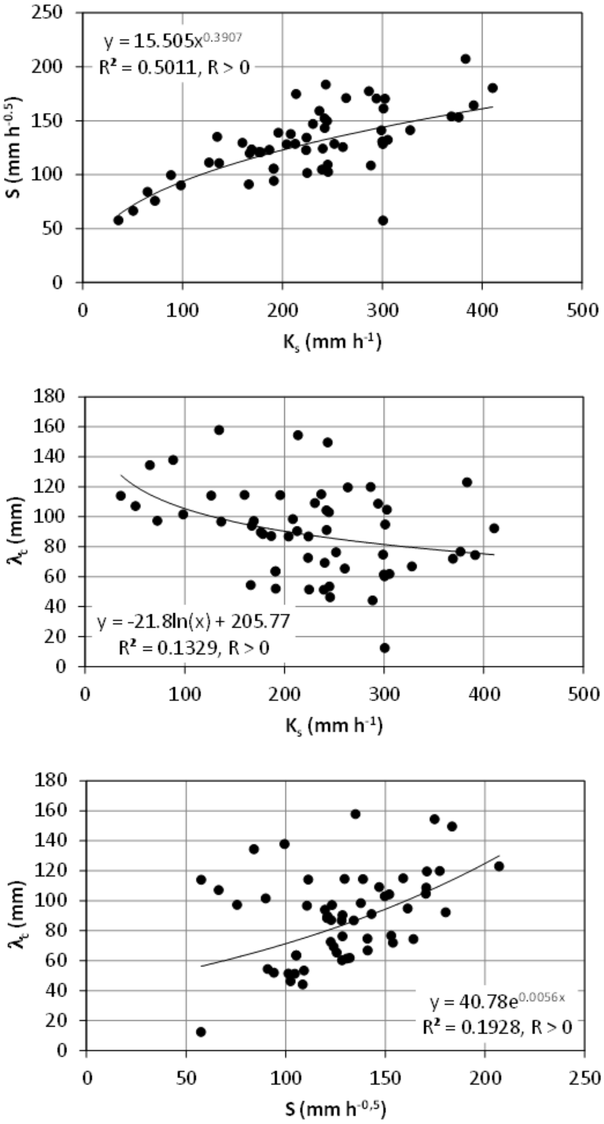

Fig. 2 *Relationships between soil sorptivity, S, saturated hydraulic conductivity, K_s, and macroscopic capillary length, λ_c (N = 56)*

As shown in Fig. 2, the run yielding the lowest λ_c value (12.4 mm) deviated considerably from the other runs, despite the generally high data scattering. This particularly low λ_c value was obtained since the cumulative infiltration curve was nearly linear from the beginning of the run and hence the b_s intercept was small. A logical implication could be excluding this run from the subsequent analysis, considering the data obtained with this run as outliers. However, the shapes of infiltration curves can be highly variable, depending on many factors and processes (e.g., Angulo-Jaramillo et al., 2019), and Pachepsky and Karahan (2022) recently suggested that there are no reasons to assume that only concave and concave-to-linear cumulative infiltration curves can exist in nature.

Moreover, BEST-steady yielded possible (i.e., positive) estimates of S and K_s and the calculated values of these two hydrodynamic parameters for this run did not deviate substantially from those obtained with the other runs (Fig. 2). In particular, S = 58 mm $h^{-0.5}$ and K_s = 301 mm h^{-1} were obtained for the run yielding the smallest λ_c value and, without this data point (N = 55), the calculated S and K_s values were in the range 58–207 mm $h^{-0.5}$ and 36–411 mm h^{-1}, respectively. Finally, λ_c was very low but physically possible (Di Prima et al., 2020). Therefore, there was no strong reason to exclude this apparent outlier from the subsequent analysis.

4.2. Wetting patterns

For a reasonable value of the water volume applied by the emitter during one irrigation, V = 10 L, which could be ascribed to q = 2.1 L h^{-1} flow rate and 4.76 h of the irrigation time, Fig. 3 plots the frequency distribution of the studied variables, z_{up} and z_{dn} (Eqs.18 and 19), for the buried source (dots), and s_0 and z_{dn} (Eqs. 20 and 21), for the surface source (circles), corresponding to the investigated dataset.

For both buried and surface sources, Fig. 3 shows that z_{up} and s_0 appear a little less influenced by the soil property variability, expressed by $\alpha^3/\bar{\theta}$, than z_{dn}, as quantified by the coefficient of variation CV that for buried sources equals $CV(z_{up})$ = 12.7% and $CV(z_{dn})$ = 18.5%, whereas for surface sources $CV(s_0)$ = 10.6% and $CV(z_{dn})$ = 15.5%. Moreover, according to the α outlier (81 m^{-1}), z_{dn} = 73.7 cm and 74.7 cm, for buried and surface sources, respectively, occurred. The latter suggests that for high α, buried sources provide vertical bulbs that do not expand appreciably above the burial plane, contrary to what is observed in other cases.

Bulb sizes were investigated in some detail, by considering the 56 sampling points, each characterised by $\alpha^3/\bar{\theta}$. Taking into account that $\bar{\theta}$ varied only a little in this investigation (N = 7, mean = 0.246 cm^3 cm^{-3}; CV = 4.3%), each sampling point was only characterised by its α value. Applications were performed by varying the irrigation volume, V (L), which depends on both the emitter flow rate and the irrigation time.

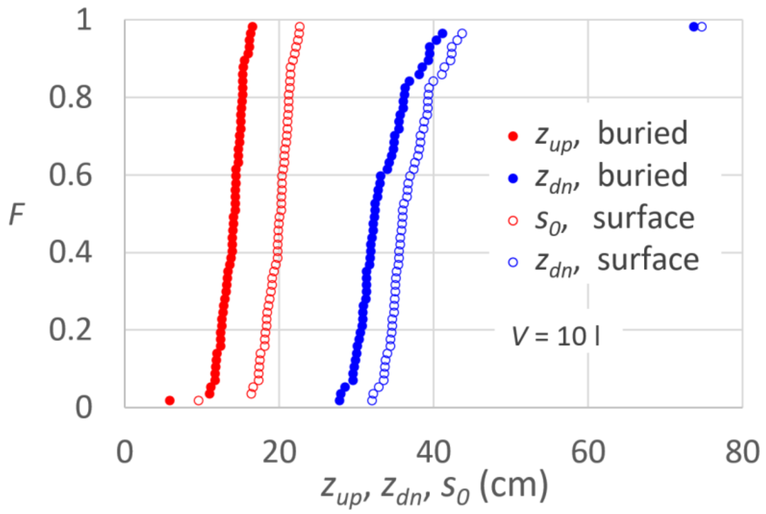

Fig. 3 *For the considered dataset, and for V = 10 l, frequency distribution of z_{up} and z_{dn}, for the buried source, and of s_0 and z_{dn}, for the surface source*

For the entire dataset, Eqs. (18) and (19), for a buried source, and Eqs. (20) and (21), for a surface source, were log-log plotted against α for different V values (5, 10, 20, and 30 L) in Fig. 4a and 4b, respectively.

For the considered soil and for any V, Fig. 4 shows that, for a buried source, $z_{dn} > z_{up}$, while, for a surface source, $z_{dn} > s_0$, indicating an elongated shape of the bulb, which becomes more and more outstretched at increasing α, according to a quite potential power law. Contrarily to z_{dn} that increases with α, z_{up} (Fig. 4a) and s_0 (Fig. 4b) decrease with α, evidencing as obvious that when gravity forces increase as compared with capillarity forces (Reynolds and Elrick, 1991), the bulb expansion upwards for buried sources and laterally for surface sources tends to be limited. Of course, the bulb expansion increases with increasing the irrigation volume, and a quite similar power law shape is maintained.

In Fig. 4, it is also interesting to observe that for any fixed α, by varying V, for both buried and surface sources, the range of variability of z_{dn} is higher than that of s_0 and z_{up}, respectively. Only in the first stages of irrigation (low V and low α), the bulb shape is more spherical than stretched down, while the opposite result is obtained for high V.

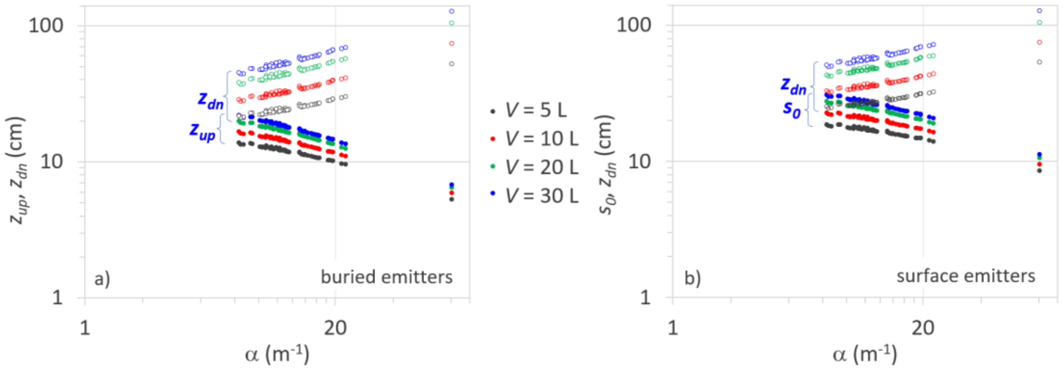

Fig. 4 *Relationship between the geometric variables,* ***a)*** *for a buried source and* ***b)*** *for a surface source, versus the* α *parameter, for different irrigation volumes*

To compare the total bulb vertical length of buried and surface sources, the dimensionless ratio between the sum $z_{up} + z_{dn}$ for the buried source, $(z_{up} + z_{dn})_{buried}$, and z_{dn} for the surface source $(z_{dn})_{surface}$ was evaluated for the entire data set, by imposing different irrigation volumes.

Figure 5a shows the ratio $(z_{up} + z_{dn})_{buried}/(z_{dn})_{surface}$ versus α for different V. The total bulb vertical length $(z_{up} + z_{dn})_{buried}$ results higher than the $(z_{dn})_{surface}$, indicating the advantages in water saving due to adopting subsurface irrigation, where buried emitters also wet the soil upwards. However, this benefit tends to vanish at increasing α (Fig. 5a), achieving $(z_{up} + z_{dn})_{buried}$ values close to $(z_{dn})_{surface}$, and more and more as the irrigation volume increases. For any α, the benefit appears more relevant in the first stages of the irrigation, that is, when small water volumes have been supplied.

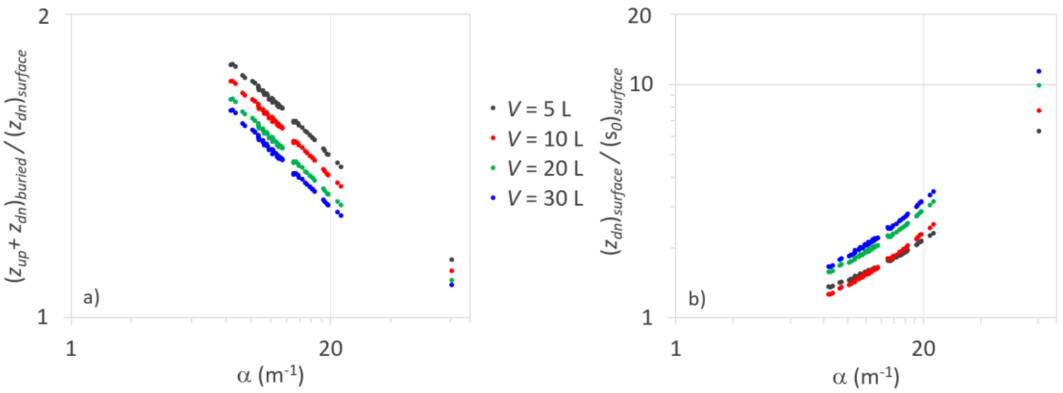

Fig. 5 *Relationship between* ***a)*** *the dimensionless $(z_{up} + z_{dn})_{buried}/(z_{dn})_{surface}$ ratio and* ***b)*** *the bulb shape index $(z_{dn})_{surface}/(s_0)_{surface}$, versus the* α *parameter, for different irrigation volumes*

For surface sources, the bulb shape index $(z_{dn})_{surface}/(s_0)_{surface}$ was also considered (Fig. 5b). In this case, the bulb shape index follows an increasing quadratic function of α. Furthermore, the increasing irrigation volume provides a higher bulb shape index, since during irrigation the bulb elongates downward more and more.

From an irrigation system design point of view, it is important to predict the vertical length of the bulb by imposing adequate irrigation times and, importantly, by accounting for the spatial variability of soil hydraulic characteristics that have been displayed in Fig. 2. Indeed, watering times that go on longer than necessary determine water waste since the bulb size may overpass the root zone.

For each soil sampling point, the geometric variables are plotted against the irrigation volume in Fig. 6a (for the buried sources) and in Fig. 6b (for the surface source). Except for the α outlier, the curves lay within a bound with an increasing width for larger irrigation volumes. The range of variability of the geometric variables is similar for both buried and surface sources, but a bit narrower bound width can be observed for surface emitters than for buried emitters. Contrarily, the geometric bulb variables corresponding to the α outlier determine very different geometric variables compared to the other values. This result means that an uncommonly large α value may provide a high z_{dn} value, and hence it could imply underwatering in the root zone.

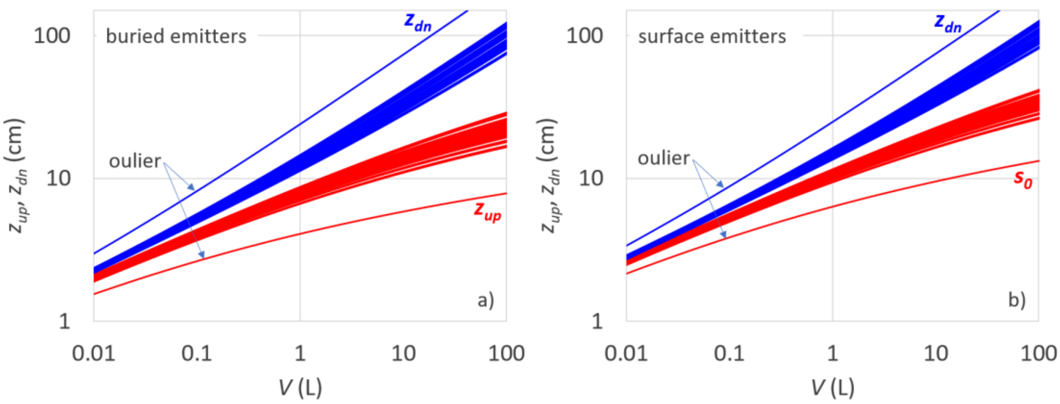

***Fig. 6** Geometric bulb variables **a)** for a buried source and **b)** for a surface source, versus the irrigation volume, V, for the 56 experimental runs. The geometric bulb variables corresponding to the* α *outlier is also indicated*

To evaluate the impact of α in estimating the irrigation volume required to achieve an imposed root depth, applications were performed for the minimum and the maximum α values retrieved in the dataset (6 and 81 m^{-1}) for a buried source. First Eq. (19) was needed to be used for determine the z_{dn} and z_{up} relationship. For the above-mentioned extreme α values, Fig. 7 shows the increasing relationship between $(z_{dn})_{buried}$ and $(z_{up})_{buried}$, and the important effect of α. In particular, Fig. 7 illustrates that for a fixed z_{dn}, e.g. 10 cm, z_{up} = 2.5 cm occurs for α = 81 m^{-1}, while z_{up} is three times higher (7.5 cm) for α = 6 m^{-1}, and the relationship between z_{dn} and z_{up} is independent of the Δθ value.

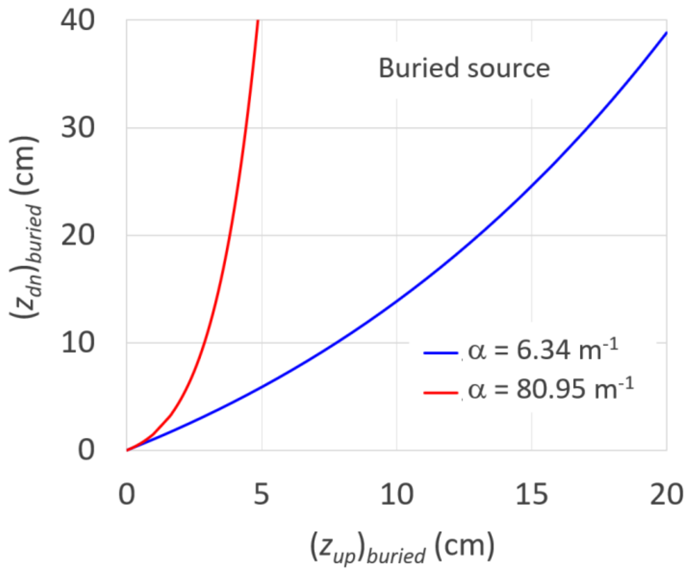

***Fig.** 7 For a buried source, the relationship between z_{dn} and z_{up}, for the minimum α = 6 m^{-1} and the maximum α = 81 m^{-1}*

For the pairs (z_{dn}, z_{up}) obtained by using Eq. (19), the irrigation volume required to achieve an imposed root depth was determined by Eq. (14) (or by Eq. 15). Figure 8 plots the irrigation volumes required to achieve an assigned vertical bulb length for both a buried source $(z_{up} + z_{dn})_{buried}$, and for a surface source (Eq. 20), and both for α = 6 m^{-1} (Fig. 8a) and for α = 81 m^{-1} (Fig. 8b).

The comparison between Fig. 8a and 8b makes it evident that the important effect of α value occurs when the desired water irrigation volume is established. Indeed, for fixed values of $(z_{dn} + z_{up})_{buried} = (z_{dn})_{surface}$ equal to 30 cm and 50 cm, indicated by dots in Fig. 8 and reported in Table 3, it can be observed that for the highest α value, irrigation volumes much lower than those for the lowest α value are required to cover the imposed vertical bulb length. In terms of water saving, the benefit of subsurface drip irrigation can be observed for both α values, requiring less water volume for buried sources than for surface sources, with a lesser extent for the highest α value.

This is because, in soils characterised by high α values, gravity forces play a predominant role compared to capillarity; therefore, the bulb takes on a more elongated shape. While in soils characterised by low values of α, capillary forces dominate the flow, and the bulb shape is more spherical.

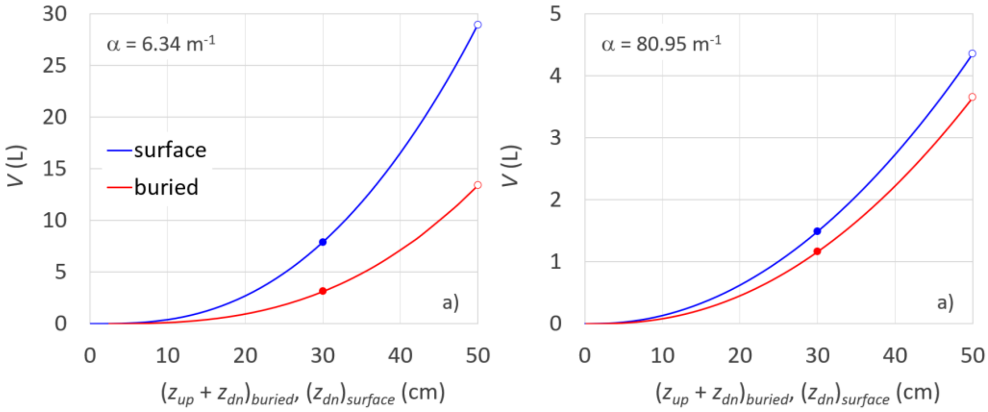

Fig. 8 *Irrigation volumes required to achieve an assigned vertical bulb length for a buried source,* $(z_{up} + z_{dn})_{buried}$*, and for a surface source* $(z_{dn})_{surface}$*,* ***a)*** *for the minimum value of α (6* m^{-1}*) and* ***b)*** *for the maximum value of α (81* m^{-1}*). The dots indicate the volumes corresponding to 30 cm and 50 cm reported in Table 3*

However, in heterogeneous soils, for a correct design and management of the irrigation system, an adequate determination of the variability of the α parameter is even more necessary because water irrigation volumes established by only considering the highest or the lowest α value could penalise both extreme conditions, and a frequency analysis would be suggested, especially for high spatial variability.

Table 3. *Irrigation volumes, V (L), required to achieve bulb vertical lengths equal to 30 cm and 50 cm, for buried and surface emitters*

Bulb vertical length (cm)	soil parameters		buried emitters			surface emitters	
	α (m^{-1})		z_{up} (cm)	z_{dn} (cm)	V (L)	z_{dn} (cm)	V (L)
30	MIN	6	12.1	17.9	3.1	30	7.9
	MAX	81	4.2	25.8	1.2		1.5
50	MIN	6	17.8	32.2	13.4	50	28.9
	MAX	81	5.1	44.9	3.7		4.4

The results obtained in this study demonstrate that the total thickness of the wetted soil layer is highly affected by the soil hydraulic characteristics. The detection of the latter has important implications in irrigation scheduling since irrigation volumes less than or greater than those determined by the suggested procedure may determine underwatering or overwatering, respectively. In the first case, the root development will be confined within a thinner depth than that established for the crop; in the second case, irrigation water is wasted.

In consideration of the above, predicting the variability in bulb expansion resulting from different soil hydraulic properties is essential to estimate the wetting patterns in trickle irrigation systems. Therefore, this proposed approach represents a valuable and straightforward method for designing more efficient irrigation systems that can contribute to water conservation in a context of water resource scarcity.

5. Conclusions

In this study, a wide dataset of the soil hydraulic properties measured for a sandy-loam to loam soil was used to investigate the impact of their variability in predicting the bulb size for surface and buried emitters. To analyse the bulb size, the solutions provided by Philip’s (1984) model were reformulated in dimensional terms and applied to the above dataset. The results showed that hydraulic properties influenced the geometric variables of the bulb with a similar variability range for both buried and surface sources. In terms of water management, a buried source always allows water saving compared to a surface source. However, in soils characterised by the highest values of α, this benefit is less accentuated due to the downward vertical bulb expansion. Due to the spatial variability of the soil hydraulic properties, which highly impacts the bulb size, more accurate design procedures should be developed, avoiding only characterising the soil in rough terms, such as based on its textural characteristics. In other terms, the methodology applied in this investigation helps include the hydrological behaviour of the soil, which has to affect the emitters’ position in the design choice, also considering the crop root distribution. A forward step of the analysis could be establishing a link between the hydrological properties and the design variables. Likely, a development of the design procedure should include some kind of probabilistic analysis of the individually wetted soil volumes. This approach could help to consider, and hence to minimise, the risks of an improper design and management of the irrigation apparatus, since uncontrolled irrigation duration can cause the bulb's vertical length to go beyond the root zone, thus wasting irrigation water.

6. References

Agosta, M., Alagna, V., Bagarello, V., Caltabellotta, G., Iovino, M., Vaccaro, G., 2023. Hydrodynamic response of a loam soil after wetting with different methods. J. Hydrol. 623, 129770. https://doi.org/10.1016/j.jhydrol.2023.129770

Al-Ogaidi, A.A.M., Wayayok, A., Rowshon, M.K., Abdullah, A.F., 2016. Wetting patterns estimation under drip irrigation systems using an enhanced empirical model. Agric. Water. Manag. 176, 203–213. https://doi.org/10.1016/j.agwat.2016.06.002

Angulo-Jaramillo, R., Bagarello, V., Di Prima, S., Gosset, A., Iovino, M., Lassabatere, L., 2019. Beerkan Estimation of Soil Transfer parameters (BEST) across soils and scales. J. Hydrol. 576, 239-261. https://doi.org/10.1016/j.jhydrol.2019.06.007

Autovino, D., Provenzano, G., Monserrat, J., Cots, L., Barragán, J., 2016. Determining Optimal Seasonal Irrigation Depth Based on Field Irrigation Uniformity and Economic Evaluations: Application for Onion Crop. J. Irrig. Drain E-ASCE 142(10). https://doi.org/10.1061/(ASCE)IR.1943-4774.0001048

Ayers, R.S., Westcot, D.W., 1985. Water Quality for Agriculture. FAO of the United Nations, Rome, Italy

Bagarello, V., Caltabellotta, G., Concialdi, P., Iovino, M., 2023. Comparing two methods to perform a beerkan infiltration run in a loam soil at different dates. J. Hydrol. 617, 129095. https://doi.org/10.1016/j.jhydrol.2023.129095

Bagarello, V., Castellini, M., Di Prima, S., Iovino, M., 2014. Soil hydraulic properties determined by infiltration experiments and different heights of water pouring. Geoderma 213, 492-501. https://doi.org/10.1016/j.geoderma.2013.08.032

Baiamonte, G., 2016. Simple Relationships for the Optimal Design of Paired Drip Laterals on Uniform Slopes. J. Irrig. Drain. E-ASCE, 142(2), 04015054. Doi: 10.1061/(ASCE)IR.1943-4774.0000971

Baiamonte, G., Agnese, C., Singh, V.P., 2023. Multiple Non-linear Reservoirs to Model Water Balance Components in Sandy Soils. In: Sherif, M., Singh, V.P., Sefelnasr, A., Abrar, M. (eds) Water Resources Management and Sustainability. Water Science and Technology Library, vol 121. Springer, Cham. https://doi.org/10.1007/978-3-031-24506-0_3

Barragan, J., Cots, Ll., Monserrat, J., Lopez, R., Wu, I.P., 2010. Water distribution uniformity and scheduling in micro-irrigation systems for water saving and environmental protection. Biosyst. Eng. 107(3), 202–211. https://doi.org/10.1016/j.biosystemseng.2010.07.009

Broadbridge, P., Daly, E., Goard, J., 2017. Exact solutions of the Richards equation with nonlinear plant-root extraction. Water Resour. Res. 53(11), 9679–9691. https://doi.org/10.1002/2017WR021097

Cook, F.J., Thorburn, P.J., Fitch, P., Bristow, K.L., 2003. WetUp: A software tool to display approximate wetting patterns from drippers. Irrig. Sci. 22, 129-134. https://doi.org/10.1007/s00271-003-0078-2

Das Gupta, S., Mohanty, B.P., Köhne, J.M., 2006. Soil Hydraulic Conductivities and their Spatial and Temporal Variations in a Vertisol. Soil Sci. Soc. Am. J. 70(6), 1872-1881. https://doi.org/10.2136/sssaj2006.0201

Di Prima, S., Stewart, R. D., Castellini, M., Bagarello, V., Abou Najm, M. R., Pirastru, M., Giadrossich, F., Iovino, M., Angulo-Jaramillo, R., Lassabatere, L., 2020. Estimating the macroscopic capillary length from Beerkan infiltration experiments and its impact on saturated soil hydraulic conductivity predictions. J. Hydrol. 589, 125159. https://doi.org/10.1016/j.jhydrol.2020.125159

Elrick, D.E., Reynolds, W.D., 1992. Methods for Analyzing Constant-Head Well Permeameter Data. Soil Sci. Soc. Am. J. 56(1), 320-323. https://doi.org/10.2136/sssaj1992.03615995005600010052x

Fernández-Gálvez, J., Simmonds, L. P. 2006. Monitoring and modelling the three-dimensional flow of water under drip irrigation. Agric. Water Manag., 83(3), 197–208. https://doi.org/10.1016/j.agwat.2005.11.008

Gardner, W.R., 1958. Some steady-state solutions of the unsaturated moisture flow equation with application to evaporation from a water table. Soil Sci. 85(4), 228-232. https://doi.org/10.1097/00010694-195804000-00006

Glantz, S.A., 2012. Primer of biostatistics. McGraw-Hill, New York

Goyal, M.R. 2014. Sustainable micro irrigation: Principles and practices. New York. https://doi.org/10.1201/b17155

Haverkamp, R., Ross, P.J., Smettem, K.R.J., Parlange, J.Y., 1994. Three-dimensional analysis of infiltration from the disc infiltrometer: 2. Physically based infiltration equation. Water Resour. Res. 30(11), 2931-2935. https://doi.org/10.1029/94WR01788

Horton, R.E., 1941. An Approach Toward a Physical Interpretation of Infiltration-Capacity. Soil Sci. Soc. Am. J. 5, 399-417. https://doi.org/10.2136/sssaj1941.036159950005000c0075x

Kandelous, M.M., Šimůnek, J., 2010a. Comparison of numerical, analytical, and empirical models to estimate wetting patterns for surface and subsurface drip irrigation. Irrig. Sci. 28(5), 435–444. https://doi.org/10.1007/s00271-009-0205-9

Kandelous, M.M., Šimůnek, J., 2010b. Numerical simulations of water movement in a subsurface drip irrigation system under field and laboratory conditions using HYDRUS-2D. Agric. Water Manag. 97(7), 1070–1076. https://doi.org/10.1016/j.agwat.2010.02.012

Keller, J., Bliesner, R.D. 1990. Sprinkle and Trickle Irrigation. The Blackburn Press, New York, pp. 652.

Lafolie, F., Guennelon, R., van Genuchten, M.Th., 1989. Analysis of Water Flow under Trickle Irrigation: I. Theory and Numerical Solution. Soil Sci. Soc. Am. J. 53(5), 1310–1318. https://doi.org/10.2136/sssaj1989.03615995005300050002x

Lassabatère, L., Angulo-Jaramillo, R., Soria Ugalde, J.M., Cuenca, R., Braud, I., Haverkamp, R., 2006. Beerkan Estimation of Soil Transfer Parameters through Infiltration Experiments-BEST. Soil Sci. Soc. Am. J., 70(2), 521-532. https://doi.org/10.2136/sssaj2005.0026

Lilliefors, H.W., 1967. On the Kolmogorov-Smirnov Test for Normality with Mean and Variance Unknown. J. Am. Stat. Assoc. 62(318), 399-402. https://doi.org/10.1080/01621459.1967.10482916

Lubana, P. P. S., Narda, N.K., 2001. SW-Soil and Water: Modelling Soil Water Dynamics under Trickle Emitters - a Review. J. Agric. Eng. Res. 78(3), 217-232. https://doi.org/10.1006/jaer.2000.0650

Lubana, P.P.S., Narda, N.K., Brown, L.C., 2004. Application of a hemispherical model to predict radius of wetted soil volume under point source emitters for trickle irrigated tomatoes in Punjab state, India. ASAE Annual Meeting, 042243. https://doi.org/10.13031/2013.16434

Mubarak, I., Mailhol, J.C., Angulo-Jaramillo, R., Bouarfa, S., Ruelle, P., 2009. Effect of temporal variability in soil hydraulic properties on simulated water transfer under high-frequency drip irrigation. Agric. Water Manag. 96(11), 1547–1559. https://doi.org/10.1016/j.agwat.2009.06.011

Nakayama, F.S., Bucks., D.A. 1986. Trickle Irrigation for Crop Production. Design, Operation and Management, Elsevier, Amsterdam

Pachepsky, Y., Karahan, G., 2022. On shapes of cumulative infiltration curves. Geoderma 412, 115715. https://doi.org/10.1016/j.geoderma.2022.115715

Philip, J.R., 1984. Travel times from buried and surface infiltration point sources. Water Resour. Res. 20(7), 990–994. https://doi.org/10.1029/WR020i007p00990

Provenzano, G., Alagna, V., Autovino, D., Juarez, J. M., Rallo, G. 2016. Analysis of Geometrical Relationships and Friction Losses in Small-Diameter Lay-Flat Polyethylene Pipes. J. Irrig. Drain. E-ASCE, 142(2), 04015041. https://doi.org/10.1061/(ASCE)IR.1943-4774.0000958

Regalado, C.M., Muñoz-Carpena, R., 2004. Estimating the saturated hydraulic conductivity in a spatially variable soil with different permeameters: A stochastic Kozeny-Carman relation. Soil Tillage Res. 77(2), 189-202. https://doi.org/10.1016/j.still.2003.12.008

Revol, P., Clothier, B. E., Mailhol, J.-C., Vachaud, G., Vauclin, M., 1997. Infiltration from a surface point source and drip irrigation: 2. An approximate time-dependent solution for wet-front position. Water Resour. Res. 33(8), 1869–1874. https://doi.org/10.1029/97WR01007

Reynolds, W.D., Bowman, B.T., Drury, C.F., Tan, C.S., Lu, X., 2002. Indicators of good soil physical quality: Density and storage parameters. Geoderma 110(1-2), 131-146. https://doi.org/10.1016/S0016-7061(02)00228-8

Reynolds, W.D., Elrick, D.E., 1991. Determination of Hydraulic Conductivity Using a Tension Infiltrometer. Soil Sci. Soc. Am. J. 55(3), 633-639. https://doi.org/10.2136/sssaj1991.03615995005500030001x

Richards, L.A., 1931. Capillary conduction of liquids through porous mediums. Physics, 1(5), 318–333. https://doi.org/10.1063/1.1745010

Singh, D.K., Rajput, T.B. S., Singh, D.K., Sikarwar, H.S., Sahoo, R.N., Ahmad, T., 2006. Simulation of soil wetting pattern with subsurface drip irrigation from line source. Agric. Water Manag. 83(1–2), 130-134. https://doi.org/10.1016/j.agwat.2005.11.002

Stewart, R.D., Rupp, D.E., Najm, M.R.A., Selker, J.S., 2013. Modeling effect of initial soil moisture on sorptivity and infiltration. Water Resour. Res. 49(10), 7037-7047. https://doi.org/10.1002/wrcr.20508

Subbaiah, R. (2013). A review of models for predicting soil water dynamics during trickle irrigation. Irrig. Sci. 31(3), 225–258. https://doi.org/10.1007/s00271-011-0309-x

Thorburn, P.J., Cook, F.J., Bristow, K.L., 2003. Soil-dependent wetting from trickle emitters: Implications for system design and management. Irrig. Sci., 22, 121-127. https://doi.org/10.1007/s00271-003-0077-3

Warrick, A.W., 1998. Spatial variability, in: Environmental Soil Physics Appendix 1. D. Hillel, California, pp. 665–675

White, I., Sully, M.J. 1987. Macroscopic and microscopic capillary length and time scales from field infiltration. Water Resour. Res., 23(8), 1514-1522. https://doi.org/10.1029/WR023i008p01514

Youngs, E.G., Elrick, D.E., Reynolds, W.D., 1993. Comparison of steady flows from infiltration rings in “Green and Ampt” and “Gardner” soils. Water Resour. Res. 29(6), 1647-1650. https://doi.org/10.1029/93WR00006

CHAPTER 4

Exploring the Impact of Average Water Content on Wetting Bulb Expansion from a Buried Point Source

Based on the **published** paper:

Baiamonte, G., Franco, L., Vaccaro, G., **2025**. Exploring the impact of average water content on wetting bulb expansion from a buried point source. *Agric. Water Manag.* 321, 109889.
https://doi.org/10.1016/j.agwat.2025.109889

CHAPTER 4: Exploring the Impact of Average Water Content on Wetting Bulb Expansion from a Buried Point Source

Giorgio Baiamonte[1*], Loris Franco[2], Girolamo Vaccaro[1]

[1]Dept. of Agricultural, Food and Forest Sciences (SAAF), Univ. of Palermo, viale delle Scienze, Bldg. 4, 90128 Palermo, Italy. *Corresponding Author, E-mail: giorgio.baiamonte@unipa.it

[2]IRRITEC S.p.A. via Gambitta Conforto, 98071 Capo d'Orlando, Messina, Italy

Abstract

Subsurface drip irrigation (SDI) represents a significant innovation in water-saving irrigation methods. However, accurately predicting the shape and expansion of the wetting bulb remains a challenge due to the complex interaction between soil hydraulic properties and emitter characteristics. This study investigates the influence of the average volumetric water content, θ_{avg}, in determining the wetting bulb expansion from a buried point source. The analysis is based on six years (2018−2023) of experimental data collected in a citrus orchard in Sicily, Italy, equipped with an SDI system and a soil moisture probe. The simplified analytical model proposed by Philip (1984) was applied, with calibration of θ_{avg} using a k parameter, which provides θ_{avg} varying between the initial (θ_0) and the saturated (θ_s) volumetric soil water content. After characterising the soil hydraulic properties required by Philip's model, results from 832 travel time (t_t) and θ_0 measurements showed that the simplified assumption of k equal to 0.5 often leads to significant overestimations of travel times. In contrast, calibrating the model substantially improved the accuracy of t_t estimation, reducing the standard error of the estimate from 4 hours to 26 minutes, which is moderate considering the temporal resolution of data acquisition (20 min). These findings highlight the impact of the average volumetric water content for accurately predicting the shape of the wetting bulb using Philip's model, while also accounting for uncertainties associated with the simplified assumptions of the original model.

Keywords: Philip's model, Irrigation modelling, Travel time estimation, Soil moisture dynamics, Subsurface drip irrigation

List of symbols

A	Constant of Haverkamp's model (mm^{-1})	t_i	Irrigation time (h)
b_s	Intercept of the straight line fitted to the data describing steady-state conditions on the I vs. t plot (mm)	t_t	Wetting front dimensional travel time (h)
C	Constant of Haverkamp's model (-)	w_0	Initial gravimetric soil water content ($g\ g^{-1}$)
d	Number of days after t_t measurement (-)	z	Dimensional vertical distance (cm)
h	Soil water pressure head (m)	Z	Dimensionless vertical distance (-)
I	Cumulative infiltration of the water in the soil (mm)	z_s	Depth of the Drill & Drop sensors (cm)
i_s	The slope of the straight line fitted to the data describing steady-state conditions on the I vs. t plot ($mm\ h^{-1}$)	Z_s	Dimensionless depth of the Drill & Drop sensors (-)
k	Parameter to estimate θ_{avg} (-)	α	Parameter of the Gardner's hydraulic conductivity function (m^{-1})
K	Soil hydraulic conductivity ($mm\ h^{-1}$)	β	Shape constant of Haverkamp's model (-)
K_0	Initial soil hydraulic conductivity ($mm\ h^{-1}$)	$\Delta\theta$	Difference between θ_{avg} and θ_0 ($cm^3\ cm^{-3}$)
K_s	Saturated soil hydraulic conductivity ($mm\ h^{-1}$)	$\Delta\theta_s$	Difference between θ_s and θ_0 ($cm^3\ cm^{-3}$)
m	Scale parameter of the power law to estimate k (-)	γ	Correction constant of Haverkamp's model (-)
n	Shape parameter of the power law to estimate k (-)	θ	Volumetric water content ($cm^3\ cm^{-3}$)
q_n	Source strength, i.e. emitter flow rate ($L\ h^{-1}$)	θ_0	Initial volumetric water content before wetting ($cm^3\ cm^{-3}$)
r	Dimensional radius distance (cm)	$\theta_0\|_{d=0}$	ISMC at the start of the first irrigation (-)
R	Dimensionless radial distance (-)	θ_{avg}	Average volumetric soil water content behind the wetting front ($cm^3\ cm^{-3}$)
r_s	Radius of the infiltration surface (mm)	θ_s	Saturated volumetric soil water content ($cm^3\ cm^{-3}$)
s	Dimensional horizontal distance (cm)	λ_c	Macroscopic capillary length (mm)
S	Dimensionless horizontal distance	ρ_b	Dry soil bulk density ($g\ cm^{-3}$)
S_e	Emitter spacing (m)	ϕ	Angle from the polar direction (rad
T	Dimensionless travel time of marked particles (-)	Φ_m	Matrix flux potential ($mm^2\ h^{-1}$)
t	Time (h)	ϕ_s	Soil porosity ($cm^3\ cm^{-3}$)

1. Introduction

Efficient water management is essential for irrigated agriculture, particularly in light of climate change and increasing water scarcity in arid and semi-arid regions (Galindo et al., 2018).

Among irrigation methods, drip irrigation is widely recognised as one of the most water-efficient and precise, as it significantly reduces losses from evaporation, surface runoff, and deep percolation (Ravikumar, 2023; Singh and Su, 2022). Subsurface drip irrigation, SDI, advances this technology by employing buried emitters to further minimise surface evaporation and limit weed growth (Cahn and Hutmacher, 2024; Camp, 1998). When properly managed, SDI systems ensure uniform wetting of the root zone, enhancing water use efficiency, with significant implications for agricultural sustainability and the conservation of water resources (Arbat et al., 2013; Bogle et al., 1989; Kisi et al., 2021).

However, SDI systems can be affected by emitter clogging, primarily due to root intrusion and the suction of soil particles, which can significantly compromise irrigation uniformity (Lamm et al., 2021; Shi et al., 2022). Additionally, the development of a positive pressure occurring around the buried emitter, also denoted as back pressure head (Gil et al., 2008; Nogueira et al., 2021; Philip, 1992; Shani et al., 1996; Wang et al., 2024), may limit the emitter flow rate. To mitigate the effect of root intrusion, emitters that contain root-growth inhibitors can be applied, enhancing system performance over time (Baiamonte et al., 2024b).

To effectively wet the root zone using SDI systems, a comprehensive understanding of the water movement within the soil volume surrounding the emitter is essential. This knowledge is a prerequisite for the optimal design of irrigation systems and the efficient management of water applications (Cook et al., 2003b; Khan et al., 1996; Thorburn et al., 2003; Zur, 1996). Indeed, to minimise water losses, the design and management of the SDI system must ensure that the wetted bulb matches the depth of the root zone and that its width aligns with the spacing between emitters and laterals (Zur, 1996).

Water emitted from a buried point source moves vertically and laterally through the soil, wetting a volume that can often be approximated by the shape of a truncated ellipsoid (Zur, 1996). The shape and extent of the wetting pattern around a buried emitter depend on several factors, including emitter flow rate, total volume of the applied water, initial soil water content, θ_0, soil properties and travel time from infiltration point sources (Philip, 1984, 1968; Revol et al., 1997). The latter denotes the time required for water particles to move from the infiltration point to a given location, usually matching the root depth (Philip, 1984). Quantifying the travel time and estimating both the vertical and horizontal expansion of the wetted bulb make it possible to determine the irrigation scheduling, emitter spacing, and burial depth in subsurface drip irrigation system design, ensuring efficient water use and optimal crop growth (Baiamonte, 2024; Baiamonte et al., 2024a). Several studies over the past decades have focused on assessing the dimensions of the wetting bulb in surface and subsurface drip irrigation systems supplied by point sources (Baiamonte, 2024; Singh et al., 2006). These efforts have led to various modelling approaches that simulate the spatial and temporal water distribution into the soil resulting from localised point sources, considering the flow conditions, soil heterogeneity, root uptake, and climatic interactions. These models can be categorised into empirical, numerical and analytical models.

Empirical models rely on observed field data and employ regression, dimensional analysis, or machine learning algorithms, such as artificial neural networks, to establish predictive relationships for wetting patterns (Elnesr and Alazba, 2017; Hinnell et al., 2010; Jamei et al., 2022). Despite being relatively easy to use and requiring limited input data, these models are often site-specific and may not generalise well across diverse soil types or irrigation scenarios (Subbaiah, 2013).

Numerical models solve the Richards equation (Richards, 1931) and are commonly implemented through simulation tools such as HYDRUS-2D/3D (Šimůnek et al., 2007). In contrast to empirical approaches, these models offer enhanced flexibility, enabling realistic representations of water flow under varying initial conditions and boundary scenarios. Provenzano (2007) evaluated the accuracy of HYDRUS-2D by comparing simulated and experimental matric potential data for an SDI system installed at a 10 cm depth in a sandy loam soil and reported a satisfactory agreement between model outputs and observed values. Nevertheless, their application necessitates detailed knowledge of soil hydraulic properties, technical expertise, and can be computationally intensive.

Analytical models follow a classical mathematical approach to solving differential equations, yielding exact solutions for well-defined problems. However, such solutions are typically confined to simplified transport systems and regular geometries of the transport domain. Analytical models often rely on strong assumptions, including steady-state conditions, soil homogeneity, and simplified hydraulic functions, such as the exponential hydraulic conductivity model (Gardner, 1958). Although these simplifications limit the applicability of analytical solutions for real field conditions, they offer valuable insights into fundamental processes, enable computationally efficient solutions, and reduce the number of involved variables. Calibrating analytical models helps overcome the previously mentioned assumptions, broadening their applicability (Baiamonte, 2019, 2020; Blöschl et al., 2013; Sivapalan, 2003).

Philip (1984) developed an analytical solution to estimate wetting front positions from surface and buried point sources. Specifically, Philip (1984) provided closed-form dimensionless solutions in spherical polar coordinates for the travel times of marked particles emitted under the assumption of homogeneous soil hydrologic properties. However, the model accuracy diminishes in cases involving heterogeneous soils, dynamic boundary conditions, or significant gravitational effects (Subbaiah, 2013). Moreover, in Philip's model, uncertainties arise when selecting the average volumetric water content behind the wetting front, θ_{avg}, which is required from the analytical procedure. Indeed, the definition of this parameter is little guided in the article and seems contradictory in the scientific literature.

Cook et al. (2003a) and Thorburn et al. (2003) assumed the water content at the wetting front as the θ_{avg} value when the soil hydraulic conductivity was equal to 1 mm d^{-1} and 1 mm h^{-1}, respectively. In addition, Cook et al. (2003a) calculated θ_{avg} at the burial plane, using the steady-state solution proposed by Raats (1971), which incorporates an exponential dependence of diffusivity on water content across a wide range of soils. Specifically, a comparison with a constant value of θ_{avg} was performed, generally resulting in θ_{avg} underestimation at small radii of the wetted bulb and θ_{avg} overestimation at large radii.

Differently, to evaluate the impact of soil hydraulic properties variability on the development of the wetting front, Baiamonte et al. (2024a) assumed the average volumetric water θ_{avg} = 0.5 (θ_s + θ_0), for a large soil data set of soil hydraulic parameters sampled in the studied site.

To bridge the above knowledge gap, in this work, the impact of average volumetric soil content on the expansion of the wetting bulb emitted from a buried point source was investigated by monitoring the volumetric soil water content, θ, and the travel time, t_t, over a long observation period. Specifically, the travel times of marked particles released from a buried emitter were determined using soil moisture probe data collected at different soil depths. The hydraulic characterisation of the soil, necessary to apply the Philip (1984) model, was first carried out. Subsequently, the Philip model was calibrated according to 832 θ_{avg}, θ_0, and t_t measurements. The intraseasonal variability of θ_{avg} was also analysed and interpreted.

2. Theoretical background

2.1. Philip model for buried point source

Assuming homogeneous soil hydraulic properties, Philip (1984) provided a closed-form solution for the dimensionless wetting front travel time, *T*, from a buried infiltration point source. In polar coordinates, for any dimensionless radial distance, *R*, the solution is written here in the domain ϕ = [0, π], because of the bulb symmetry (Fig. 1):

$$T(R,\phi) = \frac{e^{2R\sin^2\frac{\phi}{2}}}{2\cos^2\frac{\phi}{2}} \left\{ \begin{array}{l} R^2 - R + \left[ln\left(cos\frac{\phi}{2}\right) - R\,sin^2\frac{\phi}{2} + \frac{1}{2}\right]\ ln\frac{e^{2R\,sin^2\frac{\phi}{2}} - cos^2\frac{\phi}{2}}{sin^2\frac{\phi}{2}} + \\ -\frac{1}{2}\left[Li_2\left(1 - \left(sec^2\frac{\phi}{2}\right)e^{2R\,sin^2\frac{\phi}{2}}\right) - Li_2\left(1 - sec^2\frac{\phi}{2}\right)\right] \end{array} \right\} \tag{1}$$

where, according to Baiamonte (2024), the dilogarithm function *L*(.) used by Philip (1984) was expressed as special case of the polylogarithmic function for *n* = 2 (Kemp, 2006):

$$Li_n(1-x) = \sum_{k=1}^{\infty}\frac{(1-x)^k}{k^n} /;\ |1-x| < 1 \tag{2}$$

For any n, Eq. (2) was successfully applied to study meteorological drought and, particularly, to derive the mass probability function of dry spells (Baiamonte et al., 2019). Compared to $L(.)$, Eq. (2) offers practical advantages, as it is readily available in many commercial software packages; moreover, its differentiation was applied by Baiamonte (2024) to derive the maximum lateral bulb expansion.

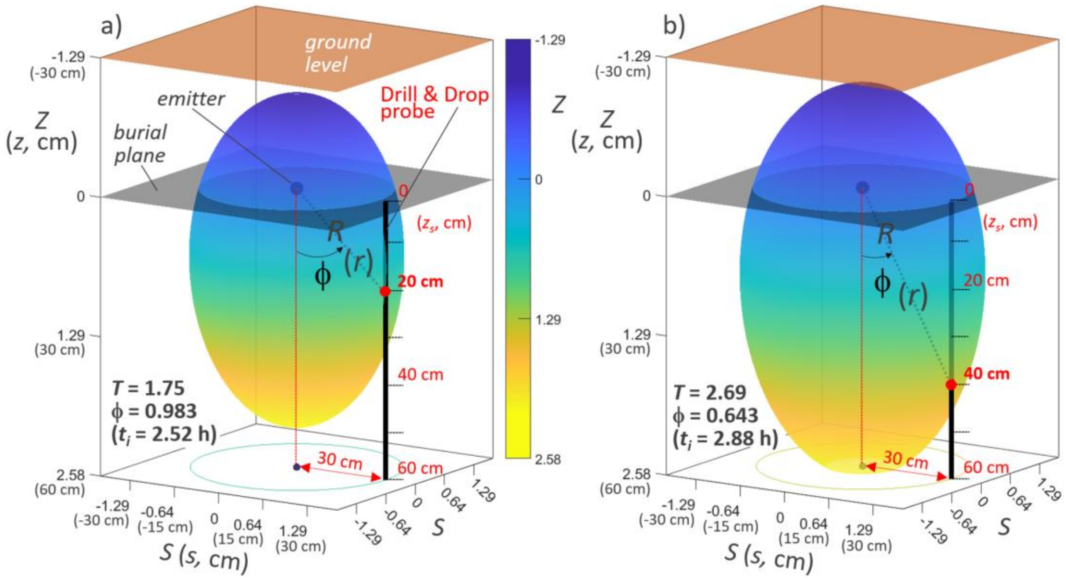

***Fig. 1** For **a)** T = 1.75 and **b)** T = 2.69, wetted bulbs derived by the Philip model (Eq. 1). The figures also indicate that according to the calibrated θ_{avg} (Eqs. 15 and 19, Table 3), the wetting front exactly matches the Drill & Drop sensors, at the depth z_s = 20 cm (ϕ = 0.983, Fig. 1a) and z_s = 40 cm (ϕ = 0.673, Fig. 1b)*

For example, Fig. 1a and b plot the wetted bulb in dimensionless units (R, S and Z) from a buried point source obtained by Eq. (1), for T = 1.75 and T = 2.69, respectively. Deriving the bulb shape in dimensional units requires considering the following relationships linking the dimensionless and dimensional sizes:

$$R = \frac{\alpha\, r}{2} \tag{3}$$

$$S = \frac{\alpha\, s}{2} \tag{4}$$

$$Z = \frac{\alpha\, z}{2} \tag{5}$$

where $S = R \sin \phi$ and $Z = R \cos \phi$ are the dimensionless horizontal and vertical sizes, respectively, r is the dimensional radial distance, s and z are the corresponding dimensional sizes, and α (m^{-1}) is the parameter of the exponential hydraulic conductivity function by Gardner (1958), $K(h)$:

$$K(h) = K_s\, exp(\alpha\, h) \tag{6}$$

where K_s (mm h^{-1}) is the saturated soil hydraulic conductivity, and h (m) is the soil water pressure head. Assuming α = 8.6 m^{-1}, Fig. 1a and b also display, in round brackets, the corresponding dimensional sizes, r, s and z in cm.

The dimensional wetting front travel time, t_t (h), corresponding to T, can also be derived by Philip (1984), who first introduced it in his foundational work (Philip, 1969):

$$T = \frac{\alpha^3 q_n\, t_t}{16 \cdot 10^3\, \pi\, \Delta\theta} \tag{7}$$

where q_n (L h^{-1}) is the source strength, i.e. the emitter flow rate, and Δθ (cm^3 cm^{-3}) is equal to:

$$\Delta\theta = \theta_{avg} - \theta_0 \tag{8}$$

where θ_0 (cm^3 cm^{-3}) is the initial soil moisture content (ISMC) before wetting, and θ_{avg} (cm^3 cm^{-3}) is the average volumetric water content in the soil behind the wetting front.

It is important to note that the term t_t (h) appearing in Eq. (7), when experimentally measured, differs from the irrigation time, t_i (h), which is of interest in practice. Indeed, Philip's model does not account for soil water redistribution, which influences the wetting pattern during and after the irrigation event.

Applying Philip's model requires knowledge of soil hydraulic characterisation, which is addressed in the following section.

2.2. Soil hydraulic characterisation

Soil hydraulic properties can be determined using the Beerkan method, which involves a single infiltration experiment at a null pressure head. This method applies a fixed and small volume of water to the soil surface, and the infiltration time for each application is recorded, thereby generating a cumulative infiltration curve, *I* (mm), versus time, *t* (h), curve (Lassabatère et al., 2006). The saturated hydraulic conductivity, K_s (mm h^{-1}), can be determined by applying the BEST-steady algorithm, and using the intercept, b_s (mm), and slope, i_s (mm h^{-1}), of the steady-state portion of the cumulative infiltration curve (Bagarello et al., 2014):

$$K_s = \frac{C\, i_s}{A\, b_s + C} \tag{9}$$

where *A* (mm^{-1}) and *C* are numerical constants that can be expressed as (Haverkamp et al., 1994; Lassabatère et al., 2006):

$$A = \frac{\gamma}{r_s\, \Delta\theta_s} \tag{10}$$

$$C \approx \frac{1}{2(1-\beta)} \ln\left(\frac{1}{\beta}\right) \tag{11}$$

where $\Delta\theta_s$ (cm^3 cm^{-3}) is the difference between the saturated volumetric water content, θ_s (cm^3 cm^{-3}), and θ_0 (cm^3 cm^{-3}), r_s (mm) is the radius of the infiltration surface, while γ and β are coefficients equal to 0.75 and 0.6, respectively (Haverkamp et al., 1994; Smetten et al., 1994). Note that Eqs. (10 and 11) can be applied for ISMC $\theta_0 < 0.25\ \theta_s$.

The α parameter that needs for the application of Eq. (7), can be estimated as the inverse of the macroscopic capillarity length, λ_c (m) (Gardner, 1958; White and Sully, 1987):

$$\alpha = \lambda_c^{-1} = \frac{10^3\, (K_s - K_0)}{\Phi_m} \tag{12}$$

where Φ_m is the matric flux potential (mm^2 h^{-1}) and K_0 (mm h^{-1}) is the initial soil hydraulic conductivity, and α in (m^{-1}).

According to Di Prima et al. (2020), the macroscopic capillary length, λ_c, indicating the relative weight of capillarity compared to gravity forces in the movement of water through unsaturated soil, can be derived from a steady-state beerkan infiltration run using the following relationship:

$$\lambda_c = 0.861 \frac{b_s}{\Delta\theta_s} \tag{13}$$

3. Material and methods

3.1 Experimental setup

The experiment was conducted over 6 years, from 2018 to 2023, in a 30-year-old citrus orchard (*Citrus reticulata* Blanco cv. Tardivo di Ciaculli grafted onto *Citrange* "Carrizo"), spaced 5 × 5 m, located near Palermo, Italy (38°4′53.4″ N, 13°25′8.2″ E). The soil is a typic Rhodoxeralf, which remained untilled, with mechanical weed cutting performed only after harvest and during the summer.

According to the United States Department of Agriculture (USDA) classification system, the soil can be classified as sandy-clay-loam or sandy loam to a depth of 0.4 m, with a moderate gravel content on the surface (Baiamonte et al., 2024b).

The experimental field site is characterised by a flat topography at an altitude of 35 m a.s.l. and is divided into four plots (Fig. 2), designated as Subunit #1 through #4, each approximately 1000 m^2 and hosting between 36 and 40 trees.

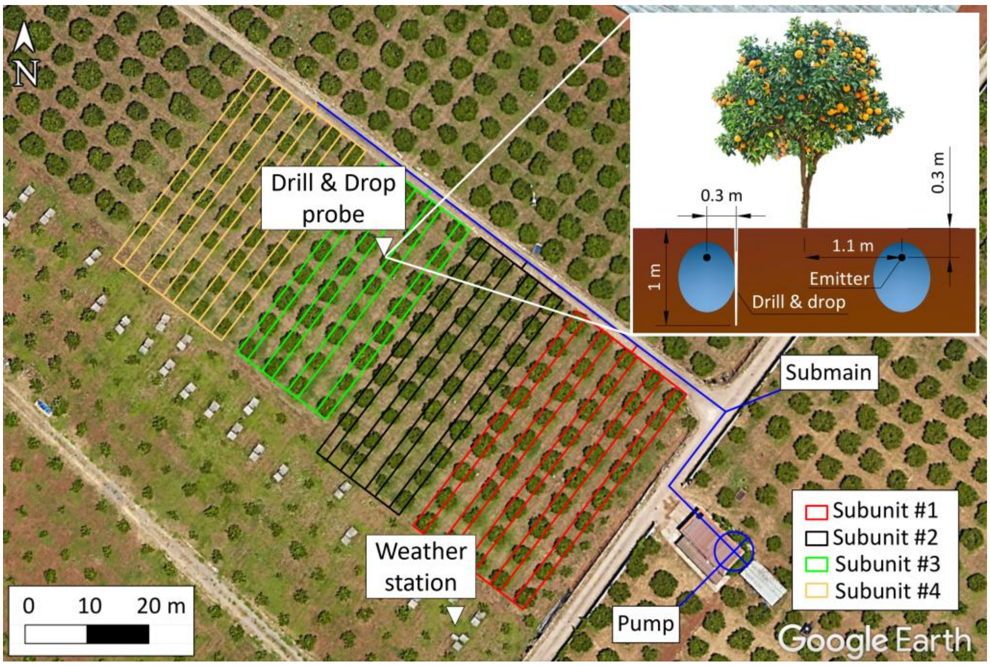

***Fig. 2** Experimental layout of the investigated Subunit #3, where the Drill & Drop probe is located*

All plots have been irrigated using a subsurface drip irrigation, SDI, system installed in 2017 and operational in 2018; however, only Subunit #3 is of interest for this study. As illustrated in Fig. 2, in each plot, the SDI system is equipped with two drip laterals per plant row, installed at a depth of 0.30 m and positioned 1.1 m from the tree trunk. The laterals were equipped with self-compensating Multibar^{TM} C emitters, incorporating an anti-siphon mechanism to prevent soil ingestion, and embedded root-growth inhibitors. The emitters were spaced at S_e = 0.5 m, with a nominal emitter flow rate q_n = 2.1 L h^{-1} and a pressure-compensating range of 50−300 kPa.

For each subunit, Table 1 reports the main characteristics of the SDI system and the range of variability of the emitter flow rate, q_n, which depends on the root guard treatment. Moreover, in the upstream mid-manifold of each plot, an electric control valve, a 100 µm disc filter, and a volumetric water meter (resolution 0.1 L) were installed to monitor irrigation volumes.

Irrigation scheduling was remotely managed using a programmer (Commander Evo, Irritec®) to maintain well-watered soil water content conditions and prevent crop water stress (Vaccaro et al., 2025), ensuring precise control of the SDI system.

***Table 1** Characteristics of experimental subunits*

Subunit	q_n (L/h) min - max	CV (%)	L_L (m)	S_e (m)	L_M (m)	S_{rows} (m)	N	N_{rows}
#1	1.87−2.28	7.6	43.0	0.5	25	2 – 3 m alternating (Fig. 2)	860	10
#2	1.97−2.13	3.4	42.5		20		680	8
#3	2.28−2.41	2.6	38.0		20		608	8
#4	2.25−2.40	4.1	37.0		25		740	10

As shown in Fig. 2, in Subunit #3, a 100 cm long “Drill & Drop” probe (Sentek Pty Ltd., Stepney, Australia) was installed beneath a representative tree, positioned 0.3 m from a single emitter and approximately 0.8 m from the tree trunk. According to Sentek’s recommendations, the default calibration coefficients, derived from a range of soil types, were applied. The specified precision of the moisture sensor is ±0.03% vol. The probe, based on frequency domain reflectometry (FDR) technology, measured both volumetric soil water content and temperature at 0.1 m intervals down to a depth of 1 m, for a total of 10 sensors, with data recorded every 20 minutes.

Installation took place in 2017 while trenches for the drip laterals were still open, ensuring accurate placement with respect to the emitters.

Once installed, the probe remained in place throughout the monitoring period, from 1st January 2018 to 11th November 2023. The probe placement was strategically chosen to capture the development of the wetting front during irrigation events, enabling effective monitoring of the wetted soil volume. Based on sensor readings, irrigation time, t_i, was standardised at 3.5 hours per event to confine water application within the active root zone. To determine the soil texture along the vertical soil profile, eight soil cores were collected from two locations adjacent to the soil moisture probe, at 0.1 m depth intervals down to a depth of 0.8 m, matching the sensor spacing of the Drill & Drop probe.

For each θ_0, the travel times, t_t, were estimated along the soil profile when the Drill & Drop probe indicated a 0.1% increase in volumetric water content, θ, and continued to rise during the irrigation application. Whereas the θ_0 values were assumed equal to the θ reading before the irrigation event starts. Of course, the measured t_ts may be far from the effective irrigation time, because of the water redistribution that the Philip model does not consider.

Meteorological data were collected using a WatchDog 2000 Series weather station (Spectrum Technologies, Inc., Aurora, IL, USA) installed in an adjacent area approximately 8.0 m from Subunit #1 (Fig. 2). The station recorded half-hourly data on precipitation, solar radiation, wind speed and direction (at 2 m height), air temperature, and relative humidity.

To estimate the α Gardner parameter, a total of 15 infiltration beerkan experiments (Lassabatère et al. 2006) were conducted at locations randomised in the area delimited by the planting pattern of four neighbouring plants close to the probe. Small rings with an inside diameter of 0.08 m and a height of 0.05 m were gently inserted into the soil to a depth of 0.01 m, and 20 successive water applications (57 mL each) were performed per beerkan run. The infiltration time for each water volume (from the 1st to the 20th) was recorded from the moment of application until the complete infiltration of water, immediately before the next dose.

Six undisturbed soil cores (0.05 m in height and 0.05 m in diameter) were collected from three sampling points at two depths (0−0.05 m and 0.05−0.10 m). These cores were used to determine the dry soil bulk density, ρ_b (g cm^{-3}), and the initial gravimetric soil water content, w_0 (g g^{-1}), from which the initial volumetric soil water content, θ_0 (cm cm^{-3}). The averages of ρ_b and θ_0 were then associated with beerkan runs and assumed to be representative of the site conditions.

3.2. The average wetting water content estimation

Selecting an appropriate average volumetric water content is essential for accurately applying Philip's (1984) model and obtaining realistic estimates of bulb expansion, a topic that has been discussed in the literature (Cook et al, 2003a; Thorburn et al., 2003). To evaluate the impact of soil hydraulic properties variability on the development of the wetting front, Baiamonte et al. (2024a) assumed the θ_{avg} as:

$$\theta_{avg} = 0.5\ (\theta_s+\theta_0) \tag{14}$$

In this work, to investigate the role of θ_{avg} on bulb expansion from a buried point source, in Eq. (14), 0.5 was replaced by the parameter k that needs to be calibrated according to experimental measurements:

$$\theta_{avg} = k\ (\theta_s+\theta_0) \tag{15}$$

Low values of the k parameter (< 0.5) indicate that the θ_{avg} is closer to θ_0, whereas high k values (> 0.5) suggest that θ_{avg} approaches the θ_s. Substituting Eq. (15) into Eq. (8) and rearranging provides:

$$\Delta\theta = k\ \theta_s - (1-k)\ \theta_0 \tag{16}$$

Limiting values of k, namely k_{min} and k_{max}, arise because i) $\Delta\theta$ must be positive, and ii) k cannot yield a θ_{avg} greater than θ_s, leading to, respectively:

$$k_{min} \geq \frac{\theta_0}{\theta_s+\theta_0} \tag{17}$$

$$k_{max} \leq \frac{\theta_s}{\theta_s+\theta_0} \tag{18}$$

Indeed, for $k = k_{min}$, Eq. (17) provides the limiting conditions, $\theta_{avg} = \theta_0$ and $\Delta\theta = 0$, while for $k = k_{max}$, from Eq. (18) $\theta_{avg} = \theta_s$ is obtained. Substituting Eq. (16) into Eq. (7) and solving with respect to k, yields:

$$k = \frac{16\pi\, T\, \theta_0 + \alpha^3 q_n t_t}{16\pi\, T\, \theta_0 + 16\pi\, T\, \theta_s} \tag{19}$$

Equation (19) states that the k parameter, which is linked to θ_{avg} (Eq. 15), can be easily determined for any assigned hydrological characteristics of the soil (α and θ_s) by applying the Philip model to calculate T (Eq. 1). Of course, the latter also requires performing experimental campaigns aimed at measuring the emitter flow rate, q_n, the travel time, t_t, and the ISMC, θ_0. In turn, once the k parameter has been analysed and interpreted, the travel time, t_t, can be estimated by inverting Eq. (19):

$$t_t = \frac{16\pi\, T\, (k\, \theta_s - (1-k)\, \theta_0)}{\alpha^3 q_n} \tag{20}$$

where k can be estimated by using power law relationships, as described later:

$$k = m\, d^n \tag{21}$$

where d (day) is the number of days after the first t_t measurement, and m (k value for d = 1 day) and n are parameters to be estimated according to the experimental measurements. Substituting Eq. (21) into Eq. (15), the average wetting water content θ_{avg} can be determined:

$$\theta_{avg} = m\, (\theta_s + \theta_0)\, d^n \tag{22}$$

Of course, the k parameter, estimated as above described, accounts for all the simplified assumptions that the Philip model requires, which are seldom satisfied in practice.

3.3. Philip model calibration

The knowledge of the hydrological characteristics α and θ_s, along with the availability of experimental data on emitter flow rate, q_n, travel time, t_t, and θ_0 measurements, enabled the application of Eq. (20) to determine k. Subsequently, the dimensionless time T of the Philip model (Eq. 1), was evaluated. Indeed, applying Eq. (20) requires the estimation of the dimensionless time T, which depends on the spherical polar coordinates R and ϕ, both of which must be determined based on the sensor position in the Drill & Drop probe with respect to the emitter. Table 2 reports R and ϕ values corresponding to each sampling depth, z_s, of the Drill & Drop sensors, measured with respect to the burial plane (Fig. 1). The corresponding T values calculated from Eq. (1) are also reported, along with the dimensional radial distance, r.

Table 2 *For all the sensors of the Drill & Drop probe, dimensional, z_s (cm), and dimensionless depths, Z_s, polar coordinates of the bulb, ϕ, R, and the corresponding dimensional radius, r (cm). The dimensionless travel time, T, according to the Philip model (Eq. 1) is also included*

z_s (cm)	Z_s	ϕ (rad)	r (cm)	R	T
−30	−1.29	2.3562	42.4	1.823	41.40
−20	−0.86	2.1588	36.1	1.552	13.17
−10	−0.43	1.8925	31.6	1.359	4.80
0	0.00	1.5708	30.0	1.290	2.36
10	0.43	1.2490	31.6	1.359	1.72
20	**0.86**	**0.9828**	**36.1**	**1.552**	**1.75**
30	1.29	0.7854	42.4	1.823	2.10
40	**1.72**	**0.6435**	**50.0**	**2.150**	**2.69**
50	2.15	0.5404	58.3	2.507	3.49
60	2.58	0.4636	67.1	2.885	4.48
70	3.01	0.4049	76.2	3.277	5.66

Note: Bold values refer to Figs. 1a and b

For fixed α, θ_s and q_n, along with the t_t and θ_0 observations, the k parameter was calculated from Eq. (20), making it possible to determine the average water content θ_{avg}. Subsequently, the Philip model was applied with the estimated θ_{avg} values, yielding travel times that match the experimental t_t measurements.

For the considered soil hydrological characteristics (α, θ_s), for z_s = 20 and 40 cm, Table 3 reports q_n, t_t, θ_0 measurements and the corresponding T values, 1.75 and 2.69, for which the wetting patterns in Fig. 1a and 1b were plotted. The same figures show that considering the k values calculated from Eq. (20), 0.372 and 0.45, i.e. $\Delta\theta = 0.0424$ and 0.0314 (Eq. 18), respectively, the Philip model provides T values that match the experimental ones. The latter can be observed in Fig. 1, where the wetted bulb achieves the Drill & Drop probe at the depths 20 cm ($\phi = 0.983$, Fig. 1a) and 40 cm ($\phi = 0.673$, Fig. 1b). Table 3 also reports the k_{min} and k_{max} values calculated from Eqs. (18 and 19).

Table 3 *For the considered soil hydrological characteristics (α and θ_s), and emitter flow rate, q_n (L/h), bulb sizes (S, s, Z, z) corresponding to Fig. 1a (z_s = 20 cm) and to Fig. 1b (z_s = 40 cm). The dimensionless (T) and dimensional (t_t) travel times obtained by the Philip model (Eq. 1), calibrated in line with the k values (Eq. 19), the corresponding average water content, θ_{avg} (Eq. 15), Δθ (Eq. 16), k_{min} (Eq. 17), and k_{max} (Eq. 18) are also reported*

Symbol	Values	
α (m^{-1})	8.6	
θ_s ($cm^3\ cm^{-3}$)	0.521	
ϕ	0.9828	0.6435
R (r, cm)	1.550 (36 cm)	2.150 (50 cm)
S (s, cm)	1.29 (30 cm)	1.29 (30 cm)
Z (z, cm)	0.86 (20 cm)	1.72 (40 cm)
q_n (L/h)	2.323	
t_t (h)	2.522	2.877
θ_0 ($cm^3\ cm^{-3}$)	0.241	0.370
k	0.372	0.450
k_{min}	0.316	0.415
k_{max}	0.684	0.585
θ_{avg}	0.284	0.401
$\Delta\theta$	0.0424	0.0314
T	1.75	2.69

For the depths z_s = 10, 20, 30, 40, 50, and 60 cm, the k parameter was computed for the entire dataset. Although sample sizes varied due to probe malfunctions, the #141 recorded irrigation events over six years yielded N = 114, 204, 192, 156, 113, and 53, respectively, with a total of 832 paired t_t and θ observations. Whereas, for depths z_s = −30, −20, −10, and 70 cm, no k estimation was performed, since no θ variations were observed for all irrigation events and seasons, which was reasonable. For each depth z_s, N was equal to 139, except for z_s = 60 cm, where N = 137.

4. Results and discussion

4.1. Soil characteristics

The average dry soil bulk density, ρ_b, and the average initial gravimetric soil water content, w_0, from the six soil cores were 1.269 g cm^{-3} and 0.094 g g^{-1}, respectively. The coefficient of variation, *CV*, calculated as the ratio between the standard deviation and the mean, was 4.0% for ρ_b and 11% for w_0. The mean initial volumetric soil water content, $\theta_0 = \rho_b\, w_0$, was then calculated as 0.119 cm^3 cm^{-3}. The saturated volumetric soil water content, θ_s (cm^3 cm^{-3}), was determined from soil porosity, ϕ_s (cm^3 cm^{-3}), which in turn was determined from the ρ_b measurements, assuming a soil particle density of 2.65 g cm^{-3}, resulting in 0.521 cm^3 cm^{-3} (Bagarello et al., 2011; Mubarak et al., 2010). The θ_0/θ_s ratio was 0.228, below the threshold of 0.25 cm^3 cm^{-3} for the BEST-steady procedure (Lassabatère et al. 2006).

Figure 3 shows that for the content in clay and sand measured as described in section 3.1, according to the USDA classification system, soil samples were classified as sandy loam at the depth with respect to the burial plane, z_s, from −30 cm to 30, with step 10 cm (Fig. 1a and b), and sandy clay loam for z_s = 30−50 cm, evidencing a nearly uniform texture along the soil profile.

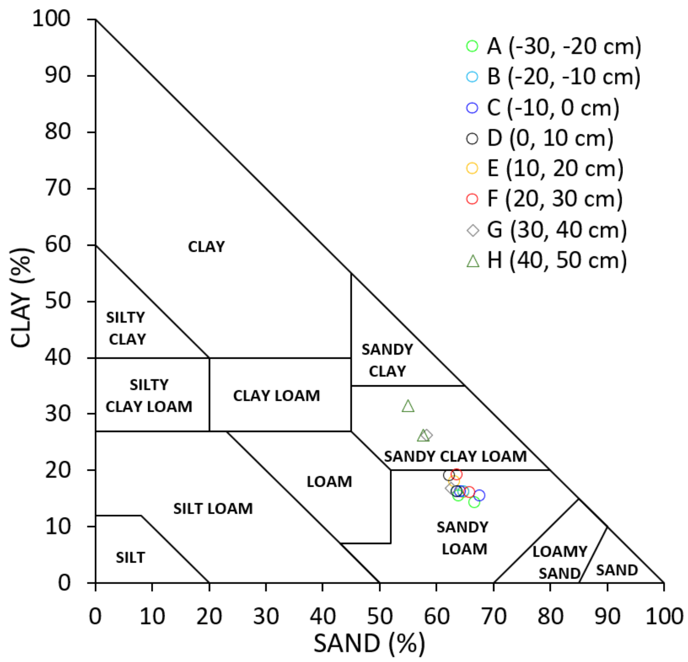

Fig. 3 *Content in clay and sand according to the USDA classification system, measured close to the Drill and Drop probe, for different soil depths*

Using Eq. (9), the saturated soil hydraulic conductivity, K_s (mm h^{-1}), was estimated for the 15 sample points. Therefore, by using Eq. (13) and Eq. (12), the λ_c and α parameters were estimated. Figure 4 shows the cumulative frequency empirical distribution of *ln* K_s (Fig. 4a) and α (Fig. 4b), respectively, together with the fitting of the normal distribution (N2). The α parameter measured in the upper layer was attributed to the entire soil profile, based on the nearly uniform soil texture throughout the profile, which aligns with the soil homogeneity assumption required by the Philip model. Of course, this requested assumption may overlook the potential decrease of α parameter with increasing soil depth.

The Lilliefors test statistic (kstat) was equal to 0.164, lower than the critical value of 0.219 at a significance level of 0.05. Therefore, there is sufficient evidence to accept the null hypothesis of normality (Lilliefors, 1967), thereby supporting the representativeness of the mean.

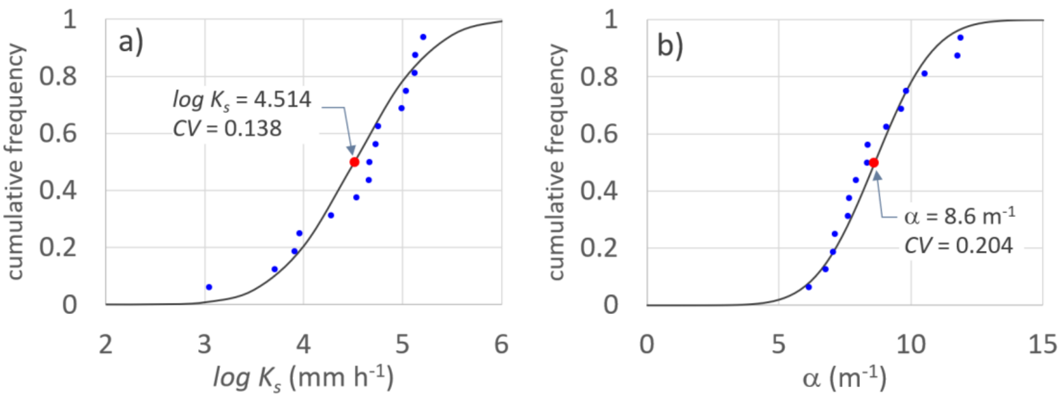

Fig. 4 *Cumulated frequency distribution of **a)** the log K_s parameter and **b)** the Gardner shape parameter, α. Solid lines refer to the fitted Normal Distribution (N2), and red dots indicate the mean values*

The *p*-value associated with the fitted normal distribution was equal to 0.330. Considering the N2 good fitting, the mean value of α = 8.6 m^{-1} was assumed to be representative of the soil profile to estimate the normalised time, T.

4.2. Average wetting water content as the mean between θ_0 and θ_s

When applying Eq. (7) to estimate the travel time, a major concern is that there is no rigorous methodology to determine the exact value of θ_{avg}, and some researchers have addressed this issue (Philip 1984; Cook et al., 2003a; Khan et al., 1996; Thorburn et al., 2003; Revol et al., 1997).

In the preliminary analysis, the θ_{avg} was assumed equal to the mean between θ_0 and θ_s (Baiamonte et al., 2024a), as reported in Eq. (14). The travel times calculated using Eq. (20) under this simplified assumption (k = 0.5) were then compared with the experimental t_t values.

For all six irrigation seasons, Fig. 5 depicts a comparison between the t_t values measured by the Drill & Drop probe with those derived by applying Eqs. (14 and 20), at a fixed depth, z_s. Figure 5 shows that t_t is generally highly overestimated, with a high standard error in the estimate, SEE = 4.17 h, evidencing that further inspection is needed. Moreover, t_t measurements exceeding the irrigation time (t_i = 3.5 h), observed at the deepest layers ($z_s \geq 50$ cm), indicate the delay caused by soil water redistribution, which is not considered in Philip's model.

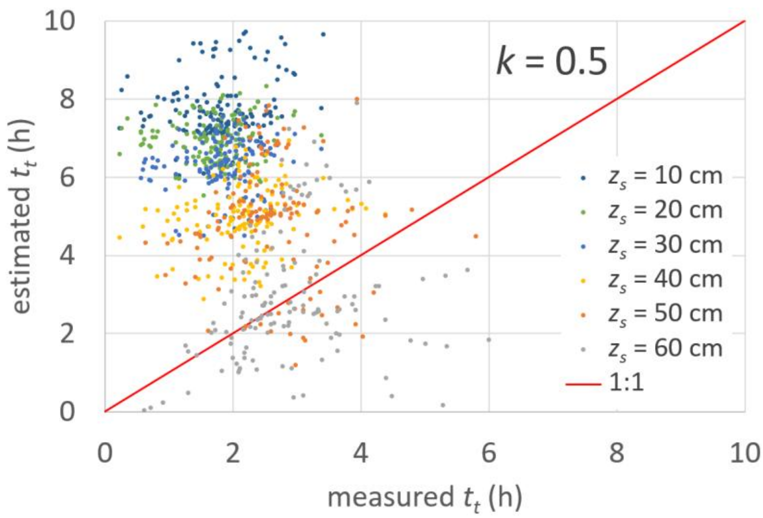

Fig. 5 *Comparison between the measured travel times,* t_t *(h), and those estimated from Eq. (20), with* $k = 0.5$

4.3. Variability in soil depth of the average wetting water content

In the six years of observation, the emitter flow rate of Subunit #3, which was treated with herbicide to prevent root intrusion phenomena (Baiamonte et al. 2024b), exhibited the lowest variability (2.6%, Table 1), denoting the effectiveness of herbicide treatments in root intrusion protection compared to the other Subunits. For a nearly constant emitter flow rate, depending on the ISMC, low variability of the average water content (i.e. of k) was expected for fixed depth, z_s.

Figure 6 plots the empirical distribution of k values for each z_s, evidencing the occurrence of a regular trend versus z_s. The latter could be ascribed to a bulb enrichment in water moving downward. Indeed, as previously observed, high *k* values correspond to high θ_{avg} values.

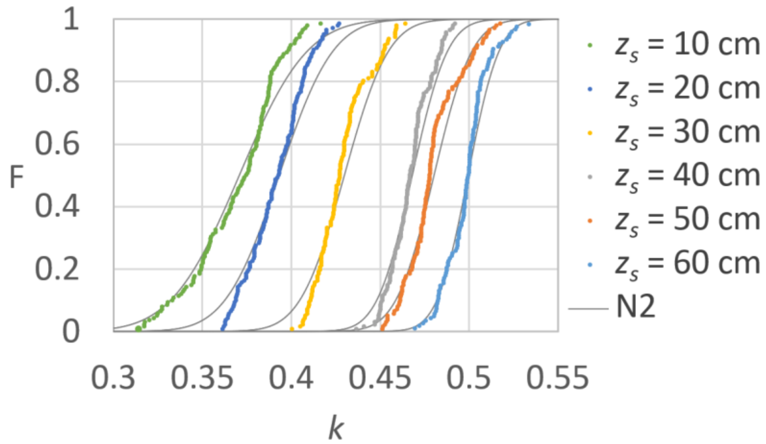

Fig. 6 *Cumulated frequency distribution of the calibrated k values, obtained from Eq. (19), for the six irrigation seasons (2018−2023) and depths of the Drill & Drop sensors, z_s. The solid line refers to the fitted Normal Distribution (N2)*

Moreover, in Fig. 6 can be observed that the assumption $k = 0.5$ considered in some cases (Baiamonte et al., 2024a) is seldom achieved in practice and only at high depths. Thus, in such cases, assuming $k = 0.5$ results in an overestimation of the travel time determining wastewater.

The mean of *k* values, $<k>$, and the coefficient of variation, *CV*, are plotted in Fig. 7a and 7b, showing that the two statistics are described by a linear and a power-law relationship, respectively. It's worth noting that at the deepest layers, the *CV* diminishes, likely due to flow accumulation phenomena, and reduced influence from evaporation compared to the upper layers.

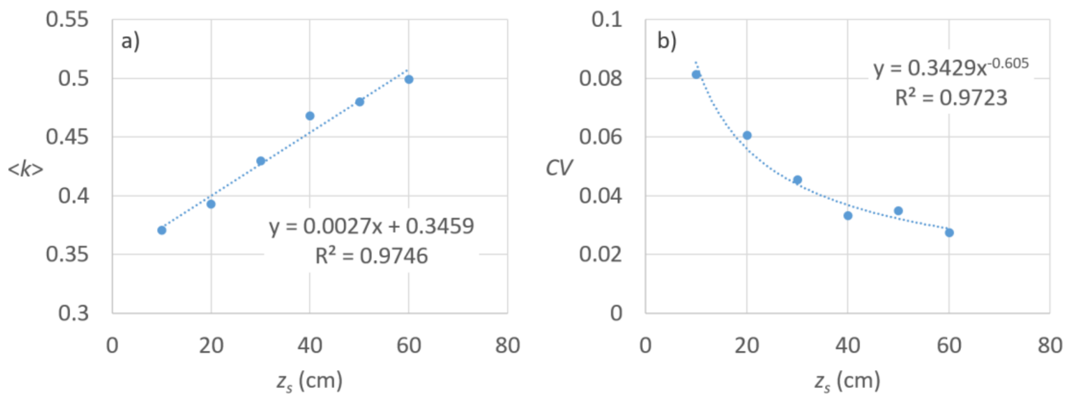

Fig. 7 a) *Mean k values, $<k>$ and **b)** coefficient of variation, CV, versus the depths of the Drill & Drop sensors, z_s. The fitted linear and power law relationships are also indicated*

Using <k> in place of the fixed $k = 0.5$ value reduces the standard error of the estimate from $SEE = 4.17$ h to $SEE = 1.44$ h. This improvement is also evident in Fig. 8, which compares the measured t_t values with those calculated from Eq. (20) with k = <k>, showing that the data points align more closely with the line of perfect agreement compared to when using $k = 0.5$.

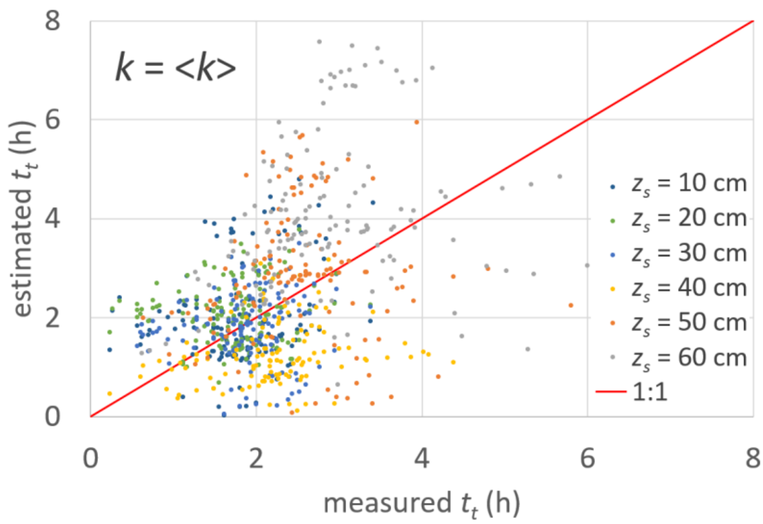

Fig. 8 *Comparison between the measured travel times, t_t (h), and those estimated from Eq. (20), by assuming the mean k values, <k>, derived from the linear relationship illustrated in Fig. 7a*

4.4. Intra-seasonal variability of the average wetting water content

The analysis described in the previous sections highlights that the average wetting water content can be influenced by other factors, also considering that the Lilliefors test statistic applied to the k mean values, <k>, revealed that the <k> distributions do not follow the normal distribution, evidencing the non-representativeness of the mean k values. Therefore, this section analyses the intra-seasonal variability of the average wetting water content, thereby investigating a potential soil moisture buffering effect.

For all irrigation seasons and depths, Fig. 9 depicts the calibrated k values along with the monthly rainfall and irrigation data (*Rain* and *Irr.*, mm, secondary axis), the daily maximum and minimum temperature T_{max} and T_{min} (°C, secondary axis), collected in the experimental field. The total number of θ measurements collected over the 6-year observation period is also reported. The θ values used to determine the mean

k are concentrated around irrigation events to capture the Drill & Drop probe response to the wetting.

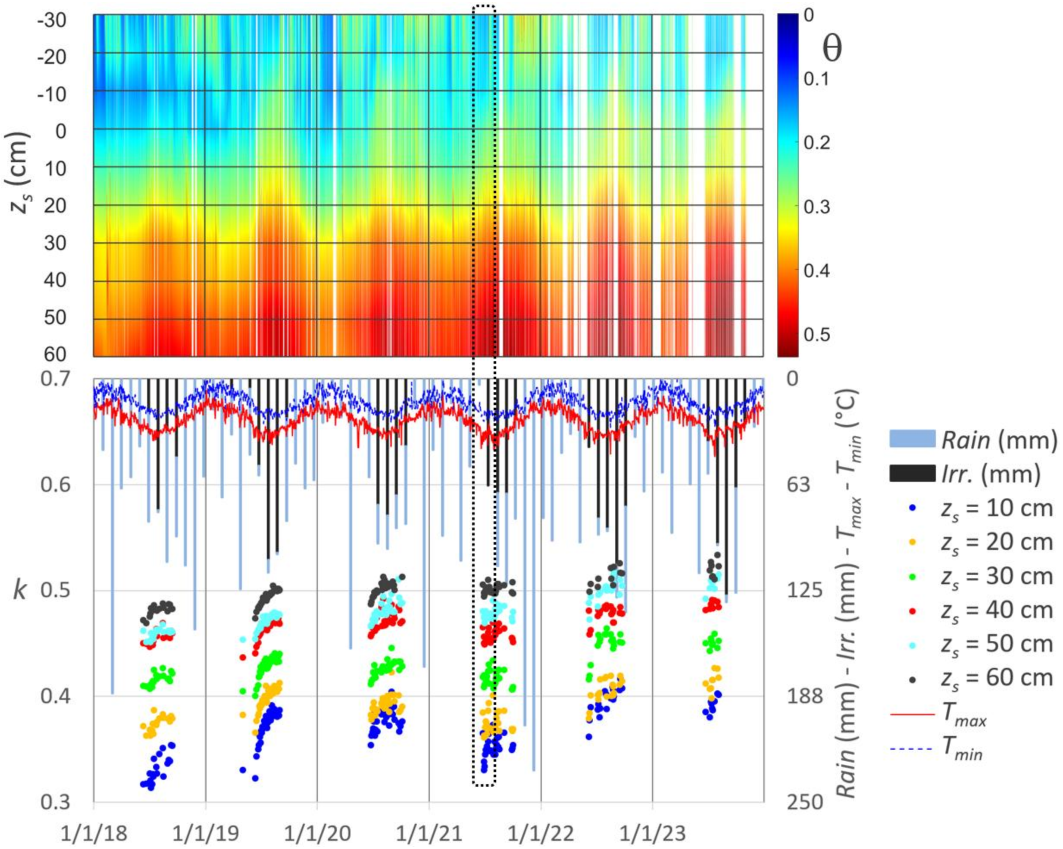

Fig. 9 *Volumetric water content measurements, θ (cm^3 cm^{-3}), monthly rainfall and irrigation data, Rain and Irr. (mm, secondary axis), maximum and minimum temperature T_{max} and T_{min} (°C, secondary axis), collected in the experimental field, during the observation period (2018−2023). The calibrated k values obtained by using Eq. (19) are also plotted (primary axis)*

Figure 9 clearly shows that in each irrigation season, k tends to increase, corroborating the presence of soil moisture memory, whereby water retained from previous irrigation events contributes to the formation of a progressively wetter bulb, corresponding to higher water contents, on average. The increase in θ can also be observed in the upper graph, by the trend during the six irrigation seasons, especially in the z_s = 0.3–0.4 cm range. Naturally, the k increase also depends on ISMC and the initial k condition at the beginning of the irrigation season. This k initial condition is reasonably influenced by the seasonal water retention effect, whereby water stored in deeper soil layers from substantial spring precipitation contributes to higher overall water content.

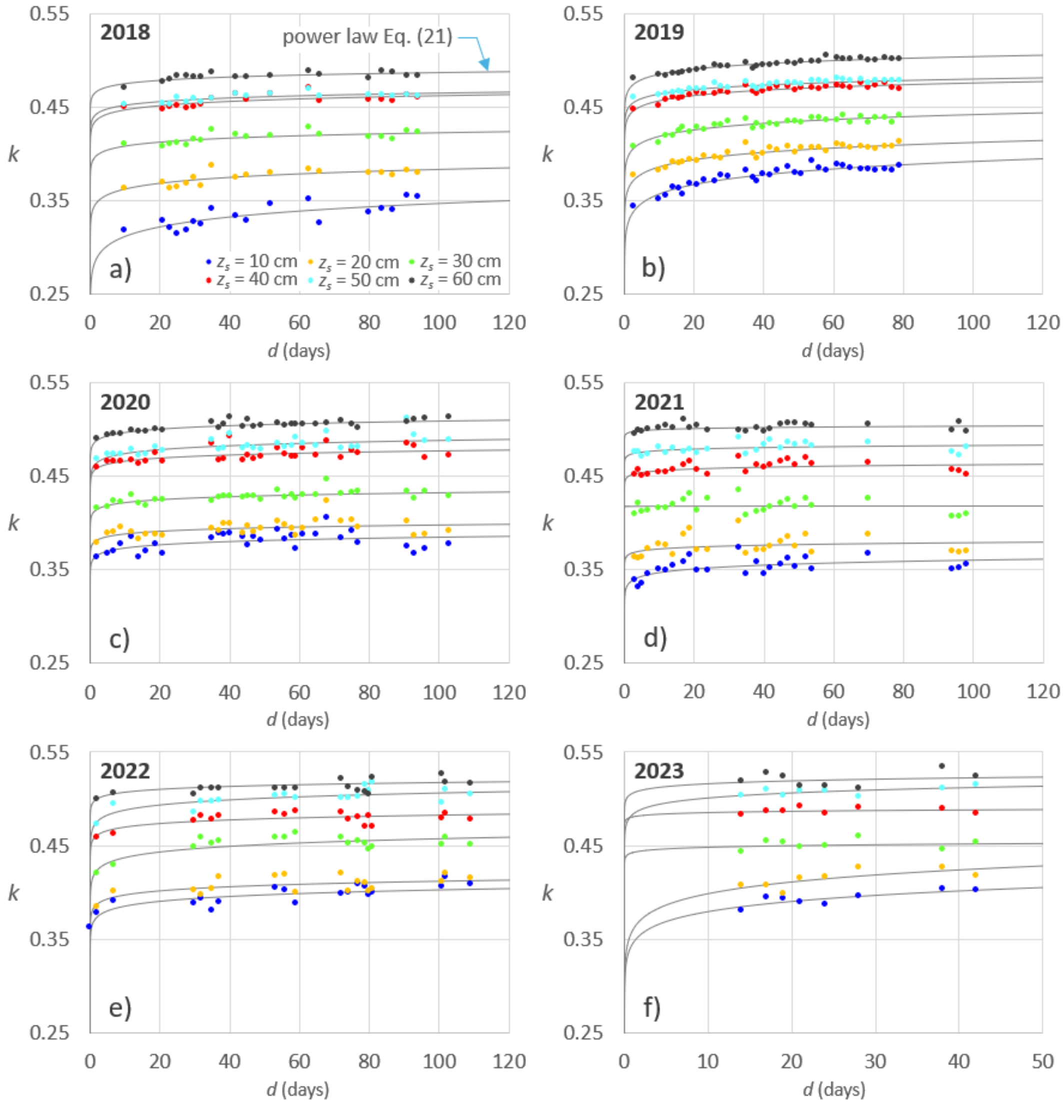

Fig. 10 *Temporal variation of the calibrated k values, calculated by using Eq. (19), for the six irrigation seasons* ***a)*** *2018,* ***b)*** *2019,* ***c)*** *2020,* ***d)*** *2021,* ***e)*** *2022, and* ***f)*** *2023. The fitted power law relationships (Eq. 21, solid lines), with the parameters m and n reported in Table 4, are also indicated.*

A drop in the antecedent k value, especially at the depth z_s = 10 cm, can be observed during the 2021 irrigation season. This decrease can reasonably be attributed to a prolonged dry spell before the beginning of the irrigation season, in conjunction with temperature peaks, as evidenced by the dashed rectangle. Considering the above, an analysis was conducted to investigate the k increasing trend vs the number of days after the first t_t measurement, d (day), for each irrigation season and depth. Fig. 10 illustrates the calibrated k values against d, by varying the sensor depth, z_s, in each irrigation season.

Figures 10a-f clearly show the increasing k trend vs d and depict the fitted power law relationship described by Eq. (21). The corresponding m and n parameters are reported in Table 4, together with the correlation coefficient, R, ranging from R = 0.940 (2019, z_s = 60 cm) to R = 0.013 (2021, z_s = 30 cm), where k is almost constant ($\cong m$) during the irrigation period (e.g. in 2021, z_s = 30 cm, m = 0.417, n = 0.0002, Fig. 10d). However, this is an isolated case, as k generally follows the observed increasing trend with the number of days after the t_t measurement. This confirms that wetted bulbs are enriched more in water than the increase in their volume, determining the increase in k (i.e. in Eq. 16).

Table 4 *The m and n parameters obtained by fitting the power law (Eq. 21) to the calibrated k values, along with the corresponding correlation coefficient R, for the considered depths, z_s (cm), of the Drill & Drop probe across six irrigation seasons (2018−2023)*

Parameter	z_s (cm)	2018	2019	2020	2021	2022	2023
	10	0.2795	0.3249	0.3621	0.3335	0.3696	0.3458
	20	0.3417	0.3615	0.3789	0.3651	0.3836	0.3601
m	30	0.3940	0.3959	0.4114	0.4169	0.4185	0.4432
	40	0.4318	0.4379	0.4555	0.4494	0.4571	0.4807
	50	0.4385	0.4486	0.4610	0.4712	0.4708	0.4834
	60	0.4632	0.4662	0.4848	0.4963	0.4943	0.5068
	10	0.0466	0.0404	0.0132	0.0164	0.0190	0.0407
	20	0.0245	0.0284	0.0105	0.0078	0.0157	0.0444
n	30	0.0149	0.0235	0.0107	0.0002	0.0195	0.0055
	40	0.0145	0.0177	0.0100	0.0061	0.0116	0.0041
	50	0.0123	0.0147	0.0126	0.0049	0.0159	0.0154
	60	0.0107	0.0166	0.0105	0.0032	0.0082	0.0085
	10	0.763	0.935	0.501	0.592	0.735	0.815
	20	0.759	0.931	0.490	0.288	0.666	0.723
R	30	0.675	0.918	0.734	0.013	0.812	0.186
	40	0.663	0.933	0.583	0.451	0.722	0.236
	50	0.771	0.921	0.675	0.424	0.791	0.625
	60	0.730	0.940	0.866	0.391	0.556	0.218

Figure 10 makes it possible to observe that the average wetting water content, θ_{avg}, calculated as the mean between the initial and saturated volumetric water content (θ_{avg} with k = 0.5, Eq. 14), is rarely achieved in field conditions. k values exceeding 0.5 are observed only at the deepest layer, z_s = 60 cm, in the irrigation seasons 2019−2023.

In line of the primary objective of this study to explore the impact of average water content on wetting bulb expansion, the θ_{avg} values were also illustrated in Fig. 11, thus accounting for the ISMC, θ_0, by using Eq. (22).

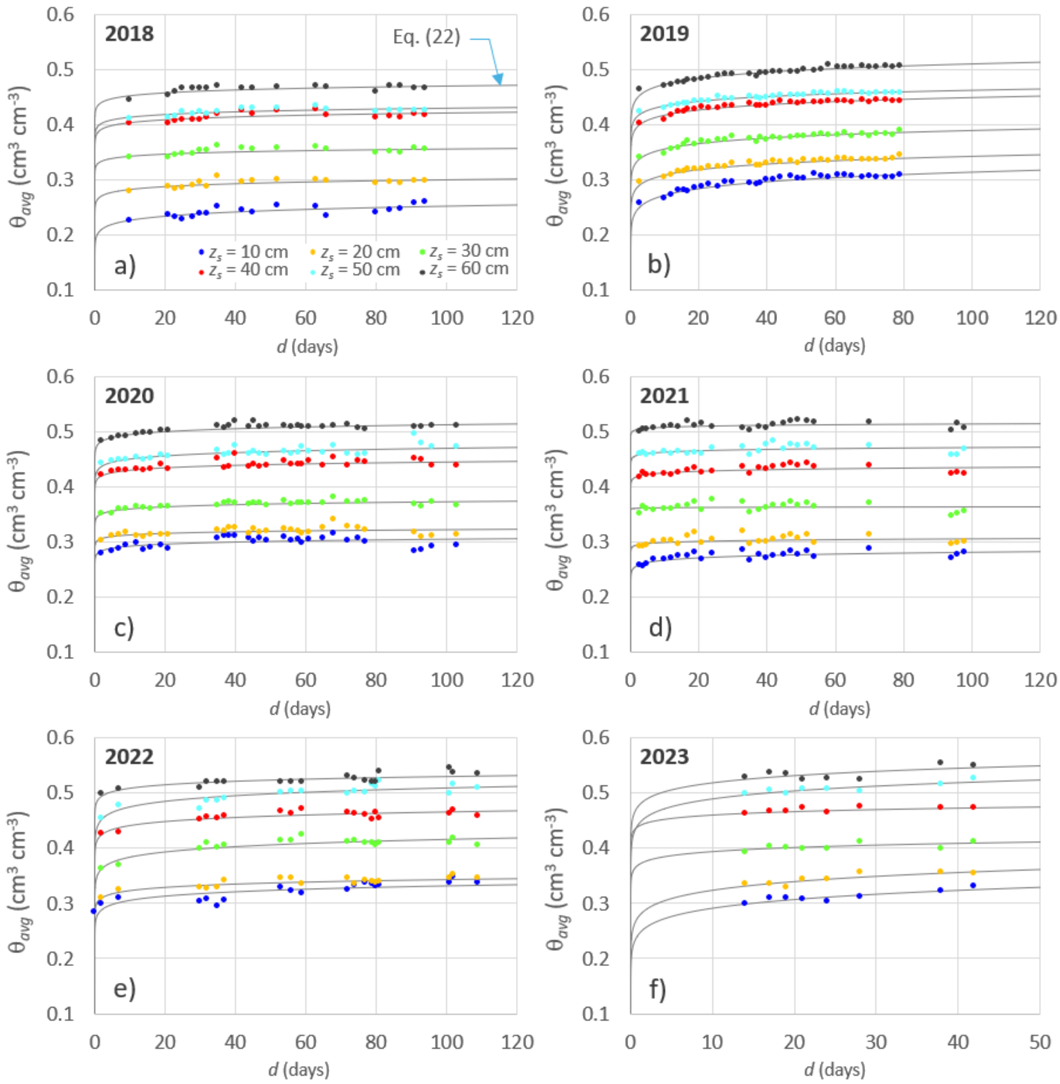

Fig. 11 *Temporal variation of the calibrated θ_{avg} calculated by using Eqs. (15 and 19), for the six irrigation seasons **a)** 2018, **b)** 2019, **c)** 2020, **d)** 2021, **e)** 2022, and **f)** 2023. The power law relationship (Eq. 22, solid lines), with the parameters m and n reported in Table 4, is also indicated*

Figure 11 shows a temporal variation in θ_{avg} values that closely mirrors the variation in k (Fig. 10), despite the differing roles that ISMC plays on θ_{avg} and k, over the years and along soil depth. Figure 11 also illustrates that for the assumed $\theta_s = 0.521$ cm^3 cm^{-3}, at the deepest layer, when $k > 0.5$, θ_{avg} values approach θ_s. This occurs because, at such depths, the ISMC is nearly equal to θ_s.

A comparison between the experimental travel times and those obtained by estimating *k* in line with the power law to describe the variability of the average wetting water content is performed by using Eqs. (20 and 21). For all irrigation seasons and fixed depths, as in Figs. 5 and 8, the comparison between the estimated and observed t_ts is shown in Fig. 12.

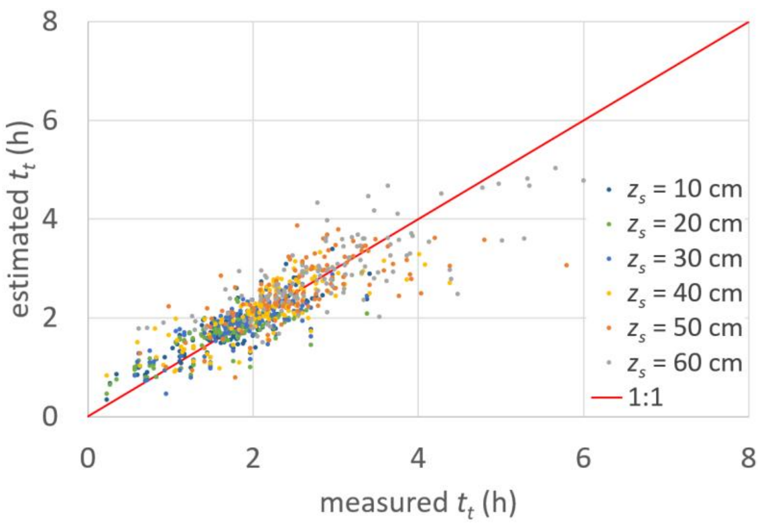

Fig. 12 *Comparison between the measured travel times, t_t (h), and those estimated from Eqs. (20 and 21), with the parameters m and n reported in Table 3*

Using the *k* values estimated via the power law, according to the *m* and *n* parameters of Table 4 reduces the standard error in the t_t estimate, providing a *SEE* of 26 min. As can be observed in Fig. 12, the dots are much closer to the line of perfect agreement compared to the cases in which *k* = 0.5 (Fig. 5) and *k* = <*k*> (Fig. 8) were assumed. This suggests that an accurate analysis of the *k* parameter is essential when operating under field conditions, as it can significantly contribute to predict more accurate wetted bulb expansion, aimed at improving water-saving.

For *k* = 0.5, <*k*> and *k* accounting for the intra-seasonal variability, estimated with Eq. (21), Table 5 reports the sum square error, *SSE*, the sample size, *N*, the mean square error, *MSE*, and the standard error in the estimate, *SEE*, of travel times.

Table 5 *Sum square error, SSE, sample size, N, mean square error, MSE, and standard error in the estimate of the irrigation time, SEE, for the three considered cases of k estimate*

k	*SSE*	*N*	*MSE*	*SEE* (h)	*SEE* (min)
0.5	14438.7	832	17.35	4.17	250
<*k*>	1718.9	832	2.07	1.44	86
Eq. (21)	149.5	798	0.19	0.43	26

While low time resolutions complicate θ data collection over the six years of observation, further improvements in the t_t estimation are expected if θ measurements had been collected at a time resolution finer than the 20-minute interval used in this study.

Finally, Fig. 13 presents an analysis of the variability in the *m* and *n* parameters of Eq. (21) against ISMC, for $d = 0$, and all depths across the 6 years. The *m* parameter, which corresponds to the *k* value after one day from the first t_t measurement ($d = 1$), as expected, is well explained by the ISMC at the start of the first irrigation, $\theta_0|_{d=0}$ (Fig. 13a), as the differences between the volumetric water contents at $d = 0$ and $d = 1$ in all irrigation seasons are reasonably similar. In contrast, the *n* parameter, which defines the shape of the power law described by Eq. (21), shows a weaker correlation with $\theta_0|_{d=0}$ (Fig. 13b, $R^2 = 0.48$).

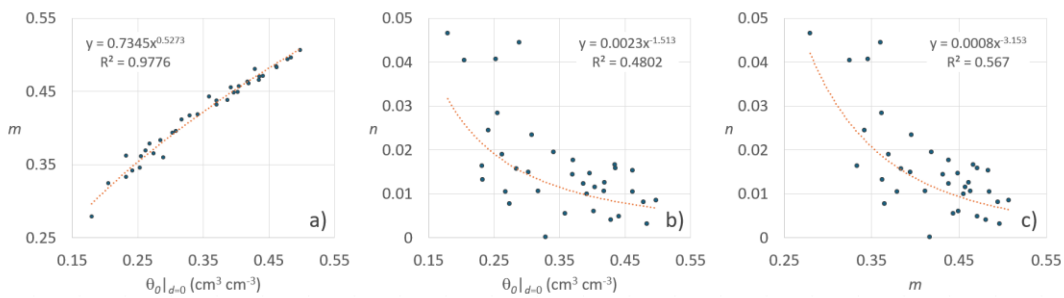

Fig. 12 *Comparison between the measured travel times, t_t (h), and those estimated from Eqs. (20 and 21), with the parameters m and n reported in Table 3*

Figure 13b also reveals an inverse trend of the *n* parameter with $\theta_0|_{d=0}$, compared to *m*. The latter indicates that at increasing $\theta_0|_{d=0}$, *m* increases while *n* decreases, meaning that at high ISMCs, *k* exhibits less temporal variability than for low ISMCs. This behaviour can also be observed in Fig. 10a (2018), where at increasing depth, z_s, i.e. higher $\theta_0|_{d=0}$, *k* temporal variation during the subsequent irrigation events is more evident than for upper layers.

A slightly better fit of *n* parameter is observed in the power law shown in Fig. 13c ($R^2 = 0.567$), where *n* is plotted against *m*. This confirms that, generally, at high $\theta_0|_{d=0}$, i.e. high *m*, the average volumetric water content, θ_{avg}, is less sensitive to time than for low $\theta_0|_{d=0}$, i.e. low *n*.

As a final remark, it should be noted that operating conditions differing from the assumptions made in this work (soil hydrological characteristics, soil tillage methods, interaction between contiguous wetted bulbs, field slope, and others) naturally lead to results that differ from those presented here. However, this work suggests a methodology to interpret the average water content of the Philip model, which could be applied in practice to predict the expansion of the wetting bulbs from a buried point source. Additionally, the accuracy of the results could be enhanced by increasing the temporal resolution of water content data acquisition beyond the 20-minute intervals used in this study, which has been recently emphasised, although in a different context of preferential flow (Nimmo et al., 2025).

5. Conclusions

This study analyses the role of average soil water content, θ_{avg}, in the shape of the wetting bulbs generated from a buried point source in an SDI system. The key findings can be summarised as follows:

- A k parameter, incorporating the simplified assumptions considered in the Philip model, was introduced to study the θ_{avg} variability in the range between the initial and the saturated soil water content.
- The k parameter enables accurate estimation of travel times for various soil depths and across the number of days from the first t_t measurement during the irrigation season.
- Calibration was performed according to 832 average soil water contents, θ_{avg}, initial soil moisture conditions, θ_0, and travel times, t_t, measurements, once the soil hydraulic characteristics were determined.
- It was shown that assuming θ_{avg} equal to the mean between the initial and saturated volumetric water content provided significant overestimations of the travel times of the wetting front. Only at the deepest layers, the assumption $\theta_{avg} = 0.5\ (\theta_s + \theta_0)$ appears to be reasonable.
- An examination of the intra-seasonal variability of θ_{avg} evidenced its dynamic behaviour, which is strongly influenced by the previous irrigation event.
- The calibrated k values were fitted as a function of time, using power law relationships that improved the accuracy of Philip model predictions, reducing the standard error, *SEE*, in the travel time estimates from over four hours, when $k = 0.5$ is assumed, to 26 minutes, a bit higher than the adopted time resolution of the soil moisture probe data acquisition (20 min).

6. References

Arbat, G., Puig-Bargués, J., Duran-Ros, M., Barragán, J., Ramírez De Cartagena, F., 2013. Drip-Irriwater: Computer software to simulate soil wetting patterns under surface drip irrigation. Comput. Electron. Agric. 98, 183–192. https://doi.org/10.1016/j.compag.2013.08.009

Bagarello, V., Di Prima, S., Iovino, M., Provenzano, G., Sgroi, A., 2011. Testing different approaches to characterize Burundian soils by the BEST procedure. Geoderma 162, 141–150. https://doi.org/10.1016/j.geoderma.2011.01.014

Bagarello, V., Di Prima, S., Iovino, M., 2014. Comparing Alternative Algorithms to Analyze the Beerkan Infiltration Experiment. Soil Sci. Soc. Am. J. 78, 724–736. https://doi.org/10.2136/sssaj2013.06.0231

Baiamonte, G., 2019. SCS Curve Number and Green-Ampt Infiltration Models. J. Hydrol. Eng. 24, 04019034. https://doi.org/10.1061/(ASCE)HE.1943-5584.0001838

Baiamonte, G., 2020. Analytical solution of the Richards equation under gravity-driven infiltration and constant rainfall intensity. J Hydrol E – ASCE 25 (7). https://doi.org/10.1061/(ASCE)HE.1943-5584.0001933

Baiamonte, G., 2024. Maximum Lateral Expansion of Wetting Bulbs from Buried and Surface Point Sources: Implications for Drip Irrigation Design. J. Hydrol. Eng. 29, 04024037. https://doi.org/10.1061/JHYEFF.HEENG-6235

Baiamonte, G., Alagna, V., Autovino, D., Iovino, M., Palermo, S., Vaccaro, G., Bagarello, V., 2024a. Influence of soil hydraulic parameters on bulb size for surface and buried emitters. Agric. Water Manag. 295, 108756. https://doi.org/10.1016/j.agwat.2024.108756

Baiamonte, G., Vaccaro, G., Palermo, S., 2024b. Quantifying local losses due to root intrusion in subsurface drip irrigation systems by monitoring inlet discharge and pressure head. Irrig. Sci. https://doi.org/10.1007/s00271-024-00990-y

Blöschl, G., Sivapalan, M., Wagener, T., Viglione, A., Savenije, H.H.G., 2013. Runoff prediction in ungauged basins: Synthesis across processes, places and scales. Cambridge University Press. https://doi.org/10.1017/CBO9781139235761

Bogle, C.R., Hartz, T.K., Nunez, C., 1989. Comparison of Subsurface Trickle and Furrow Irrigation on Plastic-mulched and Bare Soil for Tomato Production. J. Am. Soc. Hortic. Sci. 114, 40–43. https://doi.org/10.21273/JASHS.114.1.40

Cahn, M., Hutmacher, R., 2024. Subsurface drip irrigation. Microirrigation for Crop Production. Elsevier Science, pp 257–301

Camp, C.R., 1998. Subsurface Drip Irrigation: A Review. Trans. ASAE 41, 1353–1367. https://doi.org/10.13031/2013.17309

Cook, F.J., Thorburn, P.J., Bristow, K.L., Cote, C.M., 2003a. Infiltration from surface and buried point sources: The Average wetting water content. Water Resour. Res. 39, 2003WR002554. https://doi.org/10.1029/2003WR002554

Cook, F.J., Thorburn, P.J., Fitch, P., Bristow, K.L., 2003b. WetUp: a software tool to display approximate wetting patterns from drippers. Irrig. Sci. 22, 129–134. https://doi.org/10.1007/s00271-003-0078-2

Di Prima, S., Stewart, R.D., Castellini, M., Bagarello, V., Abou Najm, M.R., Pirastru, M., Giadrossich, F., Iovino, M., Angulo-Jaramillo, R., Lassabatere, L., 2020. Estimating the macroscopic capillary length from Beerkan infiltration experiments and its impact on saturated soil hydraulic conductivity predictions. J. Hydrol. 589, 125159. https://doi.org/10.1016/j.jhydrol.2020.125159

Elnesr, M.N., Alazba, A.A., 2017. Simulation of water distribution under surface dripper using artificial neural networks. Comput. Electron. Agric. 143, 90–99. https://doi.org/10.1016/j.compag.2017.10.003

Galindo, A., Collado-González, J., Griñán, I., Corell, M., Centeno, A., Martín-Palomo, M.J., Girón, I.F., Rodríguez, P., Cruz, Z.N., Memmi, H., Carbonell-Barrachina, A.A., Hernández, F., Torrecillas, A., Moriana, A., Pérez-López, D., 2018. Deficit irrigation and emerging fruit crops as a strategy to save water in Mediterranean semiarid agrosystems. Agric. Water Manag. 202, 311–324. https://doi.org/10.1016/j.agwat.2017.08.015

Gardner, W.R., 1958. Some steady-state solutions of the unsaturated moisture flow equation with application to evaporation from a water table. Soil Sci. 85, 228–232. https://doi.org/10.1097/00010694-195804000-00006

Gil, M., Rodríguez-Sinobas, L., Juana, L., Sánchez, R., Losada, A., 2008. Emitter discharge variability of subsurface drip irrigation in uniform soils: effect on water-application uniformity. Irrig. Sci. 26, 451–458. https://doi.org/10.1007/s00271-008-0116-1

Haverkamp, R., Ross, P.J., Smettem, K.R.J., Parlange, J.Y., 1994. Three-dimensional analysis of infiltration from the disc infiltrometer: 2. Physically based infiltration equation. Water Resour. Res. 30, 2931–2935. https://doi.org/10.1029/94WR01788

Hinnell, A.C., Lazarovitch, N., Furman, A., Poulton, M.M., Warrick, A.W., 2010. Neuro-Drip: estimation of subsurface wetting patterns for drip irrigation using neural networks. Irrig. Sci. 28, 535–544. https://doi.org/10.1007/S00271-010-0214-8

Jamei, M., Karimi, F., Ali, M., Karimi, B., Karbasi, M., Aminpour, Y., 2022. Experimental and computational assessment of wetting pattern for two-layered soil profiles in pulse drip irrigation: Designing a novel optimized bidirectional deep learning paradigm. J. Hydrol. 614, 128496. https://doi.org/10.1016/j.jhydrol.2022.128496

Kemp, A.W., 2006. Polylogarithmic distributions. In Encyclopedia of statistical science, edited by S. Kotz, D. L. Banks, and C. B. Read, New York: Wiley

Khan, A.A., Yitayew, M., Warrick, A.W., 1996. Field Evaluation of Water and Solute Distribution from a Point Source. J. Irrig. Drain. Eng. 122, 221–227. https://doi.org/10.1061/(ASCE)0733-9437(1996)122:4(221)

Kisi, O., Khosravinia, P., Heddam, S., Karimi, B., Karimi, N., 2021. Modeling wetting front redistribution of drip irrigation systems using a new machine learning method: Adaptive neuro- fuzzy system improved by hybrid particle swarm optimization – Gravity search algorithm. Agric. Water Manag. 256, 107067. https://doi.org/10.1016/j.agwat.2021.107067

Lamm, F.R., Colaizzi, P.D., Sorensen, R.B., Bordovsky, J.P., Dougherty, M., Balkcom, K., Zaccaria, D., Bali, K.M., Rudnick, D.R., Peters, R.T., 2021. A 2020 Vision of Subsurface Drip Irrigation in the U.S. Trans. ASABE 64, 1319–1343. https://doi.org/10.13031/trans.14555

Lassabatère, L., Angulo-Jaramillo, R., Soria Ugalde, J.M., Cuenca, R., Braud, I., Haverkamp, R., 2006. Beerkan Estimation of Soil Transfer Parameters through

Infiltration Experiments—BEST. Soil Sci. Soc. Am. J. 70, 521–532. https://doi.org/10.2136/sssaj2005.0026

Lilliefors, H.W., 1967. On the Kolmogorov-Smirnov Test for Normality with Mean and Variance Unknown. J. Am. Stat. Assoc. 62, 399–402. https://doi.org/10.1080/01621459.1967.10482916

Mubarak, I., Angulo-Jaramillo, R., Mailhol, J.C., Ruelle, P., Khaledian, M., Vauclin, M., 2010. Spatial analysis of soil surface hydraulic properties: Is infiltration method dependent? Agric. Water Manag. 97, 1517–1526. https://doi.org/10.1016/j.agwat.2010.05.005

Nimmo, J.R., Wiekenkamp, I., Araki, R., Groh, J., Singh, N.K., Crompton, O., Wyatt, B.M., Ajami, H., Giménez, D., Hirmas, D.R., Sullivan, P.L., Sprenger, M., 2025. Identifying preferential flow from soil moisture time series: Review of methodologies. Vadose Zone Journal, 24, e70017. https://doi.org/10.1002/vzj2.70017

Nogueira, V.H.B., Diotto, A.V., Thebaldi, M.S., Colombo, A., Silva, Y.F., Lima, E.M.D.C., Resende, G.F.L., 2021. Variation in the flow rate of drip emitters in a subsurface irrigation system for different soil types. Agric. Water Manag. 243, 106485. https://doi.org/10.1016/j.agwat.2020.106485

Philip, J.R., 1968. Steady Infiltration From Buried Point Sources and Spherical Cavities. Water Resour. Res. 4, 1039–1047. https://doi.org/10.1029/WR004i005p01039

Philip, J.R., 1969. Theory of Infiltration, Advances in Hydroscience. Elsevier, pp. 215–296. https://doi.org/10.1016/B978-1-4831-9936-8.50010-6

Philip, J.R., 1984. Travel Times From Buried and Surface Infiltration Point Sources. Water Resour. Res. 20, 990–994. https://doi.org/10.1029/WR020i007p00990

Philip, J.R., 1992. What happens near a quasi-linear point source? Water Resour. Res. 28, 47–52. https://doi.org/10.1029/91WR02600

Provenzano, G., 2007. Using HYDRUS-2D Simulation Model to Evaluate Wetted Soil Volume in Subsurface Drip Irrigation Systems. J. Irrig. Drain. Eng. 133, 342–349. https://doi.org/10.1061/(ASCE)0733-9437(2007)133:4(342)

Raats, P.A.C., 1971. Steady Infiltration from Point Sources, Cavities, and Basins. Soil Sci. Soc. Am. J. 35, 689–694. https://doi.org/10.2136/sssaj1971.03615995003500050020x

Ravikumar, V., 2023. Sprinkler and drip irrigation: theory and practice. Springer Nature, Cham

Revol, P., Clothier, B.E., Mailhol, J. -C., Vachaud, G., Vauclin, M., 1997. Infiltration from a surface point source and drip irrigation: 2. An approximate time-dependent solution for wet-front position. Water Resour. Res. 33, 1869–1874. https://doi.org/10.1029/97WR01007

Richards, L.A., 1931. CAPILLARY CONDUCTION OF LIQUIDS THROUGH POROUS MEDIUMS. Physics 1, 318–333. https://doi.org/10.1063/1.1745010

Shani, U., Xue, S., Gordin-Katz, R., Warrick, A.W., 1996. Soil-Limiting Flow from Subsurface Emitters. I: Pressure Measurements. J. Irrig. Drain. Eng. 122, 291–295. https://doi.org/10.1061/(ASCE)0733-9437(1996)122:5(291)

Shi, K., Lu, T., Zheng, W., Zhang, X., Zhangzhong, L., 2022. A Review of the Category, Mechanism, and Controlling Methods of Chemical Clogging in Drip Irrigation System. Agriculture 12, 202. https://doi.org/10.3390/agriculture12020202

Šimůnek, J., Šejna, M., Van Genuchten, M.T., 2007. The HYDRUS software package for simulating the two- and three-dimensional movement of water, heat, and multiple solutes in variably-saturated media. User Manual, Version 1.0. Prague, Czech Republic: PC Progress

Singh, D.K., Rajput, T.B.S., Singh, D.K., Sikarwar, H.S., Sahoo, R.N., Ahmad, T., 2006. Simulation of soil wetting pattern with subsurface drip irrigation from line source. Agric. Water Manag. 83, 130–134. https://doi.org/10.1016/j.agwat.2005.11.002

Singh, V.P., Su, Q., 2022. Irrigation engineering. Principles, processes, procedures, design, and management. Cambridge University Press, Cambridge

Sivapalan, M., 2003. Prediction in ungauged basins: a grand challenge for theoretical hydrology. Hydrol. Process. 17, 3163–3170. doi: 10.1002/hyp.5155

Smettem, K., Parlange, J.Y., Ross, P.J., Haverkamp, R., 1994. Three-dimensional analysis of infiltration from the disc infiltrometer: 1. A capillary-based theory. Water Resour. Res. 30, 2925–2929. https://doi.org/10.1029/94WR01787

Subbaiah, R., 2013. A review of models for predicting soil water dynamics during trickle irrigation. Irrig. Sci. 31, 225–258. https://doi.org/10.1007/s00271-011-0309-x

Thorburn, P.J., Cook, F.J., Bristow, K.L., 2003. Soil-dependent wetting from trickle emitters: implications for system design and management. Irrig. Sci. 22, 121–127. https://doi.org/10.1007/s00271-003-0077-3

Vaccaro, G., Fusco, M., Alagna, V., Franco, L., Motisi, A., Iovino, M., 2025. Assessing microtensiometers for monitoring stem water potential in mandarin (Citrus reticulata Blanco) orchard under different irrigation regimes. Agricultural Water Management 320, 109873. https://doi.org/10.1016/j.agwat.2025.109873

Wang, J., Tian, Z., Yang, T., Li, X., He, Q., Wang, D., Chen, R., 2024. Characteristics of limited flow and soil water infiltration boundary of a subsurface drip irrigation emitter in silty loam soil. Agric. Water Manag. 291, 108636. https://doi.org/10.1016/j.agwat.2023.108636

White, I., Sully, M.J., 1987. Macroscopic and microscopic capillary length and time scales from field infiltration. Water Resour. Res. 23, 1514–1522. https://doi.org/10.1029/WR023i008p01514

Zur, B., 1996. Wetted soil volume as a design objective in trickle irrigation. Irrig. Sci. 16, 101–105. https://doi.org/10.1007/BF02215617

CHAPTER 5

Assessing microtensiometers for monitoring stem water potential in mandarin (*Citrus reticulata* Blanco) orchard under different irrigation regimes

Based on the **published** paper:

Vaccaro, G., Fusco, M., Alagna, V., Franco, L., Motisi, A., Iovino, M., **2025**. Assessing microtensiometers for monitoring stem water potential in mandarin (Citrus reticulata Blanco) orchard under different irrigation regimes. *Agric. Water Manag.* 320, 109873.
https://doi.org/10.1016/j.agwat.2025.109873

CHAPTER 5: Assessing microtensiometers for monitoring stem water potential in mandarin (*Citrus reticulata* Blanco) orchard under different irrigation regimes

Girolamo Vaccaro[1] Mariachiara Fusco[1] Vincenzo Alagna[1*] Loris Franco[2] Antonio Motisi[1] Massimo Iovino[1]

[1]Dept. of Agricultural, Food and Forest Sciences (SAAF), Univ. of Palermo, Viale delle Scienze, Bldg. 4, 90128 Palermo. *Corresponding Author, E-mail: vincenzo.alagna01@unipa.it

[2]IRRITEC S.p.A. via Gambitta Conforto, 98071 Capo d'Orlando, Messina, Italy

Abstract

Stem water potential (Ψ_{stem}) is the standard indicator of crop water status, commonly estimated using the Scholander pressure chamber (PC). However, it does not allow continuous monitoring, limiting real-time decision-making. The recently developed microtensiometer (MT) offers continuous Ψ_{stem} monitoring, overcoming the PC limitations. This study assesses the MT's reliability in monitoring Ψ_{stem} dynamics in a mandarin orchard in Sicily, Italy, under two irrigation regimes: i) a frequent irrigation regime via subsurface drip irrigation (SDI) system, employed to ensure well-watered conditions, and ii) an ordinary irrigation management typical of the area, provided by a micro-sprinkler (SPR) system. Over two seasons, Ψ_{stem} measurements obtained with the MT (Ψ_{mt}) were compared with those from the PC (Ψ_{pc}). Shading trials were also conducted to evaluate the sensor's ability to detect the plant reactions to external perturbations. A step-change in solar radiation imposed by artificial shading revealed different signal dynamics of MT sensors compared to pressure chamber Ψ_{pc} measurements, characterised by a 4-fold increase in signal time constant. This led to a consequential impact on Ψ_{stem} estimation, resulting in both a substantial time lag and attenuation, consistent with first-order sensor dynamics. Across both seasons and irrigation regimes, daily Ψ_{mt} overestimated Ψ_{stem} compared to Ψ_{pc}, along with a clear time lag coherent with the first-order response shown by the sensor-tree-

complex. Under the SDI irrigation regime, Ψ_{mt} was significantly correlated with vapour pressure deficit, indicating a strong plant-atmosphere coupling under stable soil moisture conditions. Normalised cross-correlation analysis between reference evapotranspiration and Ψ_{mt} showed variable time lags, specifically in the SPR plot, subjected to alternating soil moisture conditions. These findings suggest that MTs are a promising tool for real-time monitoring of mandarin water status. However, the first-order dynamics of the sensor-tree-complex response signal preclude the use of Ψ_{mt} as a direct replacement for pressure-chamber Ψ_{stem} measurements. Consequently, suitable compensation protocols accounting for a large time constant should be developed to apply Ψ_{mt} readings to currently published crop-specific Ψ_{stem} thresholds for irrigation scheduling protocols.

Keywords: Stem potential, Microtensiometer, Scholander pressure chamber, Irrigation regimes, Subsurface drip irrigation, Micro-sprinkler irrigation

1. Introduction

Efficient water management is crucial for irrigated agriculture, particularly in light of climate change and increasing water scarcity in arid and semi-arid areas (Galindo et al., 2018). The expected intensification of drought events under climate change scenarios is expected to increase crop stress due to rising thermal gradients and reduced precipitation, negatively affecting agricultural productivity (Ciais et al., 2005). For citrus crops in a Mediterranean semi-arid environment, yield success relies heavily on adequate irrigation (Rallo et al., 2017). Therefore, to optimise the productivity of citrus orchards, it is essential to manage the available water resources sustainably and, at the same time, also consider their potential cultivation under water shortage conditions.

One of the most water-efficient and precise methods of surface irrigation systems is drip irrigation, which can minimise water losses due to evaporation, surface runoff, and deep percolation (Ravikumar, 2023; Singh and Su, 2022). Unlike drip irrigation systems, subsurface drip irrigation (SDI) systems are characterised by buried emitters, effectively reducing water loss due to evaporation (Cahn and Hutmacher, 2024; Camp, 1998; Provenzano, 2007). Lamm et al. (2021) summarised recent research progress of SDI systems (from 2010 to 2020). They highlighted SDI's advantages, including high water use efficiency, uniform water application and the ability to apply water and nutrients directly and efficiently within the crop root zone compared to other systems, such as sprinkler irrigation.

Optimising water use efficiency requires selecting and designing appropriate irrigation systems and implementing management practices that supply water in volumes precisely aligned with crop water requirements. A fundamental aspect of fine-tuning irrigation scheduling is understanding the plant water status. Several studies have specifically highlighted the importance of stem water potential (Ψ_{stem}), which is widely recognised as the key indicator of a plant's water status and a valuable index for making irrigation decisions (Choné, 2001; Jones, 2004; Ortuño et al., 2006). Stem water potential assessments are typically conducted at pre-dawn or midday. In citrus trees, which exhibit low resistance to water stress, irrigation scheduling is often guided by plant water stress thresholds, with midday Ψ_{stem} values commonly ranging between −1.3 and −1.5 MPa (Ballester et al., 2011; García-Tejero et al., 2010; González-Altozano and Castel, 1999).

Traditionally, Ψ_{stem} is estimated with the Scholander pressure chamber (Scholander et al., 1965). Although this is a reliable measurement, it is destructive, time-consuming, and does not provide real-time continuous data on the plant water status. Additionally, Levin (2019) investigated several factors affecting the pressure chamber (PC) method, including the impact of re-cutting the petiole before placing the leaf in the chamber, the period between sample excision and pressurisation, the sample equilibration duration, and the operator's influence. The operator's effect consistently outweighed the other effects, thus demonstrating that proper training of technicians is crucial for achieving reliable and accurate estimations of Ψ_{stem} by the PC technique (Ψ_{pc}).

Physiologically, certain species, such as mandarin trees, are less drought-tolerant than other crops, primarily due to their low hydraulic conductance (Romero-Trigueros et al., 2021). Water stress can lead to cavitation-induced embolism in the xylem (Hacke and Sperry, 2001; Poggi et al., 2007), reducing xylem flow and weakening the hydraulic connection between the trunks and stems. While this phenomenon is reversible, it plays a crucial role in regulating transpiration in plants under water stress

(Clearwater and Goldstein, 2005). For such crops, Ψ_{pc} may be prone to inaccuracies, failing to reflect the actual water status.

The practical limitations of the PC technique impede its application for determining optimal irrigation timing and management. However, in the context of precision irrigation or plant stress diagnostics, continuous monitoring of plant water status is of utmost importance; thus, research efforts have increasingly focused on enhancing existing devices and developing new technologies for easily and accurately monitoring plant water status.

Over the years, various plant-based monitoring technologies, including sap flow probes, leaf pressure probes and psychrometers for measuring plant water potential, have been developed to enhance irrigation management.

Sap flow measurement is a widely used method for directly quantifying plant water use and transpiration by assessing water transport within the vascular system. Unlike indirect methods, which rely on environmental parameters, this technique provides accurate, plant-based physiological data, enabling precise irrigation scheduling tailored to actual plant water requirements and significantly reducing water waste (Capurro et al., 2024; Mancha et al., 2021; Venturin et al., 2020). However, sap flow methods have inherent limitations. They are primarily applicable to woody species, and their measurement accuracy can be compromised by natural temperature gradients, radial variations in sap flow, and the selection of data-processing methods, all of which introduce uncertainty (Rabbel et al., 2016). Furthermore, upscaling from individual tree measurements to whole stands requires careful sampling strategies and precise quantification of sapwood area, as variability among trees can be substantial (Lundblad et al., 2001).

The ZIM-probe method measures leaf turgor pressure using a highly sensitive pressure sensor, which is clamped to a leaf and evaluates the pressure transfer function across a patch of intact leaf tissue, showing an inverse correlation with turgor pressure (Zimmermann et al., 2008). The ZIM-probe has been recognised as a user-friendly and easily installable technique, offering significant potential for field application by growers (Fernández, 2014). However, limitations include the need for accurately species-specific calibration to interpret turgor pressure, as well as potential variability due to microclimate effects and leaf anatomical differences across different canopy positions (Bader et al., 2014; Martínez-Gimeno et al., 2017).

Recognising the importance of Ψ_{stem} as a key indicator of crop water status, various sensors have been developed to facilitate its continuous measurement. Among these, the thermocouple psychrometer emerges as an effective device for assessing Ψ_{stem} by employing psychrometric principles to determine the water potential in stem tissue through vapour pressure measurements. This sensor provides real-time data and has been proven to monitor water potential reliably (Dainese et al., 2022). However, despite its reliability, the thermocouple psychrometer has several drawbacks, including the necessity for calibration with standard solutions, a challenging installation procedure, and relatively high costs (Quick et al., 2016). The relative humidity of the air surrounding the sensing junction is crucial, as it significantly influences the temperature difference between the wet sensing junction and the dry reference junction (Rawlins, 1966). Moreover, its accuracy can decline under relative humidity nearing vapour saturation, corresponding to water potential values approaching zero (Bulut and Leong, 2008).

More recently, Pagay et al. (2014) developed the so-called microtensiometer (MT), a device capable of measuring water potentials of external matrices below −10 MPa, using a microelectromechanical pressure sensor. The MTs, which are inserted directly into the plant tissue, represent an innovative technology for continuous real-time monitoring of stem water potential (Ψ_{mt}). Several studies have assessed the performance of MTs under field conditions for different crops, including kiwifruit (Di Biase et al., 2025), cotton (Christenson et al., 2024), pear (Blanco and Kalcsits, 2023), nectarine (Conesa et al., 2023), and grapevines (Pagay, 2022).

Despite their successful use in other crops, the application of MTs to mandarin species remains unexplored. Citrus orchards are one of the best-adapted tree species to Mediterranean environments. Traditionally, in Sicily, mandarin orchards have been irrigated using under-canopy micro-sprinkler (SPR) irrigation systems with low-frequency scheduling. However, due to the region’s semi-arid climate and frequent water scarcity, there is a growing shift toward adopting more efficient irrigation technologies, such as the SDI system, to enhance water use efficiency.

The main objective of this study was to fill the existing knowledge gap regarding the potential benefits of using MTs to monitor Ψ_{stem} of mandarin trees under Mediterranean climate conditions, within the framework of precision irrigation. For this purpose, MT performance was tested under two irrigation regimes: a frequent irrigation regime to ensure a well-watered condition maintained through an SDI system, and an ordinary irrigation management typical of the growing area, provided by a SPR system. Specific objectives also aimed at analysing (i) the accuracy of Ψ_{mt} in comparison with the established Ψ_{pc}, (ii) the MT's ability to detect plant reaction to external perturbations induced by shading trials, and (iii) the sensitivity of Ψ_{mt} values to varying climatic conditions.

2. Material and methods

2.1. Experimental site

The experiment was conducted during the 2022 and 2023 irrigation seasons in a 30-year-old mandarin orchard (*Citrus reticulata* Blanco cv. Tardivo di Ciaculli grafted onto *Citrange* "Carrizo"), spaced 5 × 5 m and located near Palermo, Italy (38°4′53.4″ N, 13°25′8.2″ E). The climate is classified as Csa under the Köppen-Geiger system, indicating a warm temperate humid climate with hot, dry summers. The mean annual temperature reaches approximately 17 °C, while average annual rainfall amounts to 655 mm, primarily concentrated during the autumn and winter seasons.

The mandarin orchard is divided into two plots, with one representative tree selected in each plot to monitor stem water potential under different irrigation regimes. One plot has been equipped with a subsurface drip irrigation system (SDI plot) since 2018 to improve water use efficiency (Fig. 1, red polygon). To check that the tree was under well-watered conditions for the duration of the irrigation season, a 0.60 m long "Drill & Drop" probe (Sentek Pty Ltd., Stepney, Australia) was positioned 0.3 m from a single emitter and approximately 0.8 m from the tree trunk (Fig. 1). The probe measured both volumetric soil water content (SWC) and temperature from the surface to a depth of 0.60 m at 0.10 m intervals with data recorded every 20 minutes. The second plot (Fig. 1, green polygon) uses a traditional under-canopy micro-sprinkler irrigation system (SPR plot) commonly employed in Sicily for citrus orchards. In both plots, the soil (typic Rhodoxeralf) remained untilled, with weed control carried out mechanically during harvest or in summer.

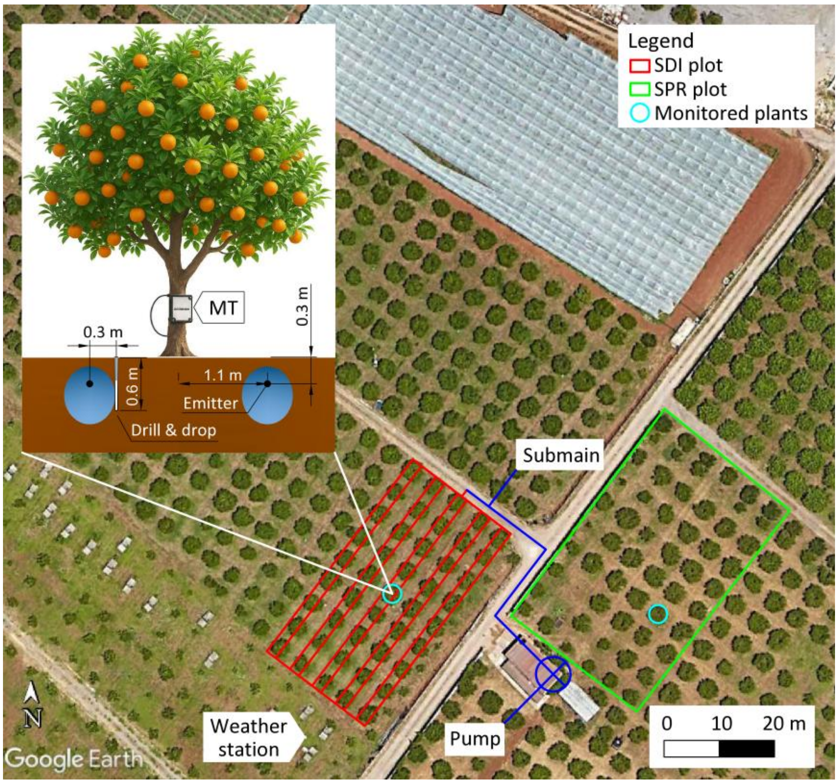

Fig. 1 *Experimental layout of the SDI and SPR plots. For the SDI plot, the positions of the emitters and the soil water content probe are also displayed*

The SDI plot features a relatively uniform soil texture that, according to the USDA (United States Department of Agriculture) classification, is classified as sandy clay loam or sandy loam, with a moderate gravel content in the top layer. The hydrological soil characteristics, for the 0−0.60 m depth profile, were determined using pressure plate extractors (Dane et al., 2002) for pressure head values of −1 m and −150 m. The average volumetric SWC at field capacity (θ_{fc}) and at wilting point (θ_{wp}) were 0.254 and 0.143 cm^3 cm^{-3}, respectively, resulting in an available water fraction of 0.111 cm^3 cm^{-3}. Soil organic matter was determined using the loss-on-ignition method (Bengtsson and Enell, 1986; Dean, 1974), yielding an average of 2.44%. The SPR plot exhibited a more heterogeneous soil texture, ranging from clay to sandy clay loam (USDA). In the 0−0.60 m soil profile, the θ_{fc} and θ_{wp} were 0.317 and 0.195 cm^3 cm^{-3}, respectively, resulting in an available water fraction of 0.122 cm^3 cm^{-3}. The average soil organic matter content in this plot was higher than that of the SDI plot, reaching 3.38%.

The SDI irrigation system features two drip lines per row, buried at a depth of 0.30 m and positioned approximately 1.1 m on both sides of the tree trunk. The drip lines are equipped with self-compensating drippers discharging 2.1 L h^{-1} at a pressure of 100 kPa (Multibar C model, Irritec®) spaced 0.5 m apart. The SPR irrigation system is characterised by two micro-sprinklers per tree, delivering a flow rate of 200 L h^{-1} at a pressure of 150 kPa, wetting an area almost corresponding to the projection of the mandarin tree canopy.

The SDI plot was managed with a high-frequency irrigation regime aimed at preventing crop water stress. At this aim, the SWC along the root zone was monitored with the Drill & Drop sensor, ensuring that the values remained consistently close to θ_{fc}. In contrast, the SPR plot was managed by the farmer following a nearly uniform, lower-frequency irrigation schedule. Irrigation events typically occurred according to a biweekly plan, unless there were no rainfall events, and water application volumes were determined by his practical experience.

2.2. Climate and micrometeorological data

Air temperature, T (°C), relative humidity, RH (%), thus vapour pressure deficit, VPD (kPa), precipitation, P (mm), solar radiation, SR (MJ m^{-2} h^{-1}), wind speed, u (m s^{-1}) were recorded, with a time-step of 30 min, by a WatchDog 2000 series weather station (Spectrum Technologies, Inc., Aurora, IL, USA) installed inside the field (Fig 1). The hourly average values of meteorological variables were used to estimate the hourly grass reference evapotranspiration, ETo (mm h^{-1}), using the FAO-56 Penman-Monteith equation (Allen et al., 1998).

2.3. Stem water potential estimations

Continuous monitoring of stem water potential (Ψ_{mt}) was conducted using four commercial microtensiometers (FloraPulse, Davis, CA, USA), with two sensors installed in the trunk of a representative tree in each plot. These microtensiometers (MT) were connected to the FloraPulse data logger, which automatically records Ψ_{mt} every 20 minutes and uploads the data to the FloraPulse cloud. Sensor calibration is not required before field installation, as each MT is individually factory-calibrated (https://www.florapulse.com/resources). The MT installation, following the manufacturer's recommendation, involved several key steps to ensure precise attachment and optimal functioning. The tree trunk phloem tissue was exposed by carefully removing the bark from a selected flat section. A stainless-steel sleeve was inserted into the trunk with a hammer to position it securely. A drill was used to penetrate the sleeve and drill into the xylem tissue, removing the tissue within. This cavity was filled with a kaolin-based mating compound to create a stable interface between the sensor and the tree's xylem. The hydrated MT was then placed into the compound. To seal the installation, a stainless-steel cap was added to close the sleeve, and the sleeve's exterior was covered with silicone to ensure an airtight and waterproof seal. Finally, thermal insulation was applied by wrapping the sensor to minimise external temperature fluctuations. The sensors equilibrated with the mandarin trunk through the mating compound within two days of installation. The collected data were then aggregated at an hourly scale, and the average values recorded from the two MT were used for analysis.

Estimation of stem water potential by Scholander pressure chamber (Ψ_{pc}) was conducted on the same mandarin trees monitored with MT, following the protocols suggested by Turner (1988). During the two irrigation seasons, Ψ_{pc} were carried out throughout the day on two healthy stems, each wrapped in an aluminium foil approximately one hour before the test, and the average value was considered. Specifically, Ψ_{pc} tests were scheduled considering the farmer's irrigation management carried out in the SPR plot, aiming to capture potential water stress three days before irrigation and to assess plant water status recovery the following day. This low-frequency irrigation management was expected to induce marked fluctuations in soil moisture and, consequently, in tree water status. In the SDI plot, Ψ_{pc} tests were performed simultaneously with those in the SPR plot, regardless of whether they occurred before or after irrigation application, since this irrigation regime involved more frequent water application. At each measurement day, Ψ_{pc} tests were performed every three hours, from 06:00 am to 06:00 pm, in the 2022 irrigation season, and every two hours, from 06:00 am to 08:00 pm, in the 2023 irrigation season.

To evaluate the short-term responsiveness of Ψ_{mt} to external perturbations, two shading experiments were conducted at the peak and end of summer to assess the sensor behaviour under different *SR* conditions. An 80% black shading net was applied from noon on 3 August 2023 until the same time the following day. During the shading trial, Ψ_{pc} measurements were also performed at two-hour intervals from dawn to dusk. The same trial was replicated on 21−22 September.

2.4. Statistical analyses

Correlation analysis was performed using data collected simultaneously from MTs and the PC over the two experimental years to validate Ψ_{mt} against Ψ_{pc} for both irrigation regimes.

Scatter group analysis was performed to assess the correlation between Ψ_{mt} and VPD across different phases of tree diurnal water dynamics, and 90% confidence ellipses were determined for each group for the two monitored mandarin trees under different irrigation regimes.

Time-lagged normalised cross-correlation was performed in MATLAB programming software (v.9.14.0, R2023a, The MathWorks, Inc., Natick, MA, USA) using 1-minute interpolated continuous data between ETo and Ψ_{mt}. Normalised cross-correlation assesses the correlations between two temporally shifted time series datasets (Chatfield and Xing 2019), repeatedly computing the Pearson Product Moment Correlation (cross-correlation) Coefficient (XCC) after each shift. In this study, the resulting 'offset' values, each representing a 1-minute interval, are identified at the highest absolute normalised XCC within the series and indicate the time shift between the two specific time series. The time shift and XCC were computed on a daily basis across both seasons for the SDI and SPR irrigation regimes.

3. Results

3.1. Climate conditions, irrigation amounts, and soil water content dynamics

Maximum vapour pressure deficit (VPD_{max}), daily crop reference evapotranspiration (ETo), daily maximum air temperature (T_{max}), precipitation (P) and irrigation amounts (I) delivered in the SDI and SPR plots for the two monitored irrigation seasons (2022−2023) are shown in Fig. 2. The study period was characterised by consistently high temperatures, with T_{max} values regularly exceed 30 °C in both seasons. Extreme T_{max} peaks reached 44.2 °C in August 2022 and 45.4 °C in July 2023. However, in 2022, the variability of T_{max} increased markedly toward the end of the season, whereas in 2023, greater T_{max} variability was observed primarily during the early part of the season.

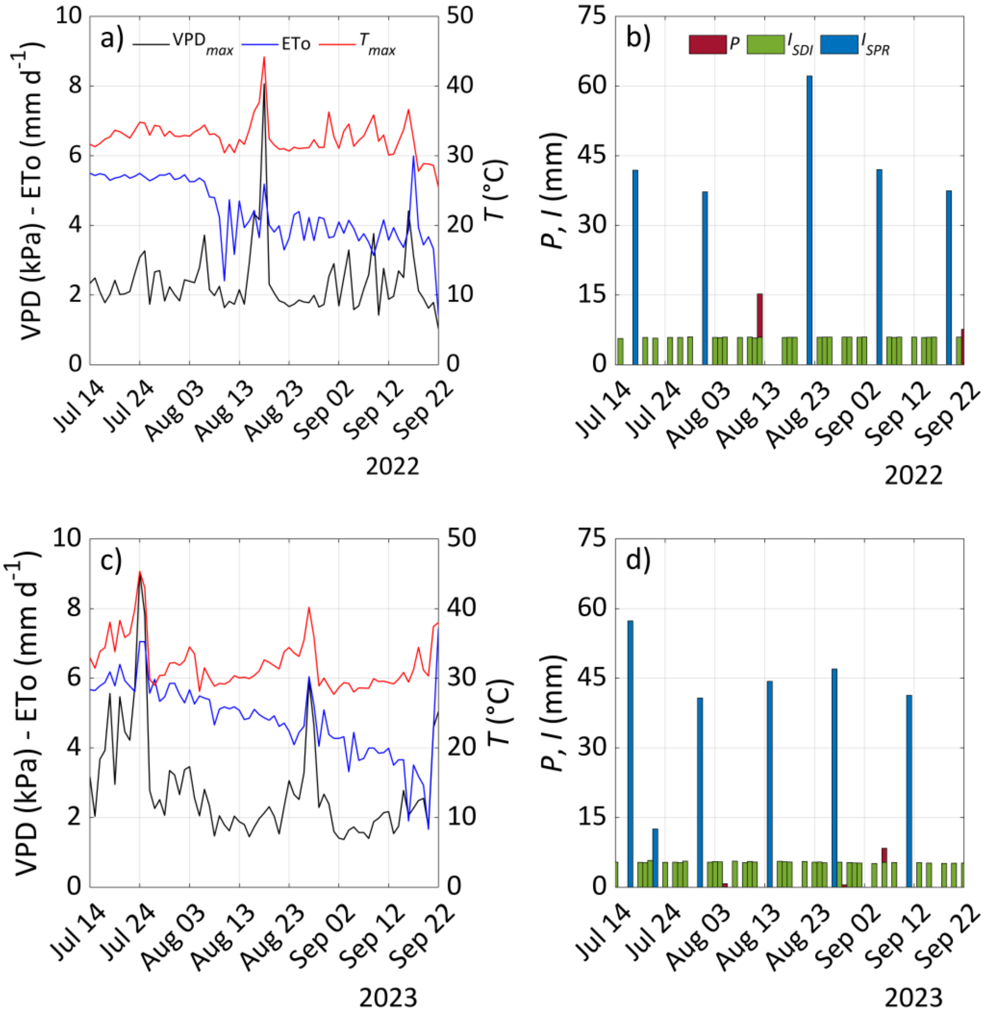

Fig. 2 *Time evolution of maximum vapour pressure deficit (VPD$_{max}$), daily reference evapotranspiration (ETo) and maximum daily temperature (T_{max}) during* ***a)*** *the 2022 and* ***c)*** *the 2023 irrigation seasons. Precipitation and irrigation amount under the SDI (I_{SDI}) and SPR (I_{SPR}) irrigation regimes for* ***b)*** *the 2022 and* ***d)*** *the 2023 irrigation seasons*

Daily ETo values were generally greater than 5.4 mm d^{-1} until early August, after which they gradually declined. Late-season peaks reached 6.0 mm d^{-1} on 17 September 2022 and 7.4 mm d^{-1} on 22 September 2023, both associated with concurrent high temperatures, low *RH*, and increased wind speed (*u* data not shown). For the observation periods, total ETo was 340.38 and 367.87 mm in 2022 and 2023, respectively.

VPD$_{max}$ exhibited pronounced diurnal fluctuations in both seasons. Notably, the 2023 season experienced a higher frequency of days in July with VPD$_{max}$ values exceeding 4 kPa and peaking up to 9 kPa, indicating a stronger atmospheric water demand compared to 2022, which showed a single extreme event on 18 August. Extreme VPD events likely intensified crop transpiration rates, thereby exposing plants to water stress conditions, particularly in the presence of limited soil moisture availability.

Rainfall during the monitoring periods consisted of three events in 2022 (15.2 mm on 12 August, 2.8 mm on 24 August, and 4.4 mm on 21 September) and two in 2023 (2.8 mm on 4 August and 8.4 mm on 6 September).

Figure 2b and d illustrate the SPR irrigation events (blue bars) during the Ψ_{mt} monitoring period. Across the full irrigation season (June-October), the farmer applied nine irrigation events in both 2022 and 2023, corresponding to total irrigation volumes of 296.43 mm and 351.66 mm, respectively. In contrast, 59 and 54 irrigation applications were employed in the SDI plot, delivering seasonal irrigation volumes of 323.21 mm and 292.94 mm, in 2022 and 2023, respectively.

Soil water content dynamics for the SDI plot are shown in Fig. 3a and b for the 2022 and 2023 seasons, respectively.

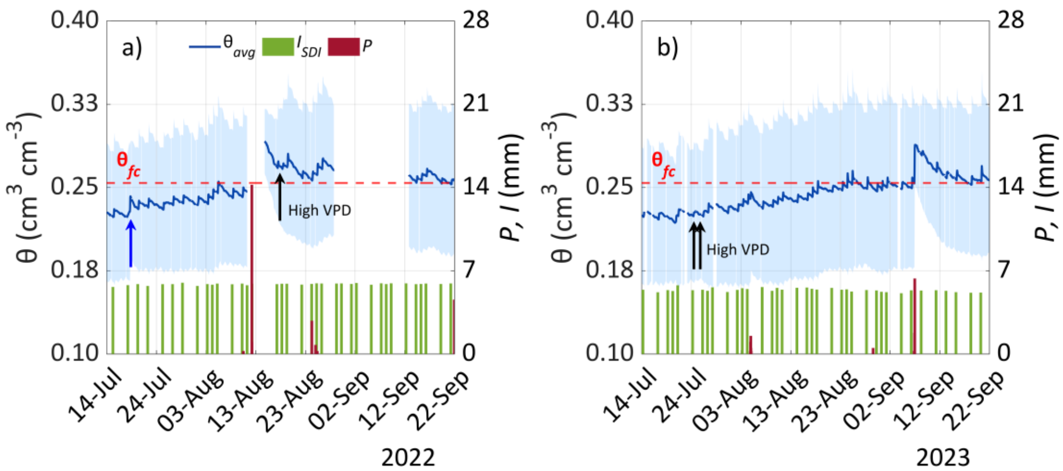

Fig. 3 *Daily dynamics of the average soil water content (θ_{avg}) and its standard deviation (blue shaded area) along the 0–0.6 m soil profile within the SDI plot during **a)** the 2022 and **b)** the 2023 irrigation seasons. Irrigation events (I_{SDI}) and precipitation (P) are also shown. The red dashed horizontal line indicates the soil water content at field capacity (θ_{fc}). The blue arrow indicates a supplementary irrigation event applied by the farmer*

Across the 0–0.60 m soil profile, SWC values ranged from 0.160 to 0.376 cm^3 cm^{-3}. As shown, the frequent irrigation management adopted in this plot successfully maintained well-watered conditions, with average SWC consistently close to the red horizontal line representing the θ_{fc} threshold. It is noteworthy that the SWC values marked by the black arrows in Fig. 3a and 3b exhibited no appreciable variation in response to the VPD peaks recorded on 18 August 2022 (Fig. 2a) and 24−25 July 2023 (Fig. 2c), respectively. In Fig. 3a, the blue arrow indicates an increase in SWC resulting from a small irrigation event applied by the farmer using the existing micro-sprinkler system, aimed at moistening the soil surface to facilitate mechanical weed control.

3.2. Stem water potential monitored with microtensiometer

Temporal patterns of Ψ_{mt} under frequent irrigation (via SDI) and ordinary irrigation (via SPR) regimes during the 2022 and 2023 growing seasons are shown in Fig. 4. Continuous MT monitoring revealed the difference in Ψ_{mt} dynamics between the two regimes, evident both on an hourly basis and on longer time intervals (i.e., on a day-to-day time scale). Specifically, diurnal changes in Ψ_{mt} showed the expected hourly pattern, with minimum values occurring during midday hours, corresponding to the increase in air temperature, *SR* and VPD from dawn to midday, followed by a gradual rebound of Ψ_{mt} in the afternoon and nighttime. Dependence of Ψ_{mt} on ETo, VPD and *SR* was particularly evident during the heat-wave events that occurred in both seasons. During such events, with air temperature, VPD and ETo values as high as 45°C, 8−9 kPa and 9 mm day^{-1}, respectively (Fig. 2), the lowest Ψ_{mt} values were observed (Fig. 4) for both irrigation regimes.

In the SDI plot, day-to-day changes of the Ψ_{mt} remained relatively stable compared to those recorded in the mandarin tree under the SPR regime, reflecting the stabilising effect of the high-frequency irrigation schedule, which maintained a consistent SWC across the seasons (Fig. 3). As reported in Table 1, lower coefficients of variation (*CV*) were observed in pre-dawn (Ψ_{pd}) and midday (Ψ_{md}) Ψ_{mt} compared to the SPR plot. However, Ψ_{pd} values, despite non-limiting soil water conditions, can be influenced by environmental factors. For instance, on 25 July 2023, during the heat-wave event, a high-VPD occurred (Fig. 2c), and the mandarin tree exhibited more negative Ψ_{pd} values (Fig. 4b, black arrows) compared to the preceding day, indicating an incomplete overnight recovery from atmospheric stress.

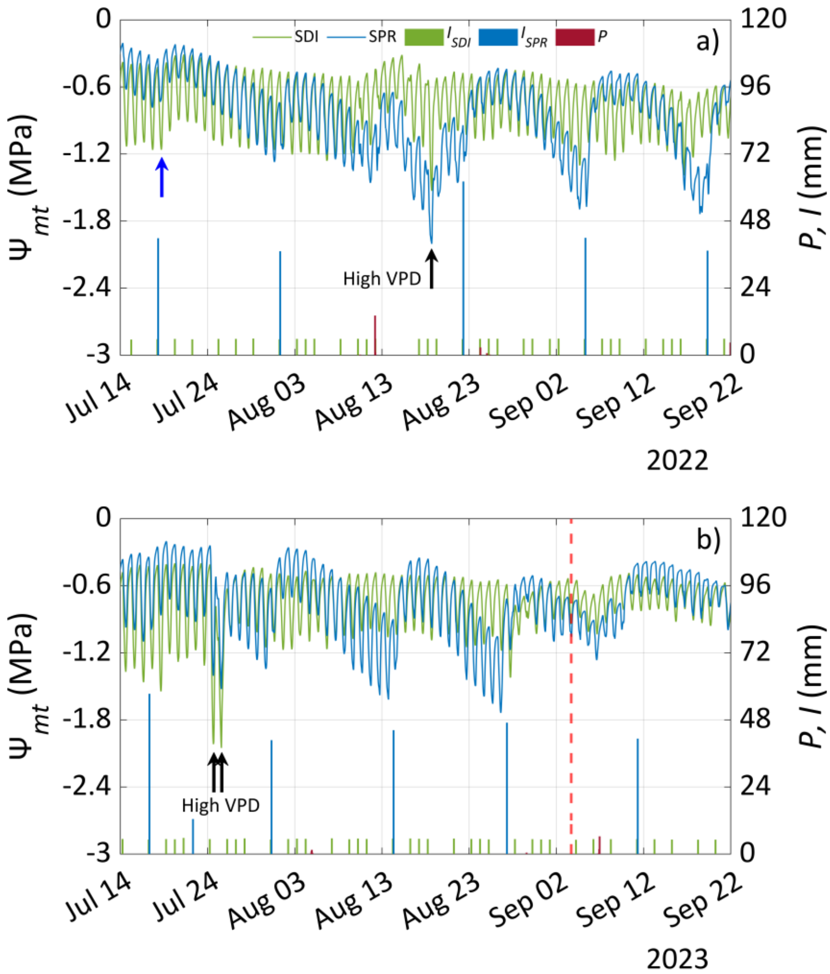

Fig.4 *Time series of Ψ_{mt} for **a**) the 2022 and **b**) the 2023 growing seasons, under both SDI and SPR irrigation regimes. Precipitation and the corresponding irrigation events of the SDI (I_{SDI}) and SPR (I_{SPR}) irrigation regimes are also shown. The blue arrow indicates a supplementary irrigation event applied by the farmer*

The most substantial recovery occurred within the first 24 hours, with increases of 40.68% from the Ψ_{pd} value recorded during the peak stress. Full recovery to pre-event levels was achieved four days later. On the same date, Ψ_{md} reached its most negative value, equal to −2.05 MPa (Fig. 4b, black arrows), indicating that Ψ_{md} is also highly responsive to environmental drivers. The atypical increase in Ψ_{mt} recorded between in early 2022 season (Fig. 4a, blue arrow), which can be ascribed to the small irrigation event previously described, highlights the MT sensitivity to short-term changes in plant water status.

Due to the low-frequency irrigation scheduling, the day-to-day changes of hourly Ψ_{mt} values in the SPR plot were more pronounced. Indeed, *CV* values (Table 1) of Ψ_{pd} and Ψ_{md} were higher compared to the SDI plot, especially in the 2022 season. Notably, in the SPR plot, a major pruning carried out on September 3rd, 2023 (indicated by the dashed red line in Fig. 4b), reduced the crop transpiration (Ye et al., 2021), dampening plant water potential fluctuations.

Regarding the Ψ_{pd}, the most negative values are usually recorded on the day of the water application, as the farmer generally begins irrigating after pre-dawn. Following each irrigation event, the tree exhibited a progressive recovery of its stem water potential over the subsequent days followed by a almost linear decrease.

Table 1 *Summary statistics of stem water potential at predawn, Ψ_{pd} (MPa), and midday, Ψ_{md} (MPa), for SDI and SPR systems across both 2022 and 2023 irrigation seasons*

Statistics	2022				2023			
	SDI		SPR		SDI		SPR	
	Ψ_{pd}	Ψ_{md}	Ψ_{pd}	Ψ_{md}	Ψ_{pd}	Ψ_{md}	Ψ_{pd}	Ψ_{md}
Min	−0.71	−1.53	−1.31	−2.00	−0.87	−2.05	−0.98	−1.74
Max	−0.31	−0.71	−0.21	−0.52	−0.40	−0.69	−0.20	−0.68
Mean	−0.48	−1.08	−0.61	−1.06	−0.53	−1.07	−0.52	−1.05
δ	0.09	0.14	0.26	0.36	0.08	0.23	0.19	0.27
CV (%)	18.22	13.00	41.81	33.50	15.88	21.65	36.73	25.61

The observed linear decline in Ψ_{mt} following the progressive soil drying, along with the onset of crop water stress, is consistent with the near-anisohydric behaviour attributed to mandarins. Unlike other citrus species, mandarins tend to lower their water potential in response to decreasing soil moisture availability within the irrigation cycle (Romero-Trigueros et al., 2021). The extent and rate of this recovery depended primarily on the initial Ψ_{pd} values before the irrigation event, which can also be influenced by external factors such as VPD. Table 2 shows all pre-irrigation Ψ_{pd} values for SPR plot, together with the corresponding daily percentage recovery relative to the pre-irrigation condition. In all water applications, Ψ_{pd} showed a marked recovery on the first day after the irrigation event, followed by a reduced rate of recovery over the subsequent days.

In the most stressed periods, maximum recovery increases up to 40% of the initial value (Table 2, bold values) with the highest recovery rate after one day (43.1%) when the most negative initial Ψ_{pd} values (e.g., −1.32 MPa) occurred. Additionally, the effect of irrigation ends within the first 24−48 hours, after which the recovery tends to stabilise or decline. Notably, the sharp decrease of −166.94% is attributable to the VPD peak event that occurred in 2023 (Fig. 2c), which likely counteracted the benefits of irrigation.

Table 2. *Daily percentage recovery of predawn stem water potential, %ΔΨ_{pd} (t), relative to the Ψ_{pd} pre-irrigation condition for both irrigation seasons in the SPR plot*

Year	Date	Ψ_{pd} pre-irrig. (MPa)	%ΔΨ_{pd} (t)						
			$t = 1$	$t = 2$	$t = 3$	$t = 4$	$t = 5$	$t = 6$	$t = 7$
2022	18 Jul	−0.35	24.54	10.90	−2.14	−6.79	−10.36	−7.94	−12.46
	1 Aug	−0.74	**28.42**	8.50	−1.17	−4.80	−7.84	−12.29	−7.01
	22 Aug	−0.98	**35.00**	12.11	5.71	2.08	−0.68	−2.81	−4.38
	5 Sep	−1.24	**43.11**	15.49	4.37	−2.54	0.71	−0.23	−5.31
	19 Sep	−1.32	**43.72**	11.91	5.26	4.23	2.37	−0.32	−1.27
2023	17 Jul	−0.34	26.84	13.64	−7.44	−5.10	−9.39	6.52	2.83
	22 Jul	−0.28	8.01	3.48	−166.94	82.81	−7.63	7.50	−3.14
	31 Jul	−0.62	43.23	14.82	−1.54	−2.17	−12.59	−7.66	−7.90
	14 Aug	−0.90	**40.75**	16.95	3.36	−1.53	−6.90	−5.46	−8.83
	27 Aug	−0.73	**18.59**	9.59	2.37	−4.35	−6.52	−15.68	−0.15
	11 Sep	−0.41	4.31	−0.33	−1.90	−5.88	−9.88	−0.64	−5.93

Following this extreme event, Ψ_{pd} did not return to its pre-event level until the subsequent water application (Fig. 4b), suggesting a plant's hydraulic dysfunction. The most negative Ψ_{pd} (−1.31 MPa) and Ψ_{md} (−2.00 MPa) values (Fig. 4a, black arrow) recorded in the SPR plot were again attributed to the high VPD and ETo levels observed during a heat-wave event, in this case registered on 18 August 2022 (Fig. 2a), when the farmer withheld irrigation due to a preceding rainfall event.

3.3. *Microtensiometer vs pressure chamber*

An example of the daily patterns of stem water potential estimated using the pressure chamber (Ψ_{pc}) and the microtensiometer (Ψ_{mt}) along with vapour pressure deficit (VPD), over two days of the 2023 season for both irrigation regimes is illustrated in Fig. 5. The data refer to Ψ_{pc} tests conducted three days before (Fig. 5c) and one day after (Fig. 5d) the irrigation event in the SPR plot; the simultaneous tests performed in the frequently irrigated SDI plot are representative of post-irrigation (Fig. 5a) and pre-irrigation (Fig. 5b). Both MT and PC methods effectively distinguished the impacts of the two different irrigation regimes on tree water status, showing significant differences in stem water potential under similar VPD conditions. In general, Ψ_{mt} values were consistently less negative than Ψ_{pc} values, with the differences between the two methods being greater in the afternoon and more pronounced before irrigation (Fig. 5b and c for SDI and SPR irrigation regimes, respectively).

For both irrigation regimes, the most negative values of the Ψ_{pc} were usually recorded at 14:00. Conversely, the minimum value of the Ψ_{mt} generally occurred approximately two hours later, emphasising a certain time lag between the two methods. Additionally, the higher VPD were recorded at midday on both sampling days, further indicating a time lag of two and four hours between the atmospheric water demand and Ψ_{pc} and Ψ_{mt}, respectively.

Daily pattern of Ψ_{mt} provides to identify the well-known three distinct time slots of plant water dynamics (Fig. 5): (i) the equilibrium phase (00:00−07:00, blue line), (ii) the emptying phase (08:00−16:00, orange line), and (iii) the refilling phase (17:00−23:00, green line). These time slots and/or phases were used to assess the scatter group analysis between Ψ_{mt} and VPD, which is discussed in the next Section.

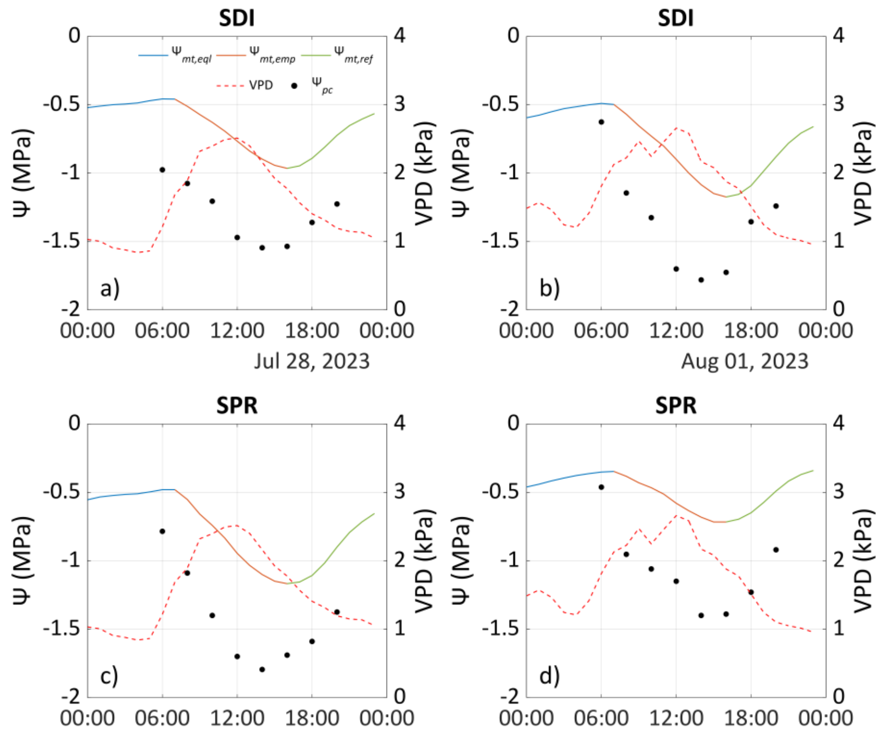

***Fig. 5** Daily dynamics of Ψ_{pc} and Ψ_{mt} at the equilibrium ($\Psi_{mt,eql}$), emptying ($\Psi_{mt,emp}$) and refilling ($\Psi_{mt,ref}$) phases under SDI and SPR irrigation regimes. Vapour pressure deficit (VPD) data are also plotted*

Figure 6 illustrates the two shading experiments conducted under similar conditions of solar radiation (*SR*) to assess the ability of Ψ_{mt} and Ψ_{pc} to evaluate the plant reaction to covering and uncovering with a black shade net. The MTs responded readily to the shading experiment, especially during the peak of summer (Fig. 6a and b), in contrast to the attenuated response observed at the end of summer (Fig. 6c and d). This dynamic was evident from the change in the slope of the Ψ_{mt} vs time relationship, which decreased after covering and increased after uncovering. The application of the shade net resulted in consistently less negative Ψ_{mt} values during the covered intervals, as a consequence of the physiological response to reduced transpiration demand due to decreased incident *SR*. Upon removal of the shade, Ψ_{mt} immediately declined, as a consequence of an increase in transpiration rate and a swift shift in plant water status, suggesting a prompt responsiveness of the MT to the microclimate change. Similar trends were observed for Ψ_{pc} in both shading experiments.

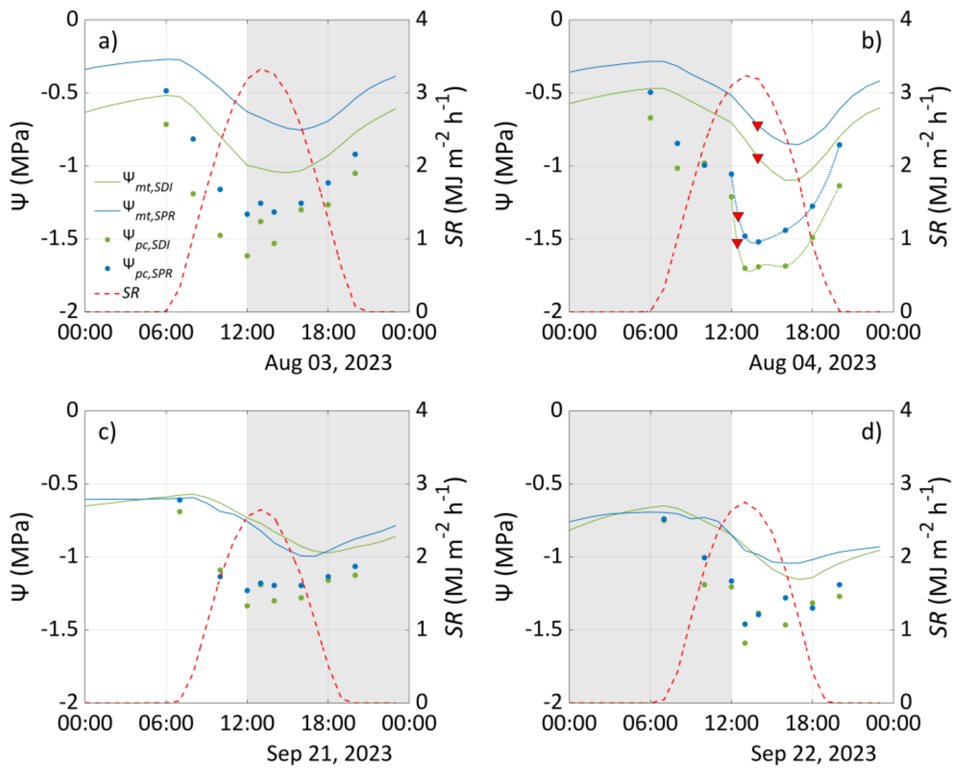

Fig. 6 *Daily evolution of Ψ_{mt} and Ψ_{pc} under the SDI ($\Psi_{mt,SDI}$ and $\Psi_{pc,SDI}$, respectively) and the SPR ($\Psi_{mt,SPR}$ and $\Psi_{pc,SPR}$, respectively) irrigation regimes, along with solar radiation (SR) levels during the shading tests. The grey areas correspond to the trees' shading period. For both irrigation regimes, red triangles represent the Ψ_{stem} values of both PC and MT methods at their respective time constants (τ), defined as the time following a disturbance when 63% of the total change has been recorded*

Compared to Ψ_{mt}, Ψ_{pc} remained responsive to changes in microclimatic conditions even in late summer. It is worth noting that, following the disturbance events, Ψ_{pc} values remained consistently more negative than Ψ_{mt}. This divergence is related to the dynamics of both Ψ_{mt} and Ψ_{pc} at the time of disturbance: at the moment of covering, Ψ_{stem} was in the decreasing stage within the diurnal cycle and shading halted the decreasing trend of Ψ_{stem}. This effect was observed using both techniques (MT or PC), but with a different dynamic. The Ψ_{pc} stabilised almost immediately, while the Ψ_{mt} displayed a more gradual response, slowing down but continuing to decrease for up to four hours before stabilising (Fig. 6a and 6c). Interestingly, these contrasting dynamics were evident not only during the transition from full sunlight to shade but also upon shade to full sunlight. Ψ_{pc} decreased almost immediately after exposure to sunlight (Fig. 6b and d), reaching a minimum within two hours; in contrast, Ψ_{mt} showed a slower response, reaching the minimum 4−5 hours later.

To further characterise the dynamic response of the sensor-tree complex, an approximate estimation of the time constant (τ), defined as the time required to reach 63% of the change following a disturbance in a first-order system (Nobel, 2009; Phillips et al., 2004), was calculated for both Ψ_{mt} and Ψ_{pc}. The calculation was limited to the uncovering phase of the experiment performed at the peak of summer (3−4 August session, Fig. 6b), when the dynamics of the changes were sufficiently large. For Ψ_{pc}, 63% of the change occurred 29 and 32 minutes after disturbance (sunlight exposure), respectively, in SDI and SPR; in contrast, Ψ_{mt} reached 63% of the total change after 122 and 125 minutes (Fig. 6b, filled triangles).

Linear regression analysis (Fig. 7) was performed between Ψ_{mt} and Ψ_{pc} for the SDI and SPR irrigation regimes, pooling the data collected in the two irrigation seasons.

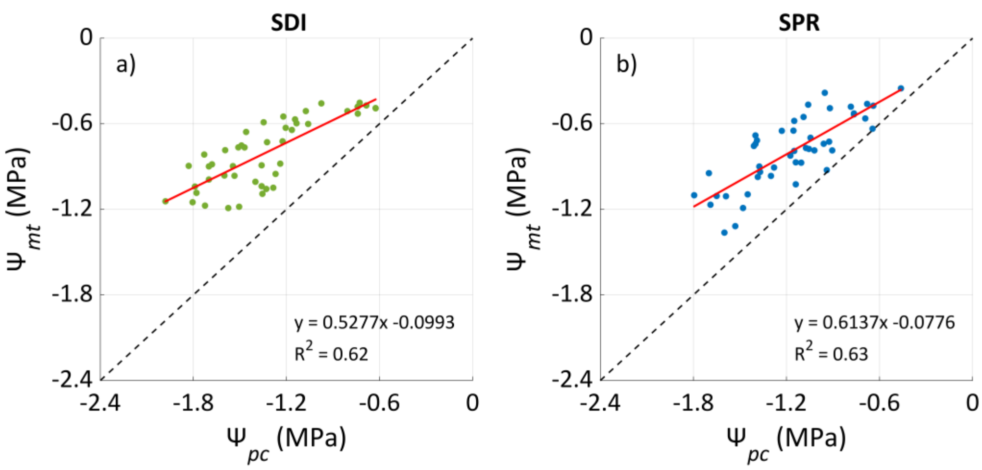

***Fig.** 7 Linear relationship between stem water potential estimated with the microtensiometers, Ψ_{mt}, and the pressure chamber, Ψ_{pc}, under the **a)** SDI and **b)** SPR irrigation regimes*

The relationship between Ψ_{mt} and Ψ_{pc} exhibited similar slopes and coefficient of determination, with R^2 of 0.62 ($p < 0.0001$) in the SDI plot (Fig. 7a) and R^2 of 0.63. ($p < 0.0001$) in the SPR plot (Fig. 7b), showing a significant relationship between the Ψ_{stem} estimated by the two methods. However, the relationship between Ψ_{mt} and Ψ_{pc} deviated from the identity line, especially for the SDI plot, with more negative values for Ψ_{pc} compared to Ψ_{mt} (Fig. 7a).

3.4. Correlation between Ψ_{mt} and vapour pressure deficit

Figure 8 shows the relationship between Ψ_{mt} and VPD under SDI and SPR irrigation regimes using scatter plots of hourly data collected in both years during the monitoring period. The scatterplots generally align with the expected negative relationship between Ψ_{mt} and VPD. However, the two irrigation regimes exhibited different levels of dispersion, with the frequently irrigated SDI (Fig. 8a and c) showing lower variability than the ordinary irrigated SPR plot (Fig. 8b and d). In the SDI plot, where SWC remained consistently stable over time (Fig. 3a and b), Ψ_{mt} showed a strong sensitivity to VPD. This relationship was particularly evident in the 2022 season, in which VPD variability was comparatively lower ($R^2 = 0.57$, $p < 0.0001$; Fig. 8a). Conversely, in the SPR irrigation regime, Ψ_{mt} displayed weaker correlations with VPD, indicating a stronger influence of SWC on Ψ_{mt} dynamics.

Further analysis of the scatterplots shows that, even at the same VPD level, Ψ_{mt} values vary depending on the time of day. Specifically, higher water potential values were recorded in the early morning, while the lowest values were observed during midday and early afternoon. To capture these diurnal dynamics, data were divided into the three distinct time slots mentioned before. For each time slot, a 90% confidence ellipse was calculated to better visualise the distribution of data. These phases reflect the tree's water dynamics throughout the day: an equilibrium phase in which stem and soil water potentials are balanced under minimal transpiration (Yang et al., 2013; Zhang et al., 2023); an emptying phase in which increasing VPD drives water loss from plant reserves; and a refilling phase in which decreasing VPD allows plants to replenish water stores (Phillips et al., 2004; Vogel et al., 2017).

The analysis showed significant variation between the time slots and the irrigation regimes across both seasons. In the SDI irrigation regime and for both seasons (Fig. 8a and c), Ψ_{mt} vs VPD values recorded in the equilibrium phase exhibit a small size of the ellipse, especially in the 2023 irrigation season (Fig. 8c), indicating more concentrated data around the mean (−0.54 MPa for the 2022 season and −0.58 MPa for the 2023 season).

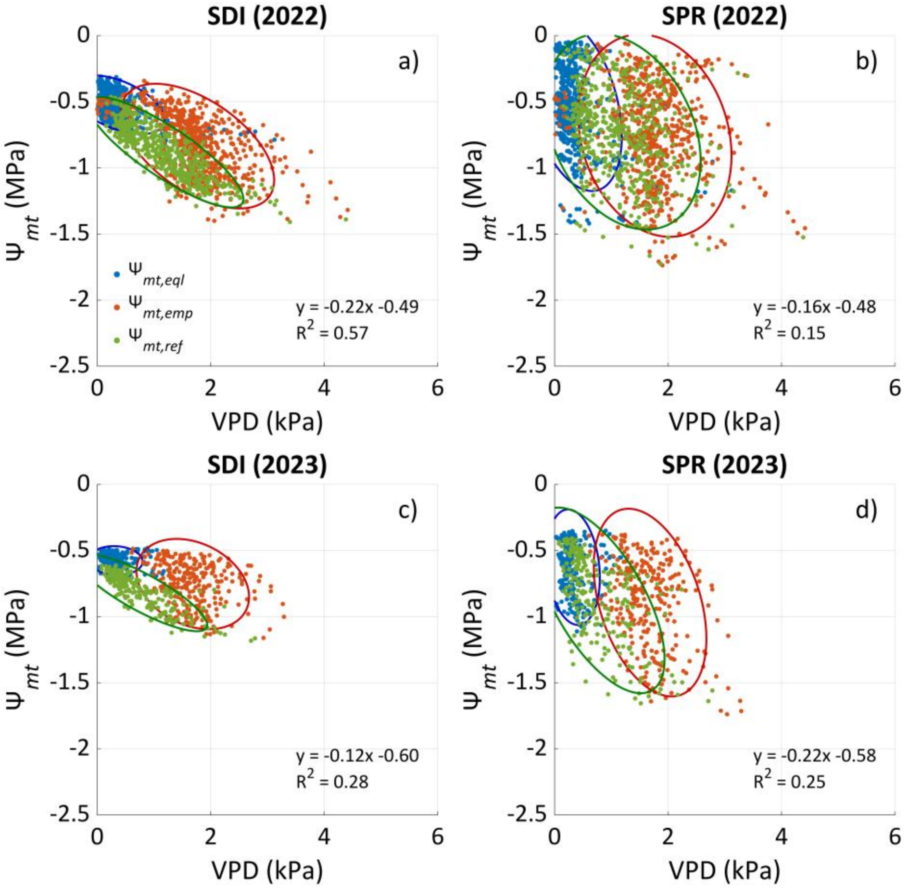

Fig. 8 *Scatter group plot between Ψ_{mt} and VPD in the three distinct dynamic hydraulic phases of the tree (00:00−07:00 equilibrium, $\Psi_{mt,eql}$, 08:00−16:00 emptying, $\Psi_{mt,emp}$, and 17:00−23:00 refilling, $\Psi_{mt,ref}$) for the 2022 and 2023 irrigation seasons under (**a**, **c**) the SDI and (**b**, **d**) the SPR irrigation regimes. The ellipse function draws a 90% confidence level for each phase group*

For the emptying phase, the ellipse is larger than in the equilibrium phase, suggesting greater variability in the data. For the refilling phase, a more elongated ellipse is shown, indicating a stronger correlation between Ψ_{mt} and VPD ($R^2 = 0.70$ for both irrigation seasons). In the SPR irrigation regime and for both seasons (Fig. 8b and d), the sizes of the ellipses of the three distinct time slots are larger than in the SDI plot, suggesting less predictability in the data, with a weaker correlation between Ψ_{mt} and VPD, due to circular shapes of the ellipses, especially in the 2022 irrigation season

(Fig. 8b). Moreover, the data are more diffusely and irregularly distributed, reflecting greater variability within the group.

3.5. Sensitivity of Ψ_{mt} to reference evapotranspiration

Time-lagged normalised cross-correlation analysis was used to examine the interpolated 1-minute time series (Phillips et al., 1997, 2004) datasets of ETo and Ψ_{mt} for SDI and SPR irrigation regimes across the 2022 and 2023 growing seasons.

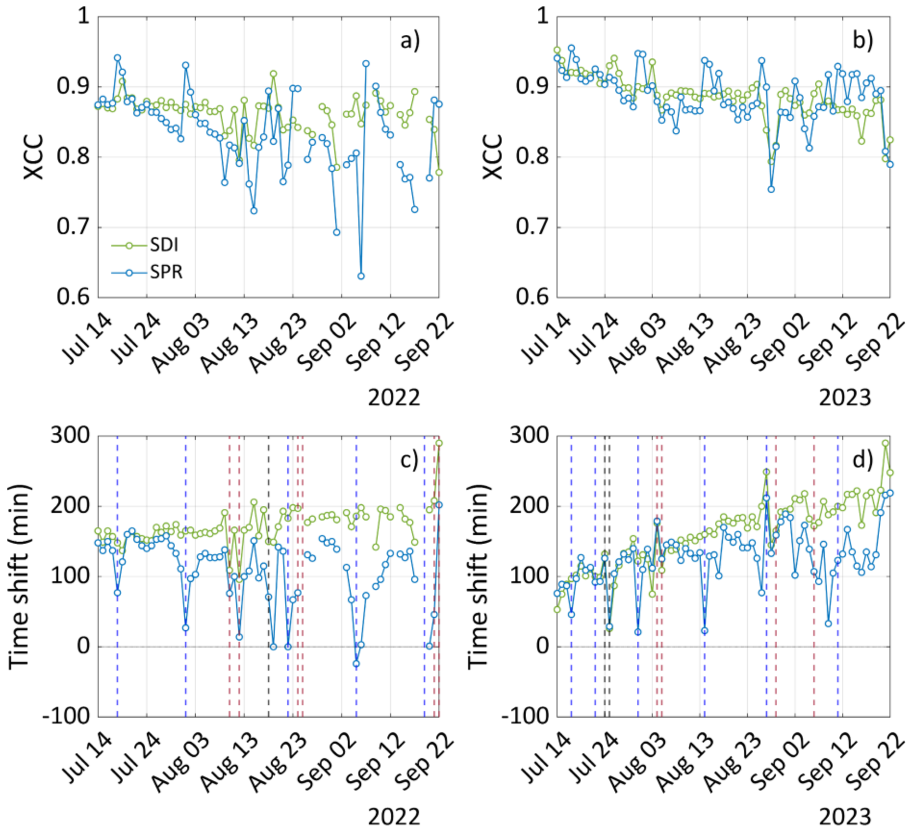

Fig. 9 *Daily dynamics of (**a**, **b**) maximum normalised cross-correlation coefficient (XCC) and (**c**, **d**) corresponding time shift between Ψ_{mt} and daily reference evapotranspiration (ETo) under the SDI and SPR irrigation regimes across both seasons. Black dashed lines denote days with VPD_{max} > 6 kPa; red dashed lines indicate precipitation events; and blue dashed lines show farmer irrigation events in the SPR plot*

Figure 9 illustrates the highest values of normalised cross-correlation coefficient (XCC, Fig. 9a and b), and the daily values of the time shifts (Fig. 9c and d) for both seasons. Additionally, the maximum water pressure deficit (VPD_{max}) values exceeding 6 kPa (black dashed lines), the precipitation (red dashed lines), and, only for the SPR plot, the irrigation events (blue dashed lines) are also displayed (Fig. 9c and d).

For both seasons, the highest XCC values declined over time in both irrigation regimes, with fluctuations on days of high VPD_{max} or rainfall. In the SPR plot, XCC also responded to farmer-applied irrigation events, and on these days, time shifts varied markedly.

To characterise the dynamic response of the sensor-tree complex over a longer period than the two-day shading trials, daily values of Ψ_{mt} time constant (Fig. 10) were estimated from the inversion of the relation between τ and the phase delay (φ), calculated from the normalised cross-correlation analysis performed against ETo, for the response of a first-order system to a sinusoidal input with angular frequency ω, according to the following equation:

$$\tau = \frac{-tan(\varphi)}{\omega} \quad (1)$$

with ω equal to $2\pi f$ and f representing the frequency of the 24-hour diel cycle, with the simplifying assumption that ETo follows a sinusoidal pattern (Monteith and Unsworth, 2008).

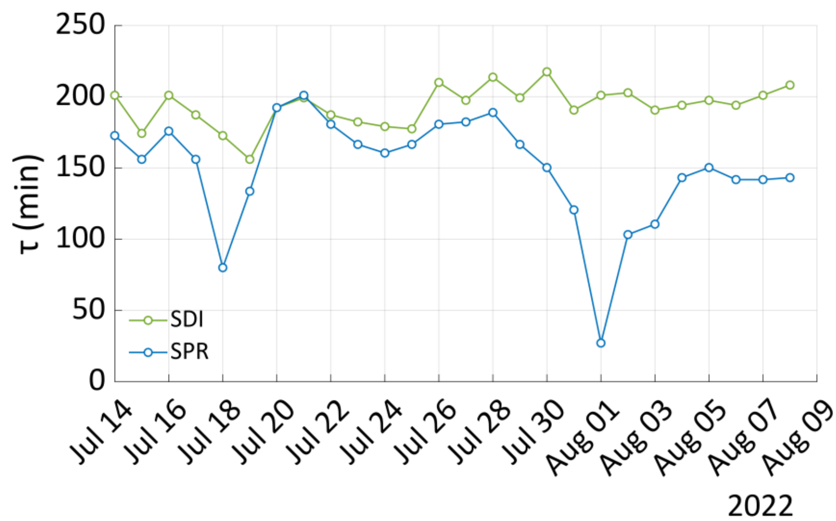

Fig. 10 *Daily changes of time constant (τ) for Ψ_{mt} observations under the SDI and SPR irrigation regimes over one SPR irrigation cycle in the 2022 season. Values reported were estimated, in cloudless days, from phase lags obtained by cross-correlation between ETo and Ψ_{mt}*

The analysis was limited to cloudless days of the 2022 season (Fig. 9c). Data are shown for a period covering and extending over a full cycle of SPR irrigations (Fig. 10). Over the observation period, Ψ_{mt} time constant showed a different dynamic between SDI and SPR irrigation regimes. In SDI, τ resulted fairly stable, with minor fluctuations during the observation period, whereas in SPR, daily τ changes exhibited a distinctive pattern within the irrigation cycle, decreasing progressively in the days following irrigation, then increasing sharply after the subsequent irrigation event (Fig. 10).

4. Discussion

Although this study was not specifically designed to assess water use efficiency, the differing irrigation frequencies and volumes applied generated distinct soil moisture dynamics, providing valuable conditions for evaluating plant water status using microtensiometers and assessing their performance in a mandarin orchard. Frequent water applications through SDI maintained relatively stable SWC over time, as evidenced by soil moisture sensor data (Fig. 3), while the farmer's 14-day irrigation schedule caused pronounced fluctuations in Ψ_{mt} and, consequently, in soil water content. These contrasting irrigation regimes offered an effective framework to evaluate the sensor's sensitivity in detecting variations in stem water potential under dynamic soil moisture and atmospheric conditions, representative of Mediterranean climates.

Vapour pressure deficit is an environmental variable which, under steady-state SWC conditions, regulates plant water relations and, in turn, stem water potential by affecting leaf transpiration and water transport (Mayr, 2021). In the monitored period, VPD_{max} frequently exceeded 3 kPa and peaked up to 9 kPa, especially in the 2023 season (Fig. 2c). On such extreme days, even when the soil water content was not a limiting factor, a prolonged but moderate increase in VPD and air temperature led to hydraulic dysfunctions, including limited stomatal closure, elevated transpiration, and more negative plant water potentials (Schönbeck et al., 2022). These phenomena were observed in the mandarin tree within the SDI plot (Fig. 4b, black arrows), in which well-water conditions were ensured by high irrigation frequency, maintaining SWC nearly at the field capacity (Fig. 3a and b). Exposure to high VPD conditions led to a noticeable decline in Ψ_{pd} values on the following morning compared to pre-event values, suggesting that plants were unable to fully recover overnight from the stress imposed by these extreme atmospheric demands. These results align with those obtained in cotton by Christenson et al. (2024), in which the plants were subjected to continued, high evaporative demand conditions. In our study, the most significant recovery (40.68%) occurred within the first 24 hours, yet full restoration of pre-event levels required up to four days. The observed recovery dynamics align with previous studies on mandarin trees' hydraulic responses under fluctuating atmospheric demands (Dzikiti et al., 2010). Notably, the absence of full recovery in the SPR-irrigated tree (Table 2 and Fig. 4b, black arrows) further indicates that less frequent irrigation exacerbates these delays, likely due to insufficient soil water availability.

Under constant SWC conditions, a relatively stable VPD (Fig. 2a) satisfactorily drives Ψ_{mt}, especially during the 2022 season (Fig. 8a, $R^2 = 0.57$). These results align with those in well-watered kiwi fruits (Di Biase et al., 2025), pear (Blanco and Kalcsits, 2023), apple (Gonzalez Nieto et al., 2023) and grapevine (Pagay, 2022). Focusing on the refilling phase (Fig. 8a and c, green ellipse), the correlation between Ψ_{mt} and VPD strengthens considerably, reaching an R^2 of 0.70 in both irrigation seasons. Moreover, it is interesting to note that the separation between morning and afternoon data is preserved, reflecting an underlying hysteresis daily cycle that can be recognised even by pooling all the seasonal data gathered throughout each year of observation, with data dispersed within a well-defined envelope over an approximately elliptical boundary (Fig. 8a and c). Even if specific data on the hourly-based relationship between Ψ_{mt} and VPD are not available for mandarin, a similar dispersion for the Crop Water Stress Index (CWSI), which is indirectly linked to water potential, can be inferred for this citrus crop (Appiah et al., 2022, figure 8). In tree species with significant capacitance effects, such separation can be expected by observing these relations within a short-term diurnal cycle, often showing a hysteresis-like pattern because of the lag between potential transpiration demand and root water uptake (Phillips et al., 1997, 2004; Zhuang et al., 2014).

In contrast, the SPR irrigation regime exhibited weaker correlations between Ψ_{mt} and VPD across the three plant water dynamic phases (Fig. 8b and d), with a larger scatter and overlap of observations of both the emptying (red dots) and refilling (green dots), suggesting no steady-state condition of SWC was achieved. This variability was particularly evident during the equilibrium phase (Fig. 8b and d, blue ellipse), where Ψ_{mt} values spanned from well-watered to water-stressed soil moisture conditions.

Given that Ψ_{pd} reflects equilibrium between the stem and soil water potential under minimal transpiration (Yang et al., 2013; Zhang et al., 2023), these fluctuations suggest that Ψ_{mt} under the SPR irrigation regime was predominantly influenced by soil water potential rather than atmospheric demand (VPD). During the most water-stressed periods, the SPR irrigated mandarin trees displayed marked physiological responses to the farmer's irrigation events, with Ψ_{pd} recovering up to 40% of the pre-irrigation value (Table 2) within 24 hours post watering, highlighting the tree's capacity to respond rapidly when relieved from severe water deficit. Most of the recovery occurred within the first 24−48 hours, after which the tree's water status improvements plateaued or declined, indicating a limited plant's recovery window. Overall, the ability of trees to rapidly restore physiological processes after irrigation highlights the importance of timely water management in mitigating the impacts of drought and supporting tree health and productivity (Cermak et al., 1993; Jamshidi et al., 2021).

To evaluate the microtensiometers' ability to quantify stem water potentials relative to known and traditional approaches, a comparison was performed with those estimated using a pressure chamber. Diurnal observation of Ψ_{mt} and Ψ_{pc} follows similar daily trends, with slight differences between the MT and PC methods in both irrigation regimes. The Ψ_{pc} consistently recorded more negative values than the Ψ_{mt} ones, particularly during early afternoon when transpiration demand peaked (Fig. 5). However, this discrepancy tends to reduce at higher values of stem water potential (Di Biase et al., 2025; Pagay, 2022; Zucchini et al., 2023), indicating better alignment between the two methods. Our findings showed an average 0.66 MPa offset in the afternoon between Ψ_{pc} and Ψ_{mt}. The lowest Ψ_{mt} values were usually recorded between 16:00 and 17:00, while the lowest Ψ_{pc} values were recorded at 14:00, showing a time-lag regardless of the irrigation regime adopted. Similar lags between Ψ_{mt} and Ψ_{pc} can also be observed in Pagay (2022) for grapevine.

The observed time shift in the Ψ_{mt} response compared to Ψ_{pc} denotes a slower dynamic behaviour, indicating a marked time constant of the microtensiometer, which could be linked to its intrinsic characteristic or the result of the whole complex sensor installation (the sensor itself, the mating paste and wood characteristics), as observed by Lakso et al. (2022). The slow sensor response not only determines a lag in the timing of minimum values but can also be the cause of overestimation of Ψ_{mt} relative to Ψ_{pc}, as a consequence of the smoothing effect exerted by the sensor (or the sensor-tree complex) time constant on the expected true signal of the tree water potential (Ψ_{stem}), acting as a "first-order filter" (similar to a resistance-capacitance network, under the assumption that the Ohm's law analogy holds).

On the contrary, the Ψ_{stem} time-course can be more closely approximated by Ψ_{pc}. While it is arguable that neither Ψ_{mt} or Ψ_{pc} can be assumed as the "true" Ψ_{stem}, since manual readings of water potential (leaf or stem) by pressure chamber is well known to be biased by a significant "operator effect" (Turner, 1988; Levin, 2019), these factors primarily affect only the absolute value of Ψ_{pc} rather than the temporal dynamics. In this sense, differently from Ψ_{mt}, a zero-time lag can be assumed between Ψ_{pc} and the actual Ψ_{stem}.

Sensor time constant (τ) was reported by Lakso et al. (2022) as less than 15 minutes for the sensor itself; however, the Authors recognise that the τ value of the complex "sensor - mating paste - plant tissue" is difficult to determine, and it may vary on a species- or even plant-basis. Additionally, they highlighted that such an effect could sum up to stem capacitance effects and wood characteristics, to be specifically addressed. A non-zero sensor time constant implies a time lag in Ψ_{mt} vs. Ψ_{pc} readings, particularly during the most dynamic parts of the day when rapid changes in Ψ_{stem} following transpiration demand peaks occur. However, Lakso et al. (2022) reported a good correlation with maximal (pre-dawn) and minimal (afternoon) values (i.e., the values occurring in the less dynamic parts of the day), which are the most relevant values for irrigation management.

In the present study, Ψ_{mt} and Ψ_{pc} in mandarin trees were significantly correlated under both irrigation regimes ($R^2 = 0.62$, p <0.0001, for SDI tree and $R^2 = 0.63$, p <0.0001, for SPR). However, the slopes of the linear regression lines (Fig. 7) deviated from the identity line, indicating a dissimilarity between the two methods. Similar deviations have been reported in other woody crops, such as grapevines (Pagay, 2022), olive orchards (Zucchini et al., 2023) and orange orchards (Vanella et al., 2025). In contrast, near-unity slopes have been observed in smaller or well-watered annual crops, such as nectarines (Conesa et al., 2023) and cotton (Christenson et al., 2024). For cotton, in particular, the stronger agreement could be related to its smaller canopy size, compared to the mandarin tree, which allows microtensiometers to better reflect the whole plant water potential (Blanco and Kalcsits, 2021; Pagay, 2022).

The slopes of the linear regression lines (Fig. 7) observed in our study suggest that Ψ_{mt} changed at a more attenuated extent compared to the Ψ_{pc}, resulting in a systematic overestimation of Ψ_{stem} compared to Ψ_{pc} readings. From a practical point of view, this aspect does not necessarily preclude the use of Ψ_{mt} for irrigation management in mandarin orchards. However, appropriate adjustments are required to account for the low (less-than-one) slope values of the regression lines, as observed under both SDI and SPR irrigation regimes. Similar conclusions were expressed by other Authors (e.g., Pagay, 2022; Conesa et al., 2023) who suggested that, in cases where absolute Ψ_{stem} values are required, the need for crop-specific thresholds is necessary for integrating Ψ_{mt} into irrigation scheduling protocols.

The varying degrees of scattering observed in tree-based measurements, such as Ψ_{mt} vs VPD or ETo, may be linked to the differing levels of dynamic coupling between tree-level processes and changes in atmospheric variables influenced by the irrigation regime. The time lags between tree water potential, estimated by microtensiometer, and atmospheric variables like ETo or VPD create hysteresis-like patterns that may add up to other better-known sources of hysteresis (Wan et al., 2023; Zhang, 2014; Tuzet et al., 2003; Phillips, 1997). This raises the need for a careful assessment of these effects to evaluate the reliability of microtensiometer data as an indicator of water status in mandarin trees. In this sense, it is necessary to consider the importance of the timing of readings. Lags in diurnal changes in Ψ_{mt} compared to VPD (Fig. 5) or other atmospheric demand variables, such as ETo (Fig. 9), need to be properly addressed, considering both the diurnal and seasonal effects. Hourly Ψ_{mt} values can be used to identify the daily time lag, using the cross-correlation coefficient (Fig. 9). Over the season, a decrease in the maximum cross-correlation coefficient could be observed for both irrigation regimes. Such a decrease paralleled the seasonal reduction of ETo (Fig. 2), but other effects could be involved (Kaner et al., 2020; Phillips et al., 2004; Vogel et al., 2017) since time constant effects can be modulated by changes in physiological aspects other than capacitance (Zhuang et al., 2014).

The substantial time shift and signal attenuation observed across both years make the direct use of raw MT signals as a proxy for Ψ_{stem} challenging. The minimum

Ψ_{mt} occurred up to two hours after the observed Ψ_{pc} minimum, while signal attenuation led to systematic overestimation of Ψ_{stem} due to the first-order response characteristics of the sensor-tree complex. Indications of the presence of such features in the dynamic response of MT sensors and about the difference in the technical behaviour of sensors when characterized in laboratory (with a 15-minutes time shift) in comparison to their response when installed on the tree were reported by Lakso et al. (2022), stating the need to consider the output signal as the result of the interaction of the xylem with the sensor and the interfacing compound. Other subsequent studies (Di Biase et al., 2025; Zucchini et al., 2023; Pagay, 2022) reported the presence of such effects and their impact on the correlations between Ψ_{mt} and Ψ_{pc} on different species. In the present study on mandarin citrus, such effects had a large impact on the possibility of a direct comparison of Ψ_{mt} vs. Ψ_{pc}.

At a more general level, directly comparing Ψ_{mt} and Ψ_{pc} in the presence of large time constants would be problematic, particularly on an hourly basis. The predictable differences between signals due to the substantial time shifts observed (up to two hours in this study) would make comparisons with currently published irrigation thresholds of limited practical value. Moreover, a comparison with measurements taken in a specific moment of the day, such as the commonly used "midday" or "pre-dawn" Ψ_{stem}, would discard the valuable time information provided by MTs. Under these ideas, an appropriate characterisation of the dynamic behaviour of the sensor-tree interaction as a composite system could provide a useful insight of trees' condition. In this context, the time constant should not be viewed merely as a hindrance to sensor adoption, but rather as an informative indicator of tree physiological status. Both the time shift and time constant demonstrated sensitivity to different irrigation regimes in the present study, as shown in Fig. 10. Developing suitable models of the sensor-tree complex's dynamic response to environmental variables would significantly improve the quality of information obtainable from MTs by fully utilising the temporal information provided by the sensors.

Overall, these findings underscore that microtensiometers provide valuable high-resolution monitoring of tree water status, yet their integration into irrigation scheduling protocols requires a sophisticated understanding of the temporal coupling between plant water potential and evaporative demand. This consideration becomes even more critical when attempting to predict stem water potential indirectly from its relationship with environmental drivers such as VPD or ETo, particularly in scenarios where the use of microtensiometers is limited by technical constraints or economic inaccessibility, particularly for small-scale growers.

4.1. Limitations and future research

Continuous MT readings captured stem water potential dynamics with high temporal resolution, demonstrating their potential to rapidly detect physiological responses that could be missed by discrete pressure chamber data. These findings support the use of in situ microtensiometers as reliable tools for real-time irrigation scheduling and stress monitoring under fluctuating environmental conditions. However, several practical limitations were also observed.

In both irrigation seasons, unrealistic Ψ_{mt} values were observed in late September, likely due to water infiltration into the sensor insulation that degraded after 2−3 months of operation. Figure 11a illustrates the MT failure that occurred in 2023 following consecutive rainfall events. Additionally, in 2023, a second monitored mandarin tree under the SDI plot experienced sensor malfunction following the two consecutive days of elevated VPD (Fig. 11b, black arrows). The Ψ_{mt} readings deviated from expected patterns, suggesting poor xylem contact or internal disconnection. Notably, reinstallation of the sensor was unsuccessful in restoring signal continuity (Fig. 11b, red arrow).

Our findings indicate that predawn Ψ_{mt}, as the most stable indicator unaffected by diurnal or plant-driven fluctuations (i.e., the sensor-tree-complex response), can be used for real-time irrigation management of mandarin orchards in Mediterranean climates under well-watered conditions, with a threshold of −0.51 ± 0.09 MPa. To define physiologically meaningful thresholds of Ψ_{pd} and Ψ_{md} for irrigation scheduling and support the implementation of water-saving strategies such as regulated deficit irrigation, further research is warranted.

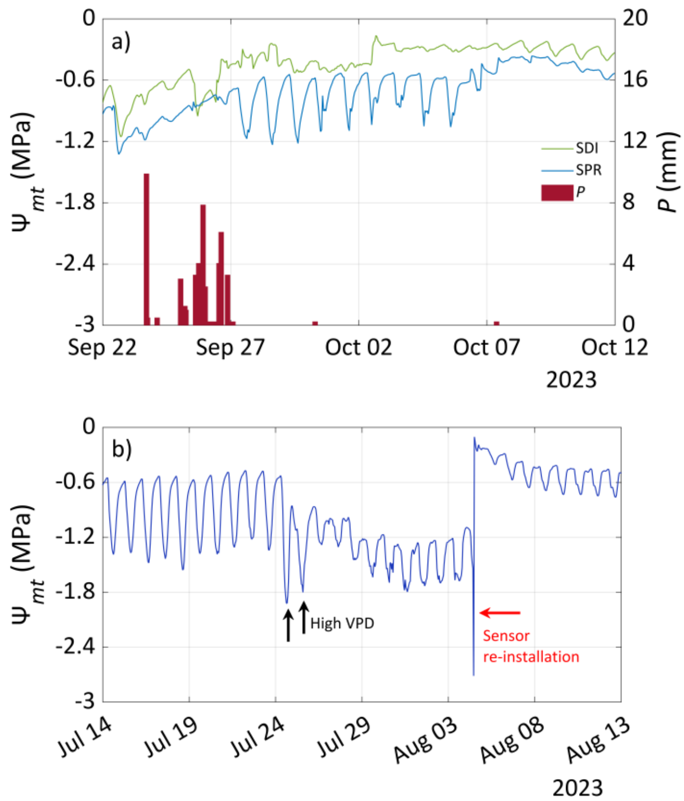

Fig. 11 *Observed limitations of MT:* ***a)*** *sensor failure following a sequence of precipitation events in late September 2023, and* ***b)*** *sensor failure following high VPD events (black arrows) for another monitored tree of the SDI plot (red arrow indicates sensor re-installation)*

In particular, a comprehensive assessment incorporating stem water potential, soil water content, and transpiration rate, will be essential to characterise the water status across a range of stress levels (from moderate to severe) and to evaluate the hydraulic responses of mandarin trees under different SWC conditions, such as those observed in the SPR plot, where greater variation in Ψ_{pd} and Ψ_{md} occurs (Table 1).

5. Conclusions

This study demonstrates the potential of microtensiometers as a reliable tool for continuously monitoring stem water potential (Ψ_{stem}) in *C. reticulata* under Mediterranean climate conditions and different irrigation regimes. The high temporal resolution of microtensiometers' readings (Ψ_{mt}) allows the detection of diurnal variations in plant water status, reflecting the combined effect of atmospheric demand, soil water content, and irrigation management. Frequent irrigation via subsurface drip irrigation ensured a more stable Ψ_{mt} and a tighter coupling between plant and atmospheric conditions. Whereas the ordinary low-frequency irrigation scheduling via micro-sprinkler resulted in greater variability and stronger dependence on soil water availability. The comparison between Ψ_{mt} and conventional pressure chamber readings (Ψ_{pc}) revealed a significant correlation, although differences in magnitude and timing were observed. Following an external disturbance induced by shading of the tree, Ψ_{pc} and Ψ_{mt} responded similarly in trend but differed substantially in dynamics, with Ψ_{pc} reacting promptly to microclimate changes, while Ψ_{mt} exhibited a delayed and smoothed response. This delay, quantified through the markedly higher time constant of Ψ_{mt} compared to Ψ_{pc}, reflects the slower response of the microtensiometer sensor-tree complex as a whole, leading to overestimation of Ψ_{stem} when compared to pressure chamber estimations. These findings suggest that the first-order dynamics of the sensor-tree-complex response signal hinder the direct use of Ψ_{mt} as a direct replacement of pressure-chamber Ψ_{stem} measurements. Consequently, compensation protocols accounting for a large time constant should be developed to apply Ψ_{mt} readings to currently published crop-specific Ψ_{stem} thresholds for irrigation scheduling protocols, generally obtained by pressure chamber, that could suitably take into account the full dynamics of the signal. In this respect, the sensitivity shown by Ψ_{mt} time constant to different irrigation regimes and the changes occurring within each irrigation cycle seems to be a promising feature of MTs that could allow for making full use of the timing information provided by the sensor, continuous by nature, in contrast to the point measurements as “midday” and “pre-dawn” water potentials.

6. References

Allen, R.G., Pereira, L.S., Raes, D., Smith, M., 1998. Crop evapotranspiration. FAO Irrig Drain Pap 56. 65–88

Appiah, S.A., Li, J., Lan, Y., Darko, R.O., Alordzinu, K.E., Al Aasmi, A., Asenso, E., Issaka, F., Afful, E.A., Wang, H., Qiao, S., 2022. Real-Time Assessment of Mandarin Crop Water Stress Index. Sensors 22, 4018. https://doi.org/10.3390/s22114018

Bader, M.K. -F., Ehrenberger, W., Bitter, R., Stevens, J., Miller, B.P., Chopard, J., Rüger, S., Hardy, G.E.S.J., Poot, P., Dixon, K.W., Zimmermann, U., Veneklaas, E.J., 2014. Spatio-temporal water dynamics in mature *Banksia menziesii* trees during drought. Physiol. Plant. 152, 301–315. https://doi.org/10.1111/ppl.12170

Ballester, C., Castel, J., Intrigliolo, D.S., Castel, J.R., 2011. Response of Clementina de Nules citrus trees to summer deficit irrigation. Yield components and fruit composition. Agric. Water Manag. 98, 1027–1032. https://doi.org/10.1016/j.agwat.2011.01.011

Bengtsson, L., Enell, M., 1986. Chemical analysis. Handbook of Holocene palaeoecology and palaeohydrology: 423-451.

Blanco, V., Kalcsits, L., 2023. Long-term validation of continuous measurements of trunk water potential and trunk diameter indicate different diurnal patterns for pear under water limitations. Agric. Water Manag. 281, 108257. https://doi.org/10.1016/j.agwat.2023.108257

Bulut, R., Leong, E., 2008. Indirect measurement of suction. Geotechnical and Geological Engineering 26: 21–32.

Cahn, M., Hutmacher, R., 2024. Subsurface drip irrigation. Microirrigation for Crop Production. Elsevier Science, pp 257–301

Camp, C.R., 1998. Subsurface drip irrigation: a review. Trans. ASAE 41, 1353–1367. https://doi.org/10.13031/2013.17309

Capurro, M.C., Ham, J.M., Kluitenberg, G.J., Comas, L., Andales, A.A., 2024. A novel sap flow system to measure maize transpiration using a heat pulse method. Agric. Water Manag. 301, 108963. https://doi.org/10.1016/j.agwat.2024.108963

Cermak, J., Matyssek, R., Kucera, J., 1993. Rapid response of large, drought-stressed beech trees to irrigation. Tree Physiol. 12, 281–290. https://doi.org/10.1093/treephys/12.3.281

Chatfield, C., Xing, H., 2019. The analysis of time series: an introduction with R. Chapman & Hall/CRC texts in statistical science series, Seventh edition. edn. CRC Press, Taylor & Francis Group, Boca Raton

Choné, X., 2001. Stem Water Potential is a Sensitive Indicator of Grapevine Water Status. Ann. Bot. 87, 477–483. https://doi.org/10.1006/anbo.2000.1361

Christenson, C.G., Gohardoust, M.R., Calleja, S., Thorp, K.R., Tuller, M., Pauli, D., 2024. Monitoring cotton water status with microtensiometers. Irrig. Sci. 42, 995–1011. https://doi.org/10.1007/s00271-024-00930-w

Ciais, Ph., Reichstein, M., Viovy, N., Granier, A., Ogée, J., Allard, V., Aubinet, M., Buchmann, N., Bernhofer, Chr., Carrara, A., Chevallier, F., De Noblet, N., Friend, A.D., Friedlingstein, P., Grünwald, T., Heinesch, B., Keronen, P., Knohl, A., Krinner, G., Loustau, D., Manca, G., Matteucci, G., Miglietta, F., Ourcival, J.M., Papale, D., Pilegaard, K., Rambal, S., Seufert, G., Soussana, J.F., Sanz, M.J., Schulze, E.D., Vesala, T., Valentini, R., 2005. Europe-wide reduction in primary productivity caused by the heat and drought in 2003. Nature 437, 529–533. https://doi.org/10.1038/nature03972

Clearwater, M.J., Goldstein, G., 2005. Embolism Repair and Long Distance Water Transport, in: Vascular Transport in Plants. Elsevier, pp. 375–399. https://doi.org/10.1016/B978-012088457-5/50020-4

Conesa, M.R., Conejero, W., Vera, J., Ruiz-Sánchez, M.C., 2023. Assessment of trunk microtensiometer as a novel biosensor to continuously monitor plant water status in nectarine trees. Front. Plant Sci. 14, 1123045. https://doi.org/10.3389/fpls.2023.1123045

Dainese, R., De Cfl Lopes, B., Tedeschi, G., Lamarque, L.J., Delzon, S., Fourcaud, T., Tarantino, A., 2022. Cross-validation of the high-capacity tensiometer and thermocouple psychrometer for continuous monitoring of xylem water potential in saplings. J. Exp. Bot. 73, 400–412. https://doi.org/10.1093/jxb/erab412

Dane, J H., Hopmans, J.W., Topp, G.C., 2002. Pressure plate extractor. Methods of soil analysis: Physical methods. 3rd ed. Madison: Soil Science Society of America, 688-90.

Dean, W.E., 1974. Determination of carbonate and organic matter in calcareous sediments and sedimentary rocks by loss on ignition; comparison with other methods. J. Sediment. Res. 44(1), 242-248.

Di Biase, R., Calabritto, M., Mininni, A.N., Montanaro, G., Dichio, B., 2025. Microtensiometer-based trunk water potential as a plant water status indicator in kiwifruit under different soil water availability. Irrig. Sci. https://doi.org/10.1007/s00271-025-01020-1

Dzikiti, S., Verreynne, J.S., Stuckens, J., Strever, A., Verstraeten, W.W., Swennen, R., Coppin, P., 2010. Determining the water status of Satsuma mandarin trees [Citrus Unshiu Marcovitch] using spectral indices and by combining hyperspectral and physiological data. Agric. For. Meteorol. 150, 369–379. https://doi.org/10.1016/j.agrformet.2009.12.005

Fernández, J.E., 2014. Plant-based sensing to monitor water stress: Applicability to commercial orchards. Agric. Water Manag.

Galindo, A., Collado-González, J., Griñán, I., Corell, M., Centeno, A., Martín-Palomo, M.J., Girón, I.F., Rodríguez, P., Cruz, Z.N., Memmi, H., Carbonell-Barrachina, A.A., Hernández, F., Torrecillas, A., Moriana, A., Pérez-López, D., 2018. Deficit irrigation and emerging fruit crops as a strategy to save water in Mediterranean semiarid agrosystems. Agric. Water Manag. 202, 311–324. https://doi.org/10.1016/j.agwat.2017.08.015

García-Tejero, I., Romero-Vicente, R., Jiménez-Bocanegra, J.A., Martínez-García, G., Durán-Zuazo, V.H., Muriel-Fernández, J.L., 2010. Response of citrus trees to deficit irrigation during different phenological periods in relation to yield, fruit quality, and water productivity. Agric. Water Manag. 97, 689–699. https://doi.org/10.1016/j.agwat.2009.12.012

Gonzalez-Altozano, P., Castel, J.R., 1999. Regulated deficit irrigation in 'Clementina de Nules' citrus trees. I. Yield and fruit quality effects. J Hortic Sci Biotechnol 74(6):706–713

Gonzalez Nieto, L., Huber, A., Gao, R., Biasuz, E.C., Cheng, L., Stroock, A.D., Lakso, A.N., Robinson, T.L., 2023. Trunk Water Potential Measured with Microtensiometers for Managing Water Stress in "Gala" Apple Trees. Plants 12, 1912. https://doi.org/10.3390/plants12091912

Hacke, U.G., Sperry, J.S., 2001. Functional and ecological xylem anatomy. Perspectives in plant ecology, evolution and systematics, 4(2), 97-115.

Jamshidi, S., Zand-Parsa, S., Niyogi, D., 2021. Physiological responses of orange trees subject to regulated deficit irrigation and partial root drying. Irrig. Sci. 39, 441–455. https://doi.org/10.1007/s00271-020-00709-9

Jones, H.G., 2004. Irrigation scheduling: advantages and pitfalls of plant-based methods. J. Exp. Bot. 55, 2427–2436. https://doi.org/10.1093/jxb/erh213

Kaner, A., Preisler, Y., Grünzweig, J.M., Mau, Y., 2020. Internal water storage buffering maintains plant function under drought as described by a general hydraulic model. https://doi.org/10.1101/2020.02.11.943563

Lakso, A.N., Santiago, M., Stroock, A.D., 2022. Monitoring Stem Water Potential with an Embedded Microtensiometer to Inform Irrigation Scheduling in Fruit Crops. Horticulturae 8, 1207. https://doi.org/10.3390/horticulturae8121207

Lamm, F.R., Colaizzi, P.D., Sorensen, R.B., Bordovsky, J.P., Dougherty, M., Balkcom, K., Zaccaria, D., Bali, K.M., Rudnick, D.R., Peters, R.T., 2021. A 2020 Vision of Subsurface Drip Irrigation in the U.S. Trans. ASABE 64, 1319–1343. https://doi.org/10.13031/trans.14555

Levin, A.D., 2019. Re-evaluating pressure chamber methods of water status determination in field-grown grapevine (Vitis spp.). Agric. Water Manag. 221, 422–429. https://doi.org/10.1016/j.agwat.2019.03.026

Lundblad, M., Lagergren, F., Lindroth, A., 2001. Evaluation of heat balance and heat dissipation methods for sapflow measurements in pine and spruce. Ann. For. Sci. 58, 625–638. https://doi.org/10.1051/forest:2001150

Mancha, L., Uriarte, D., Prieto, M., 2021. Characterization of the Transpiration of a Vineyard under Different Irrigation Strategies Using Sap Flow Sensors. Water 13, 2867. https://doi.org/10.3390/w13202867

Martínez-Gimeno, M.A., Castiella, M., Rüger, S., Intrigliolo, D.S., Ballester, C., 2017. Evaluating the usefulness of continuous leaf turgor pressure measurements for the assessment of Persimmon tree water status. Irrig. Sci. 35, 159–167. https://doi.org/10.1007/s00271-016-0527-3

Mayr, S., 2021. Relevance of time and spatial scales in plant hydraulics. Tree Physiol. 41, 1781–1784. https://doi.org/10.1093/treephys/tpab093

Monteith, J.L., Unsworth, M.H., 2008. Principles of Environmental Physics. Plants, Animals, and the Atmosphere. Academic Press.

Nobel, P.S., 2009. Physicochemical and Environmental Plant Physiology. Fourth edition. Chapter 9 - Plants and Fluxes, Pages 438-505. Academic Press.

Ortuño, M.F., García-Orellana, Y., Conejero, W., Ruiz-Sánchez, M.C., Alarcón, J.J., Torrecillas, A., 2006. Stem and leaf water potentials, gas exchange, sap flow, and trunk diameter fluctuations for detecting water stress in lemon trees. Trees 20, 1–8. https://doi.org/10.1007/s00468-005-0004-8

Pagay, V., 2022. Evaluating a novel microtensiometer for continuous trunk water potential measurements in field-grown irrigated grapevines. Irrig. Sci. 40, 45–54. https://doi.org/10.1007/s00271-021-00758-8

Pagay, V., Santiago, M., Sessoms, D.A., Huber, E.J., Vincent, O., Pharkya, A., Corso, T.N., Lakso, A.N., Stroock, A.D., 2014. A microtensiometer capable of measuring water potentials below -10 MPa. Lab Chip 14, 2806–2817. https://doi.org/10.1039/C4LC00342J

Phillips, N., Nagchaudhuri, A., Oren, R., Katul, G., 1997. Time constant for water transport in loblolly pine trees estimated from time series of evaporative demand and stem sapflow. Trees 11, 412. https://doi.org/10.1007/s004680050102

Phillips, N.G., Oren, R., Licata, J., Linder, S., 2004. Time series diagnosis of tree hydraulic characteristics. Tree Physiol. 24, 879–890. https://doi.org/10.1093/treephys/24.8.879

Poggi, I., Polidori, J.J., Gandoin, J.M., Paolacci, V., Battini, M., Albertini, M., Améglio, T., Cochard, H., 2007. Stomatal regulation and xylem cavitation in Clementine (*Citrus clementina* Hort) under drought conditions. The Journal of Horticultural Science and Biotechnology, 82(6), 845–848. https://doi.org/10.1080/14620316.2007.11512316

Provenzano, G., 2007. Using HYDRUS-2D Simulation Model to Evaluate Wetted Soil Volume in Subsurface Drip Irrigation Systems. J. Irrig. Drain. Eng. 133, 342–349. https://doi.org/10.1061/(ASCE)0733-9437(2007)133:4(342)

Quick, D.D., Espino, S., Morua, M.G., Schenk, H.J. 2016. Effects of thermal gradients in sapwood on stem psychrometry. In International Symposium on Sensing Plant Water Status-Methods and Applications in Horticultural Science 1197 (pp. 23-30)

Rabbel, I., Diekkrüger, B., Voigt, H., Neuwirth, B., 2016. Comparing ΔTmax Determination Approaches for Granier-Based Sapflow Estimations. Sensors 16, 2042. https://doi.org/10.3390/s16122042

Rallo, G., González-Altozano, P., Manzano-Juárez, J., Provenzano, G., 2017. Using field measurements and FAO-56 model to assess the eco-physiological response of citrus orchards under regulated deficit irrigation. Agric. Water Manag. 180, 136–147. https://doi.org/10.1016/j.agwat.2016.11.011

Ravikumar, V., 2023. Sprinkler and drip irrigation: theory and practice. Springer Nature, Cham

Rawlins, S.L., 1966. Theory for thermocouple psychrometers used to measure water potential in soil and plant samples. Agricultural Meteorology, 3(5-6), 293-310

Romero-Trigueros, C., Gambín, J.M.B., Nortes Tortosa, P.A., Cabañero, J.J.A., Nicolás Nicolás, E., 2021. Isohydricity of Two Different Citrus Species under Deficit Irrigation and Reclaimed Water Conditions. Plants 10, 2121. https://doi.org/10.3390/plants10102121

Scholander, P.F., Bradstreet, E.D., Hemmingsen, E.A., Hammel, H.T., 1965. Sap Pressure in Vascular Plants: Negative hydrostatic pressure can be measured in plants. Science 148, 339–346. https://doi.org/10.1126/science.148.3668.339

Schönbeck, L.C., Schuler, P., Lehmann, M.M., Mas, E., Mekarni, L., Pivovaroff, A.L., Turberg, P., Grossiord, C., 2022. Increasing temperature and vapour pressure deficit lead to hydraulic damages in the absence of soil drought. Plant Cell Environ. 45, 3275–3289. https://doi.org/10.1111/pce.14425

Singh, V.P., Su, Q., 2022. Irrigation engineering. Principles, processes, procedures, design, and management. Cambridge University Press, Cambridge

Turner, N.C., 1988. Measurement of plant water status by the pressure chamber technique. Irrig. Sci. 9, 289–308. https://doi.org/10.1007/BF00296704

Tuzet, A., Perrier, A., Leuning, R., 2003. A coupled model of stomatal conductance, photosynthesis and transpiration. Plant Cell Environ. 26, 1097–1116. https://doi.org/10.1046/j.1365-3040.2003.01035.x

Vanella, D., Guarrera, S., Ferlito, F., Longo-Minnolo, G., Milani, M., Pappalardo, G., Nicolosi, E., Giuffrida, A.G., Torrisi, B., Las Casas, G., Consoli, S., 2025. Effects of organic mulching and regulated deficit irrigation on crop water status, soil and yield features in an orange orchard under Mediterranean climate. Sci. Total Environ. 958, 177528. https://doi.org/10.1016/j.scitotenv.2024.177528

Venturin, A.Z., Guimarães, C.M., Sousa, E.F.D., Machado Filho, J.A., Rodrigues, W.P., Serrazine, Í.D.A., Bressan-Smith, R., Marciano, C.R., Campostrini, E., 2020. Using a crop water stress index based on a sap flow method to estimate water status in conilon coffee plants. Agric. Water Manag. 241, 106343. https://doi.org/10.1016/j.agwat.2020.106343

Vogel, T., Votrubova, J., Dohnal, M., Dusek, J., 2017. A Simple Representation of Plant Water Storage Effects in Coupled Soil Water Flow and Transpiration Stream Modeling. Vadose Zone J. 16, 1–10. https://doi.org/10.2136/vzj2016.12.0128

Wan, L., Zhang, Q., Cheng, L., Liu, Y., Qin, S., Xu, J., Wang, Y., 2023. What determines the time lags of sap flux with solar radiation and vapor pressure deficit? Agric. For. Meteorol. 333, 109414. https://doi.org/10.1016/j.agrformet.2023.109414

Yang, Y., Guan, H., Hutson, J.L., Wang, H., Ewenz, C., Shang, S., Simmons, C.T., 2013. Examination and parameterization of the root water uptake model from stem water potential and sap flow measurements. Hydrol. Process. 27, 2857–2863. https://doi.org/10.1002/hyp.9406

Ye, M., Zhao, X., Biswas, A., Huo, G., Yang, B., Zou, Y., Siddique, K.H.M., Gao, X., 2021. Measurements and modeling of hydrological responses to summer pruning in dryland apple orchards. J. Hydrol. 594, 125651. https://doi.org/10.1016/j.jhydrol.2020.125651

Zhang, X., Yang, H., Shukla, M.K., Du, T., 2023. Proposing a crop-water-salt production function based on plant response to stem water potential. Agric. Water Manag. 278, 108162. https://doi.org/10.1016/j.agwat.2023.108162

Zhuang, J., Yu, G.-R., Nakayama, K., 2014. A Series RCL Circuit Theory for Analyzing Non-Steady-State Water Uptake of Maize Plants. Sci. Rep. 4, 6720. https://doi.org/10.1038/srep06720

Zimmermann, D., Reuss, R., Westhoff, M., Geßner, P., Bauer, W., Bamberg, E., Bentrup, F.-W., Zimmermann, U., 2008. A novel, non-invasive, online-monitoring, versatile and easy plant-based probe for measuring leaf water status. J. Exp. Bot. 59, 3157–3167. https://doi.org/10.1093/jxb/ern171

Zucchini, M., Guzmán-Delgado, P., Santos, E., Synstelien, T., Marino, G., 2023. Preliminary observations on the use of microtensiometers to continuously measure water potential in a mature olive orchard, in: 2023 IEEE International Workshop on Metrology for Agriculture and Forestry (MetroAgriFor). Presented at the 2023 IEEE International Workshop on Metrology for

Agriculture and Forestry (MetroAgriFor), IEEE, Pisa, Italy, pp. 268–272. https://doi.org/10.1109/MetroAgriFor58484.2023.10424405

General conclusion and future outlook

The doctoral research activity presented in this thesis contributed to advancing the understanding and optimisation of drip irrigation systems by integrating hydraulic systems design, soil-water dynamics, and plant water status monitoring. Through the combined use of analytical, numerical, and experimental approaches, the studies collectively addressed the dual challenge of improving water and energy-use efficiency in Mediterranean agricultural contexts.

From a hydraulic systems design perspective, for planar rectangular units of fixed geometry, the comparative analysis between open and closed irrigation circuits demonstrated that the adoption of looped configurations can significantly reduce inlet pressure head by up to 58% at equal pressure head tolerances, directly lowering pumping energy. The proposed predictive relationship of h_{ratio} accurately estimates the potential energy savings achievable by closing an open circuit with a secondary manifold, offering an operational tool that obviates iterative approaches such as the Hardy Cross method. In practical terms, the predictive relationship of h_{ratio} makes it possible to (i) examine closed circuits quickly compared with the corresponding open circuits, and (ii) to determine, from an energy-saving perspective, when it is advantageous to design with a looped network, and when it is not, an aspect that has not been previously addressed. Future work should extend the open-closed circuits comparison to sloped rectangular units to quantify the potential energy savings achievable and, for both planar and sloped cases, embed a cost-benefit analysis to identify the manifold pressure tolerance thresholds at which net benefits begin and are maximised, across different unit configurations obtained by varying the geometry of drip irrigation systems.

The quantification of local losses due to root intrusion and back pressure provided insights into the long-term hydraulic behaviour of subsurface drip irrigation systems. The modified Hardy Cross method developed in this research, which accounts for the Hazen-Williams resistance law, local losses and back pressure, enables practitioners an accurate assessment of hydraulic systems' performance over time, provided by the monitoring of inlet pressure head and flow rates. Specifically, this study highlights the high efficiency of emitters embedded with specific root-growth inhibitors, particularly He 1 and He 2, offering a diagnostic approach to analyse hydraulic system longevity. To further validate emitter performance over time, the same assessment should be repeated after an additional observation period, including the extraction of emitters from the four different treated subsurface drip irrigation subunits for inspection and validation of the results. Given that pressure-compensating emitters were employed in this research, it would also be valuable to examine the durability of the compensation mechanism by measuring the discharges of emitters removed from their buried position under a range of operating pressure heads.

The analysis of how soil hydraulic variability influences the shapes of wetting bulb expansion under both surface and subsurface drip irrigation highlights the central role of rigorous field characterisation. By dimensionally reformulating Philip's (1984) analytical model, results showed that buried emitters require lower application volumes than surface emitters, thus evidencing the high water-use efficiency. Furthermore, the natural spatial variability in soil hydraulic properties produced marked changes in bulb geometry, with a stronger effect on vertical than on horizontal expansion; accounting for this variability is therefore essential to limit deep percolation losses. Practically, this supports the recommendations that, where feasible, soil-hydraulic-characteristic-informed design and scheduling should be adopted by adjusting irrigation duration to wet the rootzone and, at the design stage, selecting emitter spacing to avoid overlap between wetted bulbs. Moreover, calibrating the k parameter used to define the average soil water content of the Philip model further improved predictions of wetting-front dynamics, which can improve design-stage estimates of application volume and emitter placement. Looking ahead, in the context of heterogeneous soils, research efforts should be focused on designing drip irrigation systems to accommodate spatial soil hydraulics variability, e.g., through variable-flow-rate emitters tailored to mapped soil zones. While such designs are demanding, as they require high-resolution soil hydraulic information, they offer a practical path toward minimising losses and maximising irrigation efficiency. Additionally, to analyse how the k parameter relates to soil physics or water retention curves, since it is affected solely by the irrigation history, supplementary investigations across different types of soils would be required. This could be a valuable objective for future research efforts.

At the plant level, use of microtensiometers proved effective for real-time monitoring of stem water potential (Ψ_{stem}) in mandarin trees. Despite operational failures occasionally triggered by high VPD or intense rainfall, the results showed a significant correlation between microtensiometer and Scholander pressure-chamber Ψ_{stem} measurements, albeit with a systematic overestimation and a phase delay of two hours. This behaviour was attributed to the first-order response of the sensor-plant complex, which attenuates and lags changes in water potential driven by atmospheric demand, yielding a measurable time constant. Notably, in the subsurface drip irrigation regime, the time constant resulted fairly stable, with minor fluctuations during the observation period, whereas in the micro-sprinkler regime, daily time constant changes exhibited a distinctive pattern within the farmer's irrigation cycle, decreasing progressively in the days following irrigation, then increasing sharply after the subsequent irrigation event. This indicates that the time constant can function as an operational marker of evolving plant water status and a practical parameter for irrigation decision-making, helping refine pressure-chamber thresholds. Moreover, predawn microtensiometer measurements of Ψ_{stem} emerged as the most stable indicator, largely unaffected by diurnal or plant-driven fluctuations, and can guide real-time irrigation of mandarin orchards in Mediterranean climates under well-watered conditions, with a threshold of -0.51 ± 0.09 MPa. To establish physiologically robust thresholds for both predawn and midday Ψ_{stem}, and to operationalise the time constant from the first-order sensor-plant response as a control variable, future research should integrate concurrent measurements of Ψ_{stem}, soil water content, and transpiration to characterise plant water status across stress levels from moderate to severe, thereby supporting water-saving strategies such as regulated deficit irrigation.

Overall, the PhD research presented in this thesis contributes to optimising drip irrigation system hydraulic performance, elucidating soil-water dynamics, and refining plant-based irrigation management. Collectively, these advances improve both water and energy use efficiency, promoting a more integrated and sustainable management of water and energy resources in Mediterranean agriculture, particularly in Citrus orchards.